

Versuchsanstalt für Wasserbau
Hydrologie und Glaziologie
der Eidgenössischen
Technischen Hochschule Zürich

Mitteilungen

257

Fish protection and fish guidance at water intakes using innovative curved-bar rack bypass systems

Claudia Beck

Zürich, 2020

Herausgeber: Prof. Dr. Robert Boes

ETH zürich

Zitiervorschlag für VAW-Mitteilungen:

Beck, C. (2020).

Fish protection and fish guidance at water intakes using innovative curved-bar rack bypass systems

VAW-Mitteilungen 257, Versuchsanstalt für Wasserbau, Hydrologie und Glaziologie (VAW), (R. M. Boes, ed.), ETH Zürich, Schweiz.

Im Eigenverlag der
Versuchsanstalt für Wasserbau,
Hydrologie und Glaziologie
ETH Zürich
CH-8093 Zürich

Tel.: +41 - 44 - 6 32 4091
Fax: +41 - 44 - 6 32 1192
e-mail: info@vaw.baug.ethz.ch

Zürich, 2020

ISSN 0374-0056

Preface

Transverse structures on rivers, e.g. hydropower plants, weirs and dams, are obstacles for migrating fish, both in upstream and downstream directions, impeding or delaying the free fish movement in many, often highly fragmented rivers. Whereas upstream fish movements have often been accounted for by constructing fish passes as early as the 1880s in Switzerland, i.e. with the advent of hydropower for electricity generation, the awareness of the need for fish protection for downstream moving fish is quite recent in most of Europe including Switzerland. The current Swiss Waters Protection Act requires rehabilitation measures at more than 700 obstacles for downstream movement to prevent or limit fish injury and mortality. The safe downstream passage is particularly important for diadromous species migrating long distances between the sea and freshwater systems, e.g. the European eel and Atlantic salmon, who often have to pass a series of hydropower plants, resulting in elevated cumulative mortality. In contrast to small hydropower plants with discharges up to about 100 m³/s, there is currently hardly any proven technology for the protection of the wide variety of indigenous fish fauna at run-of-river plants with larger design flows. This poses a special conflict of interest between preservation of fish and the generation of climate-friendly hydroelectricity. For this reason, VAW has been conducting research on effective fish protection measures since 2011 with a first project on modified bar rack bypass systems. The research project of Dr. Beck is a logical continuation, embedded into the framework of a large European Horizon 2020 research project.

Dr. Beck's research deals with an experimental, numerical and ethohydraulic investigation of curved-bar racks as mechanical behavioural fish guidance structures, followed by a bypass channel to guide fish into the tailwater at hydropower plants and water intakes. Mechanical behavioural barriers cause hydraulic cues like velocity and pressure gradients through their rack bars, resulting in an avoidance reaction of fish. The innovative fish guidance structure newly developed by Dr. Beck is planned to be tested at a pilot and demonstration hydropower plant on the Thur river in eastern Switzerland.

The financial support of the EU Horizon 2020 research and innovation program under grant agreement no. 727830 FITHydro (Fishfriendly Innovative Technologies for hydropower), and the Swiss State Secretariat for Education, Research and Innovation (SERI) (grant number 16.0153) is gratefully acknowledged. The investigation of the electrified CBR was supported by the Swiss Federal Office of Energy (grant number SI/501758-01).

My sincere thanks go to Prof. Dr. Laurent David, Hydrodynamique, Ecoulements Environnementaux, Université de Poitiers, Dr. Armin Peter, Gewässerökologie und Fischbiologie, FishConsulting GmbH, Olten, and of Dr. Ismail Albayrak for their co-reviews.

Acknowledgements

This doctoral thesis was written during my employment at the Laboratory of Hydraulics, Hydrology and Glaciology (VAW) at ETH Zurich. The project was funded by the European Union's Horizon 2020 research and innovation programme under grant agreement No. 727830, FITHydro (Fishfriendly Innovative Technologies for Hydropower). I would like to thank the State Secretariat for Education, Research and Innovation (SERI) for their support. VAW's activities in hydropower research are embedded in the Swiss Competence Centre for Energy Research, Supply of Electricity (SCCER-SoE), which is an initiative funded by the Swiss Confederation through Innosuisse (Swiss Innovation Agency). I would further like to thank all who contributed to the present work with particular acknowledgment to

- VAW director and examiner Prof. Dr. Robert Boes for the initiation of this doctoral thesis, his continuous support and expert inputs, and the detailed review of the thesis. I deeply appreciate that he enabled many rewarding field trips and exchanges with other research institutes, engineers, ecologists and policy makers, allowing me to grow a broad view and a large network in a field that I care strongly about.
- My supervisor Dr. Ismail Albayrak for initiating this doctoral thesis, his scientific support, and helpful discussions during the past 3.5 years.
- Prof. Dr. Laurent David, University of Poitiers, co-examiner, for the review and interesting discussions.
- Dr. Armin Peter, FishConsulting GmbH, co-examiner, and Dr. Oliver Selz, eawag, for their invaluable support during the live-fish tests, their expertise regarding the fish biology, and the lively discussions during our fishing trips.
- Julian Meister for his enormous support during the live-fish tests, the invaluable scientific discussions, and in particular for his endless enthusiasm.
- Dr. David Vetsch for his valuable scientific input, efforts and support for the numerical modelling.
- My Master and project theses students Claudia Leuch, Michael Ganzmann, Timon

Suter, Floriane Bühler, Caterina Rovati, and Andrea Bianchi for their conscientious work.

- Technical infrastructure team of VAW including the mechanical and electronics workshop, photographer, and graphic designers for their excellent work.
- All my friends and colleagues at VAW, in particular Cristina Rachely, Isabella Schalko and Helge Fuchs, for the great scientific and moral support, the interesting discussions, invaluable inputs, and continuous motivation.
- My parents, Monika and Thomas, for their unconditional support and continuous encouragement.
- Finally, I thank my partner Viktor for his endless patience, his amazing cooking skills, and his wonderful nature of knowing how to make me laugh.

Zürich, September 2020

Claudia Beck

Contents

Abstract	xi
Kurzfassung	xiii
1 Introduction	1
1.1 Motivation	1
1.2 Objectives and tasks	2
1.3 Thesis outline	4
2 Theoretical background and state of knowledge	7
2.1 Introduction	7
2.2 Fish behavioural biology	8
2.2.1 General swimming behaviour	8
2.2.2 Migratory behaviour	8
2.2.3 Swimming speed	10
2.3 Fish mortality during downstream movements	10
2.4 Fish protection and downstream passage technologies	12
2.5 Fish guidance structures	13
2.5.1 Hydraulic head losses of mechanical behavioural FGS	15
2.5.2 Flow fields at mechanical behavioural FGSs	19
2.6 Ethohydraulics of mechanical behavioural FGSs	23
2.6.1 Effect of hydrodynamic cues on fish behaviour	23
2.6.2 Fish swimming behaviour at mechanical behavioural FGSs	24
2.6.3 Fish guidance efficiency	27
2.7 Bypass system design	30
2.7.1 Attraction and acceptance of the bypass system	30
2.7.2 Design recommendations for unharmed bypass passage	33
2.7.3 Operational aspects of the bypass system (BS)	34
2.8 Electrified fish guidance structures	35
2.9 Handling of large wood, organic fine material and sediments	36
2.10 Hydraulic fundamentals	38
2.10.1 Turbulent flow structures in open channel flow	38
2.10.2 Spatial velocity gradients	42

3	Experimental setup and methods	45
3.1	Overview	45
3.2	Similitude and scale effects	45
3.3	Measurement accuracy and error propagation	47
3.4	Hydraulic model investigation of curved-bar racks	48
3.4.1	Model flume I - small flume	48
3.4.2	Instrumentation	49
3.4.3	Parameter range and test programme	49
3.4.4	Head loss measurements	51
3.4.5	Computation of energy losses	53
3.4.6	Flow velocity measurements	53
3.4.7	Operational aspects: Clogging of driftwood and organic fine material	56
3.5	Ethohydraulic experiments	58
3.5.1	Model flume II - Ethohydraulic flume	58
3.5.2	Instrumentation	61
3.5.3	Experimental procedure and test programme	61
3.5.4	Videometry system and fish-tracking software	65
3.6	Ethohydraulic data analysis	66
3.6.1	Residence time	69
3.6.2	Fish swimming velocity	70
3.6.3	Statistical analysis	72
3.7	Numerical model	74
4	Hydraulic head losses and flow fields of curved-bar racks	79
4.1	Hydraulic head losses of curved-bar racks	79
4.1.1	Head loss equation	79
4.1.2	Bar shape factor C_S	81
4.1.3	Head loss factor of bar depth C_L	82
4.1.4	Head loss factor of overlays $C_{V,i}$	84
4.1.5	Head loss factor of HPP layout geometry C_w	88
4.1.6	Application of total head loss formula	89
4.2	Flow fields at curved-bar racks	91
4.2.1	Up- and downstream flow fields	91
4.2.2	Flow field in the rack-parallel cross section	94
4.2.3	Hydraulics of CBRs with overlays	95
4.2.4	Downstream flow field and turbine admission flow	98
4.2.5	Effect of the HPP layout on the flow field	100
4.2.6	Comparison to the flow fields of other mechanical behavioural FGSs	104
5	Numerical modelling	107
5.1	Model validation	107
5.2	Numerical simulations of different bar shapes	109

6	Ethohydraulics of curved-bar rack bypass systems	115
6.1	Hydraulics of curved-bar rack bypass systems	115
6.1.1	Velocity field for the live-fish tests with barbel, spirlin, nase and eel	115
6.1.2	Velocity field for the live-fish tests with salmon parr and trout . . .	119
6.1.3	Bypass hydraulics	129
6.1.4	Effect of different bypass layouts on fish behaviour and guidance .	132
6.2	Protection and guidance efficiencies of curved-bar rack bypass systems . .	133
6.2.1	Spirlin	134
6.2.2	Barbel	137
6.2.3	Nase	139
6.2.4	European Eel	140
6.2.5	Atlantic salmon parr	142
6.2.6	Brown trout	143
6.2.7	Cross-comparison of the tested fish species	145
6.3	Logistic regression model	147
6.3.1	Model 1: Regression with bypass passage as the dependent variable	148
6.3.2	Model 2: Regression with rack passage as the dependent variable .	150
6.3.3	Model 3: Regression with refusal as the dependent variable	151
6.3.4	Effects of the main parameters on the fish behaviour and the guid- ance efficiency	152
6.4	Average fish protection and guidance efficiencies	153
6.5	Rack passage locations	154
6.6	Fish swimming velocities and behaviour	155
6.6.1	Fish swimming paths	155
6.6.2	Statistical analysis of fish swimming speeds	161
6.6.3	Rheotaxis changes	162
6.7	Comparison of fish protection and guidance efficiencies of the CBR to other fish guidance structures	165
6.8	Transferability of the results from laboratory to prototype	167
7	Electrified curved-bar rack	170
7.1	Fish protection and guidance efficiencies	170
7.2	Fish reaction to electric stimuli	172
7.3	Fish injuries	173
8	Operational aspects of curved-bar rack bypass systems	175
8.1	Clogging probability by organic fine material	175
8.2	Clogging probability by floating debris	176
8.3	Rack cleaning machine	180
9	Engineering application and design guideline	181
9.1	Effect of design parameters on the hydraulic and fish-biological performance of CBR-BS	181
9.2	Guideline for the design of a prototype CBR	188

10 Conclusions and outlook	195
10.1 Conclusions	195
10.2 Outlook	201
Notation	202
Bibliography	213

Abstract

Run-of-river hydropower plants (HPPs), dams and weirs pose a particular threat for downstream moving fish. The migration delay and injury or mortality during turbine or spillway passages contribute to a decline in fish populations worldwide. The overarching goal of this research study is therefore to improve the sustainable and efficient use of hydropower by providing a technical solution for the safe downstream movement of fish at run-of-river HPPs and water intakes with a minimal impact on hydropower production and operation. The focus lies on the design improvement of mechanical behavioural fish guidance structures (FGSs) consisting of vertical bars in combination with a bypass system (BS).

To this end, innovative curved bar shapes were developed for mechanical behavioural FGSs, herein called curved-bar racks (CBRs). The hydraulic performance of a large range of CBR configurations and four BS layouts, the fish guidance efficiency, the option of electrifying the CBR and operational aspects of CBR-BSs were systematically investigated. The tests were conducted in two different laboratory flumes and a numerical simulation in OpenFOAM[®] was performed to further optimise the CBR bar shape to minimise operational issues. The protection and guidance efficiencies of barbel (*Barbus barbus*), spiralin (*Alburnoides bipunctatus*), nase (*Chondrostoma nasus*), European eel (*Anguilla anguilla*), brown trout (*Salmo trutta*), and Atlantic salmon parr (*Salmo salar*) at the CBR-BS were assessed in ethohydraulic flume tests. The fish swimming behaviour at the CBR-BS was analysed with a fish-tracking software and linked to the hydrodynamic cues created by the CBR-BS. The governing parameters affecting the reaction of the fish at the CBR-BS were determined with a logistic regression model. Finally, the CBR was equipped with a low-voltage electric field to further increase the fish protection and guidance of European eels.

The main results of the present study include the extension of the existing head loss prediction equation for mechanical behavioural fish guidance structures with additional head loss factors accounting for (i) the curved bar shape, (ii) the application of overlays and (iii) different HPP layouts. The head loss coefficients of the recommended CBRs are in the same range as those of conventional intake trash racks. The curved bars promote a flow straightening effect leading to favourable flow conditions for both fish guidance and turbine operation. The ratio of bypass entrance to approach flow velocity significantly affects the bypass acceptance of fish and is therefore an important design parameter of CBR-BSs. The velocity and pressure gradients sharply increase from a distance of ~ 40 mm on the upstream side of the CBR and are particularly high between the bars triggering an avoidance reaction of the approaching fish. The live-fish tests confirmed this effect and the CBR functioned as a mechanical behavioural barrier for spiralin, barbel, nase and Atlantic salmon parr with high

fish protection and guidance efficiencies ($> 75\%$), whereas it had a lower or no behavioural effect for brown trout and European eel, respectively (guidance efficiency $< 75\%$). The electrification of the CBR increased the protection and guidance efficiency for European eel and therefore represents a promising additional protection. The curved bar shape was further optimised with a foil-shaped curved bar (f-CBR) to mitigate potential clogging issues.

This study presents a fish guidance structure design, which is applicable at all-sized run-of-river hydropower plants and water intakes. The recommended CBR and in particular the f-CBR provide minimal hydraulic head losses, a symmetric flow field downstream of the rack, minimal operational issues, and a high fish protection and guidance. This study further contributes to a detailed understanding of the fish swimming behaviour at mechanical behavioural fish guidance structures and bypass systems.

Kurzfassung

Laufwasserkraftwerke, Dämme und Wehre stellen eine besondere Gefährdung für flussabwärts wandernde Fische dar. Die Verzögerung der Fischwanderung und die Verletzungsgefahr oder Mortalität bei Turbinen- oder Wehrpassagen tragen weltweit zu einem Rückgang der Fischpopulationen bei. Das übergeordnete Ziel dieser Arbeit war es daher, die nachhaltige und effiziente Nutzung der Wasserkraft zu verbessern, indem eine technische Lösung bereitgestellt wird für die sichere, flussabwärts gerichtete Fischwanderung an Laufwasserkraftwerken mit minimalen Auswirkungen auf die Wasserkraftproduktion oder den Kraftwerksbetrieb. Der Schwerpunkt lag dabei auf der Weiterentwicklung von Fischleitrechen mit vertikalen Stäben, so genannten mechanischen Verhaltensbarrieren, in Kombination mit einem Bypass-System (BS).

Um dieses Ziel zu erreichen, wurden innovative, gebogene Stabformen für die Anwendung an Verhaltensbarrieren entwickelt, die hier als “Curved-Bar-Racks” (CBR) bezeichnet werden. Die Hydraulik verschiedener CBR-Konfigurationen und von vier Bypass-Systemen, die Fischleiteffizienz von CBR-BS, die Möglichkeit, den CBR zu elektrifizieren, und betriebliche Aspekte an CBR-BS wurden systematisch untersucht. Die Modellversuche wurden in zwei verschiedenen Versuchsrinnen durchgeführt und die gebogene Stabform wurde mit einer numerischen Simulation in Open-FOAM[®] weiter optimiert. Die Schutz- und Leiteffizienz von Barben (*Barbus barbus*), Schneider (*Alburnoides bipunctatus*), Nasen (*Chondrostoma nasus*), Europäischen Aalen (*Anguilla anguilla*), Bachforellen (*Salmo trutta*), and Atlantischen Lachs Parr (*Salmo salar*) am CBR-BS wurden in ethohydraulischen Modellversuchen ermittelt. Das Schwimmverhalten wurde mit einer *fish-tracking* Software analysiert und anhand der vom CBR-BS erzeugten hydraulischen Strömungssignaturen diskutiert. Die für das Fischverhalten entscheidenden Parameter wurden mit einem logistischen Regressionsmodell bestimmt. Schliesslich wurde der CBR mit einem schwachen Spannungsfeld ausgestattet, um die Schutz- und Leitwirkung für den Aal weiter zu erhöhen.

Zu den Hauptergebnissen der vorliegenden Arbeit gehört die Erweiterung der bestehenden Gleichung zur Bestimmung der hydraulischen Verluste von Verhaltensbarrieren mit zusätzlichen Verlustfaktoren für (i) die gebogene Stabform, (ii) Sohl- und Tauchleitwände und (iii) unterschiedliche Kraftwerkstypen. Die Verlustbeiwerte der empfohlenen CBRs sind ähnlich hoch wie diejenigen von konventionellen Einlaufrechen. Der Gleichrichtereffekt der gebogenen Stäbe führt zu günstigen Strömungsbedingungen für das Leiten der Fische zum Bypass und einen effizienten Turbinenbetrieb. Das Mass der Geschwindigkeitszunahme in den Bypass hat die Reaktion der Fische am Einlauf zum Bypass signifikant beeinflusst und ist daher eine wichtige Dimensionierungsgrösse für CBR-BS. Die Geschwindigkeits- und Druckgra-

dienten sind ab ~ 40 mm direkt vor dem CBR und zwischen den Stäben besonders hoch und lösen bei den sich annähernden Fischen eine Meidereaktion aus. Die Fischversuche haben diesen Effekt bestätigt. Der CBR fungierte als mechanische Verhaltensbarriere für Schneider, Barben, Nasen und Lachs Parr mit einer hohen Schutz- und Leiteffizienz ($> 75\%$), während er bei Bachforellen und Europäischen Aalen einen deutlich geringeren oder gar keinen Verhaltenseffekt zeigte (Leiteffizienz $< 75\%$). Die Elektrifizierung des CBR erhöhte die Schutz- und Leiteffizienz für den Europäischen Aal und stellt daher einen vielversprechenden zusätzlichen Schutz dar. Die gebogene Stabform wurde mit einem fischbauchförmigen Stab (f-CBR) weiter optimiert, um potenzielle Verklausungen zu reduzieren.

Diese Arbeit präsentiert einen neuartigen Fischleitrechen, der an kleinen bis großen Laufwasserkraftwerken einsetzbar ist. Der empfohlene CBR und insbesondere der f-CBR zeichnen sich durch minimale hydraulische Verluste, eine symmetrische Rechenabströmung, minimale betriebliche Beeinträchtigungen und eine hohe Fischschutz- und -leitwirkung aus. Die Arbeit trägt ausserdem zu einem detaillierten Verständnis des Schwimmverhaltens von Fischen an mechanischen Verhaltensbarrieren und Bypass-Systemen bei.

1 Introduction

1.1 Motivation

Hydropower is the number one renewable electric energy source worldwide with 16% of the total electricity production and will remain so in the near future (IEA, 2018). In Switzerland, hydropower accounts for some 56% of the annual electricity production and hence is the backbone of the Swiss power supply. Furthermore, the strategic plan for the future use of energy includes a gradual nuclear power phase-out. For a smooth energy transition, the increase of base load production from run-of-river hydropower plants (HPPs) is of fundamental importance to compensate for the vanishing base load from nuclear power plants. However, the extensive expansion of hydro-electric power plants in the past decades has led to the impairment of natural river systems and aquatic habitats regarding their habitat diversity and the passage of sediments and migrating organisms worldwide. Within the EU, the environmental objectives of the European Water Framework Directive (WFD) enforce the protection, mitigation and restoration of all water bodies with the goal to maintain or reach a good ecological status or potential. In Switzerland, the Swiss Waters Protection Act (WPA) and the Waters Protection Ordinance (WPO) revised in 2011 demand the revitalisation of water bodies compromised by man-made structures by 2030, which includes the restoration of the ecological continuum and thus the unharmed passage of up- and downstream moving fish. This means that in Switzerland, necessary measures have to be taken at over 1000 obstacles and existing HPPs have to be retrofitted with downstream fish passage systems (Figure 1.1).

Run-of-river HPPs pose an obstacle to the unhindered fish movement. Various technologies for the fish upstream movement have been successfully developed and operated for more than a hundred years. However, measures to protect and guide downstream moving fish at HPPs and other water intakes have been neglected in the past and therefore have to be addressed as an urgent matter in order to recover declining fish populations in European river systems. For this reason, the project “Fishfriendly Innovative Technologies for hydropower” (FITHydro) was launched as part of the Horizon 2020 EU Research and Innovation program in 2016. The main goal of FITHydro is to promote the development of innovative technologies for a sustainable, fishfriendly operation of HPPs in Europe. The Laboratory of Hydraulics, Hydrology and Glaciology (VAW) of ETH Zurich is a partner of the interdisciplinary research team consisting of various European institutes and participants. Amongst others, VAW is involved with two research projects to further develop fish guidance structures (FGSs) as a technical solution for the pressing issue of fish downstream movement at HPPs.

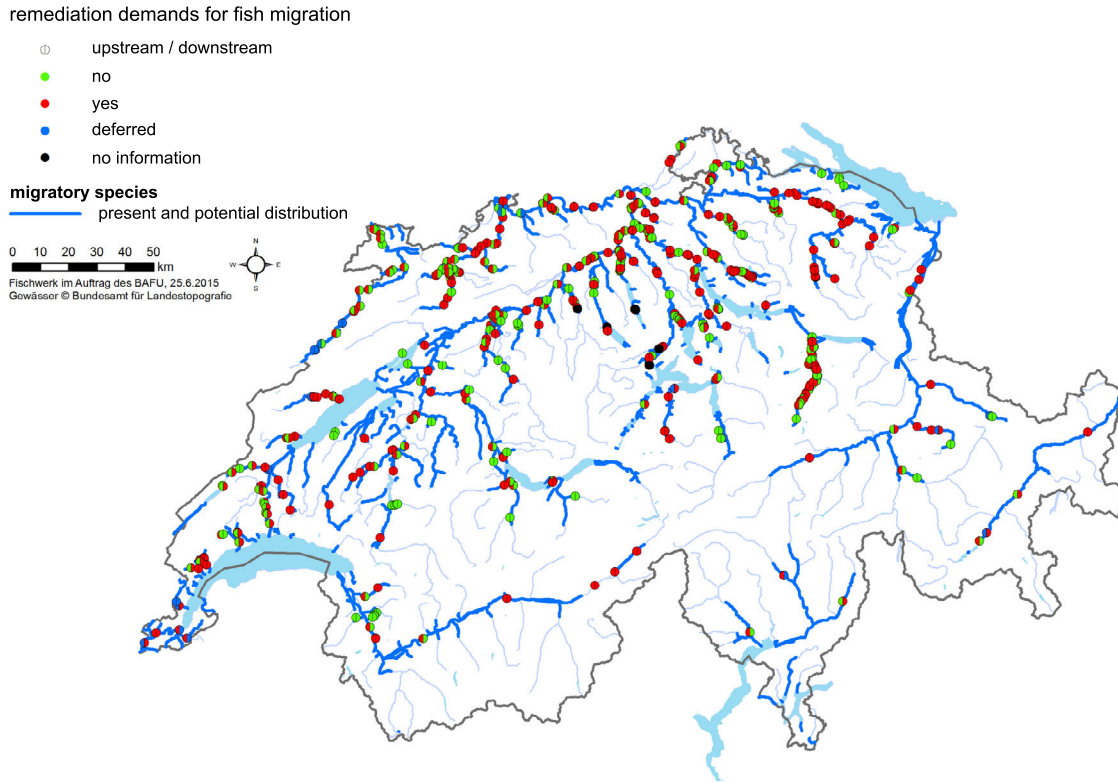


Figure 1.1 Movement and migration barriers due to hydropower structures and their restoration demands for up and/or downstream facilities concerning the defined target fish species, adapted from Dönni *et al.* (2017)

These two VAW projects are based on physical and ethohydraulic model investigations. While the present study focuses on the development of FGSs with vertical bars as a mechanical behavioural barrier for all-sized run-of-river HPPs, a second study concentrates on FGSs with horizontal bars acting as a physical barrier at smaller HPPs ($Q_d \leq 120 \text{ m}^3/\text{s}$) (Meister *et al.*, 2020b,c; Meister, 2020).

1.2 Objectives and tasks

The overarching goal of this research study is to improve the sustainable and efficient usage of hydropower by protecting, guiding and bypassing downstream moving fish with minimum impact on HPP production and operation. The focus lies on the development of mechanical behavioural FGSs consisting of vertical bars and bypass systems (BSs) for the safe downstream movement of fish at run-of-river HPPs. Louvers, angled bar racks and modified angled bar racks (MBRs), with an adjacent BS are classified as mechanical behavioural FGSs (EPRI, 1998; Albayrak *et al.*, 2020a). These FGSs are typically placed in front of a turbine or water intake at a horizontal rack angle of $\alpha = 10^\circ \dots 45^\circ$ to the flow direction and consist of vertical bars placed at a flow attack angle of $\beta = 45^\circ \dots 90^\circ$ (Figure 1.2). When

approaching the structure, fish perceive the high pressure and velocity gradients around and between the bars and react with avoidance (Amaral, 2003). The velocity component parallel to the rack guides the fish towards the bypass.

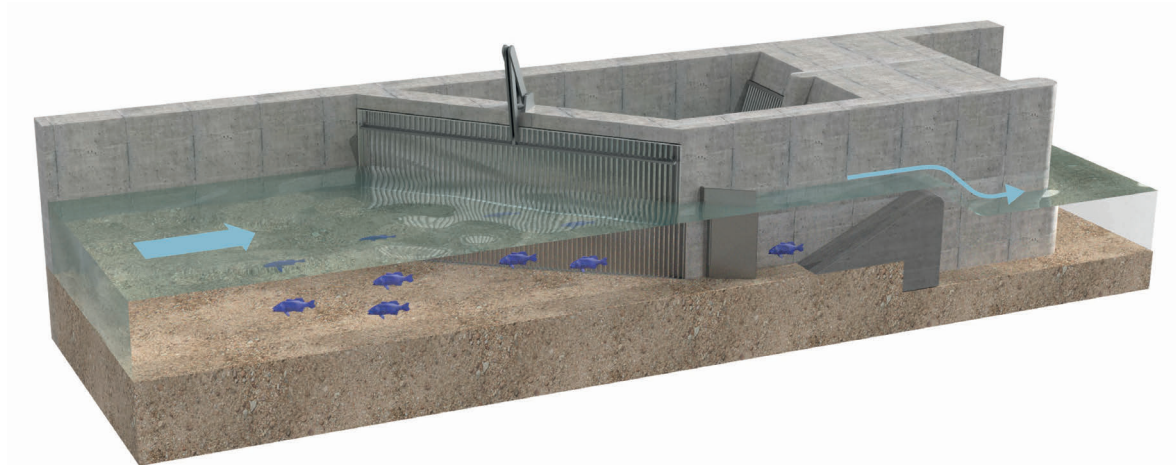


Figure 1.2 Schematic principle of a fish guidance system at a run-of-river hydropower plant; the angled bar rack with vertical bars guides the fish towards the bypass system

Despite recent advancements in the design of these FGSs, hydraulic head losses and asymmetric downstream flow fields created by these structures are still a great issue. For a sustainable, eco-friendly application at HPPs, the design of FGS-BSs has to be further improved with innovative solutions. To this end, the following objectives are set for the present study:

- Minimising head losses and improving the downstream flow fields, i.e. the turbine admission flow, by developing new bar shapes to mitigate negative impacts of a FGS on hydropower production
- Improvement of the hydraulic conditions around the FGS-BS based on fish behaviour data for a better fish protection and fish guidance efficiency
- Advancing the understanding of fish behaviour under different flow conditions created by FGS-BSs
- Investigation of a low-voltage electric field applied to the FGS to further improve the protection and guidance efficiency for fish
- Handling of large wood and organic fine material at FGSs
- Recommendation for a fishfriendly and cost-effective design of FGS-BSs

To achieve these objectives, systematic small- and large-scale model studies including etho-hydraulic tests were conducted within the following six tasks:

- Task A is devoted to the development of innovative curved bar shapes for FGSs. Herein, the new FGS with curved bars is called Curved-Bar Rack (CBR). The hydraulic performance of the CBRs was investigated in a flume with 1:2 Froude-scaled

models for a wide parameter range such as rack angle, bar attack angle, bar depth and spacing, top and bottom overlays, and HPP layout to develop a head loss prediction equation. The hydraulically optimal CBR configuration was determined from these tests and used for the large-scale ethohydraulic tests. Furthermore, a numerical model was set up with OpenFOAM® and validated with the measurements in the physical model flume. The numerical model was used to analyse the flow field in close vicinity and between the bars of different FGSs, and to further optimise and develop new bar shapes for the CBR.

- Task B focuses on the investigation of four different bypass layouts potentially used for CBRs and other FGSs. The bypass layouts were tested with the hydraulically optimal 1:1 Froude-scaled CBR in a large ethohydraulic flume. Velocity measurements were conducted using ADV and the fish behaviour was investigated for different flow conditions in the bypass with live-fish tests.
- Task C assesses the fish protection and fish guidance efficiencies of the CBR with a full-depth open channel bypass for six endemic fish species, namely barbel (*Barbus barbus*), spirlin (*Alburnoides bipunctatus*), nase (*Chondrostoma nasus*), European eel (*Anguilla anguilla*), brown trout (*Salmo trutta*), and Atlantic salmon (*Salmo salar*), by means of live-fish tests. The fish movements and behaviour were recorded with submerged high-resolution cameras and analysed with a fish-tracking software developed at VAW. The objective was to relate distinct behavioural patterns of the tested fish to the hydrodynamic cues of the CBR-BS. The effects of different parameters were quantified with χ^2 -tests and a logistic regression model.
- Task D investigates the effect of a low-voltage electric field applied to the CBR on the fish behaviour with the goal to further improve the fish protection and fish guidance of the CBR-BS for European eel and spirlin.
- Task E focuses on the potential operational issues at the CBR-BS such as the transport of large wood and organic fine material.
- Task F is devoted to the development of applicable engineering recommendations (a step by step guideline) based on the findings from the model investigations of Tasks A-E with regard to hydraulic performance, fish protection and cost-effectiveness.

1.3 Thesis outline

To achieve the above defined goals and objectives for the present study, an extensive literature review was conducted and small- to large-scale laboratory and numerical modelling approaches were applied. In Chapter 2, an in-depth review on the topic of downstream fish

movements, the link between fish behaviour and hydrodynamic cues, and fish protection technologies with a particular focus on fish guidance structures (FGSs) is given. Furthermore, Chapter 2 outlines recently developed approaches for the head loss assessment of FGSs and the hydraulic fundamentals of open channel flow. The experimental setup, techniques and data analysis approaches are described in Chapter 3. The hydraulic head losses and flow fields of CBRs are presented and discussed in Chapter 4. Chapter 5 displays the numerical model validation and the detailed investigation of the hydrodynamic cues for different bar shapes. The results of the ethohydraulic tests are presented in Chapter 6 with a detailed analysis of the flow field for different hydraulic conditions and bypass layouts, the fish protection and fish guidance efficiencies, the statistical analysis of the live-fish tests by means of a logistic regression model, and the analysis of individual fish swimming paths and velocities. Chapter 7 gives the results of the live-fish tests with the electrified CBR. Operational aspects with regard to drift wood and organic fine material are presented in Chapter 8. Recommendations for engineering applications are outlined in Chapter 9. Finally, Chapter 10 presents the conclusions and gives an outlook.

2 Theoretical background and state of knowledge

This chapter discusses the pressure put on fish habitats by movement and migration barriers such as run-of-river hydropower plants (HPPs), dams, weirs and spillways. The knowledge on the fish behaviour in their natural riverine habitat, and their movement and migration needs are presented. The chapter further illustrates the state of the art fish downstream passage technologies tested in field and laboratory studies, and presents the applied hydraulic fundamentals.

2.1 Introduction

Fish travel up- and downstream in various water bodies in search of suitable feeding or spawning grounds (Lucas *et al.*, 2001). The directed fish migration or general movements are triggered by various factors such as temperature, discharge, light conditions, oxygen content or morphological factors. Migratory fish species are classified as follows:

Diadromous: Fish species, which migrate between sea and fresh water systems. They are mostly long-distance migrators, where migration is crucial for the survival of the population. Depending on the direction of migration, they are classified as anadromous or catadromous:

Anadromous: Species, which spawn in fresh water and migrate downstream to mature in the sea (e.g. salmon, sturgeon, shad).

Catadromous: Species, which spawn in the sea and migrate upstream to mature in fresh water (e.g. American or European eel).

Oceanodromous: Species, which live and migrate only within seawater oceanic systems.

Potamodromous: Species, which migrate only in freshwater river - lake systems and are thus rather short-distance migrators (e.g. brown trout, barbel, nase, European grayling, spirlin).

The focus of this study is on anadromous, catadromous and potamodromous fish species. In Switzerland, anadromous species have completely vanished and European eels are in strong decline all over Europe due to the habitat impairment by run-of-river HPPs or other impassable movement barriers and man-made waterworks (Calles *et al.*, 2010). In Switzerland, 73% of the 66 native riverine fish species are vulnerable, endangered or extinct (Dönni *et al.*, 2017). The protection target defined in the WPA, however, includes all domestic fish species. A report on the preservation and promotion of migratory fish species was published by the Swiss Federal Office for the Environment (FOEN) (Dönni *et al.*, 2017). To set the goals for possible measures, Atlantic salmon, brown trout, nase, European eel, European grayling and

common barbel have been selected as the target fish species in the report, covering a well-balanced range of long and short distance migrators as well as anadromous, potamodromous and catadromous species.

2.2 Fish behavioural biology

2.2.1 General swimming behaviour

Fish maintain their buoyancy and stability at a certain water depth by a combination of swimming movements and (de)compressing their gas-filled swim bladder. The stimulation of optical and tactile sense organs manages the orientation of fish in a flowing water current. For the perception of vortex flows, velocity and pressure gradients, fish use the lateral line and equilibrium organs (Haro *et al.*, 1998; Liao, 2007; Silva *et al.*, 2012a). Fish react sensitively to high turbulence and flow acceleration (Adam and Lehmann, 2011). Rapid changes in flow patterns are perceived as obstacles initiating an avoidance reaction (cf. Section 2.6.2). The sensitivity of the lateral line organ only has a short distance reach, but it can trigger burst swimming or a rheotaxis change. With the inner ear, fish can sense relative flow changes, i.e. flow acceleration. This indicates that the vortices in highly turbulent flow are perceived as angular accelerations (Coutant and Whitney, 2000).

Rheotaxis characterises the orientation of fish during a directed swimming movement. Positive rheotaxis describes the alignment of the fish against the flow direction, swimming actively against the current. Negative rheotaxis describes the opposite alignment, head first with the current. For flow velocities higher than 0.2...0.3 m/s, an active-passive behaviour is often observed, where the head is oriented against the current and the fish drifts actively downstream in control of its orientation (Lehmann *et al.*, 2016). For an efficient downstream movement, fish actively swim or passively drift downstream following the main current where the highest flow velocities prevail (Pavlov, 1994; Brown *et al.*, 2009).

2.2.2 Migratory behaviour

The downstream migration of fish is most probably triggered by a combination of external factors such as the diurnal cycle, discharge, water temperature, and the lunar phase as well as physiological factors governed by their age or stage of development (Lucas *et al.*, 2001). The start of the downstream migration period is therefore different for every fish species. A discharge increase is a frequent trigger since it allows juvenile fish in particular to let themselves drift passively downstream without a high swimming effort (Achord *et al.*, 1997; Schwevers, 1998; Durif *et al.*, 2002). The enhanced turbidity of the water further ensures a better protection from predators. Accelerating flow in general seems to arouse more act-

ive movement. While in natural riverine conditions, most yearlings seem to swim head first actively downstream, they change to a positive rheotaxis near obstacles such as trash racks and intakes (Cada *et al.*, 1997). This hypothesis is supported by the observations of Haro *et al.* (1998), which showed that salmon smolts switched to positive rheotaxis in accelerating currents. While salmonid species prefer to swim a few meters below the water surface, most potamodromous species and eels have been observed to move downstream at various flow depths with an increased preference for the few meters above the riverbed (Brown *et al.*, 2009; Travade *et al.*, 2010; Russon and Kemp, 2011). Fish with lower swimming abilities also prefer to swim along the riverbed where the flow velocities are lower. Although migratory movements are reduced during the cold winter months, migration or displacements take place throughout the entire year (Figure 2.1). However, a water temperature of at least 6°C is required for the downstream migration of eels (Durif and Elie, 2008). While some potamodromous species and salmonids tend to move downstream in spring (March-June), others – for example the adult European eel – prefer the time from August to November (Sandlund *et al.*, 2017). Especially juvenile fish and the European eel were observed to move downstream at dawn or during the night (Travade *et al.*, 2010; Schmalz *et al.*, 2012; Ebel, 2016). Conversely, juvenile salmonids were shown to rely on visual as well as hydrodynamic cues (Kemp and Williams, 2009; Vowles and Kemp, 2012; Vowles *et al.*, 2014). Potamodromous species perform long distance movements mainly in their juvenile and in their reproductive age. Most species synchronize the migration within the population meaning that a large number of individuals migrate simultaneously. Especially for small fish, schooling might improve energy expenditure and protection from predators. The main downstream migration time for Atlantic salmon smolts lies between February and June (Hendry and Cragg-Hine, 2003; Peter, 2015). The transition from fresh to salt water (smoltification) is triggered by genetic as well as environmental factors (Schwinn *et al.*, 2017). Various obstructions and the associated delay can negatively affect this process.

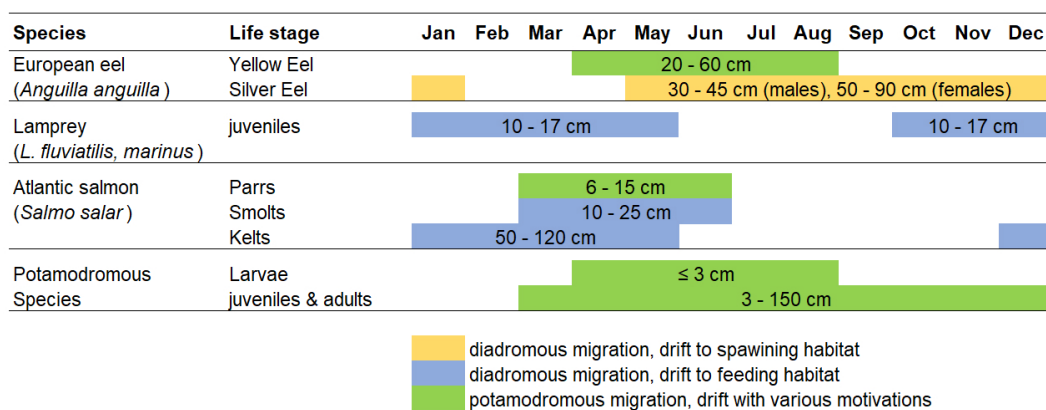


Figure 2.1 Main migration times of selected species and life stages; adapted from Ebel (2016)

2.2.3 Swimming speed

The swimming behaviour and capacity of the selected target fish species are commonly used as a reference for the development of mitigation measures and FGSs. The fish swimming capacity is determined by the red (aerobic) and white muscles (anaerobic) and depends on the fish size and shape as well as the water temperature. The fish swimming speed is often used as an indicator for the swimming capacity. Three different fish swimming speeds are classified in the following (Blaxter, 1969; Beamish, 1978; Pavlov, 1989; Wardle *et al.*, 1995; Adam and Lehmann, 2011; Ebel, 2016; Katopodis and Gervais, 2016):

Sustained swimming speed ($v_{\text{sustained}}$): Normal swimming speed of a fish, at which it can swim actively against the current for a time period longer than 200 minutes without exhaustion. The maximum sustained swimming speed of most species lies at 2-3 times their body length per second (bl/s), while it reaches up to 4 bl/s for salmonids. This swimming speed is commonly used to define the maximum flow velocity in the design of FGSs, beyond which the efficiency of these structures for the target fish species is expected to be compromised.

Prolonged swimming speed ($v_{\text{prolonged}}$): Energy consuming swimming speed, which can be maintained up to a maximum of 200 minutes until exhaustion.

Burst swimming speed (v_{burst}): Maximum sprinting speed that can only be held for 10-20 seconds corresponding to 10-12 bl/s for adult fish and 12-15 bl/s for juveniles. Afterwards, the fish are exhausted and need a regeneration time of up to 24 hours.

The above described fish swimming speeds are much lower for eels. Unfavourable environmental conditions such as low water temperatures or the lack of oxygen can further reduce the swimming capacity. Table 3.10 in Chapter 3 shows the swimming speeds of the fish species tested in this study according to Ebel (2016).

2.3 Fish mortality during downstream movements

Downstream moving fish are subject to a natural mortality rate due to a weakened immune system after spawning in case of juveniles or due to predation in general. The impoundment of rivers increases the mortality caused by predators (Larinier and Travade, 2002; Okland *et al.*, 2016).

When fish encounter a run-of-river HPP during their downstream movement they tend to follow the bulk water flow and thus end up passing through the turbines, over the spillways or through sluice gates, or are hindered by trash racks. Figure 2.2 shows the associated damage potential of various passage routes. Other passage routes such as upstream fish passes are

rarely used at medium- to large-sized HPPs, since the discharge is usually not high enough to attract the downstream moving fish (Pelicice and Agostinho, 2012).

The passage through turbines entails a high risk of injury or mortality due to direct striking by the turbine blades, sudden pressure changes, high shear stresses or turbulence intensities (Abernethy *et al.*, 2001; DWA, 2005; Deng *et al.*, 2011). For Kaplan and Francis turbines, the mortality rate lies at 5-20% and 5-90%, respectively (Larinier, 2008). For eels, these numbers are expectedly a lot higher due to their body morphology (Ebel, 2008; Calles *et al.*, 2010). Generally, the mortality increases with increasing fish size, turbine blade number and rotation speed, and with decreasing turbine size (Coutant and Whitney, 2000; EPRI and DML, 2001; Halls and Kshatriya, 2009). The lowest damage rates are expected for large, slowly rotating bulb turbines with few blades.










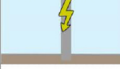
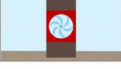
cause of damage		pressure changes	impingement	contact pressure	electrical field	predation
obstacle						
	overflow spillway	<input type="checkbox"/>	<input checked="" type="checkbox"/>	<input type="checkbox"/>	<input type="checkbox"/>	<input checked="" type="checkbox"/>
	sluice	<input checked="" type="checkbox"/>	<input checked="" type="checkbox"/>	<input type="checkbox"/>	<input type="checkbox"/>	<input checked="" type="checkbox"/>
	installations, obstructions	<input type="checkbox"/>	<input checked="" type="checkbox"/>	<input checked="" type="checkbox"/>	<input type="checkbox"/>	<input checked="" type="checkbox"/>
	screens, guiding structures	<input type="checkbox"/>	<input checked="" type="checkbox"/>	<input checked="" type="checkbox"/>	<input type="checkbox"/>	<input checked="" type="checkbox"/>
	electrical fish barrier	<input type="checkbox"/>	<input type="checkbox"/>	<input type="checkbox"/>	<input checked="" type="checkbox"/>	<input checked="" type="checkbox"/>
	turbines, pumps	<input checked="" type="checkbox"/>	<input checked="" type="checkbox"/>	<input type="checkbox"/>	<input type="checkbox"/>	<input checked="" type="checkbox"/>

Figure 2.2 Damage causes of different passage routes of downstream moving fish at run-of-river hydropower plants; adapted from Schmalz *et al.* (2015)

Partial load operation increases the fish mortality rates and the loss of orientation further leads to an enhanced predation pressure in the tailwater channel (Cada *et al.*, 1997). Especially for eels, the trash racks installed in front of the turbine intakes pose another high risk for injuries. If approach flow velocities are high, eels are impinged against the rack, where they are likely to get injured by the rack or the rack cleaning machine. No exact numbers for the mortality rates at a HPP can be specified since the delayed mortality of injured fish can be high (Ferguson *et al.*, 2006). Several models for the estimation of the number of fish harmed during turbine passage exist, however (Ebel, 2016).

For Kaplan turbines used at large HPPs in Switzerland, the mean survival rate without any downstream protection measures is estimated to range from 80% up to 95% (BAFU, 2016). Nevertheless, if the mortality rate of a single HPP amounts to 5-10%, a cascade of 10 HPPs leads to a 40-65% mortality rate. No specific survival rate per HPP or for a cascade of HPPs required for the species' preservation has been defined in Switzerland. However, it is of prime importance to define a strict objective for long distance migrators, since they will pass a larger number of HPPs during their migration. The European regulation on eels (EC Regulation No. 1100/2007) defines the target that 40% of the eel biomass should reach the sea. Belgium and the Netherlands have defined a species-specific maximum HPP-related mortality rate of 10% for salmon over the entire river reach accounting for all HPPs of the Maas and the Moselle rivers (IMK, 2011).

The fish survival rates at weirs and stilling basins are currently largely unknown, but could be substantial due to the high turbulence, pressure changes, solid obstacles or oxygen supersaturation. Note that fish protection systems - if poorly designed - can also lead to injury and mortality rates in the same range as the turbine mortality. Okland *et al.* (2016) investigated the migration routes of salmon smolts at three small German hydropower plants with downstream fish passage facilities. The total loss at the Unkelmühle power plant with a vertically inclined bar rack and a surface bypass system still amounted to 13% mostly due to increased predation and injuries in the bypass system (Wilke *et al.*, 2019). They further found that the predation in the impoundment was higher than in the river reach downstream of the HPP.

2.4 Fish protection and downstream passage technologies

The protection of downstream moving fish can entail securing a fish-friendly turbine passage or the implementation of bypass systems guiding the fish around the HPP (Table 2.1). The latter demands for innovative solutions, which have to be adapted to the ecological requirements of the local fish species and the hydraulic conditions at a specific HPP site. The present study focuses on mechanical behavioural barriers for protecting and bypassing fish. Therefore, the classification and a detailed description of other technologies can be found in the literature (Larinier and Travade, 2002; DWA, 2005; Turnpenny and O'Keeffe, 2005; USBR, 2006; Kriewitz *et al.*, 2012; Kriewitz, 2015; Ebel, 2016).

Table 2.1 Overview of downstream passage technologies for the safe passage or bypass of fish to the tailwater channel and according examples, adapted from Kriewitz (2015)

	Concept	Technology	Examples
Fish protection technologies at run-of-river power plants	Bypassing	Physical barriers	(Submerged) screens Angled / Inclined screens Eicher screen Wedgewire screen Aquatic filter barrier / barrier nets
		Mechanical behavioural barriers	Guiding structures (louvers, bar racks) Trash racks Baffles Bottom overlays / skimming walls
		Sensorial behavioural barriers	Light (strobe lights, mercury lights) Low-frequency sounds Electric screens Air bubble curtains
		Collection systems	Traveling screen Collecting channels Fish lifts Fish pumps Trap and transport
	Turbine passage	Fish-friendly turbines	Alden-Turbine Voith – Minimum Gap Runner Alstom – Fish-friendly Kaplan Turbine
		Fish-friendly plant operation	Spillway release during main migration period Overflow management Early warning systems No partial load operation

2.5 Fish guidance structures

FGSs can be divided into those with narrow bar spacings functioning as physical barriers, and those with wider bar spacings functioning as mechanical behavioural barriers. The former keeps fish from turbine entrainment with narrow clear bar spacings $s_b = 10...30$ mm based on the size of the target fish species. These physical barriers can consist of vertical or horizontal streamwise-oriented bars, herein termed ‘vertically inclined bar racks’ (VBRs) or ‘horizontal bar racks’ (HBRs), respectively (Figure 2.3). VBRs are placed with a vertical angle γ to the intake and are combined with a surface BS (Figure 2.3b), while HBRs are placed with a horizontal angle α to the flow direction combined with a lateral BS (Figure 2.3d). Most of the fish have a proportion index larger than one, which means their height is larger than their width (Ebel, 2016). Therefore, higher fish guidance efficiencies (FGEs) of physical barriers are expected for HBRs in comparison to VBRs for similar bar spacings. HBRs are widely used and approved by authorities (DWA, 2005; BAFU, 2012) and have been successfully applied at many HPPs in Germany, Switzerland and Sweden (Ebel, 2016; Meister, 2020). Until now, HBR application has been limited to relatively small HPPs with $Q_d \leq 120$ m³/s

(Meister *et al.*, 2020b), complying with the velocity limitation for physical barriers to avoid fish impingement, i.e. the average velocity component normal to the rack V_n should not exceed the sustained swimming speed of fish (Turnpenny and O’Keeffe, 2005; Ebel, 2016). In general, HBRs are placed across an intake canal or forebay at an angle to the flow direction of typically $\alpha = 30^\circ \dots 45^\circ$. Since HBRs are subject to clogging by organic fine material like leaves and branches, sophisticated rack cleaning machines are needed. HBRs can be configured with either bottom, top or both bottom & top overlays to improve the FGE and the diversion of driftwood and/or sediment to the bypass (Meister *et al.*, 2020b,c). VBRs have been investigated with regard to head losses and flow fields (Raynal *et al.*, 2013a) and are installed at HPPs in France (e.g. Las Rives, Pébernat) and Germany (e.g. Unkelmühle HPP). The vertical inclination guides the fish to a near-surface bypass, which might reduce the FGE for bottom oriented fish.

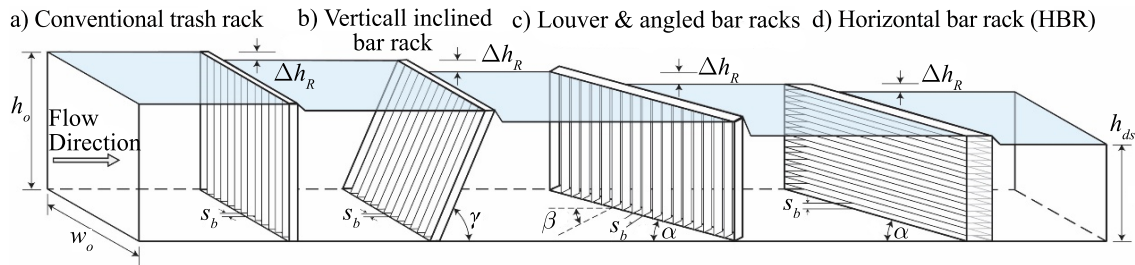


Figure 2.3 Classification of bar rack types according to rack and bar angle, adapted from Albayrak *et al.* (2020b)

The operating principle of mechanical behavioural barriers with wider clear spacings intends to protect fish with distinct hydrodynamic cues instead of physically shielding them from the turbine intake. These FGSs include louvers, angled bar racks and modified angled bar racks (MBRs) (Bates and Vinsonhaler, 1957; EPRI and DML, 2001; Amaral, 2003; Raynal *et al.*, 2013a; Albayrak *et al.*, 2020a). They typically consist of vertical bars oriented with an angle between $\beta = 45^\circ \dots 90^\circ$ to the flow direction with clear bar spacings $s_b = 25 \dots 100$ mm (Figure 2.3c). The vertical bars are oriented with a bar angle of $\beta = 90^\circ$ to the flow direction for louvers, while they are $\beta = 90^\circ - \alpha$ and $\beta \neq 90^\circ - \alpha$ for angled bar racks and MBRs, respectively (Figure 2.4). These FGSs are typically placed in front of a water intake at an angle $\alpha = 10^\circ \dots 45^\circ$. The vertical bars of all three described FGSs create flow separations and thus distinct pressure and velocity gradients, which are perceived and avoided by approaching fish. The rack-parallel velocity component V_p guides the fish towards a bypass system. Courret and Larinier (2008) introduce the ratio of the parallel to the normal velocity component V_p/V_n as the fish guidance capacity (FGC) and propose $V_p/V_n > 1$ for a high fish guidance efficiency. Mechanical behavioural barriers induce strong hydrodynamic cues

and allow for a wider bar spacing thus reducing the hydraulic resistance (EPRI and DML, 2001; Albayrak *et al.*, 2018). In contrast to physical barriers, they are therefore suitable for all-sized HPPs but in particular for medium-to-large HPPs with $Q_d > 120 \text{ m}^3/\text{s}$.

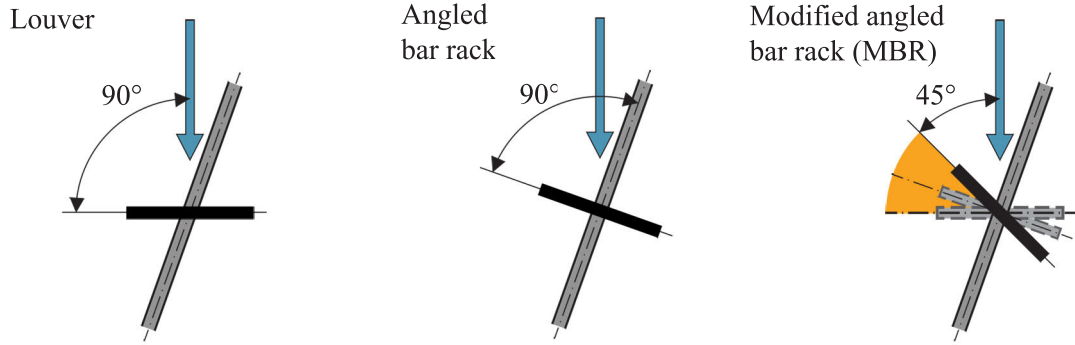


Figure 2.4 Definition of bar attack angle at angled FGSs with vertical bars, namely louvers, angled bar racks and modified angled bar racks (MBRs), adapted from Kriewitz (2015)

In addition to the angled bar racks shown in Figure 2.4, Raynal *et al.* (2014) investigated angled bar racks with vertical bars oriented in streamwise direction. These particular FGSs can act as a physical barrier with small clear bar spacings or as mechanical behavioural barriers with larger clear bar spacings.

2.5.1 Hydraulic head losses of mechanical behavioural FGS

Trash racks have always been in use at HPPs and water intakes in general to protect the turbines or other hydraulic infrastructure from large debris. At run-of-river HPPs, head losses induced by conventional trash racks are of particular interest for economic reasons (power production) as well as constructional reasons (static load). Hydraulic head losses of trash racks were first addressed by Kirschmer (1926). The head loss equation he proposed was thereafter refined by e.g. Zimmermann (1969); Meusbürger (2002); Clark *et al.* (2010).

Regarding FGSs, Raynal *et al.* (2013a) studied the head losses and the induced flow fields of angled bar racks in a straight open channel flume. In a 1:2 scale laboratory model, they investigated angled bar rack configurations with 10 - 30 mm bar spacings (prototype dimensions), rack angles $\alpha = 30^\circ, 45^\circ, 60^\circ, 90^\circ$ and the resulting bar angles $\beta = 90^\circ - \alpha = 60^\circ, 45^\circ, 30^\circ, 0^\circ$ for rectangular and hydrodynamic bar shapes. The authors emphasized the importance of taking into account the bar shape, the blockage ratio σ_{tot} (total blockage of bars and spacers) and the rack angle α and proposed the following head loss prediction equation for angled bar racks:

$$\xi_R = K_i \cdot \left(\frac{\sigma_{\text{tot}}}{1 - \sigma_{\text{tot}}} \right)^{1.6} \cdot K_\alpha \text{ with } K_\alpha = 1 + k_i \cdot \left(\frac{1 - \sigma_{\text{tot}}}{\sigma_{\text{tot}}} \right)^3 \cdot \left(\frac{90^\circ - \alpha}{90^\circ} \right)^{2.35}, \quad (2.1)$$

where K_i = bar shape factor = 2.89 or 1.7 for rectangular or hydrodynamic bars, respectively, K_α = rack angle factor depending on the bar shape and k_i = bar shape factor for the determination of K_α . Due to the geometrical design of angled bar racks with $\beta = 90^\circ - \alpha$, β was large for small α , resulting in high head losses for low rack angles α and small bar spacings.

Albayrak *et al.* (2018) studied the head losses of louvers and MBRs for a wide parameter range. They conducted systematic laboratory experiments to assess the hydraulic head losses and developed a new formula based on the functional relations between the main parameters: rack angle α , bar angle β , and clear bar spacing s_b as well as the secondary parameters: bar depth d_b , bar shape K , and submergence depth h_s (Figure 2.5). The other parameters in Figure 2.5 are the up- and downstream flow depth U_o and U_{ds} , respectively, the downstream flume width w_{ds} , the bar thickness t_b , and the up- and downstream flow depth h_o and h_{ds} .

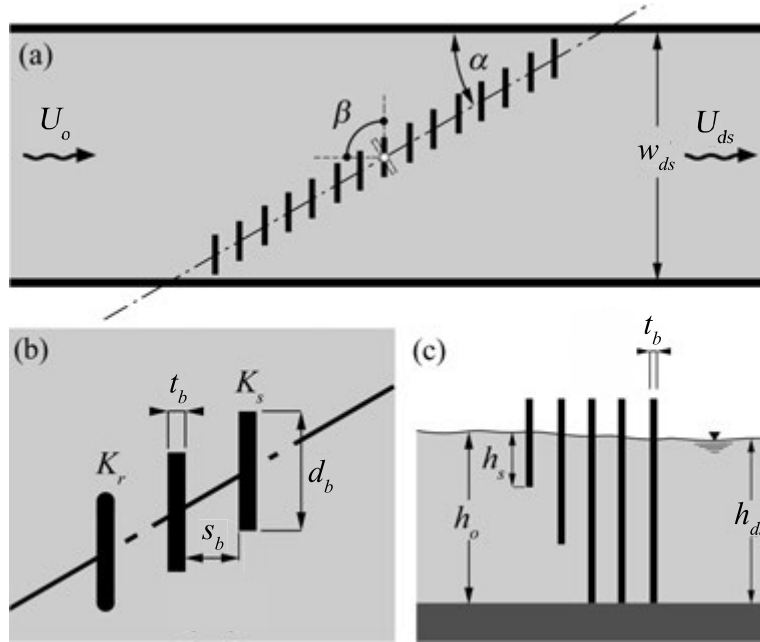


Figure 2.5 Detailed schematic illustration of (a) top view of the flume setup with a louver, (b) top view of cross-sectional bar shapes, (c) side view of geometric parameters for the physical model investigation on louvers and MBRs; adapted from Albayrak *et al.* (2018)

The rack head loss coefficient $\xi_R = f(\alpha, \beta, s_b, d_b, h_s, K)$ is a non-dimensional parameter and a function of the above described rack and bar parameters. The rack angle α , the bar angle β and the clear bar spacing s_b characterise the basic geometric rack properties. According to Albayrak *et al.* (2018), the basic (subscript B) rack head loss coefficient $\xi_B = f(\alpha, \beta, s_b)$ is a function of these main parameters. The head loss factors C_L , C_K and C_S account for effects of the secondary parameters bar depth, submergence depth and bar shape, respectively. Overall, the rack head loss coefficient ξ_R is a product of the basic head loss coefficient ξ_B and the head

loss factors:

$$\xi_R = \xi_B \cdot C_L \cdot C_\kappa \cdot C_S, \quad (2.2)$$

$$\xi_B = 245 \left[0.0275 + (\sigma - 0.0815) \left(\frac{\alpha}{90^\circ} \right) \right] \left(\frac{\beta}{90^\circ} \right)^{5\sigma^{0.44}}, \quad (2.3)$$

$$C_L = \varepsilon \left[1 + 9.4\sigma(1 - \varepsilon) - 3.8(1 - \varepsilon) \left(\frac{\alpha}{90^\circ} \right) \right], \quad (2.4)$$

$$C_\kappa = \kappa^{6.6\sqrt{\sigma}}, \quad (2.5)$$

$$C_S = \left[0.75 + \left(\frac{62^\circ - \alpha}{90^\circ} \right) 4.5\sigma \right], \text{ for rounded bars} \quad (2.6)$$

$$C_S = 1, \text{ for rectangular bars,} \quad (2.7)$$

with $\sigma = t_b/(t_b + s_b)$ = non-dimensional bar spacing = blockage ratio of the vertical bars, $\varepsilon = d_b/D_b$ = bar depth relative to the initial bar depth of $D_b = 100$ mm and $\kappa = h_s/h_o$ = relative submergence depth.

The impact of α and σ showed a strong reciprocal effect. Albayrak *et al.* (2018) found that the influence of σ on ξ_R decreased for acute angles. While the basic head loss coefficient was reduced by 78% by increasing the bar spacing from $s_b = 50$ mm to $s_b = 230$ mm for the MBR with $\beta = 45^\circ$ and a rack angle $\alpha = 45^\circ$, the head loss reduction for wider bar spacings was almost negligible with $\alpha = 15^\circ$. Decreasing the bar angle β decreased the head losses for all rack configurations. Figure 2.6 shows the measured and predicted head loss coefficients (Eq. 2.2) for all rack configurations investigated by Albayrak *et al.* (2018). The predicted head losses agree well with the measured values. Figure 2.6 demonstrates that the head loss coefficients differ greatly between rack configurations and far exceed the head losses caused by conventional trash racks. According to Meusburger (2002), the trash rack head loss coefficients for 43 investigated Swiss run-of-river HPPs lie between $0.1 \leq \xi_R \leq 5.2$, whereby $\xi_R < 3$ for most HPPs. The head losses caused by the recommended MBRs are in the range of $2.0 \leq \xi_R \leq 3.5$ (blue markers in Figure 2.6).

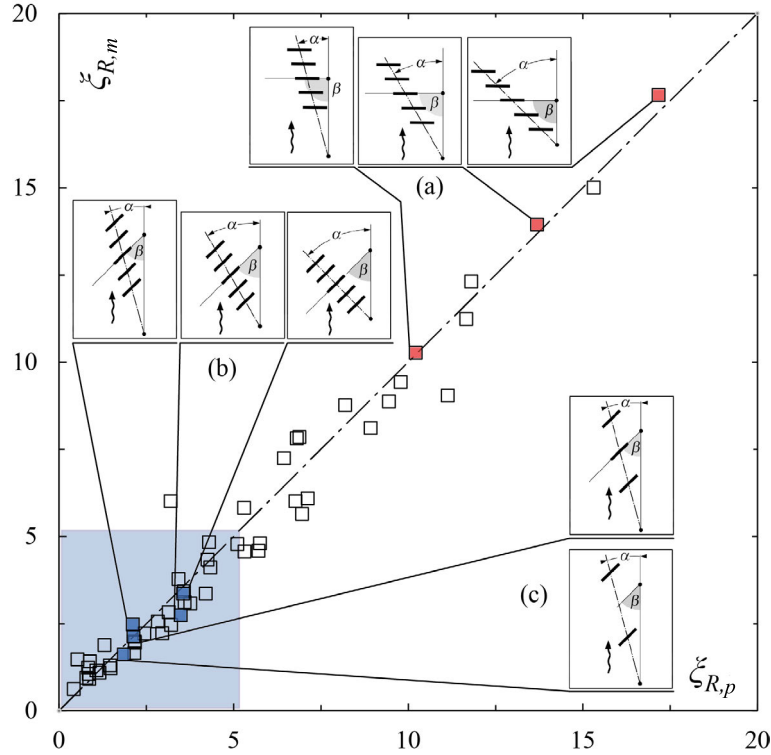


Figure 2.6 Comparison of predicted ($\xi_{R,p}$) and measured ($\xi_{R,m}$) head loss coefficients for selected louver and MBR configurations (a) louver with $\alpha = 15^\circ, 30^\circ, 45^\circ$ and $s_b = 50$ mm ($\sigma = 0.17$), (b) MBR analogous to (a), and (c) MBR with $\alpha = 15^\circ$, $s_b = 110$ mm, 230 mm ($\sigma = 0.08, 0.04$); the blue area represents typical values for trash racks found at Swiss low-head HPPs according to Meusburger (2002); adapted from Albayrak *et al.* (2018)

Meusburger (2002) additionally studied top, bottom, right, left and corner overlays attached to trash racks modelling different clogging patterns. He assessed that the head losses of racks with a small blockage ratio reacted more sensitively to an additional blockage by overlays. Since he only investigated conventional intake trash racks, he did not assess the impact of a rack angle α or bar angle β on the head losses caused by overlays. However, overlays are important components for FGSs since they can be used to guide drift wood, organic fine material and sediment to the bypass. Furthermore, several studies highlight that top and bottom overlays on FGSs could increase the guidance efficiency for surface and bottom oriented fish, respectively (EPRI and DML, 2001; Boes and Albayrak, 2017; Albayrak *et al.*, 2020a). The effect of a $h_{Bo} = 0.11 \cdot h_o$ bottom overlay (subscript *Bo*) on the head losses caused by MBRs was investigated by Moretti (2015) for different bar angles β . For large bar angles ($\beta = 90^\circ$) the rack head losses were reduced with a bottom overlay, whereas for smaller bar angles ($\beta = 45^\circ$), the rack head losses were increased with a bottom overlay resulting in the following head loss factor for bottom overlays proposed by Boes and Albayrak (2017):

$$C_{Bo} = 0.82(\sin \beta)^{-0.8}. \quad (2.8)$$

No systematic parameter study is available on the effect of overlays on the hydraulic head losses of FGSs with various rack angles or bar spacings.

2.5.2 Flow fields at mechanical behavioural FGSs

Flow field upstream of the FGS

The flow upstream of mechanical behavioural FGSs was investigated by means of laboratory experiments (Katopodis *et al.*, 2005; Shepherd *et al.*, 2007; Chatellier *et al.*, 2011; Raynal *et al.*, 2013a; Albayrak *et al.*, 2020a). These studies report that the flow velocity increases along the rack and toward the bypass, reaching up to $U_{\max} = (1.6 \dots 2.5) \cdot U_o$ for louvers and $(1.2 \dots 1.6) \cdot U_o$ for MBRs, depending on the rack angle and the bypass operation, with U_{\max} = maximum flow velocity at the downstream (d/s) rack end and U_o = mean approach flow velocity (Bates and Vinsonhaler, 1957; Ducharme, 1972; EPRI, 1998; Shepherd *et al.*, 2007; Albayrak *et al.*, 2020a). The results from field and laboratory tests with live fish revealed that the FGE through a bypass could be impaired by unfavourable hydraulic conditions at the bypass entrance, i.e. locally decreased flow velocities, even if fish guidance along the rack was high (USBR, 2011; Albayrak *et al.*, 2020a). The ratio of bypass entrance to approach flow velocity of $U_{by,in} = (1.1 \dots 1.5) \cdot U_o$ is recommended for louvers (USBR, 2006) and is expected to be similar for other FGSs. Albayrak *et al.* (2020a) conducted velocity measurements using two-dimensional Laser Doppler Anemometry (2D-LDA) and reported a strong flow deflection for louvers leading to a non-uniform flow distribution along the rack and a negative transverse velocity component through the rack of up to $V = -0.5 \cdot U_o$ directly in front of the bypass entrance (Figures 2.7a,b). Despite similar flow patterns, they reported that flow deflection and acceleration reduced and flow diversion through the rack was more uniform along the rack for MBRs compared to louvers (Figures 2.7c,d). To allow fish to actively remain in front of the rack and hence avoid fish entrainment through the rack the normal velocity component to the rack V_n should be smaller than the sustained swimming speed of fish (Bates and Vinsonhaler, 1957; Turnpenny and O’Keeffe, 2005; Ebel, 2016).

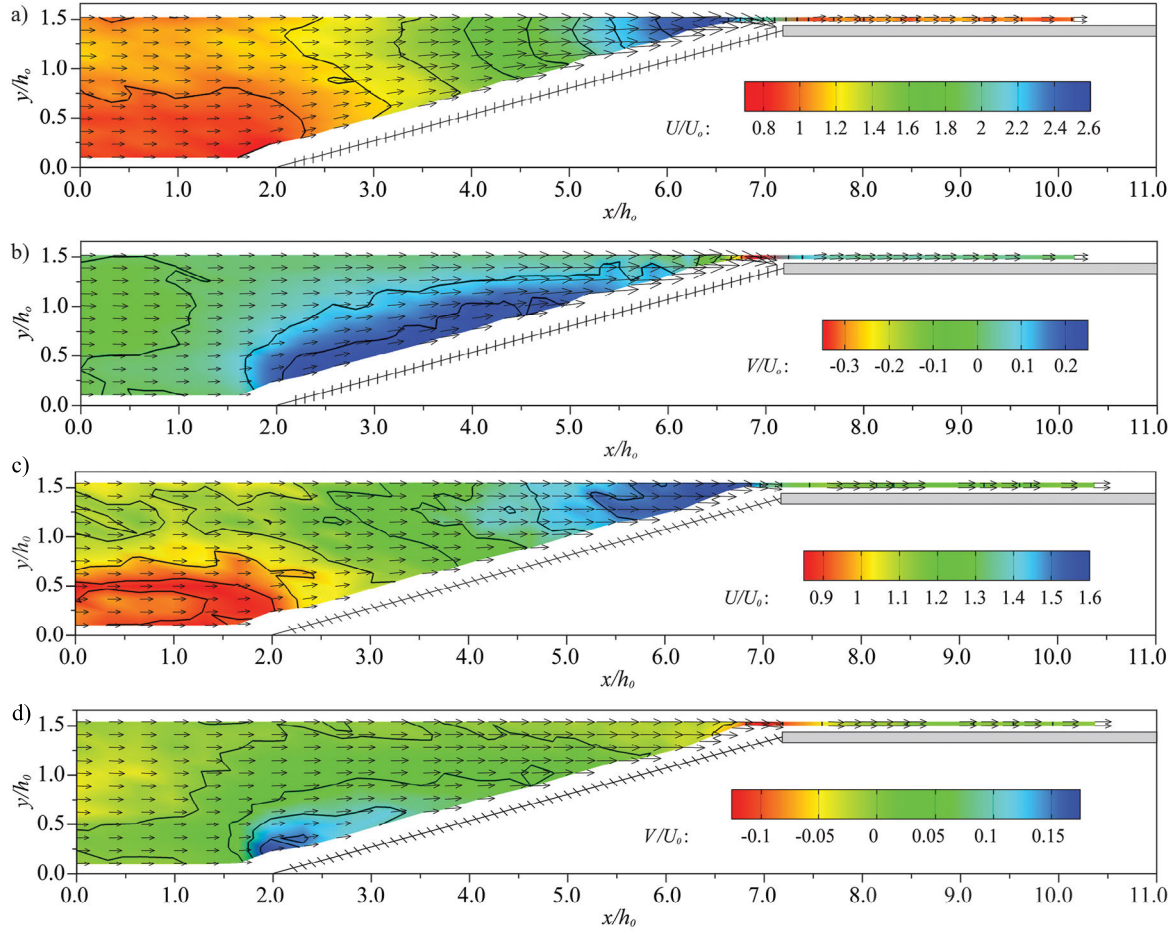


Figure 2.7 Relative flow velocities in streamwise U and spanwise V direction normalised with U_o , measured close to the flume bottom at $z/h_o = 0.06$ with 2D-LDA for (a,b) louver with $\alpha = 15^\circ$ and $\beta = 90^\circ$, and (c,d) MBR with $\alpha = 15^\circ$ and $\beta = 45^\circ$ (Albayrak *et al.*, 2020a)

Flow field around bars

Tsikata *et al.* (2009) and Tsikata *et al.* (2014) investigated the flow field around and between the bars of an intake trash rack by means of PIV measurements. They confirmed that the increasing flow velocity in combination with a reduced vortex intensity caused by narrower bar spacings led to an intense shear zone along the bars, which was responsible for the resulting energy dissipation and hence hydraulic head losses. The bar depth d_b itself, however, had hardly any effect on the flow field and thus on the head losses (Figure 2.8b). They further investigated the flow field in a straight channel around a trash rack with bars angled at $0^\circ \leq \beta \leq 12^\circ$ and confirmed the findings of Spangler (1928) that head losses increased substantially with increasing bar angle. Increasing the bar angle led to larger recirculation zones at the rear end of the bars. The effective blockage therefore became larger leading to higher flow velocities between the bars (Figure 2.8c). At the leading edge of the bars, a strong increase of the transversal flow velocity V was observed very close to the bar. The mean

velocities and turbulence intensities were barely affected by the bar inclination, however. At the downstream end of the bars, a highly turbulent region defined by two counter-rotating vortices was formed, where low flow velocities prevailed. The region became larger in length and width with increasing bar inclination or increasing flow velocity. The magnitude of the vorticity downstream of the bars increased as well (Tsikata *et al.*, 2009). Longitudinal velocity profiles along the bars and in the downstream channel showed that for more strongly angled bars a greater distance was required for re-adjustment of the flow, i.e. for the flow characteristics such as turbulence intensity and flow velocity to become uniform. In contrast, Figure 2.8d and further investigations with rounded or streamlined bar shapes showed significantly reduced head losses compared to rectangular bars (Kirschmer, 1926; Clark *et al.*, 2010; Tsikata *et al.*, 2014).

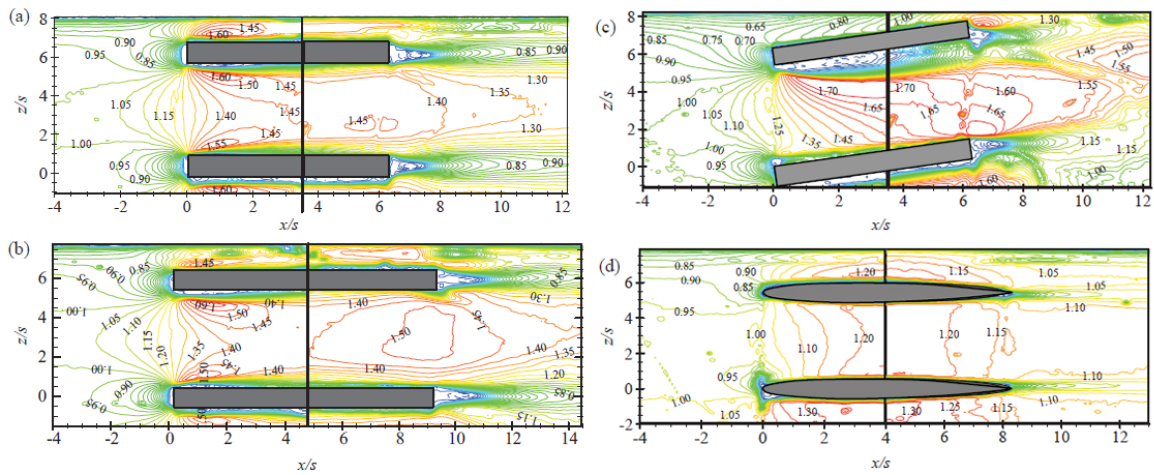


Figure 2.8 Contours of the mean normalised velocities in streamwise direction (U/U_0) from PIV measurements showing (a) the velocity field at conventional trash rack bars, (b) the effect of increased bar depth, (c) the effect of angled bars, and (d) the effect of bar shape on the flow pattern; from Tsikata *et al.* (2014)

Downstream flow field and turbine admission flow

Energy losses originate not only from the rack head losses but also from decreased turbine efficiency associated with the rack effect on the turbine admission flow. The flow field properties at the turbine intake significantly affect the turbine efficiency. According to Godde (1994), the following criteria for the turbine admission flow should be met for a symmetrical flow distribution and hence high turbine efficiency: (i) the mean flow velocity in each intake quadrant should not deviate by more than 10% from the mean admission flow velocity; and (ii) the mean flow discharge in the left and the right vertical intake half, Q_{left} and Q_{right} , should amount to between 47.5% and 52.5% of the total admission flow discharge, i.e. $\Delta Q/Q_t = |Q_{\text{left}} - Q_{\text{right}}|/Q_t \leq 5\%$. Raynal *et al.* (2013a) reported a highly asymmetric

flow field downstream of an angled bar rack with $\alpha = 45^\circ$, with a large recirculation zone on the flume side downstream of the d/s rack end leading to accelerated flow on the opposite flume side. Kriewitz (2015) and Moretti (2015) reported similar flow patterns for louvers and MBRs with larger recirculation zones for louvers due to the increased flow deflection for higher bar angles β (Figure 2.9).

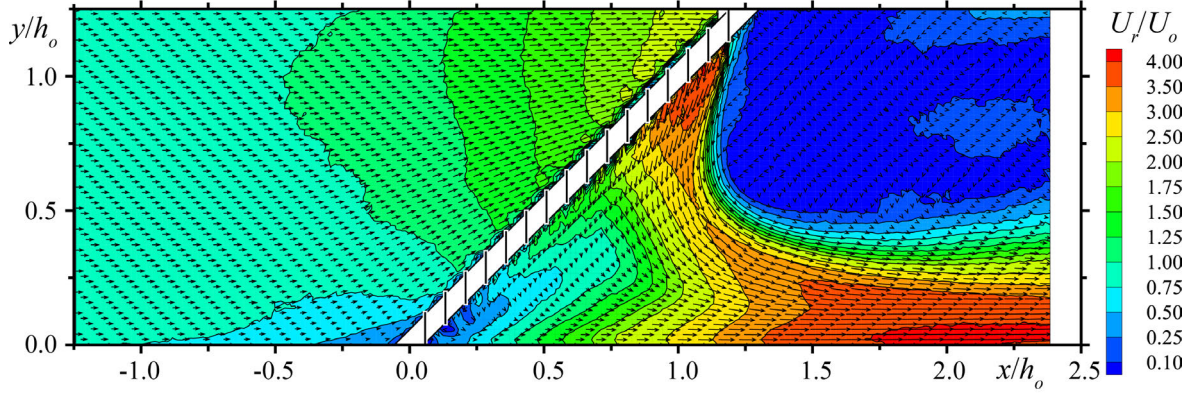


Figure 2.9 Mean resulting velocities normalised with U_o up- and downstream of a louver with $\alpha = 45^\circ$, $\beta = 90^\circ$, $\sigma = 0.17$ ($s_b = 50$ mm) resulting from PIV measurements at $z/h_o = 0.125$ (Kriewitz, 2015)

Table 2.2 shows the hydraulic performance of different MBRs and louvers investigated in a laboratory flume by Moretti (2015) and Albayrak *et al.* (2020a) regarding the head losses ξ_R , the velocity increase towards the d/s rack end U_{\max}/U_o and the turbine admission flow quality $\Delta Q/Q_t$. Merely the MBR configuration with $\alpha = 15^\circ$, $\beta = 45^\circ$ and a bottom overlay with $h_{Bo} = 0.11 \cdot h_o$ led to an acceptable admission flow.

Table 2.2 Head loss coefficients ξ_R and flow field parameters for louvers and MBRs with $s_b = 50$ mm investigated in a laboratory flume at $U_o = 0.6$ m/s (Moretti, 2015; Albayrak *et al.*, 2020a); it is indicated whether the discharge criterion proposed by Godde (1994) is met (+) or not met (–) 2 m downstream of the d/s rack end

FGS	α [°]	β [°]	ξ_R [-]	h_{Bo} [m]	U_{\max}/U_o [-]	Discharge per intake half [%]	$\Delta Q/Q_t$ [%]	
Louver	15	90	9.2	0	2.60	74.1 / 25.9	48.2	–
			7.6	$0.11 h_o$	–	60.6 / 39.4	21.2	–
MBR	15	45	1.7	0	1.60	52.8 / 47.1	5.7	–
			1.9	$0.11 h_o$	–	47.7 / 52.3	4.6	+
MBR	30	45	2.2	0	1.55	60.2 / 39.8	20.4	–
			2.3	$0.11 h_o$	–	58.9 / 41.1	17.8	–

Bates and Vinsonhaler (1957) suggested flow straightening vanes to reorganise the flow downstream of a louver, eliminate the backwater effect, and achieve an evenly distributed flow diversion toward the turbines. Shepherd *et al.* (2007) introduced curved bars with an upstream bar angle $\beta = 31.4^\circ$ or $\beta = 41.2^\circ$, and an outflow angle of $\delta \approx 20^\circ$. They tested FGSs with curved bars with rack angles of $\alpha = 7.2^\circ$ and $\alpha = 17.0^\circ$. They showed that the curved bars improved the upstream flow field with $U_{\max} = 1.7 \cdot U_o$ compared to the rectangular, straight bars with $U_{\max} = 2.5 \cdot U_o$, hence leading to lower velocity gradients and expectedly better fish guidance. Although the authors did not quantify the downstream flow fields, these results indicate that curved bars can be an alternative to vanes not only for louvers but also for MBRs.

2.6 Ethohydraulics of mechanical behavioural FGSs

2.6.1 Effect of hydrodynamic cues on fish behaviour

Fish are able to perceive spatial velocity gradients (*SVG*) due to the induced pressure difference inside the canals and pores of their lateral line organ. Various studies have linked the observed fish behaviour to hydrodynamic cues such as velocity or pressure gradients, or turbulence. Depending on their body size and shape, fish react differently to turbulent structures. It was shown that fish avoid areas of high turbulence or high Reynolds shear stresses to optimise their energy expenditure and to remain stable (Silva *et al.*, 2012a). Infrequent eddies, which are about the size of the fish body promote fish rotation and disorientation (Tritico and Cotel, 2010; Silva *et al.*, 2012a), whereas eddies much larger than the fish length do not affect fish balance (Lupandin, 2005; Webb and Cotel, 2010). While fish could be attracted to predictable turbulent flow if they are strong enough to maintain their stability and exploit the flow structures in boundary layers (Figure 2.10a), they avoid unpredictable vortex structures (Enders *et al.*, 2003). Webb and Cotel (2010) and Silva *et al.* (2012a) observed that a spread of the pectoral fins helped fish to control their stability while swimming in turbulent flows. Swimming in turbulent flows increases the energy expenditure and thus reduces the swimming capacity of fish depending on their body length. Lupandin (2005) found that the fish swimming performance tended to decrease for vortices which were about 2/3 of the fish body length (Figure 2.10b).

Fish can use the reduced wake flow behind an object to remain steady without much effort. Liao *et al.* (2003) further observed that fish exploited vortex structures to move against the current with little fin activity (Kármán gaiting). However, it can be assumed that species with extreme body shapes (e.g. eels) have more difficulty to remain stable and thus avoid highly turbulent flow (Liao, 2007). Investigations of sensory feedback by vision and the lateral line

organ suggest that fish are more likely to avoid turbulent flows at lower light levels (Pavlov *et al.*, 2000).

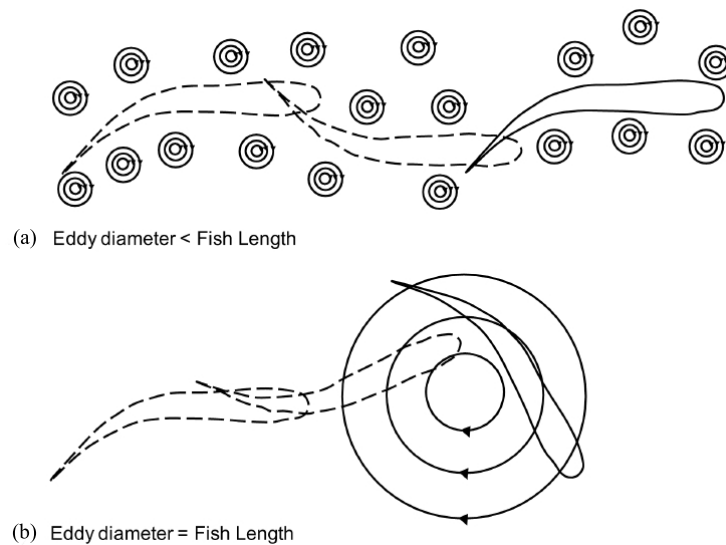


Figure 2.10 Effect of eddy size on the fish swimming stability; (a) fish can hold swimming position in small eddies and (b) larger-scale eddy can lead to instability and rotation of the fish body, adapted from Lacey *et al.* (2012)

Nestler *et al.* (2008) introduced the term “total hydraulic strain” as a distortion metric, which is defined by the sum of all nine spatial velocity gradients of the gradient tensor. They suggested that a fish is accustomed to a certain total hydraulic strain. An obstacle in the water increases the hydraulic strain. If the elevated hydraulic strain was smaller than a certain threshold value, fish swam in the direction of increasing flow velocity. Conversely, if the threshold value was exceeded, fish tended to swim in the direction of decreasing water velocity or even swam back upstream. This hypothesis was supported by a field study at the fish guidance facility of Lower Granite Dam. Within the same field study, Goodwin *et al.* (2007) observed that fish entered a bypass that they had rejected before and thus emphasized the ability of fish to acclimate to a certain total hydraulic strain.

2.6.2 Fish swimming behaviour at mechanical behavioural FGSs

Despite a few recent ethohydraulic and field studies, the knowledge about the behaviour of fish when encountering a movement barrier is highly incomplete. In several studies it was postulated that downstream moving fish switched to positive rheotaxis when they perceive the hydrodynamic cues of an approaching obstacle (Russon and Kemp, 2011; Lehmann *et al.*, 2016; Silva *et al.*, 2016).

Bates and Vinsonhaler (1957) and Anderson *et al.* (1998) examined the behaviour of salmon in a field study at a louver and of hatchery reared rainbow trout in a laboratory study at an angled bar rack with curved bars, respectively. They both observed similar behavioural patterns shown in Figure 2.11. If the flow velocity was lower than $v_{\text{sustained}}$, the fish oriented themselves tail first parallel to the flow, swimming actively against the current facing upstream (positive rheotaxis). With only little lateral movement, they approached the bypass entrance while facing upstream (Figure 2.11a). Figure 2.11b/c shows the behavioural pattern if the flow velocity was higher than $v_{\text{sustained}}$. The fish swam closer to the rack and oriented themselves parallel to the rack. They either turned their side orthogonal to the approach flow and repeatedly moving away from the rack, which led to a faster movement towards the bypass (Figure 2.11b) or they turned and dashed towards the FGS trying to get through (Figure 2.11c). If they did not succeed they turned again facing upstream moving quickly along the rack towards the bypass. Lehmann and Adam (2016) stated that by approaching the FGS, fish oriented themselves orthogonally to the rack axis leading to a slight pressure difference on either flank of the fish body. This caused the fish to be transported along the rack towards the bypass like a yawing boat.

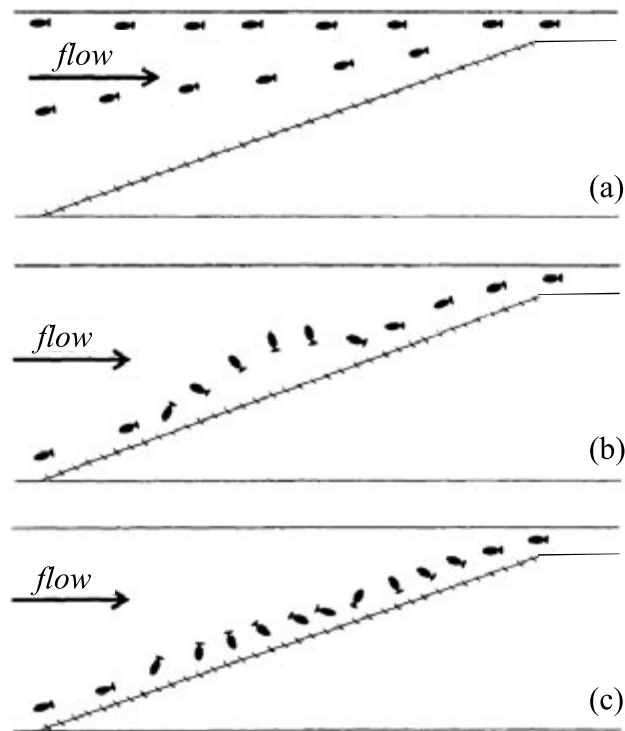


Figure 2.11 Typical movements of salmon and rainbow trout along a FGS for (a) $U_o \leq v_{\text{sustained}}$: fish are guided to the bypass with little lateral swimming movements, or for $U_o > v_{\text{sustained}}$ the fish either (b) explore the rack and avoid it with short bursts, or (c) search along the rack changing their rheotaxis; adapted from Shepherd (1998)

Adam *et al.* (2002) and Silva *et al.* (2016) reported that eels generally showed a different swimming behaviour. In both studies, the eels approached the FGS with their head first (negative rheotaxis) and did not shy away before touching or even colliding with the rack. If the eel managed to turn around, it tried to find a counterfort with its tail to push off and sprint back upstream. Due to their morphology, however, even adult individuals up to 60 cm length could pass through racks with a bar spacing of only 20 mm. The stamina of eels decreased in lower water temperatures and the fish were therefore more prone to impingement at conventional trash racks at approach flow velocities $U_o > 0.5$ m/s. For these reasons, alternative eel guidance structures have been developed, which take advantage of the fish's exploratory behaviour and the fact that eels tend to swim close to the riverbed. A system called "Bottom Gallery[®]" consists of a shelter fixed on the channel bed parallel to and directly in front of the narrowly spaced FGS to collect the eels shying away from the rack (Adam *et al.*, 2002). Another solution proposed by Hassinger and Hübner (2009) entails a collection pipe with entrance holes mounted parallel to the rack on the riverbed. However, these systems have not been approved to be efficient for high approach flow velocities or in case of sediment aggradations. The installed downstream collection and bypass system for eels at the HPP Schaffhausen on the Rhine river had to be taken out of operation due to the low efficiency and the high maintenance effort and cost. Brown *et al.* (2009) studied the behaviour of American eels in the forebay of a small HPP. Even at high approach flow velocities, the eels spent a lot of time in the forebay searching for a bypass moving up and down in the water column. The eels appeared to be repelled by light and thus preferred migrating at night. These findings confirmed the behaviour of European eels described by Durif *et al.* (2002).

In addition to turbulent structures, fish perceive accelerating or decelerating flows, i.e. spatial velocity gradients (SVG). When encountering acceleration, fish tend to switch to positive rheotaxis (Haro *et al.*, 1998). Enders *et al.* (2012) found that salmon smolts preferred stream-wise spatial velocity gradients of $SVG_x = \partial U / \partial x \leq 1 \text{ s}^{-1}$. Similar threshold values might be applicable for other fish species. Increased velocity gradients led to a higher tail-beat frequency and thus to a higher energy expenditure (Arenas *et al.*, 2015). Haro *et al.* (1998) further observed that salmon smolts avoided velocities higher than 1 m/s with burst swimming. The fish were able to escape from velocities up to 2.3 m/s. Bates and Vinsonhaler (1957) reported that a reduction of the flow velocity just in front of or inside the bypass caused confusion and triggered hesitation, which was also observed by Albayrak *et al.* (2020a). Adam and Lehmann (2011) observed that fish reacted sensitively to high SVG and shied away from bypass openings with sudden velocity changes.

2.6.3 Fish guidance efficiency

The fish guidance efficiency (FGE) of louvers was first investigated in a field study by Bates and Vinsonhaler (1957). They reported the highest FGE = 90-99% for chinook salmon (*Oncorhynchus tshawytscha*), steelhead trout (*Oncorhynchus mykiss*), striped bass (*Morone saxatilis*) and American shad (*Alosa sapidissima*) at a louver with $s_b = 50$ mm and $10^\circ \leq \alpha \leq 16^\circ$ (Table 2.3). Ruggles and Ryan (1964) studied the FGE of floating louvers with $\alpha = 11.2^\circ$ and $s_b = 60$ mm for the guidance of surface oriented fish. They reported a FGE of 50% and 87% for chinook salmon fry and steelhead trout smolts, respectively. Ducharme (1972) investigated the FGE of Atlantic salmon smolts at a V-shaped louver with $\alpha = 12^\circ$ and $s_b = 50$ mm installed in a canal. The FGE increased from 57% to 80% after the bypass was modified to increase flow velocities and reduce turbulence.

EPRI and DML (2001) investigated the FGE of louvers and angled bar racks with $\alpha = 15^\circ$ and 45° for American eels (*Anguilla rostrata*) and seven potamodromous species from hatcheries. They reported the highest FGE > 70% with a louver with $\alpha = 15^\circ$ and a 0.3 m high bottom overlay ($h_{Bo} = 0.17 \cdot h_o$) at approach flow velocities between 0.3 - 0.9 m/s (Figure 2.12a, Table 2.3). The application of the bottom overlay led to a 21% and a 13% FGE increase for louvers and bar racks, respectively. The authors concluded that louvers and angled bar racks with $\alpha = 45^\circ$ did not achieve satisfactory results regarding neither the FGE nor the economic aspects due to high head losses but considered FGSs with $\alpha = 15^\circ$ to have a high potential for fish guidance.

Flügel *et al.* (2015) and Albayrak *et al.* (2020a) conducted live-fish experiments in the laboratory with five European fish species, namely the common barbel (*Barbus barbus*), spirlin (*Alburnoides bipunctatus*), European grayling (*Thymallus thymallus*), brown trout (*Salmo trutta*) and the European eel (*Anguilla anguilla*), investigating the FGE of louvers and MBRs. They found that clear bar spacings $s_b > 50$ mm significantly decreased the FGE, whereas the approach flow velocity did not show a significant impact on the FGE. The tested louver with $\alpha = 15^\circ$ and $s_b = 50$ mm resulted in high transverse flow velocities at the d/s rack end and a strong velocity decrease at the bypass entrance. Fish avoided the area entirely, hesitated or shied back from the bypass entrance leading to a higher rack passage rate and an overall low FGE. Due to the improved flow conditions, MBRs led to a significantly higher FGE than louvers. Furthermore, the application of a bottom overlay with $h_{Bo} = 0.11 \cdot h_o$ eliminated the transverse flow near the flume bed and increased the flow velocities inside the bypass, resulting in a higher FGE. The highest FGEs of 73-100% were achieved with the MBR and a bottom overlay (Bo) independent of the rack angle α (15° or 30°) (Figure 2.12b). Only graylings showed a very hesitant behaviour. Even though no individual passed the rack, only

35% of the fish swam into the bypass, i.e. 65% refused to enter the bypass system and swam back upstream. Since the graylings were only tested with an MBR with $\alpha = 30^\circ$ without a bottom overlay, the average FGE of this FGS was affected accordingly in Figure 2.12b.

In addition to the MBR with $\alpha = 30^\circ$, $\beta = 45^\circ$, and $s_b = 50$ mm, Flügel *et al.* (2015) and Kriewitz (2015) investigated the FGE of an MBR with bars oriented in streamwise direction ($\beta = 0^\circ$). While the FGE of barbel was 100% for the MBR with $\beta = 45^\circ$, the FGE significantly decreased to 58% for the MBR with $\beta = 0^\circ$. The FGE of spiralin was equally high with 75 - 80% independent of the bar orientation. Since the flow field upstream of the MBR with $\beta = 0^\circ$ is hardly affected (Raynal *et al.*, 2014; Kriewitz, 2015), the high FGE of spiralin is unexpected and could indicate that these fish also react sensitively to visual cues.

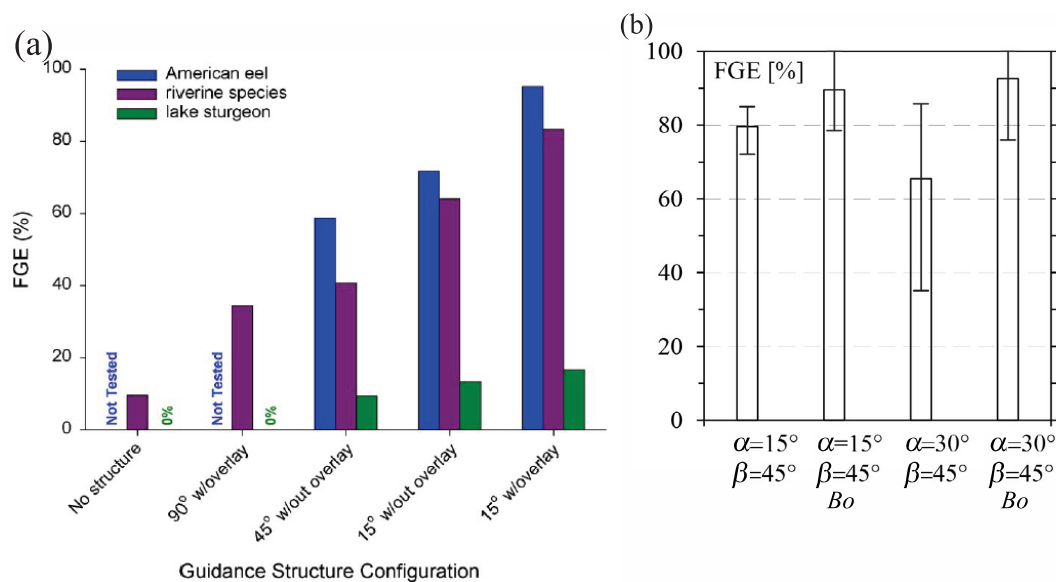


Figure 2.12 a) Average FGE of angled bar racks and louvers with different rack angles α and with or without a bottom overlay (EPRI and DML, 2001) and b) mean, minimum and maximum FGE averaged over five tested fish species for different MBR configurations with and without a bottom overlay (bo) (Albayrak *et al.*, 2020a)

The FGEs determined in laboratory and field studies for various fish species vary greatly (Table 2.3). Nevertheless, the studies in the past 20 years improved the knowledge of fish behavioural patterns near FGSs significantly and enhanced the achieved FGE. Many recently developed design guidelines therefore recommend FGSs as the “best practice” technology for fish protection at run-of-river HPPs (Turnpenny *et al.*, 1998; DWA, 2005; Turnpenny and O’Keeffe, 2005; USBR, 2006; BAFU, 2012).

Table 2.3 Fish guidance structures tested in laboratory or field studies and the achieved FGE described by different authors

Plant / Lab	FGS	α [°]	β [°]	s_b [m]	U_o [m/s]	Bypass $(h_{by} \times w_{by})$	Fish species	FGE _{max}	Author(s)
Tracy (CA)	Louver	11.5 - 40	90	0.04 - 0.14	0.15 - 1.22	$w_{by} = 0.16$ m	salmon, bass, trout, shad	90-99%	Bates and Vinsonhaler (1957)
Tracy (CA)	Floating louver	11.2	90	0.06	0.40 - 1.20	$w_{by} = 0.16$ m	salmon fry, trout	50-87%	Ruggles and Ryan (1964)
Sheet Harbour (NS)	V-shaped Louver	12	90	0.051 - 0.305	0.30 - 1.09	3.6×0.45 m $1.4 \text{ m}^3/\text{s}$	Atlantic salmon smolts	70-90%	Ducharme (1972)
Holyoke Canal (MA)	Louver	15	90	0.05	0.30 - 0.9	1.5×1.0 m $4 \text{ m}^3/\text{s}$ (2% of Q_d)	Atlantic salmon, shad, herring	85-90%	Stira and Robinson (1997)
Laboratory study	Louver	20	90	0.039 / 0.09	0.31 - 0.34	0.37 x 0.5 m	sturgeon	96-100%	Kynard and Horgan (2001)
	Angled bar rack	45	0	0.039				58-80%	
Alden Fish Testing Facility	Louver	15 / 45	90	0.05	0.30 - 0.90	0.9 x 0.15 m	bass, catfish, shiner, sturgeon, walleye	87-100%	EPRI and DML (2001)
	Angled bar rack	15 / 45	75 / 45	0.025 / 0.05			American eel	58-100%	
Laboratory of Hydraulics (VAW) at ETH Zurich	Louver	15	90	0.05 / 0.11	0.3 / 0.6 / 0.8	0.9 x 0.19 m	barbel, grayling, brown trout, European eel, spirulin	10-80%	Flügel <i>et al.</i> (2015); Albayrak <i>et al.</i> (2020a)
	Modified bar rack (MBR)	15 / 30	45					73-100%	

2.7 Bypass system design

The function of a bypass system is to safely collect, carry and reintroduce the fish to the river downstream of a movement barrier. An effective bypass design is therefore equally essential as the design of the FGS itself. Most importantly, the bypass must be designed according to the swimming capacity and behaviour of the local fish species. Previous studies demonstrated that a poor bypass design leads to low FGE (Ovidio *et al.*, 2017; Wagner *et al.*, 2019), but an optimal bypass design can significantly increase the FGE (Ducharme, 1972; Simmons, 2000; Lehmann *et al.*, 2016). A bypass entrance must be easily found, accepted and passed by all fish species without harm, delay, flight or exhaustion. This section summarises the findings and recommendations from various laboratory and field studies, and design guidelines, respectively.

2.7.1 Attraction and acceptance of the bypass system

To prevent migration or movement delays and exhaustion, fish should be guided efficiently along a FGS and quickly find and accept the bypass system (Ebel, 2016). To this end, the bypass entrance should be placed directly adjacent to the FGS, i.e. no more than 1-2 m away (USBR, 2006; Larinier, 2008; Schmalz *et al.*, 2012). Turnpenny and O’Keeffe (2005) recommend to construct several bypass entrances along the rack for very wide approach flow channels (> 100 m). Four bypasses were installed along the 98.3 m long louver of the Tracy Fish Collection Facility (USBR, 2011). The entrance to each bypass is 15.2 cm wide and 6.7 m high, and leads to a pipe via a transition section. For fish to easily find and be attracted to the bypass entrance, the flow towards the bypass created by the FGS must not be superimposed by other, stronger flow patterns. Lehmann *et al.* (2016) compared horizontal bar racks with bypass openings at the end of the rack orthogonal or in line with the approach flow in a laboratory study. They registered most fish passages for the combination of a horizontal bar rack with a directly adjacent bypass system in line with the flow. The bypass orthogonal to the main flow direction did not effectively attract the fish.

In the U.S., where FGSs are mainly designed for salmonids swimming near the water surface, many bypass systems only have one opening in the upper part of the water column or a surface collecting channel system. Since many European species swim anywhere in the water column or along the riverbed, the implementation of bottom, middle or even fully open bypass entrances need to be considered (Pavlov, 1989; Brown *et al.*, 2009; Travade *et al.*, 2010). However, field studies showed that fixed bottom entrances quickly filled up with sediments and were then no longer effective (Engler *et al.*, 2016).

Ebel (2016) first introduced an open channel bypass system, which has been implemented in

combination with a horizontal bar rack (HBR) at small HPPs in Germany, Switzerland and Sweden (Figure 2.13). A vertical axis flap gate with top and bottom openings is installed at the bypass entrance (cf. Figure 2.14), followed by a fixed or an adjustable overflow weir to regulate the bypass discharge and thus the flow velocities at the bypass entrance. Ebel (2016) proposes an inclination angle of 10° - 30° for the adjustable weir for efficient fish guidance. During the main fish movement times, the entrance flap gate is closed for controlled flow conditions at the bypass entrance. During flood events or for flushing purposes, the entire flap gate can be opened to increase the bypass discharge. If the weir is constructed as a mobile element, it can be lowered in case the channel is used for flushing purposes. The flow thereby needs to be regulated accordingly to avoid adverse surge and drawdown effects.

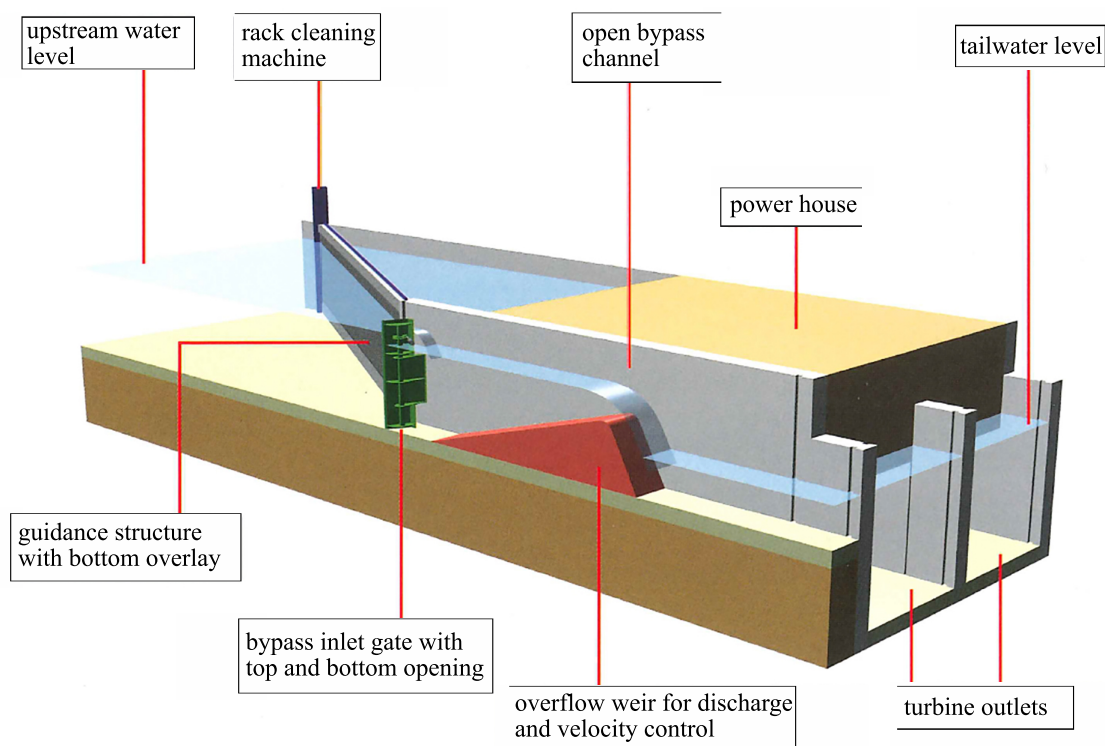


Figure 2.13 Illustration of a bypass design according to Ebel (2016) with an axial flap gate with bottom and top openings at the bypass entrance and an adjacent overflow weir for discharge control

Klopries *et al.* (2018) statistically analysed the results of 50 field studies from Australia, North America and Europe on the efficiency of surface bypasses. This bypass design can be combined with an inclined rack to guide the fish to the surface. They reported that the efficiency was as low as 0 to 27% for the eel, which is classified a bottom oriented species, but increased for surface oriented fish species, i.e. the Atlantic and Pacific salmon, and the brown trout, to 14 - 94%, 13 - 89% and 0 - 97%, respectively. Tomanova *et al.* (2018) conducted an extensive telemetry study with hatchery-reared Atlantic salmon smolts at four

small- to medium-sized HPPs in France, which are all equipped with a vertically inclined rack with $s_b = 20$ mm and a surface bypass. They report high fish guidance efficiencies of 83 - 92% for this surface oriented fish species.

Haro *et al.* (1998) compared the swimming behaviour of Atlantic salmon and American shad at a conventional sharp-crested weir and a new weir design called the NU-Alden weir, which provides a uniform spatial velocity gradient in streamwise direction ($SVG_x = \partial U / \partial x$) of 1 m/s/m. The new design minimises flow separation and turbulence and is designed to guide fish from an area of low flow velocity (0.5 m/s) to an area of high flow velocity (3 m/s) at the top of the weir. Haro *et al.* (1998) reported higher fish passage rates for the NU-Alden weir compared to the sharp-crested weir for Atlantic salmon smolts, but only a small increase of passage rates for American shad. The NU-Alden weir is currently in operation at the bypass entrance of a louver-bypass system in the Holyoke Canal. Enders *et al.* (2012) confirmed the optimum SVG_x for actively migrating Chinook salmon smolts of 1 s^{-1} . Silva *et al.* (2016) conducted similar experiments to assess the passage rates of European eels and Iberian barbel (*Luciobarbus bocagei*) at differently sloped weirs. Unfortunately, they did not report the SVG_x at the tested weir setups. Up to date, there is no systematic study available on the optimum SVG_x for the cyprinids tested in the present study, i.e. spirilin, nase and the common barbel.

Field studies and ethohydraulic laboratory experiments demonstrated that the flow conditions in front of the bypass entrance are decisive for fish acceptance and thus for high FGE (Larinier and Travade, 2002; Kriewitz, 2015; Lehmann *et al.*, 2016). High SVG_x , an abrupt velocity decrease or highly turbulent flow triggered hesitation or a flight reaction and thus decreased the FGE (Scruton *et al.*, 2003; Enders *et al.*, 2012; Kriewitz, 2015; Kammerlander *et al.*, 2020). Some authors therefore propose a velocity increase rate as a bypass design parameter expressed by the ratio of bypass entrance velocity to mean approach flow velocity $U_{by,in}/U_o$. Ducharme (1972) observed the best louver-bypass system guidance and acceptance rates for $U_{by,in}/U_o \geq 1.5$ in a field study with Atlantic salmon, which are strong swimmers. The USBR (2006) gives a general design value for all fish species of $U_{by,in}/U_o = 1.1...1.5$ for louver-bypass systems, while Ebel (2016) recommends $U_{by,in}/U_o = 1.0...2.0$ for HBR-bypass systems. Ebel (2016) further proposes maximum bypass entrance velocities of $U_{by,in} = 0.3...1.5$ m/s for all fish species. The findings of these studies indicate that the bypass discharge needs to be regulated based on site-specific fish-biological criteria. The discharge of the bypass system Q_{by} at existing FGSs amounts to 2...10% of the design discharge (Odeh and Orvis, 1998; Larinier and Travade, 1999; Ebel, 2016).

Abrupt velocity changes at the bypass entrance can be avoided with gradual transitions (Figure 2.14). Lehmann *et al.* (2016) reported the highest bypass acceptance rates of salmon smolts, European eels and several potamodromous species for a bypass with a rectangular opening and a smooth transition to an adjacent pipe with a radially symmetrical velocity profile. Various authors propose a bypass entrance width of 0.5 - 1.0 m for all species (Larinier and Travade, 2002; DWA, 2005; Turnpenny and O’Keeffe, 2005; USBR, 2006), whereas Ebel (2016) gives recommendations for different fish species and sizes based on an extensive data base from laboratory and field studies. Travade and Larinier (1992) further recommend a minimum flow depth of 0.4 m at weirs, gates or other structures for safe fish passage and to avoid a hesitant behaviour.



Figure 2.14 Vertical axis flap gate at the bypass entrance with a top and a bottom opening constructed with gradual geometric transitions to achieve a gradual velocity increase, adapted from BAFU (2012)

2.7.2 Design recommendations for unharmed bypass passage

The flow velocities inside the bypass should gradually increase until they are higher than the fish swimming speed to prevent fish from swimming back upstream. To avoid injuries, however, the flow velocity should not be higher than 5 - 6 m/s (Guensch *et al.*, 2002; Ebel, 2016). Transitions and velocity changes within the entire bypass must be gradual to avoid flow separation, high shear stresses, sudden pressure changes or high turbulence. The materials used should be smooth and non-corrosive and joints smoothly welded. Bends should be implemented with a large radius to prevent injuries. USBR (2006) recommends a radius of curvature larger than 5 times the pipe diameter or channel width ($r/d > 5$). According to Turnpenny and O’Keeffe (2005) the radius should be larger than 3 m.

The bypass outlet should be located far enough from the HPP turbine outlet and should release the fish above the water surface to avoid re-entering or schooling, which might attract predators (Figure 2.15). Furthermore, a free surface bypass outlet avoids the formation of

a hydraulic jump, which can lead to disorientation, high shear stresses, sudden pressure changes or the entrainment of too much oxygen. A high dissolved oxygen content can cause the fatal gas-bubble illness. The drop height of the bypass outlet should therefore amount to 1.8 - 2.4 m. The water depth at the impact zone should be at least 0.9 m. For higher drops, the water depth should be at least 25% of the drop height (Odeh and Orvis, 1998; BAFU, 2012), which has to be considered especially for HPPs with a fluctuating downstream water level. Larinier and Travade (2002) propose maximum impinging velocities of 10 m/s to prevent injuries.



Figure 2.15 Rocky Reach Dam with bypass tailrace outlet at Columbia River, Washington (Photo by Chelan County PUD), view against flow direction

2.7.3 Operational aspects of the bypass system (BS)

The possibility of varying approach flow conditions due to different HPP operating scenarios such as the shutdown of single turbines or flood events must be taken into account for the design of a FGS-BS. A varying upstream water level or the blocking of the bypass entrance by large wood also needs to be considered. As an example, the bypass entrance height is adjustable to the varying headwater level at the Poutès Dam in France (Larinier and Travade, 2002).

The bypass is optimally designed in a way that bed load is continually or intermittently transported or flushed downstream through the bottom opening and organic fine material is regularly removed or transported through the surface opening. The installation of fish counting devices in the bypass can be planned to monitor its effectiveness. DWA (2005) demands that the bypass system is in operation during the entire movement period of the local fish species. Ideally, the operation of the bypass system is only shut down during a turbine shut down, i.e. during flood and/or flushing events. In case of inflows higher than the HPP design discharge, fish can also use the overflow weir for a safe downstream movement

as long as the drop height is not higher than 10 m, the fall velocity is less than 16 m/s and the fish are not caught in a recirculation zone. The water volume in the stilling basin should be above 10 m^3 per $1 \text{ m}^3/\text{s}$ discharge to limit turbulence (Odeh and Orvis, 1998). The overflow weir shape might thereby also have an effect on the FGE. Silva *et al.* (2016) found that the FGE for eels increased to 90% for weirs with a 30° or 45° upstream inclination compared to a vertical upstream weir face. They observed that the fish downstream passage was delayed by the recirculation zone created in front of standard spillway crests. The opening of sluice gates can further promote the safe downstream movement of bottom oriented eels if well-designed (Engler *et al.*, 2016).

2.8 Electrified fish guidance structures

Electrical screens as a sensorial behaviour barrier were investigated in several studies (DWA, 2005; Parasiewicz *et al.*, 2016; Miehl *et al.*, 2017). Despite promising results, they were shown to be inefficient for fish protection in particular if approach flow velocities are high. Electrified FGSs are hybrid barriers, which combine the protection and guidance effects of physical and behavioural barriers, i.e. MBRs, CBRs or HBRs, and of the behavioural effect of an electric field. Equipping a FGS with a weak electric field, i.e. a low voltage (max. 80 V), leads to an additional fish avoidance reaction, similar to an electric fence for farm animals (Tutzer *et al.*, 2019). Fish recognise a rack earlier due to the electric field, so that the reaction area of the fish is larger and they are not exposed to the increased flow velocities between the bars. The rack is still installed at an angle to the flow creating a velocity component parallel to the rack guiding the fish to the bypass. These so-called hybrid FGSs could increase fish protection, especially for small fish or fish, which do not react sufficiently to the hydrodynamic cues of a mechanical behavioural barrier (e.g. European eel). In contrast to the constant direct current (cDC) used for electrofishing, the hybrid FGSs are supplied with pulsed direct current with regular bursts (pDC) or with gated bursts (gpDC), i.e. pulse groups followed by a longer pause.

Monan and Pugh (1964) determined the FGE of a widely spaced louver ($s_b = 120 \text{ mm}$) equipped with an electrical field. The bars of the louver thereby acted as electrodes. In the field tests carried out with juvenile steelhead trout, a louver with a rack angle $\alpha = 20^\circ$ was energized with 15 pulses per second, each 60 V pulse lasting for 20 ms. The tests showed no significant difference with or without electricity at an approach flow velocity of 0.76 m/s. Pugh *et al.* (1970) suggested a sequentially pulsed field along the FGS to generate a sweeping effect along the rack, which led to FGEs of up to 84% at $U_o = 0.2 \text{ m/s}$ and reduced to 43% at $U_o = 0.8 \text{ m/s}$ for chinook and coho salmon, and rainbow and steelhead trout. Since

fish are believed to have a better sense of direction in variable fields, a pulsed field with variable parameters could further increase the effectiveness of the hybrid FGS. The recently developed “low-voltage electric fish guidance system” called NEPTUN takes advantage of this effect (Parasiewicz *et al.*, 2016). The semi-randomly varying pulses further inhibit a habituation effect. Recent ethohydraulic tests on electrified FGSs have been carried out with partly promising results. Berger (2017) has generated a weak electric field behind an HBR and between the bars by electrifying the rack as the anode and a coarse steel mesh 20 cm downstream of the HBR as the cathode. Even with a bar spacing of $s_b = 30$ mm and approach flow velocities of up to 0.8 m/s, only 1% of the eels passed the rack compared to 15% without electrification. However, the study does not give detailed information about the number of eels that passed the bypass or that swam back upstream and refused the downstream movement. Similar findings were reported by Tutzer *et al.* (2019) for the so-called electric flexible fish fence consisting of electrified horizontal steel cables. They tested the fish fence with $\alpha = 40^\circ$ and a cable spacing of $s_b = 60$ mm for European grayling, chub, and brown trout at $U_o = 0.43$ m/s. The electrification reduced the number of fence passages, i.e. increased fish protection, but the number of bypass passages, i.e. the fish guidance efficiency, was not increased. Rost *et al.* (2014) electrified a trash rack with $s_b = 80$ mm with alternating current to investigate the protection and guidance of eels, salmon smolts and rainbow trout. The protection efficiency was significantly increased with the electrification, especially for eels. However, the alternating current also led to very hectic flight reactions of the fish.

An advantage of such hybrid FGSs is thus, that the bar spacing can be increased by electrifying the rack, reducing the clogging probability of floating debris. Ideally, the fish protection remains the same or increases, while negative operational aspects are minimised. However, avoidance and flight reactions are predominantly observed leading to an overall avoidance of the FGS-BS (Tutzer *et al.*, 2019). This might be effective to shield fish from intakes, but at a run-of-river HPP, efficient downstream movement might be impaired because the fish are not guided to the bypass. The question therefore arises how the FGE of a FGS can be improved by adding an electric field. This research question is partly answered in this study for the electrified CBR for European eels and spiralin.

2.9 Handling of large wood, organic fine material and sediments

Large wood (LW) can accumulate at the trash rack or the FGS at run-of-river HPPs. LW accumulations reduce the available cross section, increase flow velocities and therefore significantly increase the head losses at the rack (Lange and Bezzola, 2006). The back water

rise caused by LW accumulations affect the flow conditions at the bypass entrance and can lead to additional sediment aggradations. Furthermore, the FGE of the FGS and the attraction of the bypass are decreased by LW blockage especially for species swimming near the water surface. Gudde (2016) investigated the LW clogging probability at MBRs and a louver in laboratory experiments. She found that the probability of a single log to accumulate decreased with increasing Froude number and decreasing rack angle α . If a top overlay was installed, the LW was guided along the rack and through the bypass decreasing the clogging probability.

Pahud (2013) investigated operational counter measures during a flood event when surplus discharge is released over the weir. He showed that LW accumulated at the d/s louver end and in front of the bypass entrance if the turbines were operated during the flood event (Figure 2.16a). If the turbines were shut down, however, the LW passed the weir and was transported downstream even without a top overlay (Figure 2.16b).



Figure 2.16 LW accumulations at the louver with $\alpha = 30^\circ$ in the physical model (1:35) of a Swiss run-of-river HPP after the simulation of a 100-year flood event if (a) turbines are in operation and (b) turbines are shut down during the flood event; adapted from Kriewitz (2015)

If a large amount of LW is expected, an additional trash rack or log boom can be installed upstream of a FGS. However, these lead to further head losses and can act as an additional behavioural barrier negatively affecting the efficiency of the FGS (Nestler *et al.*, 2008).

HBRs characterized by small bar spacings ($s_b \leq 30$ mm) installed at small HPPs in Switzerland or Germany were in some instances quickly blocked by organic fine material (Ebel, 2016). MBRs and louvers characterized with larger bar spacings ($s_b \geq 25$ mm) are less prone to blockage by sediments or organic fine material and thus need to be cleaned less frequently

than VBRs or HBRs with narrow bar spacings. The processes of sediment transport in the vicinity of a FGS are practically unknown. Depending on the bar spacing and the rack angle it can be assumed that sediment might pass the FGS or settle in front of it. If parallel velocities V_p are high or a bottom overlay is installed, sediment can be transported along the FGS and through the bypass. Due to the lack of knowledge, more studies are needed to investigate the effect of FGSs on the sediment transport in the HPP forebay.

2.10 Hydraulic fundamentals

2.10.1 Turbulent flow structures in open channel flow

Rivers and open channel flows present complex 2D or 3D turbulent flow structures, which play an important role in the transport and mixing processes of sediment, nutrients and oxygen. Such turbulent flow structures affect both fish habitat quality and fish behaviour. In a Cartesian coordinate system, U , V and W denote the components of the time averaged flow velocity in the streamwise x , spanwise y and vertical z directions, respectively. Turbulent eddies of various sizes occurring above a threshold Reynolds number create velocity fluctuations in three directions. The instantaneous and corresponding fluctuating flow velocities are u , v , w , and u' , v' and w' , respectively (Figure 2.17, Eq. 2.9).

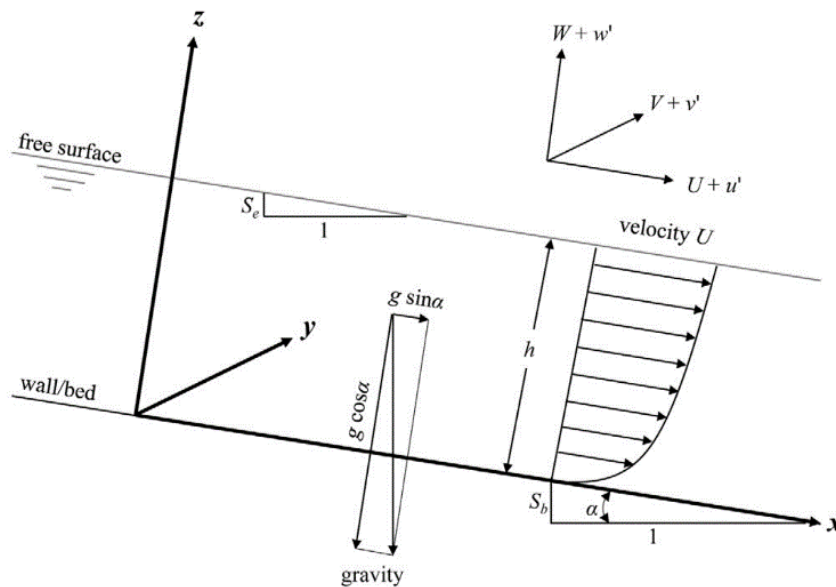


Figure 2.17 Coordinate system of open channel flow, adapted from Nezu and Nakagawa (1993)

The time averaged local streamwise flow velocity U is calculated and decomposed with the

so-called “Reynolds decomposition” as

$$U = \frac{1}{n} \sum_{i=1}^n u_i = u(t) - u'(t), \quad (2.9)$$

with n = number of time steps t . The components V and W are calculated likewise (Surek and Stempin, 2007). The time averaged velocity fluctuations (u' , v' , w') in a long enough time interval become zero.

The complete understanding of stochastic, turbulent flow processes requires the computation of the velocity fluctuation components, which allow for a statistical analysis of the experimentally acquired data. The turbulence intensity is hence defined by the root-mean-square values (*rms*-values) of the fluctuating components (Figure 2.18):

$$u_{rms} = \sqrt{\overline{u'^2}}, \quad v_{rms} = \sqrt{\overline{v'^2}}, \quad \text{and} \quad w_{rms} = \sqrt{\overline{w'^2}}. \quad (2.10)$$

Figure 2.18 shows two time series of the instantaneous streamwise velocity u and the turbulence intensity u_{rms} . Despite the same mean velocities, the turbulence level is clearly higher in the first time series than in the second time series.

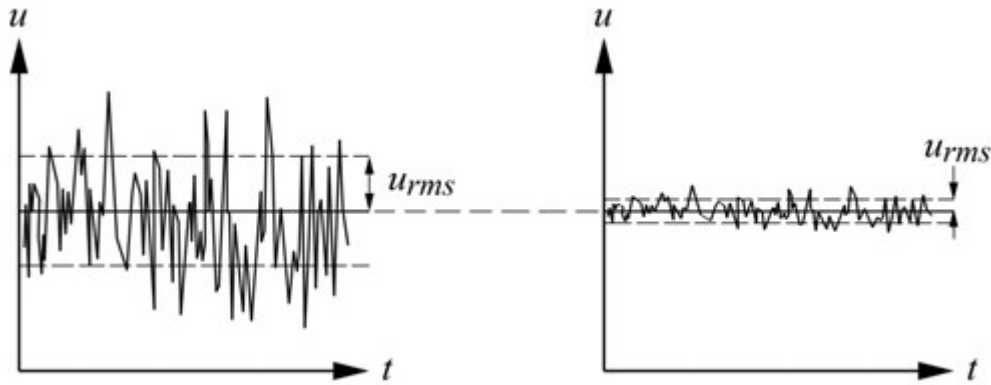


Figure 2.18 Two examples of a time series of instantaneous, streamwise velocities at a fixed position in the water column (Pope, 2013)

The total shear stress τ [N/m^2] includes the laminar or viscous shear stress and the turbulent or Reynolds shear stress. In 2D turbulent flow it yields:

$$\tau = \tau_{\text{viscous}} + \tau_{\text{Reynolds}} = \rho \nu \frac{\partial U}{\partial z} + \rho (-\overline{u'w'}), \quad (2.11)$$

with ρ = fluid density in [kg/m^3] and ν = kinematic viscosity in [m^2/s]. At the channel bed ($z = 0$), the total shear stress τ is referred to as the bed shear stress τ_{bed} . The viscous stress

only applies in the viscous sublayer close to the wall and is often neglected since its effect is small in hydraulically rough turbulent flows. The Reynolds shear stress follows a linear distribution in 2D turbulent flow where secondary currents are absent:

$$-\frac{\overline{u'w'}}{u_*} = \left(1 - \frac{z}{h}\right), \quad (2.12)$$

with u_* = friction velocity and h = flow depth. The relation to the bed shear stress τ_{bed} , which is the local shear stress, follows as:

$$u_* = \sqrt{\frac{\tau_{\text{bed}}}{\rho}}. \quad (2.13)$$

The friction velocity u_* can be calculated from the linear distribution of Reynolds shear stress or the log-law (Eq. 2.15). If no detailed velocity data is available, the wall averaged bed shear can be calculated as:

$$\overline{\tau_{\text{bed}}} = \rho \cdot g \cdot h \cdot S_e, \quad (2.14)$$

with $S_e = \sin \alpha - \cos \alpha \cdot (dh/dx)$ = energy slope (Figure 2.17). If the flow is uniform, the energy slope is replaced with the channel slope.

Open channel flow consists of two self-similar regions, namely the inner and the outer region, described by different scaling laws (Townsend, 1980). The flow in the inner region is dominated by viscous forces and scaled by the friction velocity u_* and the length scale ν/u_* . This region is defined as $z/h \leq 0.2$. In the outer layer, the flow is controlled by inertial forces and scaled with the depth averaged flow velocity \hat{U} . The log-law is valid in the inner region and may extend to the outer region and its formula universally follows (Nezu and Nakagawa, 1993):

$$U^+ = \frac{1}{\kappa} \ln\left(\frac{z}{z_o}\right), \quad (2.15)$$

with $U^+ = u(z)/u_*$, $u(z)$ = time-averaged velocity at level z , z = distance from the channel bed, z_o = zero-velocity level of the flume bed, and κ = von Kármán constant. Given the streamwise velocity profile, the friction velocity u_* can be calculated using the log-law fit (Eq. 2.15).

An important parameter to assess the fish behaviour in turbulent flows is the turbulent kinetic energy (*TKE*). It describes the kinetic energy of the velocity fluctuations and is therefore a

local indicator of the turbulence intensity (Rodi, 1984):

$$TKE = \frac{1}{2} (u_{rms}^2 + v_{rms}^2 + w_{rms}^2), \quad (2.16)$$

where TKE is in the unit $[m^2/s^2]$. In a fully developed turbulent open channel flow, the normalised turbulence intensities u_{rms}/u_* , v_{rms}/u_* , w_{rms}/u_* and the turbulent kinetic energy TKE/u_*^2 follow the following universal distributions, i.e. self-similarities (Nezu and Nakagawa, 1993):

$$\frac{u_{rms}}{u_*} = 2.30 \exp(-z/h), \quad (2.17)$$

$$\frac{v_{rms}}{u_*} = 1.63 \exp(-z/h), \quad (2.18)$$

$$\frac{w_{rms}}{u_*} = 1.27 \exp(-z/h), \quad (2.19)$$

$$\frac{TKE}{u_*^2} = 4.78 \exp(-2z/h). \quad (2.20)$$

As shown in section 2.6.1, eddy size is an important measure for fish stability and position choice. The energy cascade model described by Kolmogorov (1991) states that large eddies with low frequency and a high turbulent kinetic energy density transfers their energy into smaller eddies with higher frequency and a smaller turbulent kinetic energy dissipation (Figure 2.19). The smallest possible dissipative eddy is thus called the Kolmogorov microscale η_k . Eddies smaller than this scale dissipate their kinetic energy by viscous heating and disappear. The range of the eddy size spectrum increases as the Reynolds number increases (Rodi, 1984).

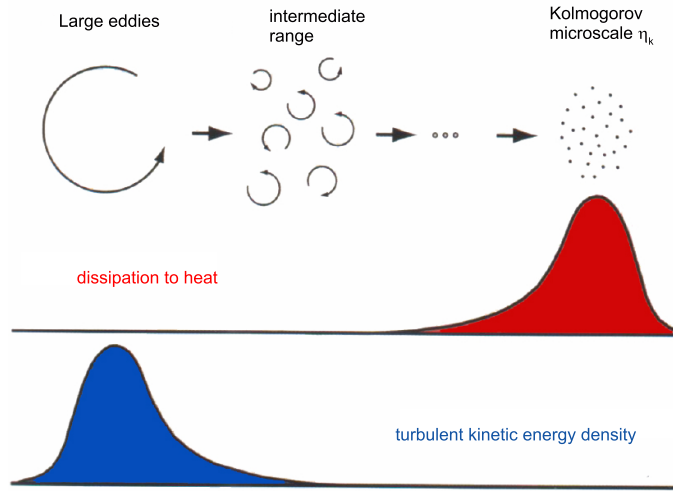


Figure 2.19 Energy cascade model with different eddy scales and their energy transfer, adapted from Heller (2009)

2.10.2 Spatial velocity gradients

The spatial variation of the velocity field is quantified by linear deformation (Eq. 2.21), rotation (Eq. 2.22) and angular deformation (Eq. 2.23). The sum of these three processes results in the spatial velocity gradient tensor $T(SVG)$ comprising the nine spatial velocity gradients (SVG) (Eq. 2.24):

$$T(SVG) = \begin{pmatrix} \frac{\partial U}{\partial x} & 0 & 0 \\ 0 & \frac{\partial V}{\partial y} & 0 \\ 0 & 0 & \frac{\partial W}{\partial z} \end{pmatrix} + \quad (2.21)$$

$$\begin{pmatrix} 0 & \frac{1}{2} \left[\frac{\partial U}{\partial y} - \frac{\partial V}{\partial x} \right] & \frac{1}{2} \left[\frac{\partial U}{\partial z} - \frac{\partial W}{\partial x} \right] \\ \frac{1}{2} \left[\frac{\partial V}{\partial x} - \frac{\partial U}{\partial y} \right] & 0 & \frac{1}{2} \left[\frac{\partial V}{\partial z} - \frac{\partial W}{\partial y} \right] \\ \frac{1}{2} \left[\frac{\partial W}{\partial x} - \frac{\partial U}{\partial z} \right] & \frac{1}{2} \left[\frac{\partial W}{\partial y} - \frac{\partial V}{\partial z} \right] & 0 \end{pmatrix} + \quad (2.22)$$

$$\begin{pmatrix} 0 & \frac{1}{2} \left[\frac{\partial U}{\partial y} + \frac{\partial V}{\partial x} \right] & \frac{1}{2} \left[\frac{\partial U}{\partial z} + \frac{\partial W}{\partial x} \right] \\ \frac{1}{2} \left[\frac{\partial V}{\partial x} + \frac{\partial U}{\partial y} \right] & 0 & \frac{1}{2} \left[\frac{\partial V}{\partial z} + \frac{\partial W}{\partial y} \right] \\ \frac{1}{2} \left[\frac{\partial W}{\partial x} + \frac{\partial U}{\partial z} \right] & \frac{1}{2} \left[\frac{\partial W}{\partial y} + \frac{\partial V}{\partial z} \right] & 0 \end{pmatrix} = \quad (2.23)$$

$$\begin{pmatrix} \frac{\partial U}{\partial x} & \frac{\partial U}{\partial y} & \frac{\partial U}{\partial z} \\ \frac{\partial V}{\partial x} & \frac{\partial V}{\partial y} & \frac{\partial V}{\partial z} \\ \frac{\partial W}{\partial x} & \frac{\partial W}{\partial y} & \frac{\partial W}{\partial z} \end{pmatrix}. \quad (2.24)$$

Eq. (2.24) includes the derivative of each velocity component in all three directions. It is unknown, which mechanism triggers a reaction in the fish movement. The magnitude of the

total spatial velocity gradient is defined as

$$SVG = \sqrt{\left(\frac{\partial U}{\partial x}\right)^2 + \left(\frac{\partial U}{\partial y}\right)^2 + \dots + \left(\frac{\partial W}{\partial z}\right)^2}. \quad (2.25)$$

Nestler *et al.* (2008) built the total hydraulic strain as the sum of the absolute values of all nine velocity gradients. They related the total hydraulic strain in the forebay of a HPP to the movement of steelhead trout and Chinook salmon at a mechanical behavioural guidance structure, a surface bypass collector and a removable spillway weir. In their study, Nestler *et al.* (2008) hypothesised that the fish swim towards areas with increasing flow velocities as long as the hydraulic strain is lower than a specific threshold value triggering an avoidance reaction. This threshold value can differ for different fish species or life stages. They confirmed this hypothesis by comparing a computational fluid dynamics (CFD) model of the HPP forebay with the movements of tagged fish. Furthermore, they observed that the fish passed areas they initially rejected, which indicates that fish can acclimate to higher hydraulic strain, thereby increasing the threshold value for an avoidance reaction. Nestler *et al.* (2008) do not specify any threshold values in their study.

Enders *et al.* (2012) investigated the fish behaviour at a vertical barrier with a bottom and a top opening in a laboratory flume. They computed the spatial velocity gradient as the velocity change across the fish's body length, i.e. the length of the lateral line organ. Since U was the dominant flow component in the straight open channel flume and the fish were generally oriented in streamwise direction while moving downstream, they approximated the spatial velocity gradients with

$$SVG_x = \partial U / \partial x. \quad (2.26)$$

They found that salmon smolts preferred spatial velocity gradients of $SVG_x = \partial U / \partial x \leq 1.0 \dots 1.2 \text{ s}^{-1}$ and showed an avoidance behaviour for higher SVG_x values. In contrast to the SVG , the SVG_x allows for the identification of areas with acceleration as well as deceleration.

Fish are known to perceive spatial pressure gradients (SPG) with their lateral line organs (Venturelli *et al.*, 2012; Ristroph *et al.*, 2015). The SPG is computed as the magnitude of the pressure gradients in each flow direction as

$$SPG = \sqrt{\left(\frac{\partial P}{\partial x}\right)^2 + \left(\frac{\partial P}{\partial y}\right)^2 + \left(\frac{\partial P}{\partial z}\right)^2}. \quad (2.27)$$

No threshold values for SPG triggering an avoidance reaction were found in the literature.

3 Experimental setup and methods

3.1 Overview

The objectives of the present study are achieved by conducting small and large scale physical model tests and a 3D numerical model study. In Section 3.2, the similitude, arising model and scale effects of the physical model tests are discussed. The accuracy and the error propagation of the measurements are explained in Section 3.3. The model setup, the instrumentation and the test programme are presented in Section 3.4 for the detailed hydraulic model investigation of curved-bar racks (CBRs) at 1:2 Froude-scale (Tasks A & E), and in Section 3.5 for the ethohydraulic experiments including the live-fish tests at 1:1 Froude-scale (Tasks B, C & D). Different methods for the ethohydraulic data analysis are described in Section 3.6. The setup for the numerical model investigation in OpenFOAM[®] is described in Section 3.7.

3.2 Similitude and scale effects

Prototype hydraulic structures can be represented by physical hydraulic models. A physical model is often scaled down and has to satisfy geometric, kinematic and dynamic similarities to avoid scale effects (Heller, 2011). Geometric similarity requires similar length dimensions between model and prototype and is therefore attained with a scale factor λ , which describes the ratio between a length in prototype (L_P) and a length in the model (L_M):

$$\lambda = \frac{L_P}{L_M}. \quad (3.1)$$

In addition to geometric similarity, kinematic similarity requires constant ratios for time-dependent processes such as velocity and acceleration. Ultimately, the ratios of all dynamic forces determining the hydraulic processes, namely gravity, viscosity, surface tension, pressure, elastic compression and inertia have to be identical in both model and prototype (Heller, 2011). One non-dimensional parameter expressing the ratio between these forces is the Froude number F , which relates inertia to gravity:

$$F = \sqrt{\frac{\text{Inertia}}{\text{Gravity}}} = \frac{v}{\sqrt{g \cdot L}}, \quad (3.2)$$

with g = gravitational acceleration [m/s^2], v = flow velocity [m/s] and L = characteristic length [m] typically defined as the flow depth h or the hydraulic radius R_h for open channel flow. The Froude number describes the wave impedance and distinguishes between subcritical ($F < 1$) and supercritical ($F > 1$) flow conditions. Another important measure accounting

for viscosity is the Reynolds law of similarity. The Reynolds number R relates inertia to viscosity:

$$R = \sqrt{\frac{\text{Inertia}}{\text{Viscosity}}} = \frac{v \cdot L}{\nu}, \quad (3.3)$$

with ν = kinematic viscosity of water = $1.01 \times 10^{-6} \text{ m}^2/\text{s}$ for $T = 20^\circ\text{C}$. The Reynolds number describes the movement of a water particle from laminar to turbulent. For pipe flow, the transition to turbulent flow starts at $R \approx 2000$. For open channel flow, where the hydraulic radius R_h defines the characteristic length L , the limit value for turbulent flow is converted to $R \approx 500$ (Jirka and Lang, 2009).

It is not possible to simultaneously fulfil all similarity laws in a physical scale model. Since a physical process is usually governed by only two main forces, the critical ratio is kept constant in the model, whereas the less relevant ratios are neglected. Open channel flow and flow through a rack are mainly governed by gravity and viscosity. The Froude's similarity law is applied for the experiments described in this thesis. The according scaling ratios are shown in Table 3.1.

Table 3.1 Scaling ratios according to Froude's law of similitude

Quantity	Ratio
Length [m]	λ
Area [m ²]	λ^2
Time [s]	$\lambda^{1/2}$
Velocity [m/s]	$\lambda^{1/2}$
Discharge [m ³ /s]	$\lambda^{5/2}$

The flow resistance induced by a rack includes friction, pressure and wave impedance. The latter depends on the Froude number and was investigated on cylindrical piers by Hsieh (1964). According to Hsieh's studies, the wave impedance depends on the ratio of flow depth to bar thickness h_o/t_b and reaches a maximum for $F = 0.5$. Since the flow depth in the model flume is much lower than in prototype, the effect of the wave impedance on the total flow resistance is relevant. Ideal fluids induce no flow resistance, which means that viscous forces must influence the flow resistance as well. If the bar Reynolds numbers R_b in the model are within the range of $0.5 \times 10^3 < R_b < 2 \times 10^5$, where the drag coefficient remains constant, the flow resistance in the model can be transferred to prototype values (Blevins, 1984). Preliminary head loss measurements were conducted to confirm this assumption. The ξ_R values versus R_b are shown in Figure 3.1 for $\alpha = 45^\circ$, $\beta = 90^\circ$, $\sigma = 0.17$ and $h_o/t_b = 20, 40, 60, 80$. The results reveal significant viscous and water depth effects for $h_o/t_b \leq 40$

in the range of studied R_b values, whereas R_b remains constant for $h_o/t_b > 40$ and $R_b > 1500$. To avoid significant scale effects, the hydraulic experiments in the present study were conducted with upstream flow depth to bar thickness ratios $h_o/t_b > 40$, bar Reynolds numbers $R_b = t_b U_o / \nu > 1500$ (Meusburger, 2002; Raynal *et al.*, 2013a; Albayrak *et al.*, 2018), and approach flow Reynolds number $R = 4R_h U_o / \nu > 10^4$ (Hughes, 2005) based on the hydraulic radius $R_h = (h_o w_o) / (2h_o + w_o)$ with U_o = approach flow velocity [m/s], h_o = approach flow depth [m], and w_o = channel width upstream of the rack [m].

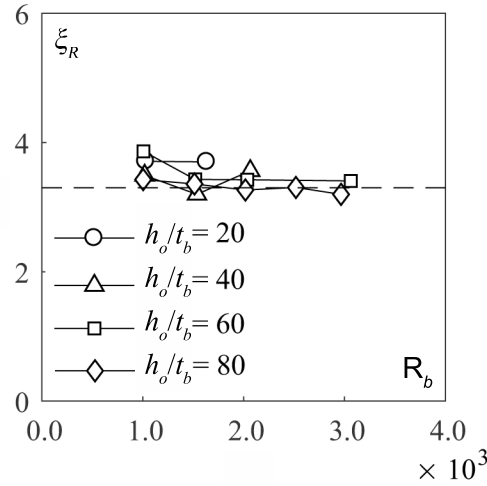


Figure 3.1 Head loss coefficients ξ_R versus bar Reynolds number R_b for $\alpha = 45^\circ$, $\beta = 90^\circ$, $\sigma = 0.17$, and $h_o/t_b = 20, 40, 60, 80$; the value of $\xi_R = 3.30$ corresponding to $h_o/t_b = 80$ and $R_b = 2500$ is marked with a dashed line

3.3 Measurement accuracy and error propagation

In order to evaluate the head losses and the flow conditions at various CBR configurations, the hydraulic parameters were quantified using the measuring equipment listed in Table 3.2.

Table 3.2 Parameters measured in the laboratory flumes and corresponding measuring instrumentation; the specified percentages for the accuracy of the single instruments refer to the measured value

Parameter	Instrument	Accuracy
Discharge	Magnetic-inductive flow meter (MID)	$\pm 0.5\%$
Water level	Ultrasonic distance sensor (UDS)	± 0.5 mm (100 Hz)
3D velocity field	Acoustic Doppler velocimetry probe (ADV)	$\pm 0.5\%$ (25/200 Hz)
Temperature	Thermometer	± 2 °C
Measurement location	Traverse system	± 1 mm
Flume geometry	Meter	± 2 mm

The test setup and the experimental procedure were optimized to minimise systematic errors. In addition to the above stated measurement errors, random errors occur due to indeterminate variations during the measurements or the data analysis. The confidence interval corresponds to the total error e_x , which is the sum of systematic and random errors. The expected value \bar{x} and the total error describe the measured quantity x_n :

$$x_n = \bar{x} \pm e_{xn}. \quad (3.4)$$

An error propagation was carried out to quantify the error of a target value e_X , which is defined by Taylor (1997) as:

$$e_X = \sqrt{\left(\frac{\partial X}{\partial x_1} e_{x1}\right)^2 + \left(\frac{\partial X}{\partial x_2} e_{x2}\right)^2 + \dots + \left(\frac{\partial X}{\partial x_n} e_{xn}\right)^2}, \quad (3.5)$$

with e_{xn} = total error of the measured parameter. In the present study, an error propagation analysis was applied and presented for the rack head loss coefficient ξ_R in Section 4.1.6.

3.4 Hydraulic model investigation of curved-bar racks

3.4.1 Model flume I - small flume

Head loss and flow field measurements (Task A) were conducted in a 0.6 m deep, 1 m wide and 12.0 m long flume with a horizontal bottom and a maximum discharge of $Q = 120 \text{ l/s}$. The flume width of 1.0 m was reduced to $w_o = w_{ds} = 0.5 \text{ m}$ using prefabricated PVC wall elements to study 1:2 Froude-scaled model racks, with w_o, w_{ds} = flume width up- and downstream of the CBR, respectively (Figure 3.2, Table 3.3). Due to the limited pump capacity, the flume width reduction was necessary to reach flow conditions comparable to prototype conditions and to avoid scale effects. The 7.0 m long test section where the measurements were conducted is equipped with a glass wall for lateral observation. The 1:2 Froude-scaled model CBRs were placed in the centre of the test section. The setup did not include a bypass. At the channel inlet, a stilling tank with an adjacent honeycomb flow straightener and a 45° sloped ramp ensured symmetrical inflow conditions. The inflow depth h_o was controlled with a flap gate at the end of the flume.

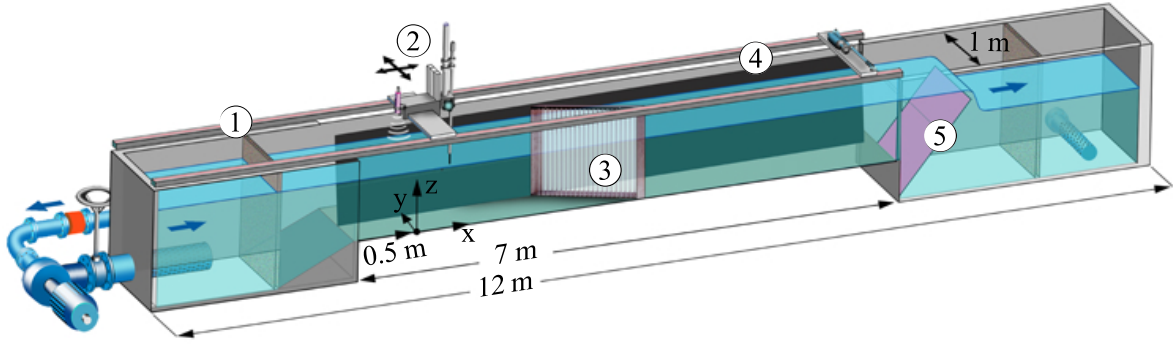


Figure 3.2 Schematic 3D view of the test flume including (1) inlet section with honeycomb flow straightener, (2) 2D traverse system with measurement instruments, (3) CBR, (4) PVC wall for channel separation, (5) flap gate

3.4.2 Instrumentation

The discharge was measured with a magnetic inductive discharge-meter (MID). A 2D traverse system was mounted on top of the model flume over the entire length of the test section (Figure 3.2). The traverse system allowed for the measuring devices to reach every point in the streamwise and spanwise directions. An ultrasonic distance sensor (UDS) and a down-looking acoustic Doppler velocimetry probe (ADV; Sontek) were mounted on the traverse system. The coordinates in the streamwise, spanwise and vertical directions are x , y and z , respectively. The origin of the coordinate system was 0.5 m downstream of the test section inlet as indicated in Figure 3.2.

The streamwise u , spanwise v , and vertical w instantaneous velocities were measured using the ADV at 25 Hz for a sampling period of 30-120 s, which is adequate for the statistical analysis of mean and turbulence flow parameters (Silva *et al.*, 2012b). Post-processing was carried out with WinADV, data points with less than 70 % correlation were excluded and all data were de-spiked with the Goring & Nikora filter as modified in Wahl (2003) (Lane *et al.*, 1998; Goring and Nikora, 2002). The time-averaged velocity components in streamwise, spanwise and vertical directions are denoted by U , V and W , respectively, with the resulting velocity $U_r = (U^2 + V^2 + W^2)^{0.5}$. Due to geometrical restrictions of the ADV probe, measurements were taken at least 0.05 m away from each flume wall and 0.06 m below the water surface.

3.4.3 Parameter range and test programme

The main parameters representing the geometric characteristics of a CBR are the rack angle α , the bar angle to the approach flow (bar attack angle) β , and the clear bar spacing s_b , while the secondary parameters are: bar depth d_b , bar shape K , and bottom and top overlay heights h_{Bo} and h_{To} , respectively. The height of the top & bottom overlay combination is denoted

$h_v = h_{Bo} + h_{To}$. To systematically investigate a wide range of parameter combinations, two types of curved bars were furnished from 45° and 90° circle segments of an acrylic pipe. Both bar types have an outflow angle $\delta = 0^\circ$ parallel to the downstream channel walls. These bar shapes correspond to the streamlined version of the straight bars with rounded ends of MBRs with $\beta = 45^\circ$ and louvers with $\beta = 90^\circ$ (Albayrak *et al.*, 2018). The curved bars have a thickness $t_b = 0.01$ m, a standard bar depth $D_b = 0.1$ m (prototype dimensions) and are rounded at both ends with a radius $r = t_b/2$. The bar depth effect was investigated by testing 30% shorter and 25% longer bars with the corresponding relative bar depths of $\varepsilon = d_b/D_b = 0.7$ and 1.25 , respectively. The inconsistency of bar depth variation is the result of limited availability of acrylic pipe diameters. The variation of bar attack angle β and bar depth d_b resulted in six different bar shapes (Figure 3.3).

The investigated CBR configurations were horizontally angled to the flow with $\alpha = 15^\circ$, 30° , and 45° (Figure 3.4a). For each CBR configuration, 10 mm and 20 mm thick PVC plates as bottom and top bar holding plates, respectively, were milled with the curvature of the six different bar shapes. The PVC plates were held together with 6 mm thick aluminium plates screwed on the sides forming a frame. The bars were slid into the carvings of the PVC plates (Figure 3.4c). This construction thus allowed for an easy adjustment of different bar spacings. Furthermore, aluminium plates of variable height were placed in front of the CBR to model bottom, top and bottom, or top overlays (Figure 3.4b).

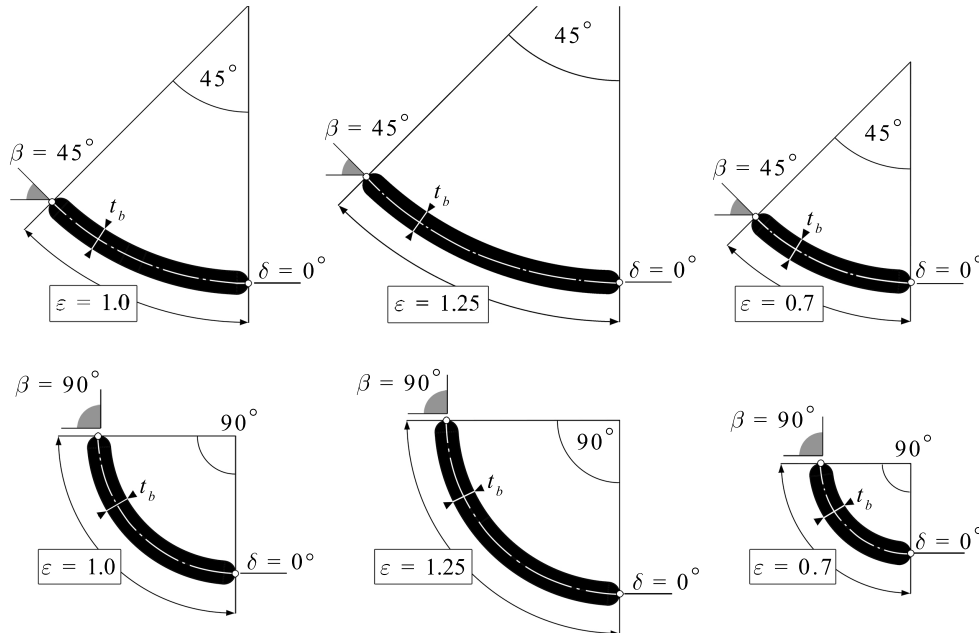


Figure 3.3 Plan view of geometric parameter definition of curved bars with bar attack angle β , bar outflow angle δ , relative bar depth ε and bar thickness t_b

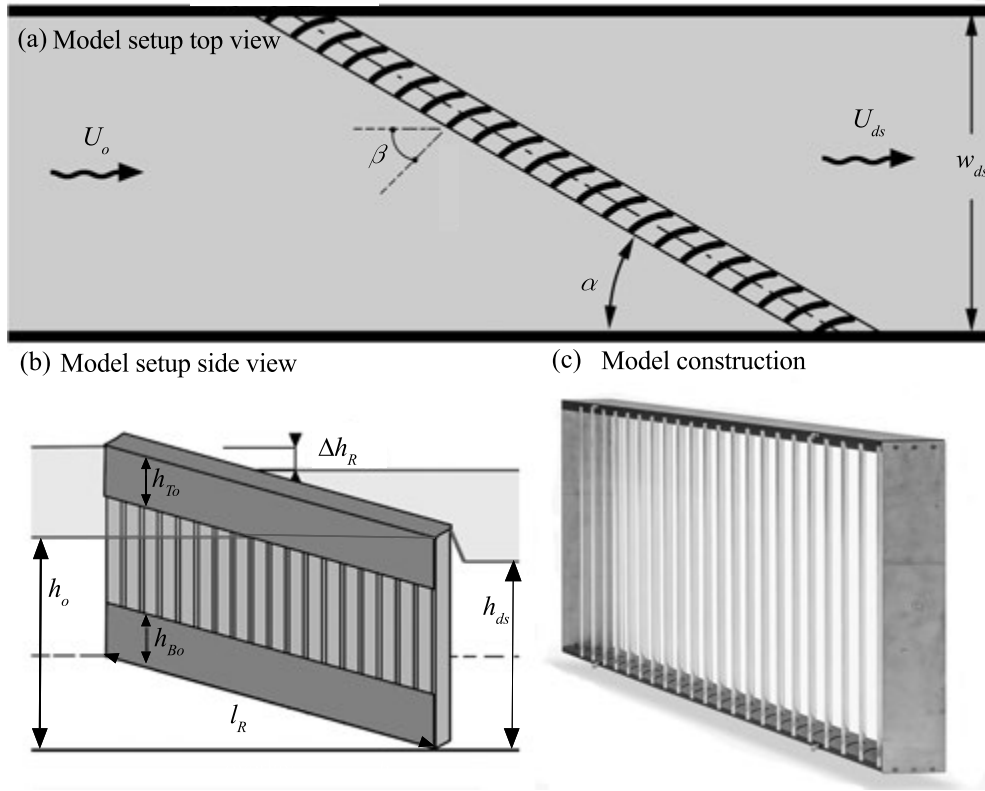


Figure 3.4 Geometric and hydraulic rack parameters (a) flume top view, (b) side view of the CBR with overlays and (c) CBR model construction with rack angle α , bar attack angle β , overlay height $h_v = h_{To} + h_{Bo}$, inflow velocity U_o , downstream flow velocity U_{ds} , downstream channel width w_{ds} , up- and downstream flow depth h_o and h_{ds} , rack length l_R , and rack head loss Δh_R

3.4.4 Head loss measurements

The hydraulic head losses were determined for the entire range of primary and secondary CBR parameters. The experimental matrix is shown in Table 3.3 for both model and prototype dimensions. The bar depth effect was only tested for $\alpha = 30^\circ$ and 45° with $d_b = 0.07$ m, 0.1 m and 0.125 m (prototype dimensions). The bars were fully submerged for all experiments. The effect of overlays was investigated for all rack configurations. Relative overlay heights of $V_1 = h_{To}/h_o$, $V_3 = h_{Bo}/h_o = 10, 15, 25\%$ were tested for top and bottom overlays separately. For the combination of top & bottom overlays, $V_2 = h_v/h_o = 20$ and 30% were considered corresponding to 10% and 15% for each top and bottom overlay, respectively. The non-dimensional bar spacing is defined as $\sigma = t_b/(t_b + s_b)$ and describes the blocking ratio by the vertical bars. Zero bar spacing results in $\sigma = 1$, which represents full blockage.

To account for the effect of different HPP layouts on the head losses, i.e. diversion and block-type HPPs, the upstream flume width w_o was increased to 0.75 m and 1.0 m (Table 3.3). The downstream flume width w_{ds} representing the turbine channel was 0.5 m for all

experiments. Figure 3.5a illustrates the standard flume setup representing a diversion-type HPP. For the block-type HPP, the CBRs were placed with the d/s rack end adjacent to a flap gate representing the weir (Figure 3.5b). A flap and underflow gate at $x/h_o = 0$ allowed for separate or simultaneous weir overflow or underflow.

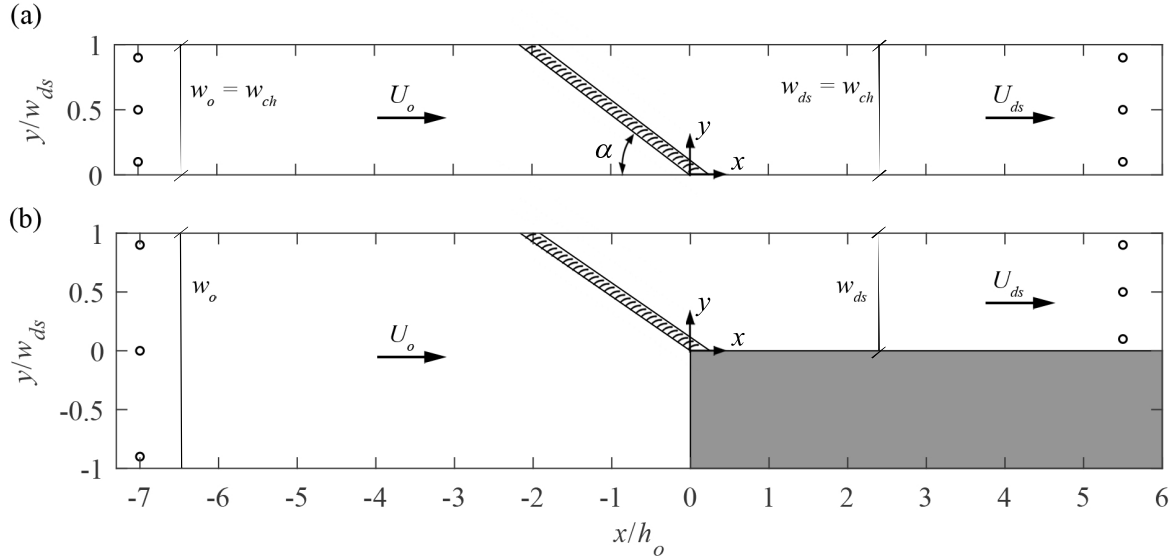


Figure 3.5 Flume coordinate system for (a) diversion and (b) block-type HPP setup, the location of UDS water depth measurements are marked with circles

Table 3.3 Hydraulic and rack parameters for the 1:2 scale model experiments and the corresponding prototype scale values

Parameter	Model scale 1:2	Prototype scale 1:1	Unit
U_o	0.50	0.71	[m/s]
h_o	0.40	0.80	[m]
w_o	0.50, 0.75, 1.0	1.0, 1.5, 2.0	[m]
w_{ds}	0.5	1.0	[m]
$R_b (\times 10^3)$	2.50	7.06	[-]
$R (\times 10^5)$	3.07	8.69	[-]
F	0.25	0.25	[-]
α	15, 30, 45	15, 30, 45	[°]
β	45, 90	45, 90	[°]
s_b	0.025, 0.055, 0.115	0.05, 0.11, 0.23	[m]
t_b	0.005	0.01	[m]
σ	0.04, 0.08, 0.17	0.04, 0.08, 0.17	[-]
d_b	0.035, 0.05, 0.0625	0.07, 0.1, 0.125	[m]
h_{To} or h_{Bo}	$(0.10, 0.15, 0.25) \cdot h_o$	$(0.10, 0.15, 0.25) \cdot h_o$	[m]
h_v	$(0.20, 0.30) \cdot h_o$	$(0.20, 0.30) \cdot h_o$	[m]

3.4.5 Computation of energy losses

For the hydraulic head loss assessment, the average up- and downstream flow depths h_o and h_{ds} , respectively, were determined from three individual measurements 0.05 m away from each flume wall and in the flume centre axis in the spanwise direction at $x/h_o = -7$ and $x/h_o = 5.5$ (cf. Figure 3.5). The rack (subscript R) head losses Δh_R in the horizontal flume were determined by applying Bernoulli's equation:

$$\Delta h_R = \left(h_o + \frac{U_o^2}{2g} \right) - \left(h_{ds} + \frac{U_{ds}^2}{2g} \right) - \Delta h_f, \quad (3.6)$$

with Δh_f = head loss due to flume friction measured without a rack $\cong 0.0018$ m. The mean cross-sectional flow velocities U_o and U_{ds} are derived from the continuity equations:

$$U_o = \frac{Q_o}{h_o \cdot w_o} \quad \text{and} \quad U_{ds} = \frac{Q_t}{h_{ds} \cdot w_{ds}}, \quad (3.7)$$

with Q_t = turbine discharge downstream of the rack [m^3/s]. Since the head loss prediction equations presented hereafter are related to the theoretical flow velocity in the downstream channel without rack presence U_{th} , they can be applied for various HPP layouts:

$$U_{th} = \frac{Q_t}{h_o \cdot w_{ds}}. \quad (3.8)$$

For small head losses, $h_o \cong h_{ds}$ and thus $U_{th} \cong U_{ds}$, independent of the HPP layout. At diversion-type HPP layouts in a straight channel with $w_{ds} = w_o$ and without a bypass, $U_{th} = U_o$ (Figure 3.5a). By using U_{th} instead of U_o or U_{ds} , the assessment is independent of potential weir and bypass discharge, e.g. in the case of a block-type HPP (Figure 3.5b), but still accounts for Δh_R . The dimensionless rack head loss coefficient ξ_R is then calculated as:

$$\xi_R = \Delta h_R \cdot \frac{2g}{U_{th}^2}. \quad (3.9)$$

3.4.6 Flow velocity measurements

A top view of the velocity measurement grids for the diversion-type and the block-type HPP layouts is shown in Figure 3.6. The velocity measurements were conducted for the CBR configurations with $\alpha = 15^\circ, 30^\circ$ and 45° , $\beta = 45^\circ$ and 90° and $s_b = 0.025$ m ($s_b = 0.05$ m in prototype, $\sigma = 0.17$) for the diversion-type HPP layout (Table 3.4, Series A). The effect of overlays on the flow field was investigated for one CBR configuration with $\alpha = 30^\circ$, $\beta = 45^\circ$ and $\sigma = 0.17$. Relative overlay heights of h_{To}/h_o or $h_{Bo}/h_o = 10, 15, 25\%$ were tested

for top and bottom overlays separately. For the combination of top and bottom overlays, $h_v/h_o = 20\%$ and 30% were considered corresponding to 10% and 15% for each top and bottom overlay, respectively (Table 3.4, Series B). The flow field around a CBR at a block-type HPP layout was investigated for $\alpha = 15^\circ, 30^\circ$ and 45° , $\beta = 45^\circ$ and $\sigma = 0.17$. The effect of overlays at this HPP layout was only investigated for h_{To}/h_o and $h_{Bo}/h_o = 15\%$ (Table 3.4, Series C). The inflow discharge $Q_o = 100 \text{ l/s}$ and the inflow depth $h_o = 0.4 \text{ m}$ were constant resulting in $U_{th} = 0.5 \text{ m/s}$ for all tests, while the mean inflow velocity was $U_{th} = U_o = 0.5 \text{ m/s}$ and 0.25 m/s for test series A/B and test series C, respectively (cf. Table 3.4).

The flow field of the six basic CBR configurations without overlays was measured in three horizontal planes at $z/h_o = 0.25, 0.50, 0.75$ (Table 3.4). The streamwise distance between measuring points was 0.1 m in the vicinity of the rack and 0.5 m further up- and downstream of the rack, while the spanwise distances were 0.1 m and 0.2 m , respectively. To assess the effect of overlays on the flow field, velocity measurements were conducted in the horizontal plane close to the bottom at $z/h_o = 0.075$ for the bottom overlay and close to the water surface at $z/h_o = 0.85$ for the top overlay (Series B, Table 3.4).

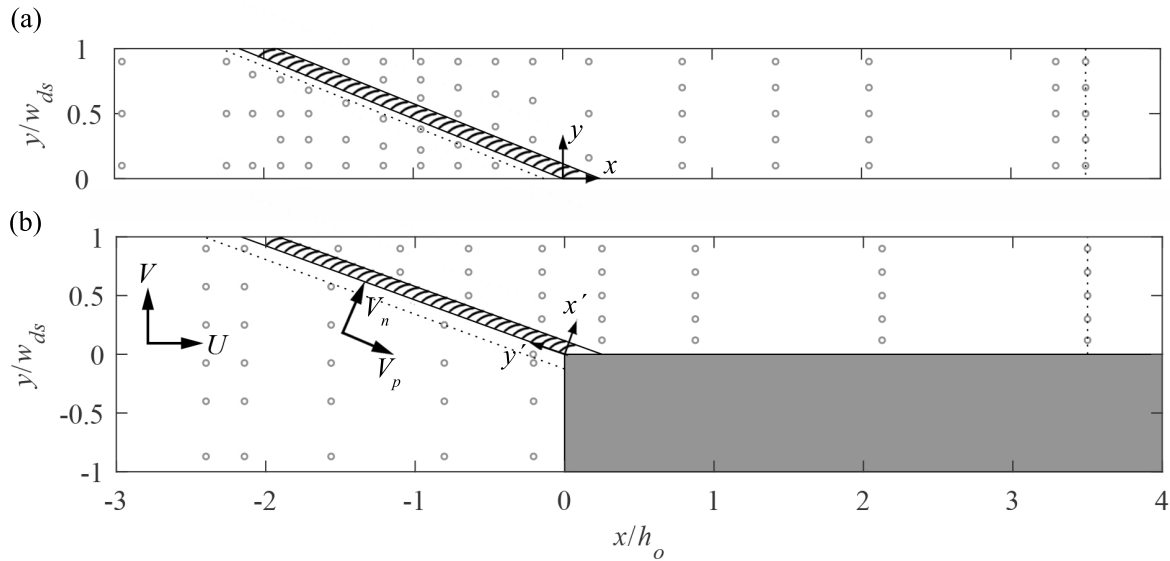


Figure 3.6 Measuring grid in the vicinity of the CBR for the ADV measurements in the 1:2 Froude-scaled experiments for (a) the diversion-type HPP and (b) the block-type HPP, the dotted lines mark the rack-parallel cross sections for the detailed ADV measurements 50 mm upstream of the CBR

The flow field at a block-type HPP layout was measured at $z/h_o = 0.5$ (Series C). For this HPP layout, additional ADV measurements were conducted without a CBR (test C0), with a pier separating the weir from the downstream channel (test C7), and with a weir discharge of

3.4.7 Operational aspects: Clogging of driftwood and organic fine material

The clogging probability (CP) of organic fine material and driftwood was investigated with 1:2 Froude scaled physical model tests in the small flume (Chapter 8). The leaves of two different tree species common in Switzerland, i.e. common beech (*fagus sylvatica*) and common hazel (*corylus avellana*) were used to determine the effects of the rack angle $\alpha = 15^\circ, 30^\circ, 45^\circ$ and the mean approach flow velocity $U_o = 0.5 \text{ m/s}, 0.75 \text{ m/s}$ on the CP at CBRs (Figure 3.7a, Table 3.5). The two tested leaf types represent two different leaf sizes. The ratio of the leaf length to clear bar spacing L_L/s_b is 2.3 for the hazel leaves and 1.5 for the beech leaves.

Table 3.5 Test parameters for the experiments assessing the clogging probability of leaves at CBRs with different rack angles

Parameter	Model scale 1:2	Prototype scale 1:1	Unit
U_o	0.50, 0.75	0.71, 1.06	[m/s]
h_o	0.40	0.80	[m]
w_{ds}/w_o	1.0	1.0	[–]
α	15, 30, 45	15, 30, 45	[°]
β	45	45	[°]
s_b	0.025	0.05	[m]
leaf type	beech, hazel	beech, hazel	[–]
leaf length L_L	0.0375, 0.058	0.075, 0.116	[m]
leaf width w_L	0.024, 0.055	0.048, 0.110	[m]
L_L/s_b	1.5, 2.3	1.5, 2.3	[–]

To assess the CP of driftwood, two different log diameters $d_L = 5 \text{ mm}, 20 \text{ mm}$, and three different log lengths $L_L = 20 \text{ mm}, 50 \text{ mm}, 100 \text{ mm}$ were tested at different U_o and HPP layouts for the CBR configurations A3 and C3 (cf. Table 3.4, Table 3.6). Two different log diameters $d_L = 10 \text{ mm}$ and 40 mm (prototype dimensions), corresponding to $d_L/s_b = 0.2$ and 0.8 , respectively, were used. Additional tests were conducted with branched logs (Figure 3.7b). The log density varied between $841 - 966 \text{ kg/m}^3$.

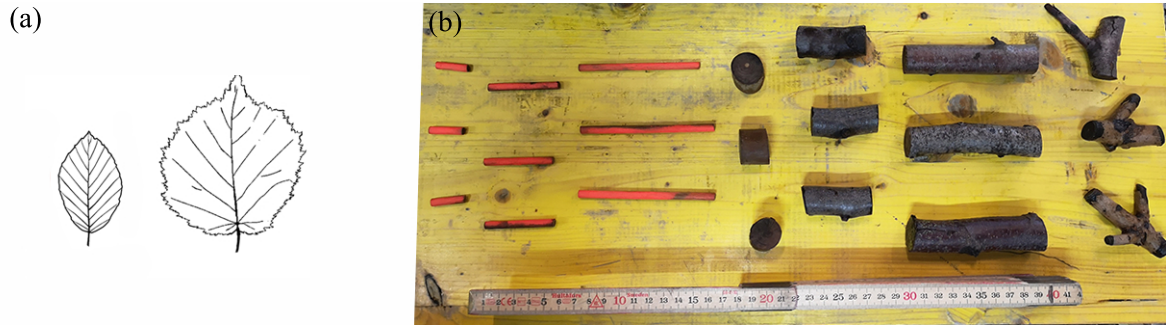


Figure 3.7 (a) Leaves of common beech (*fagus sylvatica*) and common hazel (*corylus avellana*) used for the modelling of organic fine material and (b) model driftwood; adapted from Ganzmann (2019) and Bühler (2019)

For each test, a minimum of 60 leaves or 40 logs were added individually to the approach flow ~ 1.5 m upstream of the CBR at $z \approx 0.5 \cdot h_o$. To model congested driftwood transport, a mix of all log types was added simultaneously. Finally, the application of a top overlay ($h_{To} = 0.15 \cdot h_o$) and simultaneous weir discharge of $Q_w = 0.07 \cdot Q_o$ was tested as a mitigation measure to reduce the CP of driftwood.

Table 3.6 Test programme to assess the clogging probability of driftwood at the CBR

Parameter	Model scale 1:2	Prototype scale 1:1	Unit
U_o	0.25 - 0.67	0.35 - 0.95	[m/s]
h_o	0.23 - 0.40	0.46 - 0.80	[m]
w_{ds}/w_o	0.5, 1.0	0.5, 1.0	[-]
α	30	30	[°]
β	45	45	[°]
s_b	0.025	0.05	[m]
$s_{b,eff}$	0.0155	0.031	[m]
log length L_L	0.02, 0.05, 0.10	0.04, 0.10, 0.20	[m]
log diameter d_L	0.005, 0.020	0.010, 0.040	[m]
d_L/s_b	0.2, 0.8	0.2, 0.8	[-]
$d_L/s_{b,eff}$	0.32, 1.29	0.32, 1.29	[-]
L_L/s_b	0.8, 2.0, 4.0	0.8, 2.0, 4.0	[-]
$L_L/s_{b,eff}$	1.29, 3.23, 6.45	1.29, 3.23, 6.45	[-]

3.5 Ethohydraulic experiments

3.5.1 Model flume II - Ethohydraulic flume

The ethohydraulic experiments (Tasks B, C, D) were conducted in a 30 m long, 1.50 m wide, and 1.20 m deep open channel flume with a horizontal bed (Figure 3.8a). The flume walls and bed are covered with a mortar coating of 2 mm grain size. In the test section upstream of the rack and in the vicinity of the bypass entrance, the side wall of the flume is equipped with glass for lateral observation (Figure 3.8d). The flume is equipped with a closed water circuit connected to a cooling system. At the flume inlet, a diffuser and honeycomb-shaped flow straighteners ensured symmetrical inflow conditions and surface waves were suppressed with hard foam floats (Figure 3.8b). The 1:1 scaled section model of the CBR configuration with $\alpha = 30^\circ$, $\beta = 45^\circ$, $\sigma = 0.17$, $\varepsilon = 1.0$ (A3 in Table 3.4) was placed in the flume centre with an adjacent bypass. A 15 mm thick PVC plate with sloped up- and downstream edges was milled with the curved bar shapes and fixed to the flume bottom with $\alpha = 30^\circ$ to hold the bars in place. The bars were extruded from aluminium, slid into the carvings and fixed at the top. The rack covered the downstream flume width of $w_{ds} = 1.15$ m with a resulting rack length of $l_R = 2.3$ m. The bypass channel was separated from the downstream channel by a 0.1 m thick brick wall, resulting in a bypass width $w_{by} = 0.25$ m. A hard foam wedge was placed between the d/s rack end and the brick wall to ensure a gradual transition from the rack into the bypass (Figure 3.8d). The discharge in the downstream and in the bypass channel was controlled separately with a flap gate at the end of each channel (Figure 3.8c).

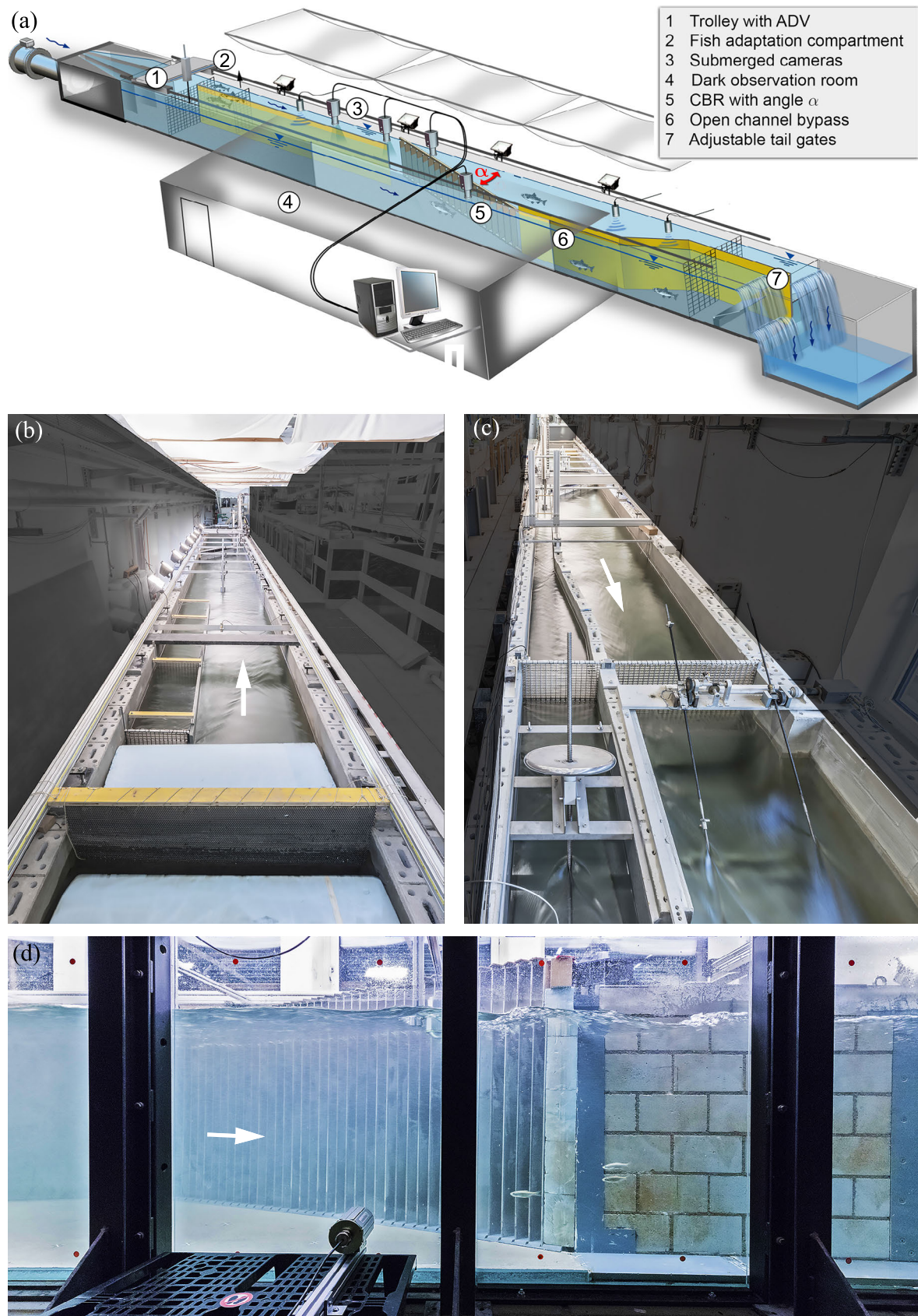


Figure 3.8 (a) Schematic 3D view of the model flume for the 1:1 ethohydraulic experiments, and photos of the ethohydraulic with (b) view in flow direction of the inflow and the starting compartment, (c) view against flow direction of the bypass and the downstream channel gates, and (d) three spiralin are guided into the 25 cm wide open channel bypass

Different bypass layouts were constructed modularly so that they could be easily exchanged and adjusted. Four bypass layouts were investigated with the following geometries: (a) a 0.25 m wide full depth open channel bypass (Figure 3.9a), (b) a 0.25 m wide full depth open channel bypass with a 2 m long, integrated flap gate 0.50 m downstream of the bypass inlet; the flap gate could be raised by up to 30° (Figure 3.9b), (c) a 0.25 m wide full depth open channel bypass with an elliptical restrictor at the bypass inlet, which created overflow and a 0.35 m long underflow transition (Figure 3.9c) and (d) a pipe bypass with a 0.50 m long transition section from a rectangular inlet of 0.25×0.25 m to a 2 m long, circular pipe of 0.20 m diameter (Figure 3.9d).

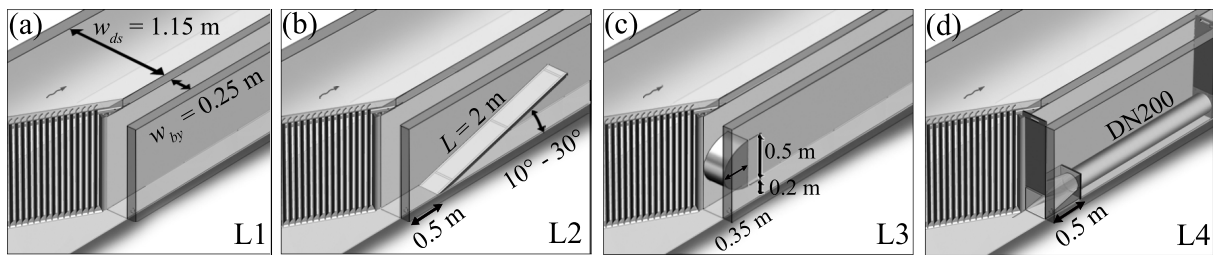


Figure 3.9 Schematic illustration of different bypass layouts

The bypass flow depth h_{by} and discharge Q_{by} was regulated by a flap gate at the end of the bypass channel to obtain the required bypass inlet velocity $U_{by,in}$ for each test setup (Table 3.7, Figure 3.8c).

Electrification of the curved-bar rack

The CBR configuration A3 was electrified with the NEPTUN system (Parasiewicz *et al.*, 2016) and tested with spiralin and European eel (Table 3.7). The electrified CBR is called e-CBR, hereafter. The goal of these ethohydraulic tests was to improve the fish protection and guidance efficiency of the CBR for eel, since low protection was obtained without electrification (cf. Section 6.2.4). The CBR without electrification showed good results for spiralin. Therefore, tests with spiralin were conducted to investigate if fish protection and guidance remain high for these fish with the e-CBR. Furthermore, tests with two different bar spacings ($s_b = 50$ mm, 110 mm) were conducted to investigate whether the electrification would allow for a larger bar spacing, while offering a high fish protection and guidance.

Each aluminium bar was alternately connected to a DC power supply (Procom Systems S.A., Poland) acting as anode or cathode (Figure 3.10a/b), and electrified with a low-voltage pulsed direct current with gated bursts (gpDC, Figure 3.10c). The electric field was built up between the bars, which were isolated by PVC plates on the bottom and the top. The parameters of the supplied pulse groups, i.e. the number of pulses N_{pulse} , the pulse length

L_{pulse} [ms], the gap length L_{gap} [ms] and the repetition time t_{rep} [ms], were adjusted with the software *NeptunTool* running on a laptop connected to the DC power supply (Figure 3.10c). The different gpDC waveforms resulting from the selected pulse parameters are described with the duty cycle, which expresses the percentage of time that any current is flowing (Table 3.8). Four different voltage supplies, i.e. 38 V, 50 V, 65 V or 80 V, could be selected. The electrification could be manually turned on or off in the software and the power supply was secured with an automatic protection against overloading.

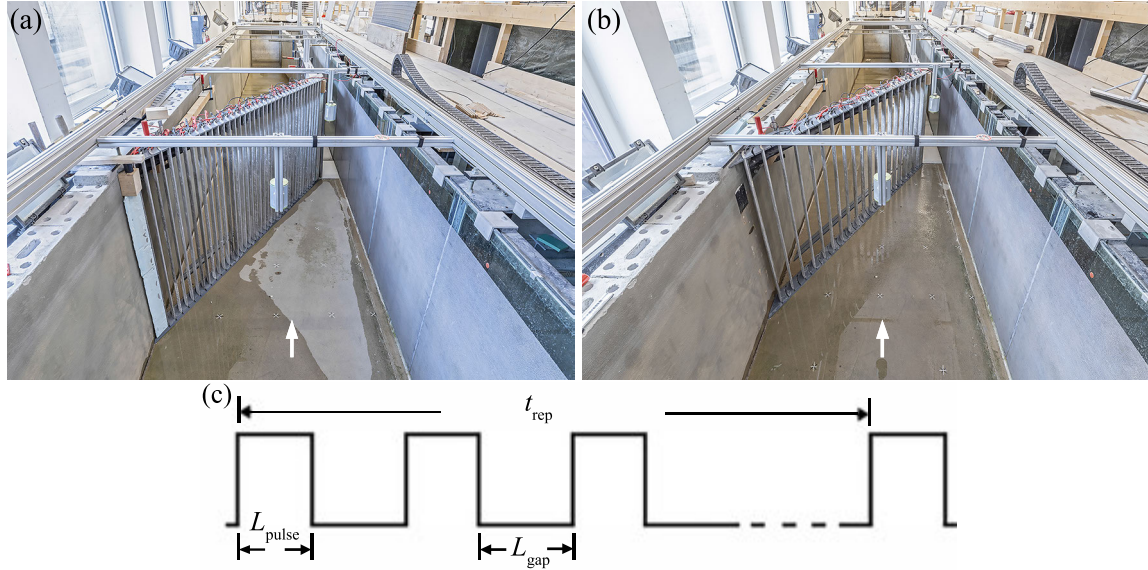


Figure 3.10 Photos of the electrified CBR with $\alpha = 30^\circ$, $\beta = 45^\circ$, $\varepsilon = 1.0$, (a) $s_b = 50$ mm and (b) $s_b = 110$ mm (Tests F1-F8, Table 3.8), and (c) illustration of the pulse parameters

3.5.2 Instrumentation

The inflow discharge was measured with a MID and regulated with a frequency converter to a maximum discharge of 1,200 l/s. The inflow depth h_o and the bypass flow depth h_{by} were measured with an Ultrasonic Distance Sensor (UDS, 'UNAM 30'). The inflow depth was kept constant at $h_o = 0.9$ m for all ethohydraulic tests. A 3D traverse system was mounted on top of the model flume over the entire length of the test section. The system allowed for the measuring devices to reach every point in the streamwise and spanwise direction. The ADV probe could further reach every point in vertical direction down to 20 mm away from the flume bed.

3.5.3 Experimental procedure and test programme

Velocity measurements

The streamwise u , spanwise v , and vertical w instantaneous velocities were measured with a down-looking ADV probe at 200 Hz for a sampling period of 30 s in the flume area upstream

of the rack and inside the bypass channel. The varying parameters were the inflow velocity U_o and the ratio of the mean flow velocity at the bypass entrance to the approach flow velocity $VR = U_{by,in}/U_o$ (Tests E4-E13 and E18-E23 in Table 3.7). The mean bypass entrance velocity $U_{by,in}$ was measured directly at the bypass entrance ($x/h_o = 0$, cf. Figure 3.12). The velocity profile in front of the bypass entrance was investigated for all four bypass layouts illustrated in Figure 3.9. Post-processing was carried out with WinADV, data points with less than 70% correlation were excluded and all data were de-spiked with the Goring & Nikora filter corrected after Wahl (2003) (Lane *et al.*, 1998; Goring and Nikora, 2002).

Live-fish tests

Three phases of live-fish tests were conducted according to the species-specific timing of main downstream movements (cf. Figure 2.1). The tests with spirlin (*Alburnoides bipunctatus*), common barbel (*Barbus barbus*), the nase (*Chondrostoma nasus*) and European eel (*Anguilla anguilla*) without electrification were conducted in autumn 2018, Atlantic salmon parr (*Salmo salar*) and brown trout (*Salmo trutta*) were tested in spring 2019 (Table 3.7). The live-fish tests with the e-CBR with spirlin and European eel were carried out in autumn 2019. Wild fish were caught by electrofishing (DC 7.5 kW, Grassl eL 64_II) in different Swiss rivers (Himmelbach, Suhre, Thur, Thur inland canal, Möhlinbach, Altbach, Mülitalbach or Murg tributary) and held in the fish holding tanks in the laboratory for a maximum of 7 days without feeding. After the tests, the fish were brought back to the same river reach. Transportation and handling processes were minimised to reduce stress. Tight confinements and rapid temperature changes were avoided and all tanks were equipped with a continuous oxygen supply. The laboratory holding tanks were connected to the closed water circuit of the flume and the cooling system with a constant water circulation. The water temperature in the river reach, where the fish were caught, was measured and adapted accordingly in the laboratory water circuit to 12-16°C. The water quality (e.g. temperature, pH, oxygen concentration and turbidity) in the holding tanks and the flume were recorded daily.

For each test run, three fish were transferred from the holding tanks to buckets with a dip net. They were photographed to measure their length and then placed in a 1 m long, 0.5 m wide starting compartment near the inlet at the flume wall opposite of the bypass (Figure 3.12) to acclimate to the flow conditions for 15 minutes in accordance with Albayrak *et al.* (2020a). The starting compartment was separated from the flume by two metal fences with meshes at the up- and the downstream ends. After the adaptation phase, the downstream fence was raised and the fish were free to swim downstream and interact with the CBR and the bypass. Five high-resolution cameras slightly submerged from top simultaneously recorded the 3D fish movements at 50 Hz (Figure 3.8a). Manual time measurements and observations were

additionally recorded with a standardized protocol for each test. The duration of each test was 30 minutes after the starting compartment was opened. The fish were immediately recaptured from the flume with a dip net after each test. They were transferred back into the holding tanks and not used for another test on the same day. To reduce the number of fish used for experimental purposes, each fish was used up to 3 times but with different configurations and on different days.

During the live-fish tests, six 1000 W lamps were positioned behind the flume and oriented towards a white linen sheet hanging over the flume for uniform illumination with a diffused light source (Figure 3.8a,b). These bright lighting conditions were chosen to motivate fish to move downstream and prevent them from hiding in darker corners. Furthermore, they enhanced the contrast for the fish tracking. Fish species like the European eel prefer darker conditions, however, which might affect their behaviour. The transferability of the results to prototype is therefore discussed accordingly (Section 6.8). Since the reflection of the fish in the glass was assumed to attract the fish to that flume side, the glass was covered with a perforated foil of identical colour as the opposite concrete flume wall. The ideal test condition for behavioural analysis requires equal numbers of test repetitions for all configurations. However, it was not possible to catch enough fish of the same size range for all tests. Furthermore, only resident yellow eel and salmon parr could be caught. Although resident fish do not move far in the river, they were actively swimming downstream in the laboratory flume. The fish minimum, maximum and mean total lengths TL_{\min} , TL_{\max} and TL_{mean} , respectively, are listed in Table 3.7 for all live-fish tests conducted in this study. The table further lists the total number of fish used in the experiments N and the number of fish leaving the starting compartment and actively swimming downstream n . The fish that did not leave the starting compartment were excluded from further analysis.

Two mean approach flow velocities $U_o = 0.5$ m/s and 0.7 m/s and two velocity increase ratios $VR = U_{by,in}/U_o = 1.2$ and 1.4 at a full depth open channel bypass were tested with most fish species (E4-13, E18-E23 in Table 3.7). These ratios were chosen based on the findings and recommendations in the literature (Haefner and Bowen, 2002; USBR, 2006; Ebel, 2016). For these main tests, detailed velocity measurements and numerical simulations were conducted (Section 6.1). The nase, the European eel and the Atlantic salmon parr could not be tested with all main flow conditions because of the limited catch rate. The effect of the rack compared to the no-rack configuration on the fish guidance efficiency (FGE) was investigated with spiralin in Test E1. The effect of a lower approach flow velocity of $U_o = 0.3$ m/s was tested with brown trout in Test E2. A lower velocity ratio of $VR = 1.1$ was tested for nase in Test E3. Different bypass layouts were tested with spiralin in Tests E14-E17. The e-CBR was

tested with spirlin and European eel for one hydraulic condition ($U_o = 0.5$ m/s, $VR = 1.2$), only varying the parameters of the supplied electric pulse pattern (Table 3.8, Tests F1-F8). The configurations were chosen based on the recommendations by Parasiewicz *et al.* (2016) and Brinkmeier *et al.* (2017). The lowest possible voltage of 38 V was used for all tests. The conductivity of the water was 230 μ S/cm.

Table 3.7 Test programme for the live-fish tests conducted in autumn 2018 (barbel, spirlin, nase, European eel) and spring 2019 (Atlantic salmon parr, brown trout)

Test	rack	U_o [m/s]	$U_{by,in}$ [m/s]	VR [–]	bypass layout	fish species	$TL_{min} - TL_{max}$ (TL_{mean}) [cm]	N [–]	n [–]
E1	no rack	0.50	0.60	1.2	OC	spirlin	8.5 - 11.9 (9.9)	21	21
E2		0.30	0.36	1.2	OC	trout	12.1 - 19.9 (16.2)	18	16
E3		0.50	0.55	1.1	OC	nase	6.5 - 8.4 (7.1)	9	9
E4						spirlin	8.6 - 12.5 (10.0)	36	32
E5						barbel	9.7 - 22.0 (14.3)	27	22
E6		0.50	0.60	1.2	OC	trout	9.5 - 20.4 (13.7)	42	25
E7						salmon	7.9 - 15.0 (11.0)	30	30
E8						nase	6.0 - 8.9 (7.3)	24	24
E9						eel	50.4 - 80.9 (67.1)	16	14
E10						spirlin	8.6 - 10.8 (9.8)	30	29
E11		0.50	0.70	1.4	OC	barbel	9.9 - 20.7 (15.3)	24	23
E12	CBR					trout	10.6 - 20.2 (14.8)	36	24
E13						salmon	9.0 - 13.3 (11.1)	30	30
E14			0.60 (1.4 ¹)	1.2	flap gate		9.5 - 12.9 (10.6)	9	9
E15		0.50	0.70 (1.5 ¹)	1.4		spirlin	8.6 - 10.6 (9.3)	15	12
E16			0.50 (0.75 ²)	1.0	restrictor		8.3 - 10.1 (9.3)	12	10
E17			0.60 (0.90 ²)	1.2			8.1 - 11.6 (9.6)	12	9
E18						spirlin	8.4 - 11.8 (10.0)	33	33
E19		0.70	0.85	1.2	OC	barbel	10.3 - 21.5 (15.9)	24	16
E20						trout	10.2 - 20.1 (13.7)	54	29
E21						spirlin	8.4 - 11.9 (10.0)	30	27
E22		0.70	1.00	1.4	OC	barbel	11.2 - 20.6 (14.7)	27	23
E23						trout	9.9 - 19.7 (14.4)	39	23

Note: OC = full-depth open channel bypass

VR = ratio of bypass inlet to mean approach flow velocity $U_{by,in}/U_o$

¹ = bypass flow velocity at the flap gate overflow

² = bypass flow velocity at the restrictor downstream end

Table 3.8 Test programme for the ethohydraulic tests with the e-CBR conducted in autumn 2019, tests marked with an asterisk had to be aborted due to injured fish

Test	s_b [mm]	U [V]	L_{pulse} [ms]	L_{gap} [ms]	N_{pulse} [–]	t_{rep} [ms]	duty cycle	fish species	$TL_{\text{min}}-TL_{\text{max}}$ (TL_{mean}) [cm]	N [–]	n [–]
F1	50	38	0.2	0	1	100	0.20%	spiralin	7.8-11.6 (9.2)	24	19
F2								eel	52.3-80.9 (71.6)	21	16
F3			0.3	7	5	200	0.75%	spiralin	9.5-12.1 (10.7)	18	18
F4								eel	57.3-85.2 (74.8)	15	13
F5*	110	38	0.4	10	7	300	0.93%	eel	56.7-84.0 (73.4)	12	11
F6			0.2	11	2	200	0.20%	spiralin	9.2-12.7 (10.8)	12	12
F7*			0.3	7	5	200	0.75%	spiralin	9.5-10.9 (10.1)	9	9
F8*								eel	57.1-83.4 (70.6)	18	15

3.5.4 Videometry system and fish-tracking software

For a detailed analysis of the fish behaviour, a sophisticated videometry system was installed in the ethohydraulic flume to record all fish movements during the live-fish tests. The details of the system hardware and software are described in Harby *et al.* (2019). A brief summary of the elemental features is given in the following.

Five cameras were arranged in series in the flume centre axis and in front of the bypass entrance with a distance of 1.5 m in streamwise direction facing vertically downwards through the water surface. Each camera (Basler ace) with a maximal resolution of 2048×1536 px² was equipped with a 185° fisheye lens (Fujifilm). This arrangement provided overlapping camera views for most of the water volume of interest. Camera settings and video recordings were managed by a software coded particularly for the present application, providing synchronous measurements with a constant frame rate of 20 frames per second.

The 2D fish movements from the uncalibrated videos were tracked by a code based on the MATLAB documentation ‘Motion-Based Multiple Object Tracking’. The code was adapted, optimised and equipped with various filtering techniques according to the boundary conditions of the ethohydraulic laboratory flume and the swimming behaviour of the fish (Harby *et al.*, 2019). The filter criteria were chosen to optimise the tracking process for all live-fish tests E1–E23 (Table 3.7) and F1–F8 (Table 3.8). The algorithm detected moving fish as groups of connected pixels. A Kalman filter was used to predict the object’s location in each video frame and to determine the likelihood of its detection. This process leads to a mean error of (5...15) ± (5...10) mm for the 2D mid-body location of the fish, which is in the order of a fish width. A track was identified if a fish with the same attributes (i.e. length, swimming speed) was detected in at least three consecutive time frames and a new track-ID was

assigned. Single fish detections were assigned to continuous fish tracks if they were within the next three time steps. Otherwise, a new track with a new track-ID was started. Faulty fish tracks primarily resulted from noise interpreted as fish tracks, i.e. shadows of fish on the flume bed, mirror images in the glass window, light reflections, and fine air bubbles (especially at $U_o \geq 0.7$ m/s). If two fish swam very closely together or overlapped, the algorithm only detected a single fish and the two fish movements were merged to one single track.

In the next step, only video frames with identified 2D fish tracks were calibrated and undistorted. The calibration of each camera was based on 9×6 crossing points detected on a checker board with square sizes of 39.9 mm. Checker board crossing points were detected by standard image processing techniques from preselected video frames with their edges enhanced with edge-aware and fast local Laplacian filters. The recorded raw images were distorted in a complex manner due to both the fisheye lens and the refraction at the air–glass and glass–water interfaces (Harby *et al.*, 2019). The MATLAB-integrated distortion-correction model transferred the fish tracks into a local coordinate system (Scaramuzza *et al.*, 2006). By using the intrinsic and extrinsic parameters of the cameras determined during the calibration procedure, the 2D tracks were transferred to a 3D metric-space. The required computation time was optimised by finding the tracks in 2D first and then doing the calibration, which contrasts with a procedure in which each full image frame would be undistorted first, and then processed by the tracking algorithm. This procedure led to numerous single tracks belonging to the fish and many faulty tracks. Since the fish mostly swam along the flume bed, the z -coordinate was set to 0.02 m above the flume bed after calibration. This yielded longer, more continuous tracks with a fixed z -coordinate. However, the fish paths still consisted of numerous single tracks, which had to be connected with a semi-automated procedure (Section 3.6). Incomplete fish tracks occurred if a fish was only observed in one camera. In this case, the track information is sparse and only the 2D tracks can be computed.

3.6 Ethohydraulic data analysis

The result of the fish-tracking algorithm described in Section 3.5.4 is a matrix (x, y, z, t) of the various detected fish-tracks from each live-fish test belonging to three individual fish. Figure 3.11a/b show the resulting x - y - and x - t -diagrams, respectively, for a test with three eel. The three individual fish paths can be distinguished, but still consist of several single tracks and some noise. Since it was not possible to further filter out the noise or automatically connect the tracks without deleting correct tracks, the tracks were manually connected for the three fish of each test. Figure 3.11c illustrates the connected continuous swimming paths of the three eel, which resulted in a bypass passage and two rack passages.

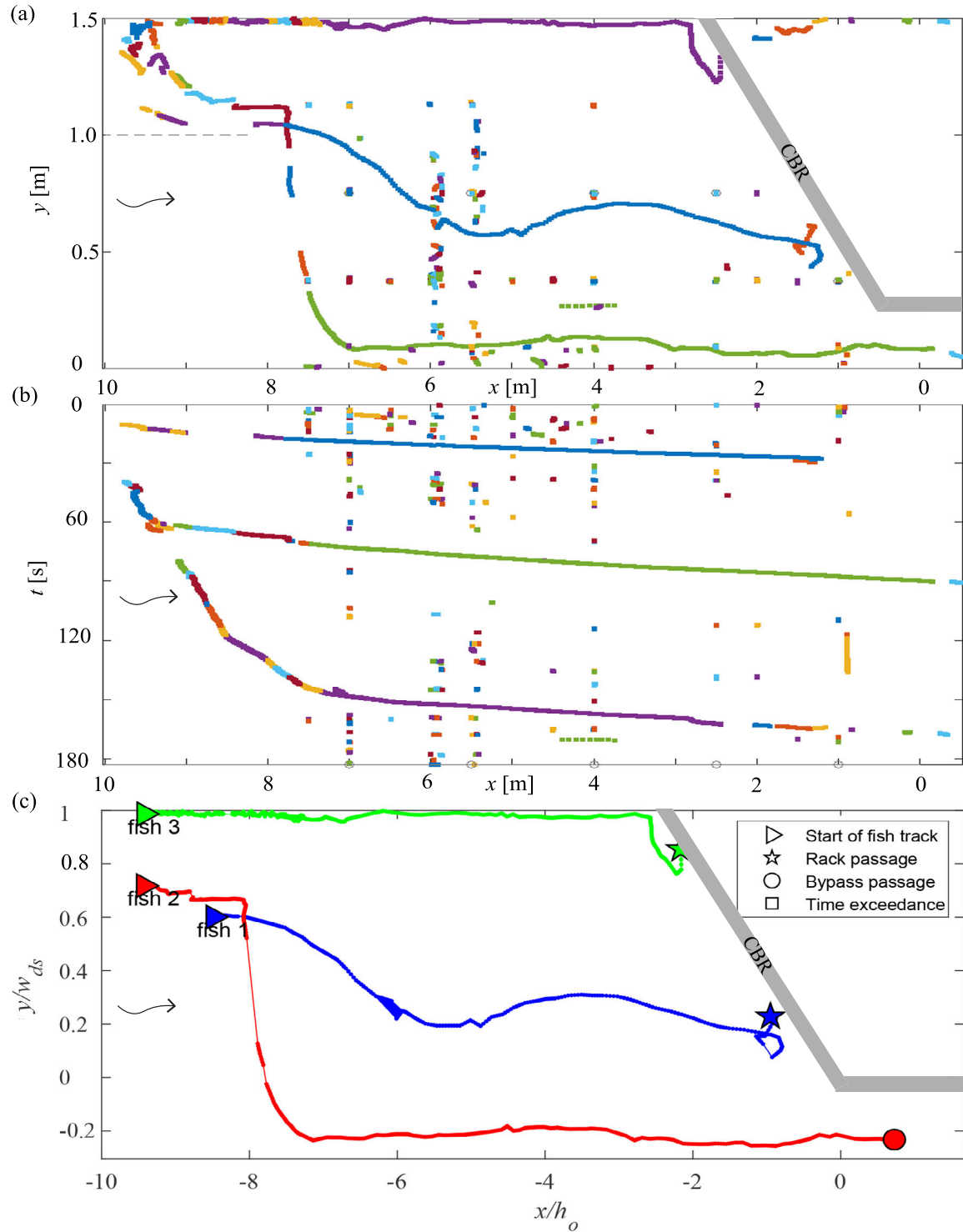


Figure 3.11 Tracks of three eel resulting from the fish-tracking algorithm illustrated in (a) x - y -diagram and (b) x - t -diagram in the local coordinate system, and (c) the manually connected continuous fish paths; the swimming speeds computed for this swimming path are shown in Figure 6.37

To analyse the fish swimming patterns in detail, the ethohydraulic flume is divided into different sectors. Sector 1 (Sec1) describes a 15 cm wide corridor along the left concrete

flume wall opposite of the bypass, Sector 2 (Sec2) and Sector 7 (Sec7) a 15 cm wide corridor along the right flume wall made of glass in front of the bypass, Sector 3 (Sec3) the flume centre upstream of line 2, Sector 4 (Sec4) the flume centre downstream of line 2, Sector 5 (Sec5) a 15 cm wide corridor parallel to the rack and Sector 6 (Sec6) describes the first 50 cm inside the bypass still recorded by the most downstream camera (Figure 3.12). The choice of 15 cm for the width of the rack-parallel Sec5 is appropriate since the hydrodynamic cues of the CBR, i.e. increased pressure and velocity gradients, only extent to about 40 mm upstream of the rack (cf. Section 6.1).

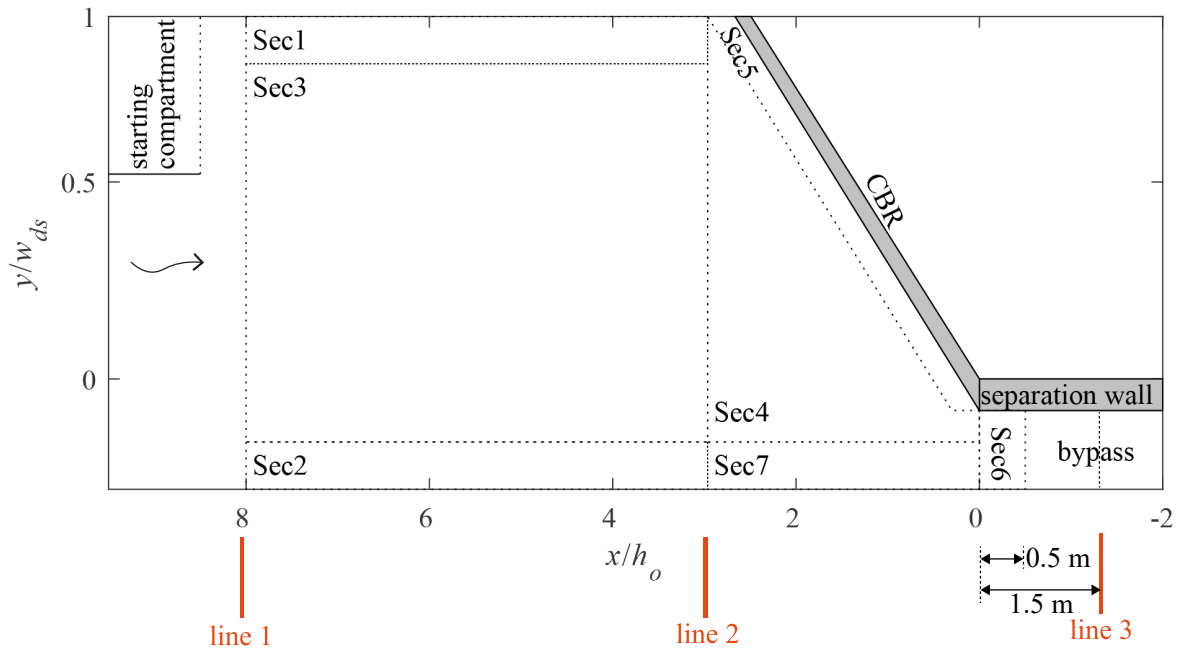


Figure 3.12 Definition of Sectors Sec1-Sec7 for the data analysis of fish swimming patterns

Each fish performed one of the following six possible actions during the tests:

1. Bypass passage: the fish swam downstream, did not pass through the rack, but swam at least 1.5 m into the bypass (line 3 in Figure 3.12) (“bypassed”, subscript $_{by,all}$)
2. Bypass passage with rack interaction: the fish swam into sector 5 (Sec5) during the test before finally swimming at least 1.5 m into the bypass (“bypassed with rack interaction”, subscript $_{by,red}$)
3. Rack passage: the fish swam downstream and eventually passed through the CBR (“rack passage”, subscript $_{rack}$)
4. Refusal: the fish swam downstream of line 2, did not pass through the rack, and also refused to swim into the bypass (“refusal”, subscript $_{refusal}$)
5. Time exceedance: the fish swam past line 1, but did not swim past line 2 (“time exceedance”, subscript $_{time}$)

6. Inactive: the fish did not swim past line 1 during the 30 minutes of the experiment (“inactive”, subscript _{inactive})

The distinction between all bypass passages ($N_{by,all}$) and bypass passages with rack interaction ($N_{by,red}$) was made because some fish swam along the right channel glass wall directly into the bypass without interacting with the CBR. To assess the effect of the CBR on the fish guidance efficiency (FGE), fish that did not enter the rack-parallel sector 5 were therefore excluded from this particular analysis. From the above listed actions, four parameters were defined to evaluate the performance of the curved-bar rack bypass system (CBR-BS): (i) the fish **guidance** efficiency (FGE) of the system including only bypass passages with rack interaction (Eq. 3.10), (ii) the fish **protection** efficiency (FPE) of the system including only bypass passages with rack interaction (Eq. 3.11), (iii) the total system fish guidance efficiency (FGE*) including all bypass passages (Eq. 3.12), and (iv) the total system fish protection efficiency (FPE*) including all bypass passages (Eq. 3.13):

$$FGE = \frac{N_{by,red}}{N_{by,red} + N_{rack} + N_{refusal}}, \quad (3.10)$$

$$FPE = \frac{N_{by,red} + N_{refusal}}{N_{by,red} + N_{rack} + N_{refusal}}, \quad (3.11)$$

$$FGE^* = \frac{N_{by,all}}{N_{by,all} + N_{rack} + N_{refusal}}, \quad (3.12)$$

$$FPE^* = \frac{N_{by,all} + N_{refusal}}{N_{by,all} + N_{rack} + N_{refusal}}. \quad (3.13)$$

Since the experimental setup allowed the fish to easily swim back out of the bypass or back upstream through the CBR, only the first reaction was considered for the further analysis. This means that if a fish passed the CBR or line 3 in the bypass, all further swimming movements were neglected in the analysis.

3.6.1 Residence time

To analyse and compare the swimming behaviour of the tested fish species for different hydraulic configurations, a residence coefficient $R_{c,i}$ was introduced. From the swimming paths obtained with the fish tracking software, the time spent in each sector (t_i) and the total time spent in the experiment (t_{tot}) were calculated for each fish. The residence time was determ-

ined by dividing the time with the area of the corresponding sector for each fish j in each sector i and for the entire flume, i.e. the sum of all sectors, as $T_{i,j} = t_{i,j}/A_i$ and $T_{\text{tot},j} = t_{\text{tot},j}/A_{\text{tot}}$ [s/m²], respectively. The average residence coefficient for one hydraulic configuration was then calculated with Eq. (3.14). For a comparative analysis between different configurations, the sector residence coefficient was normalised by its sum with Eq. (3.15).

$$R_{c,i} = \frac{1}{n} \sum_{j=1}^n \frac{T_{i,j}}{T_{\text{tot},j}}, \quad (3.14)$$

$$R_{c,i,\text{norm}} = \frac{R_{c,i}}{\sum_{i=1}^7 R_{c,i}}, \quad (3.15)$$

with i = sector number [–], j = fish number [–], n = number of active fish tested for this configuration [–], $t_{i,j}$ = time the fish j spent in sector i [s], $t_{\text{tot},j} = \sum_{i=1}^7 t_{i,j}$ = total time the fish j spent in any of the sectors 1-7 [s], A_i = area of the sector i [m²], $A_{\text{tot}} = \sum_{i=1}^7 A_i$ = total area of all sectors 1-7 [m²]. The normalised residence coefficient $R_{c,i,\text{norm}}$ is thus a parameter indicating how much time a fish on average spent in a sector in comparison to the other sectors, while accounting for the different sector areas. If $R_{c,i,\text{norm}} = 1$, all fish of the investigated configuration spent all their time in the sector i , whereas if $R_{c,i,\text{norm}} = 0$, none of the fish of the investigated configuration entered the sector i .

3.6.2 Fish swimming velocity

The fish swimming velocities were computed for the four tested main hydraulic conditions with $U_o = 0.5$ m/s, 0.7 m/s and $VR = 1.2, 1.4$. The fish ground streamwise U_g and transverse V_g velocities, i.e. the velocities of the fish relative to the flume bed, were calculated as the average over 5 time steps from the individual fish swimming paths for each experiment with

$$U_g = \frac{x_{i+5} - x_i}{t_{i+5} - t_i}, \quad V_g = \frac{y_{i+5} - y_i}{t_{i+5} - t_i}. \quad (3.16)$$

This calculation yields negative values $U_g < 0$ if the fish moves upstream, and positive values $U_g > 0$ if the fish moves downstream. For $U_g = 0$, the fish remains at the same location in the flume actively swimming against the flow. Due to slightly different inflow conditions, the velocity fields for the tests in autumn 2018 and those in spring 2019 slightly differed. The velocity field for the tests with barbel, spirlin, nase and eel in autumn 2018 was measured with ADV, whereas a numerical model was used to simulate the flow field for the tests with salmon parr and brown trout in spring 2019 (cf. Section 6.1). From these velocity fields, the streamwise and spanwise velocity components U and V , respectively, were interpolated for every fish location. The streamwise and spanwise fish swimming velocities U_{fish} and V_{fish} ,

respectively, were thus calculated by subtracting the flow velocities from the fish ground velocity (Eq. 3.17). Finally, the resulting fish swimming velocity v_{fish} in [m/s] was computed with Eq. (3.18) if $U_{\text{fish}} < 0$ and with Eq. (3.19) if $U_{\text{fish}} > 0$.

$$U_{\text{fish}} = U_g - U, \quad V_{\text{fish}} = V_g - V, \quad (3.17)$$

$$v_{\text{fish}} = -\sqrt{U_{\text{fish}}^2 + V_{\text{fish}}^2} \text{ for } U_{\text{fish}} < 0, \quad (3.18)$$

$$v_{\text{fish}} = \sqrt{U_{\text{fish}}^2 + V_{\text{fish}}^2} \text{ for } U_{\text{fish}} > 0. \quad (3.19)$$

With this analysis, different swimming patterns are identified (Table 3.9). If the fish ground speed is $U_g < U$, Eq. (3.17) yields $U_{\text{fish}} < 0$, i.e. the fish actively swims against the current with a positive rheotaxis by either moving upstream or moving downstream with a lower speed than U . For $U_g > U$, however, the fish swims downstream with a higher velocity than the flow velocity U , which is only possible with a negative rheotaxis. Eq. (3.17) thus yields $U_{\text{fish}} > 0$ in this case. If $U_g = U$, the fish drifts passively downstream with the flow velocity and its rheotaxis is unclear.

Table 3.9 Examples of possible fish swimming patterns resulting in positive or negative rheotaxis

U [m/s]	U_g [m/s]	v_{fish} [m/s]	rheotaxis	swimming pattern
0.5	0	-0.5	positive	fish swims actively against the flow with U and is thus steady in its location
0.5	0.3	-0.2	positive	fish swims actively against the current and drifts downstream
0.5	0.5	0	unclear	fish drifts passively downstream with the inflow velocity
0.5	0.7	0.2	negative	fish swims d/s at a higher velocity than the flow velocity
0.5	-0.1	-0.6	positive	fish swims upstream

Finally, the mean, the standard deviation and the 99% quantile were computed over all fish swimming velocities obtained for each fish species and each hydraulic condition. These values were compared to the fish swimming speed known from the literature. Table 3.10 shows the swimming speeds of the fish species tested in this study calculated with the model by Ebel (2016):

$$\log(v_{\text{fish}}) = 0.546 + 0.7937 \cdot \log(TL) - 0.0902 \cdot \log(t) + 0.2813 \cdot \log(T), \quad (3.20)$$

with TL = total fish length [m], t = swimming time [s] and T = water temperature [$^{\circ}\text{C}$].

Table 3.10 Swimming speeds of the tested fish species for the smallest (TL_{\min} , $v_{\text{fish},\min}$) the largest (TL_{\max} , $v_{\text{fish},\max}$) and the mean fish length (TL_{mean} , $v_{\text{fish},\text{mean}}$) according to the model by Ebel (2016) for different swimming times corresponding to the sustained swimming speed (200 min), the prolonged swimming speed (45 min = max. duration of an experiment including 15 min acclimatisation time) and the burst swimming speed (20 s) at $T = 14^\circ\text{C}$

species	swimming time	TL_{\min} [cm]	TL_{mean} [cm]	TL_{\max} [cm]	$v_{\text{fish},\min}$ [m/s]	$v_{\text{fish},\text{mean}}$ [m/s]	$v_{\text{fish},\max}$ [m/s]
barbel	200 min				0.50	0.69	0.95
	45 min	9.7	14.6	22.0	0.57	0.79	1.09
	20 s				0.89	1.22	1.70
spiralin	200 min				0.43	0.51	0.62
	45 min	8.1	9.9	12.9	0.49	0.58	0.71
	20 s				0.77	0.90	1.11
nase	200 min				0.34	0.39	0.46
	45 min	6.0	7.2	8.9	0.39	0.45	0.53
	20 s				0.60	0.70	0.83
Atlantic salmon parr	200 min				0.42	0.55	0.70
	45 min	7.9	11.1	15.0	0.48	0.63	0.80
	20 s				0.75	0.99	1.25
brown trout	200 min				0.49	0.69	0.90
	45 min	9.5	14.6	20.4	0.56	0.79	1.03
	20 s				0.87	1.22	1.60
European eel	200 min				0.52	0.61	0.68
	45 min	50.4	67.1	80.9	0.63	0.74	0.83
	20 s				1.21	1.43	1.58

3.6.3 Statistical analysis

A chi-square test χ^2 was applied to test whether the different reactions of each fish species to changes of one of the main parameters U_o or VR (= ratio of bypass inlet to mean approach flow velocities $U_{by,in}/U_o$) were significant. This test is thus a pairwise comparison of two independent data sets. Furthermore, a multivariate logistic regression model was used to quantitatively evaluate the main parameters affecting the odds of a specific fish reaction for all fish species and two different FGSs, i.e. the CBR and the HBR. The model included the entire data set of live-fish tests conducted in autumn 2018 and spring 2019 for the present study with the CBR and for the study by Meister (2020) with the HBR.

Chi-squared test

A chi-squared test was performed in Matlab for each fish species separately to test the null-hypothesis that there is no relation between the main parameters U_o and VR , and the fish reaction at the CBR-BS, i.e. that the differences in the fish reactions occurred simply by chance. The alternate hypothesis thus states that there is a significant effect of the main parameters U_o and/or VR on the fish reaction. To this end, the test value χ^2 was calculated with a significance level of $\alpha = 0.05$ with the Yates's correction for small sample sizes (Yates, 1934). The chi-squared test was applied to test whether (I) the fish reaction for different U_o was significantly different and (II) the fish reaction for different VR was significantly different. A separate test was conducted for each fish species and for each of the three main fish reactions, i.e. bypass passage, rack passage or refusal.

Multivariate logistic regression model

To determine the parameters which significantly affected the fish reaction of the entity of all tested fish, the data set resulting from the ethohydraulic tests with the CBR described in Section 3.5.3 (Table 3.7) was used as well as the data set obtained by Meister (2020) for the HBR. A logistic regression model was chosen to analyse the effects of the independent main parameters rack type, U_o , and VR , and the secondary parameters *usage* and *time of day* on the fish reaction. The parameter *usage* describes whether a fish was used for the first, the second or the third time in a test and is thus an indicator for a learning or an adaptation effect. The parameter *time of day* describes whether a fish was used for a test in the morning (07.00-13.00) or in the afternoon (13.00-19.00) and could be an indicator for changes in the fish's biorhythm.

A multivariate logistic regression is suitable for a repeated measures design with discrete outcome variables such as multinomial outcomes, i.e. three or more response categories (Quené and van den Bergh, 2004). Herein, the fish reaction can be separated into three response categories: rack passage, bypass passage, or refusal, and thus describes the categorical response variable Y . A binomial logistic regression was set up with the open source statistics software R using the generalised linear model (glm) function of the nnet library. Three different models were thus set up with either bypass passage (yes/no), rack passage (yes/no) or refusal (yes/no) as the dependent reference variable.

Eq. (3.21) expresses the probability π of Y taking category k given a set of n independent parameters $X = (X_1, X_2, \dots, X_n)$. In a logistic regression model, the odds ratio $\frac{p(X)}{1-p(X)}$ is

expressed with Eq. (3.22) or in linear form with Eq. (3.23).

$$\pi_k = P(Y = k | X = x), \quad (3.21)$$

$$\frac{p(X)}{1 - p(X)} = e^{\beta_0 + \beta_1 X_1 + \dots + \beta_n X_n}, \quad (3.22)$$

$$\log \left(\frac{p(X)}{1 - p(X)} \right) = \beta_0 + \beta_1 X, \quad (3.23)$$

where $\frac{p(X)}{1 - p(X)}$ denotes the odds ratio, i.e. the probability of the occurrence of category k divided by the probability of category k not occurring and $\beta_i = (\beta_0, \dots, \beta_n)$ = output coefficients of the logistic regression model. It is common to compare the odds ratio, which represents the constant effect of an independent parameter X on the probability that one outcome will occur. For the analysis of the model output, the coefficients for the odds ratio of one response category are compared to the coefficients of the reference category. All independent parameters X_i were therefore introduced as categorical variables with the CBR, $U_o = 0.5$ m/s, $VR = 1.2$, *usage* = 1, and *time of day* = morning as the reference categories. This means that the effect of the HBR is interpreted relative to the effect of the CBR, the effect of $U_o = 0.7$ m/s relative to the effect of $U_o = 0.5$ m/s and so on.

To find the best model fit for the present data, different logistic regression models were set up in R including all possible interaction terms for the main independent parameters rack type, U_o and VR . The Akaike Information Criterion (AIC) was used to compare the models and choose the best fit. Smaller AIC values thereby indicate a better model fit. If more variables are considered, the model complexity and the resulting AIC value increases. The AIC values for the model with only the main parameters and those for the models including different interaction terms were all in the narrow range of AIC = 836-850 (with bypass passage as the dependent variable). The simple model with all main parameters and no interaction terms was therefore chosen (AIC = 847).

3.7 Numerical model

In the scope of a MSc thesis conducted by Leuch (2019), a Computational Fluid Dynamics (CFD) model of the CBR was set up in the open-source software OpenFOAM[®] (version v1812) environment to further optimise and investigate the effect of different bar shapes on the flow field, and to gain detailed insight on the hydraulics in the vicinity of the rack and

between the bars.

In a preliminary study, the performance of different turbulence models, i.e. standard $k - \varepsilon$, realizable $k - \varepsilon$, RNG $k - \varepsilon$, Wilcox $k - \omega$, SST $k - \omega$, and different mesh resolutions were tested with regard to reproducing the velocity profile in the viscous and the logarithmic sublayer. The Shear Stress Transport (SST) $k - \omega$ model was found to best reproduce the velocity profile, whereas the $k - \varepsilon$ models overestimated the shear velocity (Figure 3.13). The SST $k - \omega$ model makes use of the advantages of the standard $k - \varepsilon$ and the Wilcox $k - \omega$ model by treating adverse pressure gradients and the velocity distribution near wall regions more accurately. Furthermore, the SST $k - \omega$ turbulence model is suitable for low to high Reynolds numbers.

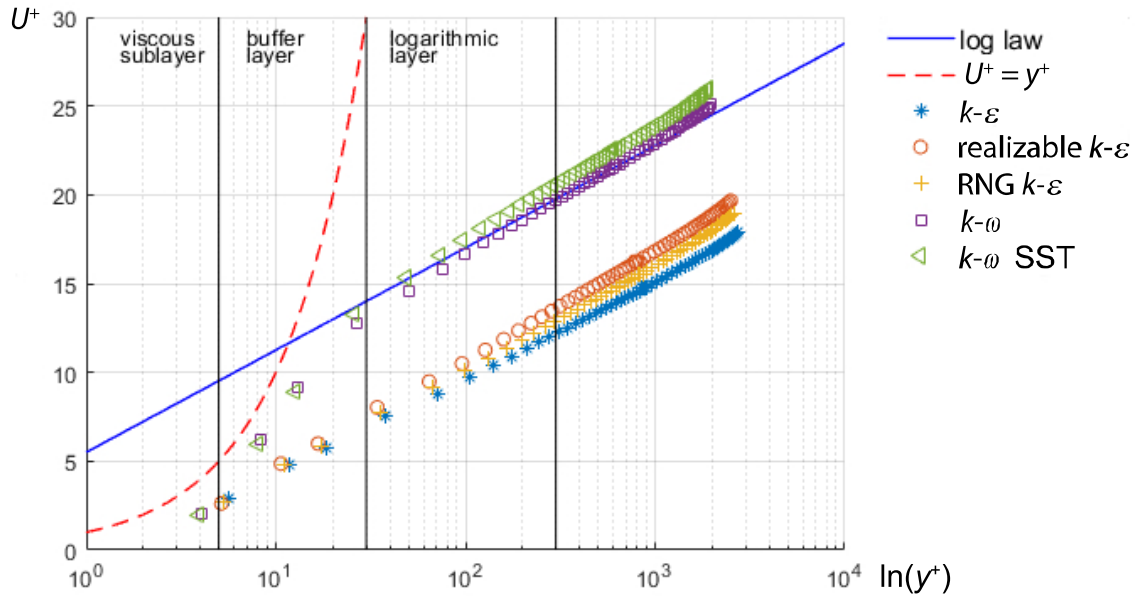


Figure 3.13 Velocity profiles simulated with different turbulence models with $U^+ = u/u_*$, $y^+ = u_*y/\nu$ and $u_* =$ simulated wall shear velocity; adapted from Leuch (2019)

A grid convergence study was carried out to determine an optimal mesh size with regard to modelling error and computational time. The OpenFOAM meshing tools *blockMesh* and *snappyHexMesh* were used for the mesh generation. Based on this study, the cell length of the base mesh was set to 2.5 mm. The mesh was refined around and between the bars to a cell length of 1.25 mm. Three additional 10 mm long and 0.625 mm thick cell layers were set around the bar surface to reduce grid-induced errors (Figure 3.14). Additionally to the mesh refinement around the bars, a wall function was implemented, which superimposes a theoretical velocity profile between the wall and the first mesh node.

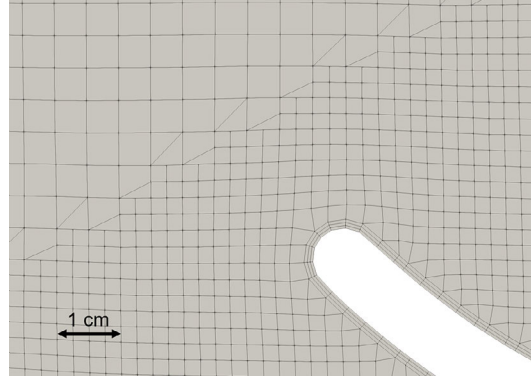


Figure 3.14 Grid structure and resolution around the upstream bar tip of the CBR (Leuch, 2019)

The *pimpleFOAM* solver was used with the numerical schemes in Table 3.11 for all simulations described hereafter. A fixed velocity and a fixed pressure were defined as inlet and outlet boundary condition, respectively. The walls and the borders of the bars were treated with a no-slip condition for velocity, and a zero-gradient condition for pressure. The free stream values at the inlet were determined according to Spalart and Rumsey (2007) with

$$TKE = 10^{-6} \cdot U_o^2, \quad \varepsilon_t = 4.5 \cdot 10^{-7} \cdot \frac{U_o^3}{d_b}, \quad \omega = 5 \cdot \frac{U_o}{d_b}, \quad (3.24)$$

with TKE = turbulent kinetic energy [m^2/s^2], ε_t = turbulent dissipation [m^2/s^2], and ω = specific rate of dissipation [$1/\text{s}$].

Table 3.11 Applied numerical schemes for the model set-up with the *pimpleFOAM* solver

	scheme
$\partial/\partial t$	Euler
$\nabla \cdot (U)$	Gauss linearUpwind
$\nabla \cdot (TKE, \varepsilon_t, \omega)$	Gauss upwind
Gradient	Gauss linear
Surface normal gradient	corrected
Laplacian	Gauss linear corrected
Wall distance	meshWave method

As a first step, the CBR in the diversion-type HPP layout tested in the small flume (Figure 3.5) was simulated to validate the numerical model with the head loss and velocity field measurements. A 2D mesh with a unit height of 10 mm in vertical direction was generated with a hexagonal base. The simulation was conducted for 50 s (real time), but reached convergence after a few seconds. The validated numerical model can be used to develop and investigate new bar shapes optimised for the hydraulic and operational conditions of

a specific prototype site. In addition to the straight bar shape of the MBR (Figure 3.15a) and the curved bar shape of the CBR (Figure 3.15b), a new bar shape was developed and investigated with the numerical model. This new bar shape represents a more foil-shaped version of the curved bar and is thus called foil-shaped CBR or f-CBR hereafter (Figure 3.15c). The smallest distance between the bars of the f-CBR is located at the upstream rack side, which is advantageous for the rack cleaning process, because logs cannot get stuck between the bars as easily as in the CBR with narrowing distance between the bars in streamwise direction (cf. Section 8.2). Figure 3.15c shows the bar shape dimensions for an f-CBR with $\alpha = 30^\circ$. The upstream bar tip with $r = 8$ mm is wider than for the CBR, hence $t_b = 16$ mm. The resulting bar blockage ratio is thus higher compared to the MBR and the CBR with $\sigma = t_b / (s_b + t_b) = 0.24$ for $s_b = 50$ mm. The downstream bar end is designed with the minimum possible steel extrusion radius of $r = 1.5$ mm. The downstream bar end is angled with 10° to the downstream channel walls compared to 0° for the CBR and 45° for the MBR. This f-CBR design leads to a widening of the bar spacing in streamwise direction for $\alpha \geq 30^\circ$. Thereby, increasing α increases the bar spacing towards the downstream bar tip since bar overlapping is reduced. For $\alpha < 30^\circ$, however, bar overlapping increases and the shape of the f-CBR has to be further optimised for lower rack angles.

Different flow features such as the spatial velocity gradient (*SVG*) and the turbulent kinetic energy (*TKE*) are reported and discussed for the different bar shapes in Chapter 5.

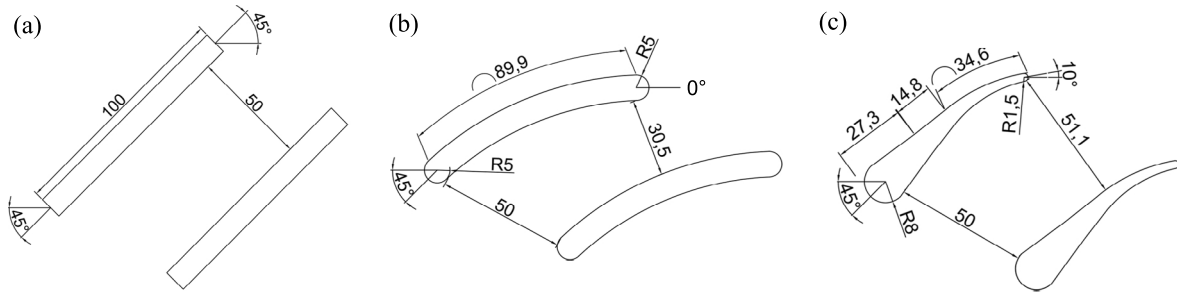


Figure 3.15 Dimensions in [mm] of different bar shapes for (a) MBR, (b) CBR and (c) f-CBR, all with $\alpha = 30^\circ$, $\beta = 45^\circ$, $s_b = 50$ mm

A 3D numerical model of the CBR-BS in the ethohydraulic flume was set up as an extension of the MSc study by Leuch (2019). The four main flow conditions used in the live-fish tests were modelled with the bypass discharge Q_{by} as an input parameter. Q_{by} was computed from water level measurements and the standard equation for weir overflow by Poleni (Bollrich, 2013). The same boundary conditions and turbulence model was used as for the 2D model of the small flume simulations. To save computational time, the mesh resolution was slightly lower, however. The mesh resolution in the far up- and downstream of the CBR was 20 mm.

The mesh was refined around the CBR to 5 mm, and three extra layers of 10 mm length and 1 mm width were created around the bars (Figure 3.16). The simulation was conducted for 200 s (real time). The 3D numerical model results were validated with ADV measurements.

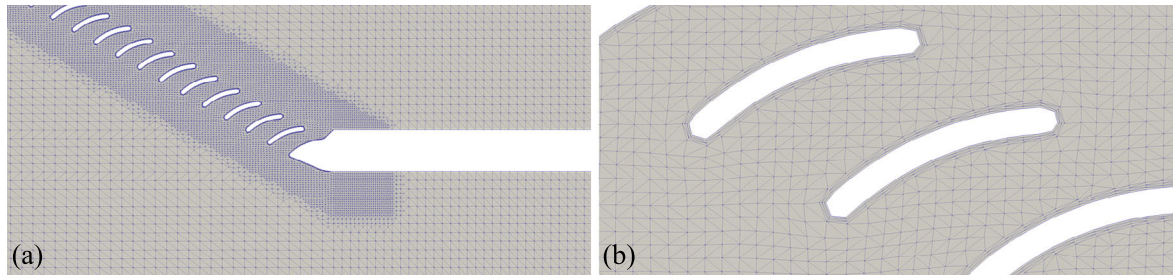


Figure 3.16 Detailed view on the mesh resolution for the 3D numerical simulations of the etho-hydraulic flume with the refined grid resolution (a) at the bypass entrance, and (b) around the bars of the CBR

4 Hydraulic head losses and flow fields of curved-bar racks

This chapter presents the results, analysis and discussion of the experimental investigation of curved-bar racks with physical scale 1:2 models. The hydraulic performance is investigated regarding the hydraulic head losses in Section 4.1 and the flow fields at CBRs in Section 4.2.

4.1 Hydraulic head losses of curved-bar racks

Parts of this section have been published in Beck et al. (2019a): Hydraulic performance of fish guidance structures with curved bars - Part 1: Head loss assessment, Journal of Hydraulic Research.

4.1.1 Head loss equation

The rack head loss coefficient $\xi_R = f(\alpha, \beta, \sigma, \varepsilon, K, V_i, w_{ds}/w_o)$ is a non-dimensional parameter and a function of the rack, bar and overlay parameters, and the HPP layout described in Section 3.4.3. The rack angle α , the bar angle of attack β and the non-dimensional axial bar distance, i.e. the blockage ratio of the vertical bars σ , characterise the basic geometric rack properties. According to Albayrak *et al.* (2018), the basic rack head loss coefficient $\xi_B = f(\alpha, \beta, \sigma)$ is a function of these parameters. The head loss factors C_S , C_L , $C_{V,i}$ and C_w describe the effects of the secondary parameters: bar shape, bar depth, additional overlays or different HPP layouts, respectively. Overall, the rack head loss coefficient ξ_R is a product of the basic head loss coefficient and the head loss factors:

$$\xi_R = \xi_B \cdot C_S \cdot C_L \cdot C_{V,i} \cdot C_w. \quad (4.1)$$

Figure 4.1 shows the experimentally obtained ξ_R values versus the main rack parameters (α , β , σ) for $w_{ds} = w_o$, i.e. a typical diversion-type HPP layout. Three fundamental correlations are observed:

1. Reducing the bar spacing s_b and hence increasing σ leads to higher rack blockage and thus to higher ξ_B values (Figure 4.1a). This effect is small for $\beta = 45^\circ$ compared to $\beta = 90^\circ$.
2. Decreasing β leads to a less pronounced deflection of the flow and hence decreases ξ_R (Figure 4.1b). The flow straightening effect of the curved bars is stronger for lower β values causing a smaller recirculation zone downstream of the CBR (compare Figures 4.2a and b).
3. Increasing α decreases the rack area and thus increases the flow velocity in front of the rack. This effect leads to higher ξ_R with increasing rack angles α . For $\sigma = 0.04$,

however, this trend is reversed because an increase of α creates gaps between the bars, i.e. no bar overlapping in flow direction, which reduces rack resistance. Both effects are stronger for $\beta = 90^\circ$ compared to $\beta = 45^\circ$ (Figure 4.1c).

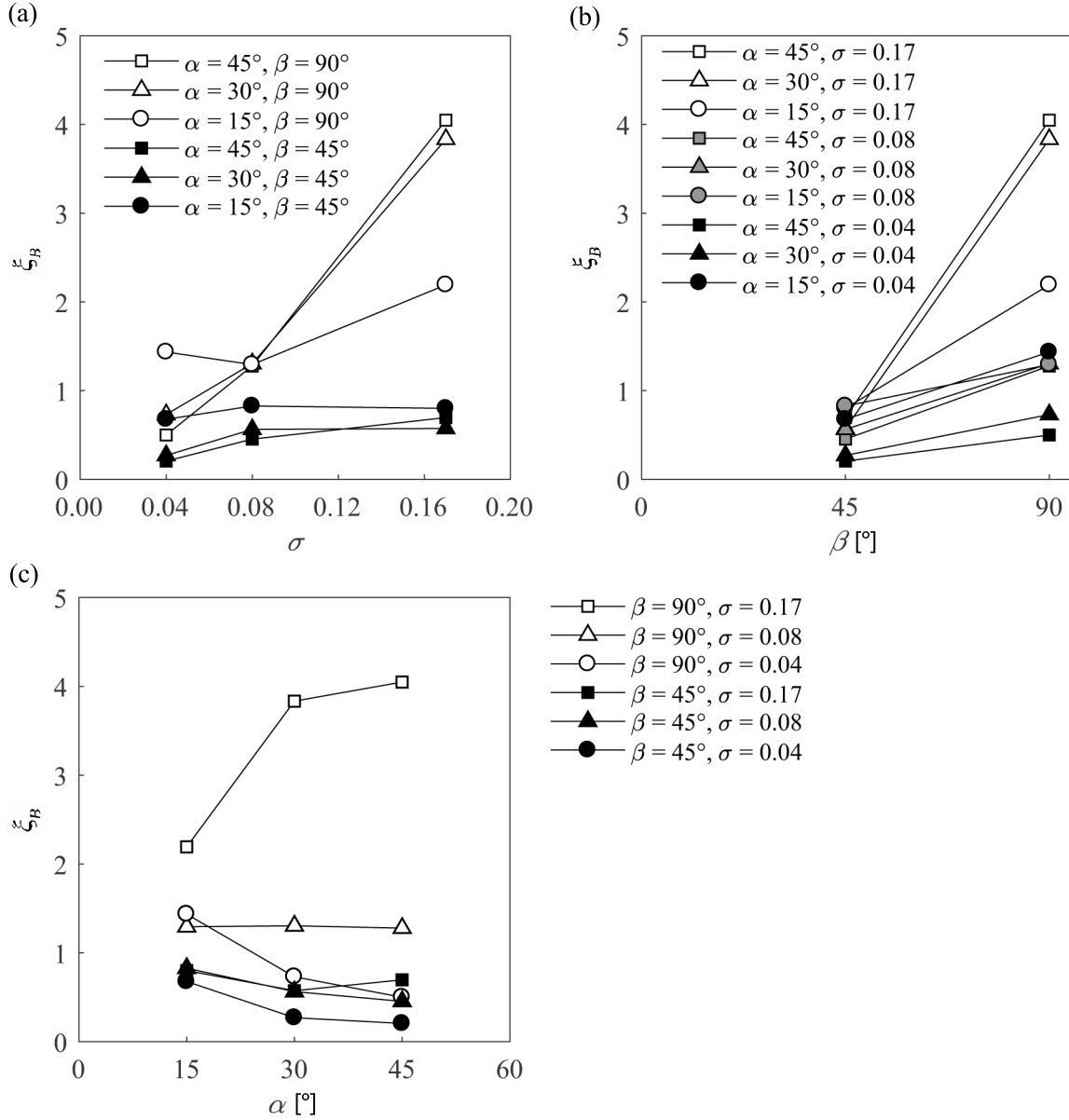


Figure 4.1 Basic head loss coefficient ξ_B versus (a) σ , (b) β and (c) α for rack configurations in the diversion-type HPP layout without overlays

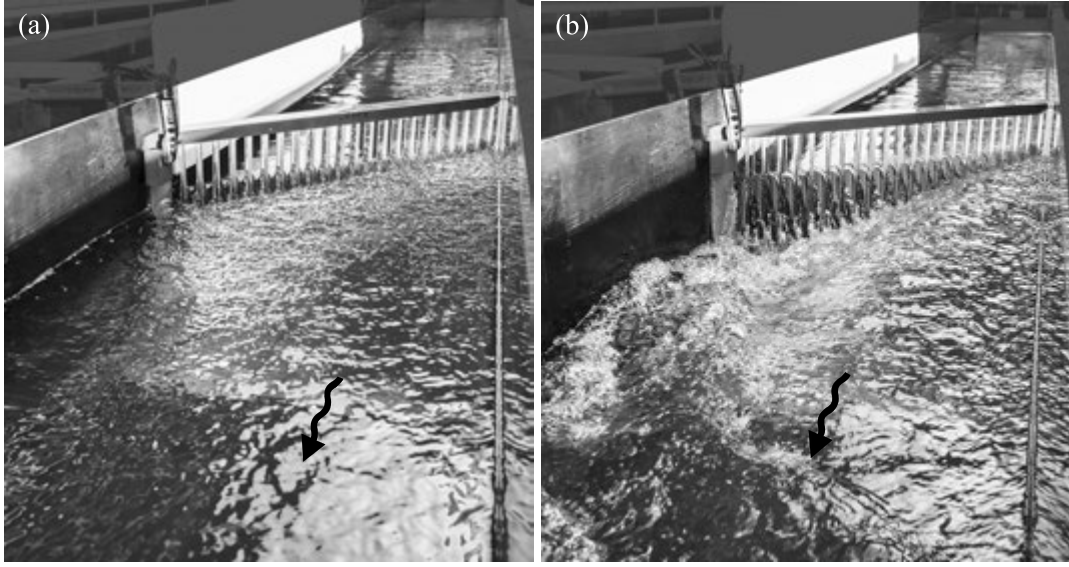


Figure 4.2 Rack head loss and downstream flow field of CBRs with (a) $\alpha = 45^\circ$, $\beta = 45^\circ$ and $\sigma = 0.17$ and (b) $\alpha = 45^\circ$, $\beta = 90^\circ$ and $\sigma = 0.17$, view against flow direction

The above observed correlations are quasi-similar to those reported by Albayrak *et al.* (2018) for MBRs. Therefore, the rack head loss prediction equation is developed in the same form as proposed by Albayrak *et al.* (2018). The equation for the basic head loss coefficient developed by Albayrak *et al.* (2018) for MBRs with straight bars is taken as a basis since it is valid for the parameter range of the present study:

$$\xi_B = 245 \left[0.0275 + (\sigma - 0.0815) \left(\frac{\alpha}{90^\circ} \right) \right] \cdot \left(\frac{\beta}{90^\circ} \right)^{5\sigma^{0.44}}. \quad (4.2)$$

4.1.2 Bar shape factor C_S

The bar shape factor for straight bars is $C_{S,\text{straight}} = 1$ (Albayrak *et al.*, 2018). To determine the shape factor for curved bars, the predicted (subscript p) head loss coefficients $\xi_{R,p}$ using Eqs. (4.1) and (4.2) are compared with the measured (subscript m) CBR head loss coefficients $\xi_{R,m}$ for the main parameters (Figure 4.1). Note that the bar depth is the standard bar depth $D_b = 0.10$ m at prototype scale ($C_L = 1$), no overlay is considered ($C_{V,i} = 1$), the HPP layout is of diversion-type ($C_w = 1$) and hence Eq. (4.1) reduces to $\xi_R = \xi_B \cdot C_S$. The resulting ratios in Figure 4.3 show that the ξ_R values for CBRs are 2.6 to 5.5 times lower than those predicted for the equivalent MBR configurations with straight bars with an average of 4.2, a standard variation of 0.94 and a variance of 0.88.

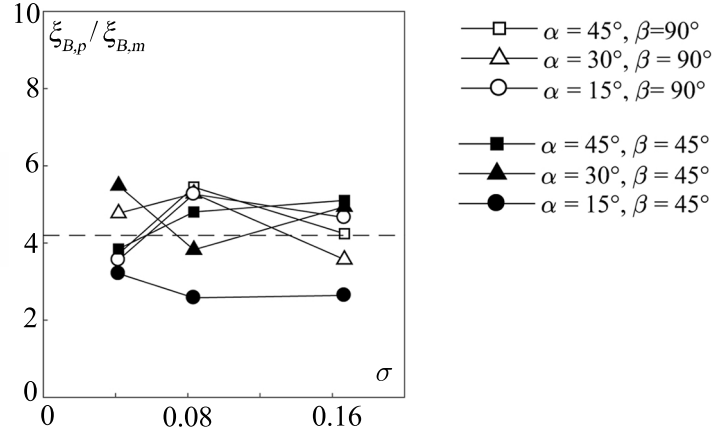


Figure 4.3 Ratio of the computed MBR head loss coefficient $\xi_{B,p}$ from Albayrak *et al.* (2018) to the measured CBR head loss coefficient $\xi_{B,m}$ of the present study versus σ

Since no specific effects or trends of α , β or σ on the ratios shown in Figure 4.3 are identified, the average value of the ratios is considered to account for the overall effects of these parameters, leading to a bar shape coefficient for CBRs of

$$C_{S,\text{curved}} = \left(\frac{1}{4.2} \right) \approx 0.24. \quad (4.3)$$

This coefficient $C_{S,\text{curved}} = 0.24$ indicates that the ξ_R values for curved bars are reduced by 76% on average as compared to straight bars for the investigated rack configurations. The coefficient of determination for the best fit of $\xi_R = \xi_B \cdot C_S$ is $R^2 = 0.95$.

4.1.3 Head loss factor of bar depth C_L

The effect of the bar depth d_b on the head loss coefficient was investigated for $\alpha = 30^\circ, 45^\circ, \beta = 45^\circ, 90^\circ$, and $\sigma = 0.04, 0.08, 0.17$. For $\varepsilon = d_b/D_b = 0.7$ and 1.25 , C_L values were computed as the ratio of ξ_R values for $\varepsilon = 0.7$ or $\varepsilon = 1.25$ to ξ_R for $\varepsilon = 1$, describing the head loss change from the standard bar depth to the shorter and longer bar depths, respectively. The curve fit analysis gives

$$C_L = \left[1 + 3.3(1 - \varepsilon) \left(\frac{\alpha}{90^\circ} \right) \right] \sigma^{2(1-\varepsilon)\left(\frac{\alpha}{90^\circ}\right)}, \quad (4.4)$$

with $R^2 = 0.75$, provided that $45^\circ \leq \beta \leq 90^\circ$, $30^\circ \leq \alpha \leq 45^\circ$, $0.7 \leq \varepsilon \leq 1.25$ and $0.04 \leq \sigma \leq 0.17$. Eq. (4.4) satisfies the following boundary conditions: $\varepsilon = 0 \rightarrow C_L = 1$ and $\varepsilon = \infty \rightarrow C_L = \infty$. The application of Eq. (4.4) to CBRs with $\alpha = 15^\circ$ is only recommended for estimates because the effect of the bar depth d_b on ξ_R was only determined for $\alpha = 30^\circ$ and 45° .

Figure 4.4 shows the curve fits of C_L , i.e. Eq. (4.4), and the corresponding experimental data versus σ . For $\varepsilon = 1$, C_L is equal to unity. The effect of ε on ξ_R is most pronounced for low σ , i.e. larger bar spacings, because the bars act as a single body in the flow and flow through gaps between the bars in flow direction occurs as for isolated bars. Decreasing the bar depth from $\varepsilon = 1.25$ to $\varepsilon = 0.7$ reduces the projected bar area and hence the bar resistance. Therefore, the head loss coefficient ξ_R decreases with decreasing ε . This trend diminishes with increasing σ since the gaps between the bars are reduced and the bars even overlap in flow direction resulting in increased bar resistance compared to the single bar. Despite the larger projected area, longer bars enhance the flow straightening effect of curved bars resulting in reduced ξ_R and C_L values below 1 at $\sigma = 0.17$. For both rack angles α , C_L values follow a power-law function with σ .

A slight effect of α on C_L is observed in Figure 4.4. For the same σ values, the lateral distance between the bars is higher for $\alpha = 45^\circ$ than for $\alpha = 30^\circ$. As a consequence, the effect of ε on C_L and hence ξ_R is slightly more pronounced for the former compared to the latter. For $\beta = 90^\circ$ at $\sigma = 0.17$, the data do not follow the trends explained above, and both shorter and longer bars strongly reduce ξ_R and hence C_L compared to the standard bar depth (Figure 4.4b). Therefore, the data point marked with a grey circle in Figure 4.4b was considered as an outlier and excluded from the fit. Except for this behaviour at $\sigma = 0.17$ and some data scatter for the other two σ values, the effect of β on C_L is assumed to be negligible within $45^\circ \leq \beta \leq 90^\circ$.

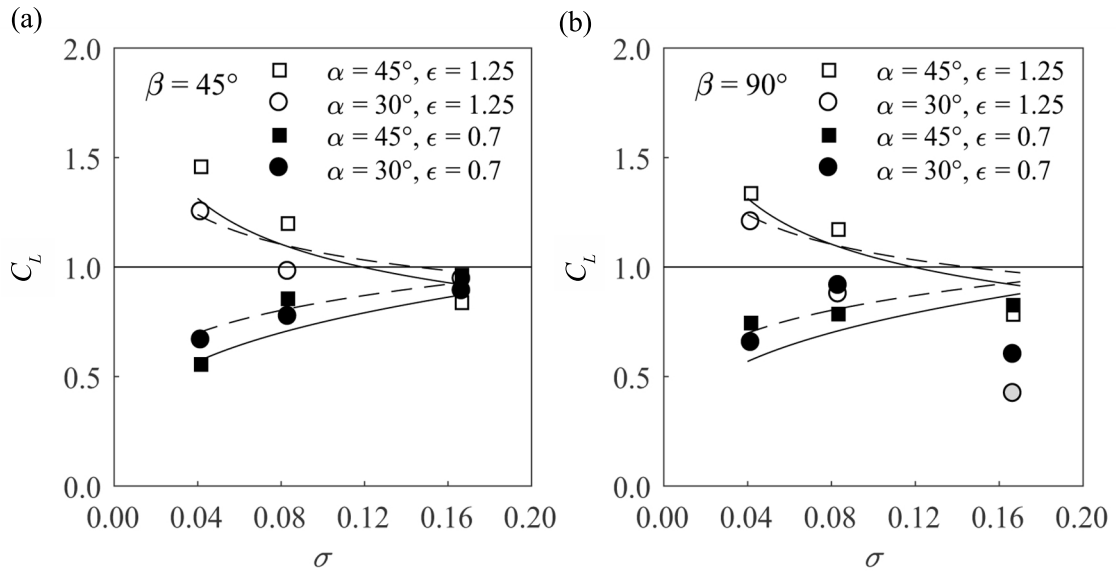


Figure 4.4 Head loss factor of bar depth C_L versus σ for (a) $\beta = 45^\circ$ and (b) $\beta = 90^\circ$ including the best fit according to Eq. (4.4); the configuration $\alpha = 30^\circ, \beta = 90^\circ, \sigma = 0.17, \varepsilon = 1.25$ marked with a grey circle in plot (b) is treated as an outlier and thus excluded from the fit

4.1.4 Head loss factor of overlays $C_{V,i}$

Different blockage ratios of top, top & bottom and bottom overlays, $V_1 = h_{To}/h_o$, $V_2 = h_v/h_o$ and $V_3 = h_{Bo}/h_o$, respectively, were investigated for all CBR configurations listed in Table 3.3.

The $C_{V,i}$ values were computed by dividing the measured $\xi_{R,m}$ values of overlay configurations with the $\xi_{R,m}$ values of corresponding no-overlay configurations. An overlay factor $K_{V,i}$ is introduced with the boundary conditions $K_{V,i} = 0 \rightarrow C_{V,i} = 1$ and $K_{V,i} = \infty \rightarrow C_{V,i} = \infty$ as

$$C_{V,i} = 1 + K_{V,i}. \quad (4.5)$$

Figure 4.5 shows $C_{V,i}$ versus V_i for $\alpha = 15^\circ, 30^\circ$ and 45° , $\beta = 90^\circ$, $\sigma = 0.04, 0.08$ and 0.17 , $\varepsilon = 1$ and top, top & bottom and bottom overlays. The experimental data reveal a different effect of individual top ($C_{V,1}$) or bottom ($C_{V,3}$) overlay on the head loss compared to the combination of top & bottom overlays ($C_{V,2}$). The values of $C_{V,1}$ and $C_{V,3}$ match well and are larger than $C_{V,2}$ at the same σ values for a given overlay blockage ratio V_i . This trend is independent of the rack angle α . For all overlay configurations, all $C_{V,1}$, $C_{V,2}$ and $C_{V,3}$ values are highest for large bar spacings ($\sigma = 0.04$) and lowest for smaller bar spacings ($\sigma = 0.17$). This result is expected because the additional blockage by overlays leads to a sharp increase of the total blockage of the rack for $\sigma = 0.04$ compared to $\sigma = 0.17$ where the blockage due to the bars is already the highest.

The rack angle α has a profound effect on $C_{V,i}$. The $C_{V,i}$ values increase with increasing overlay blockage ratio V_i for $\alpha = 45^\circ$ whereas it is opposite for $\alpha = 15^\circ$. This result is attributed to the fact that decreasing α results in: (i) lower velocities at the rack and hence lower rack resistance, and (ii) the overlays distribute the flow more uniformly along the rack resulting in lower $C_{V,i}$ values.

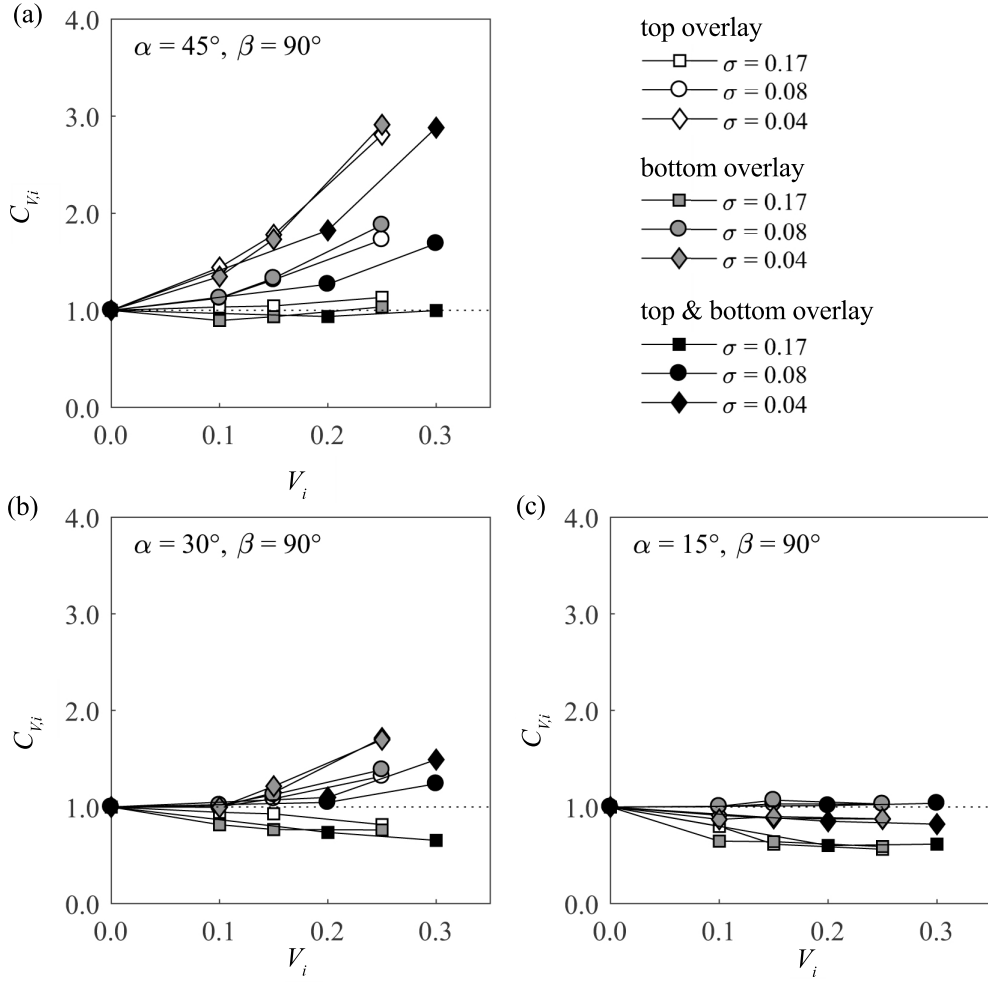


Figure 4.5 Measured overlay head loss coefficient $C_{V,i}$ versus V for top, top & bottom and bottom overlays in case of (a) $\alpha = 45^\circ$, $\beta = 90^\circ$, (b) $\alpha = 30^\circ$, $\beta = 90^\circ$ and (c) $\alpha = 15^\circ$, $\beta = 90^\circ$

Since $C_{V,i}$ and hence $K_{V,i}$ depend on the overlay positions at the rack, a separate curve-fit analysis with $K_{V,i} = f(\alpha, \beta, \sigma, V_i)$ was made. The experimental data follow the fits

$$K_{V,1,3} = \left[10 \left(\frac{90^\circ}{\beta} \right) \left(\frac{V_{1,3}}{1 - V_{1,3}} \right)^{4.3\sigma^{0.75\left(\frac{\alpha}{90^\circ}\right)}} \right] - 5.3 \left(\frac{V_{1,3}}{1 - V_{1,3}} \right)^{1.7}, \quad (4.6)$$

$$K_{V,2} = \left[7 \left(\frac{90^\circ}{\beta} \right) \left(\frac{V_2}{1 - V_2} \right)^{9.5\sigma^{1.2\left(\frac{\alpha}{90^\circ}\right)}} \right] - 1.5 \left(\frac{V_2}{1 - V_1} \right)^{1.4}, \quad (4.7)$$

provided that $0 \leq V_i \leq 0.30$. Eqs. (4.6) and (4.7) satisfy the following boundary conditions: $V_i = 0 \rightarrow K_{V,i} = 0$ and $V_i = 1 \rightarrow K_{V,i} = \infty$.

Figure 4.6 shows the factor $K_{V,1}$, i.e. top overlay, versus $V_1/(1 - V_1)$ and the corresponding power-law function for $\alpha = 15^\circ, 30^\circ, 45^\circ$, $\beta = 45^\circ, 90^\circ$, $\sigma = 0.04, 0.08, 0.17$ and $\varepsilon = 1$. These configurations are selected as an example to compare the predicted $K_{V,1}$ values using Eq. (4.6) with the experimental data. In general, the predicted $K_{V,1}$ match well with the measured $K_{V,1}$ values. Figure 4.6 also shows the effect of β on $K_{V,1}$. The $K_{V,1}$ values are generally higher for $\beta = 45^\circ$ than those for $\beta = 90^\circ$. Since ξ_B values are relatively small for $\beta = 45^\circ$ compared to $\beta = 90^\circ$, additional blockage by overlays has a stronger effect for $\beta = 45^\circ$.

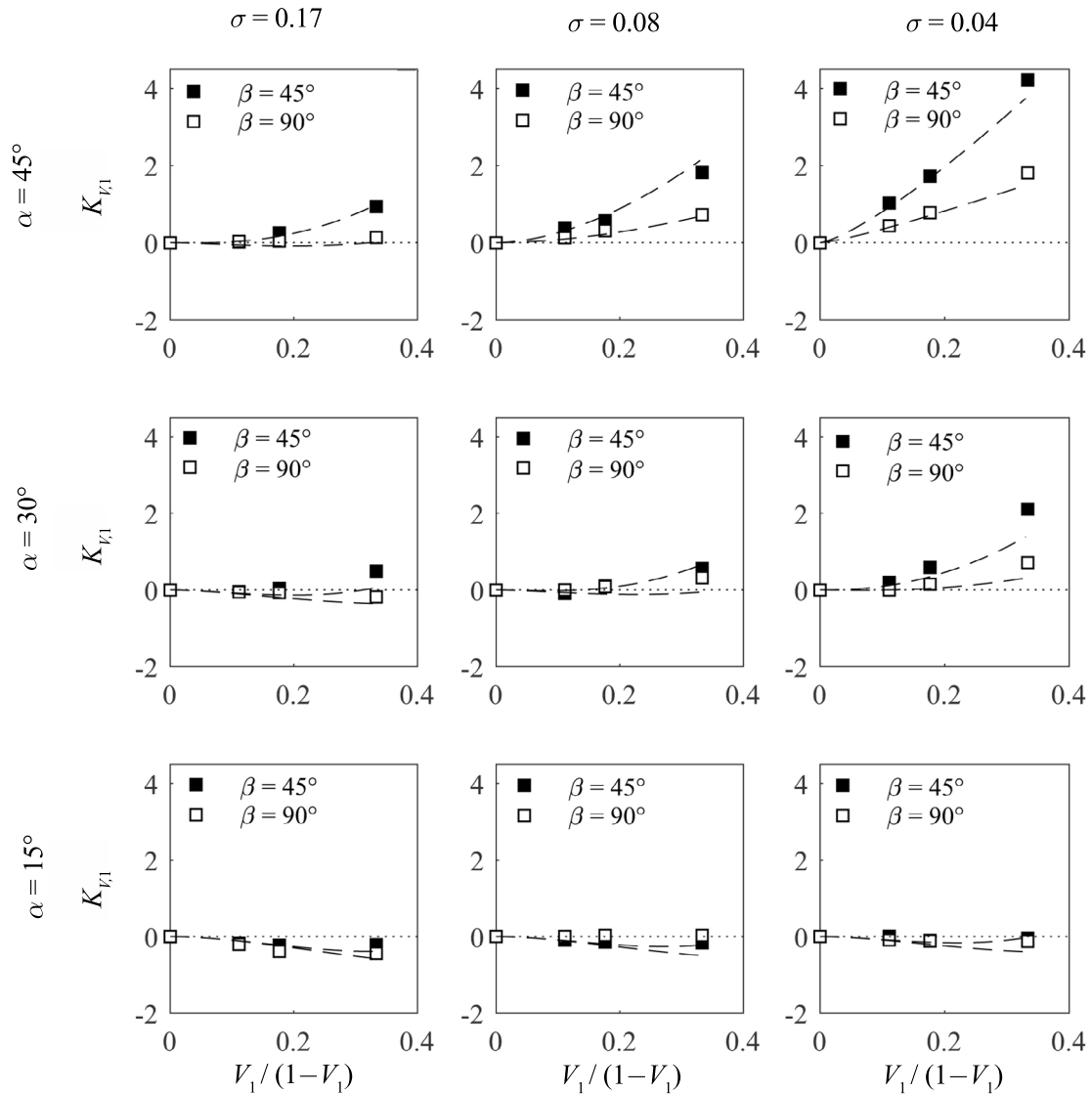


Figure 4.6 $K_{V,i}$ versus $V_1/(1 - V_1)$ for $\sigma = 0.17, 0.08$ and 0.04 , $\alpha = 45^\circ, 30^\circ, 15^\circ$, $\beta = 45^\circ, 90^\circ$ according to Eq. (4.6) (dashed lines) and experimental data (markers) for top overlays

In Figure 4.7, the predicted $K_{V,i,p}$ values are compared with the measured $K_{V,i,m}$ values for top, top and bottom, and bottom overlays. The predicted values match well with the meas-

ured values for most CBR configurations. The data points with a deviation of more than 30% correspond to CBR configurations with $\sigma = 0.04$, which are not recommended for high fish protection and guidance.

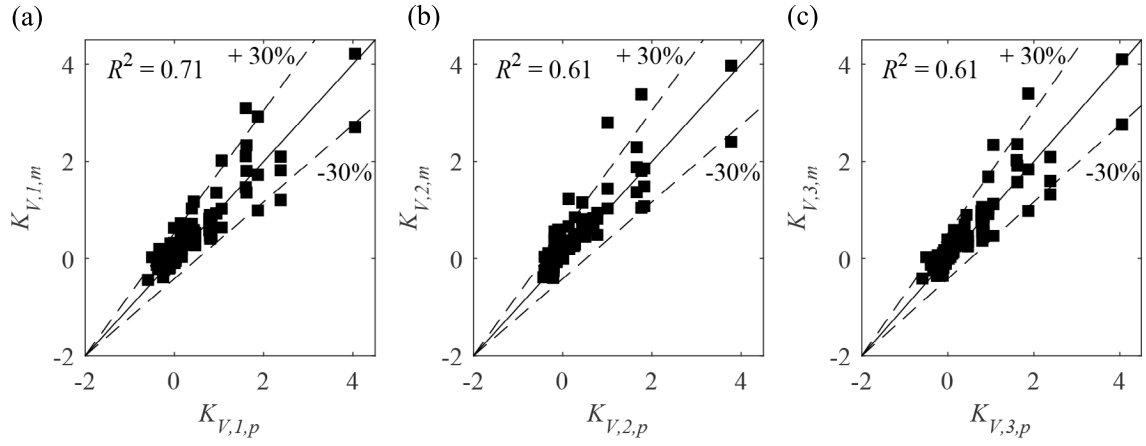


Figure 4.7 Measured versus predicted $K_{V,i}$ values for (a) top overlays, (b) top and bottom overlays, and (c) bottom overlays

4.1.5 Head loss factor of HPP layout geometry C_w

The effect of the HPP layout on the rack head loss was investigated by varying the approach flow channel width from $w_o = w_{ds}$ to $w_o = 1.5 \cdot w_{ds}$ and $w_o = 2.0 \cdot w_{ds}$. This effect was investigated for $\alpha = 15^\circ, 30^\circ, 45^\circ$, $\beta = 45^\circ, 90^\circ$, $\sigma = 0.04, 0.08, 0.17$, $h_v = 0, 0.2 \cdot h_o, 0.3 \cdot h_o$ and $\varepsilon = 1$. Figure 4.8a,b shows the measured rack head loss coefficients $\xi_{R,m}$ versus the flume downstream to upstream width ratio w_{ds}/w_o for all configurations without overlays. The ratio is $w_{ds}/w_o = 1$ for diversion-type HPPs and $w_{ds}/w_o < 1$ for block-type HPPs. The $\xi_{R,m}$ values decrease for decreasing w_{ds}/w_o ratios, i.e. for increasing upstream channel widths. The same trends are observed if overlays are installed at the CBRs. For HPP geometries with $w_o > w_{ds}$, a rotating flow develops in front of the weir and the approach flow vectors turn towards the rack, reducing the flow attack angle. The flow fields are described in detail in Section 4.2.5. The decreased flow deflection leads to lower head losses for the same CBR at a block-type HPP compared to a diversion-type HPP layout with $w_o = w_{ds}$. This effect is stronger for $\beta = 90^\circ$ compared to $\beta = 45^\circ$. The observed trend is contrary to the head loss coefficient of an abrupt contraction $\xi_c = 0.5 \cdot (1 - A_{ds}/A_o)^{0.75}$ described by Idelcik (2007). The ξ_c values increase for decreasing A_{ds}/A_o ratios because of the increasing flow separation and recirculation zone. These results indicate that the flow straightening effect of the curved bars is predominant compared to the flow separation caused by the abrupt contraction.

Figure 4.8c,d further shows the C_w values calculated as the ratio of the measured rack head loss $\xi_{R,m}$ for $w_{ds}/w_o < 1$ divided by $\xi_{R,m}$ for $w_{ds}/w_o = 1$. If $C_w > 1$, the total rack head loss increases, which is only the case for large bar spacings ($\sigma = 0.04$) and high α values, where the bars mounted in the rack act as single bars in the flow leading to a different flow-rack interaction with the sudden contraction as the dominant process. The results for CBRs with $\sigma = 0.04$ were therefore excluded from the fit. For smaller bar spacings ($\sigma = 0.08, 0.17$), the head losses are significantly reduced ($C_w < 1$) by 55 – 90% for $\beta = 45^\circ$ and by 25 – 80% for $\beta = 90^\circ$ with a block-type HPP layout as compared to the diversion-type HPP layout with

$$C_w = \left(\frac{w_{ds}}{w_o} \right)^{2.3 \left(1 - \frac{\alpha}{90^\circ} - V_i \right)}, \quad (4.8)$$

with $R^2 = 0.81$, provided that $0.5 \leq w_{ds}/w_o \leq 1$. Although for $w_o \gg w_{ds} \rightarrow C_w = 0$ and $\xi_R = 0$ according to Eq. (4.8), it is more likely that C_w converges to a certain value. More experiments with $w_{ds}/w_o < 0.5$ would be necessary to assess this value.

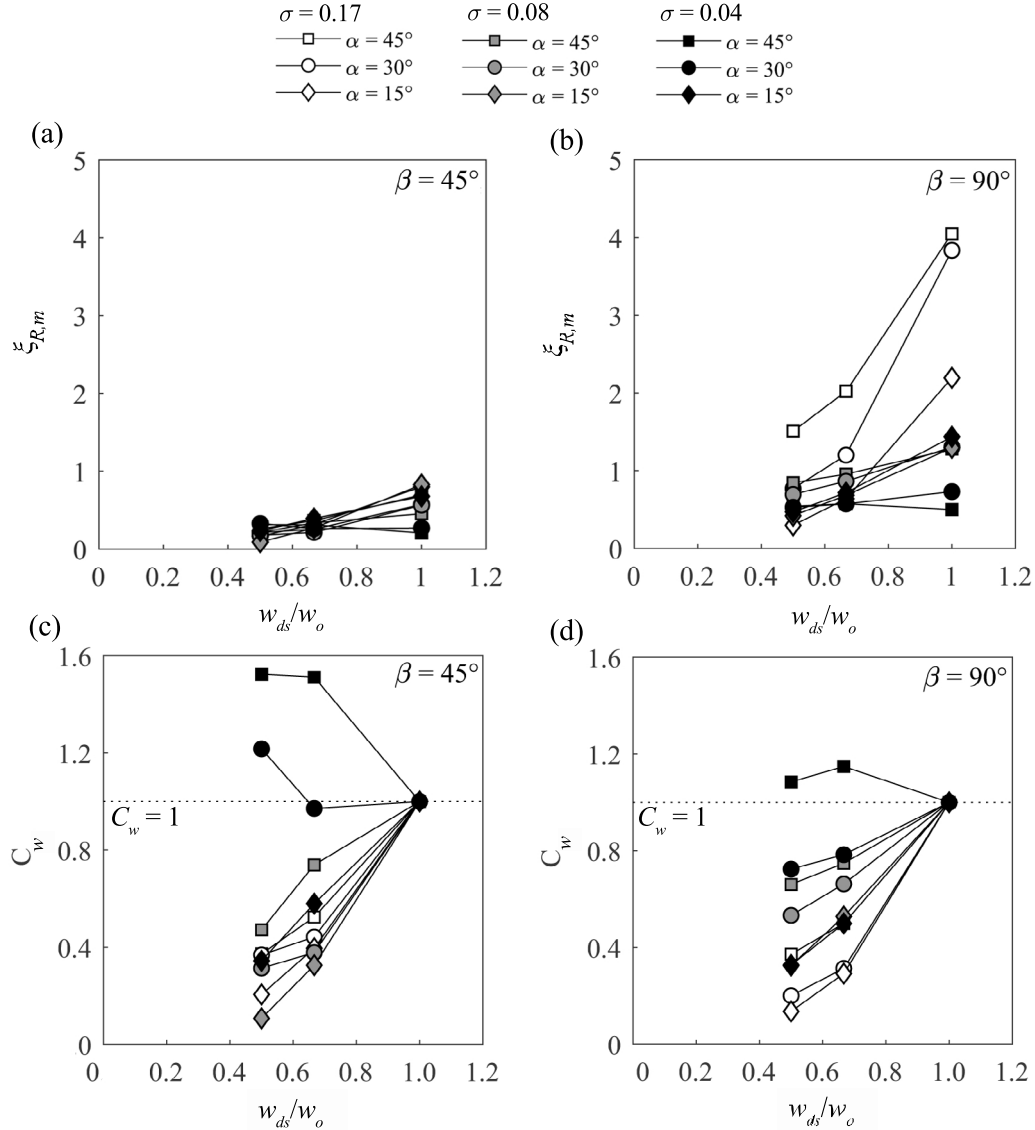


Figure 4.8 Measured rack head loss $\xi_{R,m}$ and HPP layout head loss factor C_w versus w_{ds}/w_o for (a), (c) $\beta = 45^\circ$ and (b), (d) $\beta = 90^\circ$

4.1.6 Application of total head loss formula

The head loss estimate based on Eq. (4.1) includes errors associated with the accuracy of instruments as well as assumptions made in the data analysis. The error propagation according to Eqs. (3.4) and (3.5) yields an absolute error of ~ 1.8 mm for the head loss measurements due to instrument and measurement accuracy, which corresponds to an absolute error for the rack head loss coefficient of $e_{\xi_R} = 0.14$. Figure 4.9a shows all measured head loss coefficients $\xi_{R,m}$ versus the corresponding predicted values $\xi_{R,p}$ using Eq. (4.1). The data include all rack configurations described above and listed in Table 3.3. Note that this validation is based on the data which were used to derive the equation, thus no independent data was used. The computed values $\xi_{R,p}$ are in good accordance with the measured values $\xi_{R,m}$ (Fig-

ure 4.9a). The coefficient of determination for the best fit is $R^2 = 0.92$. Figure 4.9b shows the prediction error (PE) due to assumptions made in the data analysis and the fitting process, which can reach values up to 50% for $\xi_{R,p} < 2$. For $\xi_{R,p} < 0.28$, the relative error due to the measurement accuracy ($e_{\xi_R} = 0.14$) is higher than 50%. However, this is only the case for CBR configurations with very large bar spacings ($\sigma = 0.04$), which are not recommended for fish protection (cf. Chapter 9). Therefore, to apply Eq. (4.1), errors of $\pm 50\%$, 30% and 15% should be accounted for head loss coefficients $\xi_{R,p} < 2$, < 4 and > 4 , respectively. The 20 CBR configurations with $PE > 50\%$ ($= 5.5\%$ out of a total of 360 configurations) are marked in grey in Figure 4.9b. In 14 cases, the PE is slightly higher than 50% for very small rack head losses ($\xi_{R,p} < 1$), where measurement errors might increase the total error. For the other 6 cases with $\xi_{R,p} > 1$, the rack head loss coefficient is overpredicted by more than 50% meaning that the head losses are estimated conservatively.

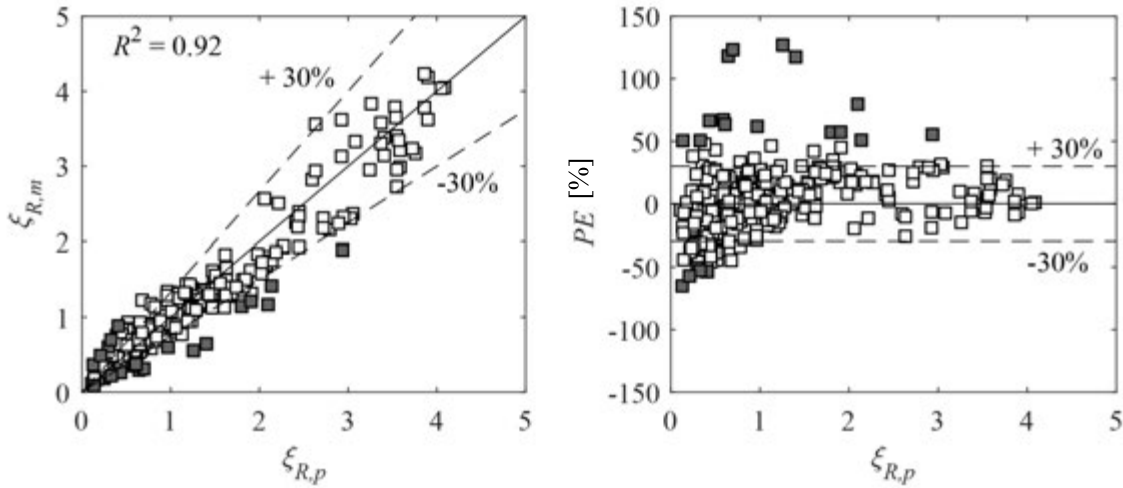


Figure 4.9 Comparison of (a) measured head loss coefficients $\xi_{R,m}$ with corresponding prediction $\xi_{R,p}$ for all rack configurations (b) prediction error $PE = (\xi_{R,p} - \xi_{R,m})/\xi_{R,m} \times 100$ [%] versus $\xi_{R,p}$

The effect of horizontal spacers or tie bars on the head losses was not included in the above depicted rack head loss analysis but is discussed in Chapter 9.

4.2 Flow fields at curved-bar racks

Parts of this subsection have been published in Beck et al. (2019b): Hydraulic performance of fish guidance structures with curved bars - Part 2: Flow fields, Journal of Hydraulic Research.

4.2.1 Up- and downstream flow fields

Figures 4.10 and 4.11 show the time-averaged longitudinal and transversal flow velocities U and V normalised by $U_{th} = 0.5$ m/s (model value), respectively, for the basic rack configurations A1-A6 measured at $z/h_o = 0.5$. The rack starts affecting the flow distribution from approx. $x/h_o = 1.5$ upstream of the upstream (u/s) rack end. Starting at the u/s rack end ($x/h_o = -1.25, -2.16, -4.66$ for $\alpha = 45^\circ, 30^\circ, 15^\circ$, respectively), the flow velocities gradually increase towards the d/s rack end (Figure 4.10). Therefore, lower rack angles α lead to a more gradual velocity increase and thus a lower spatial velocity gradient (SVG, cf. section 4.2.2). The projected area of the bars in the flow direction decreases with decreasing β values, resulting in a mild flow deflection and a more gradual velocity increase along the rack with lower U_{max}/U_o at the d/s rack end for $\beta = 45^\circ$ (A1, A3, A5) compared to $\beta = 90^\circ$ (A2, A4, A6) (Table 4.1). For $\beta = 45^\circ$, lower rack angles α lead to slightly higher U_{max}/U_o values because of the increased overlapping of the curved bars in flow direction. This overlap is highest for $\alpha = 15^\circ$, which is why the application of overlays improves the flow distribution through the rack and decrease the head losses (cf. Figure 4.5c). Table 4.1 lists the U_{max}/U_o values for all basic CBR configurations and the overlay configurations, which are further discussed in section 4.2.3. The flow deflection along the rack causes positive transverse velocities V along the upstream side of the rack for all rack configurations (Figure 4.11). Although V decreases towards the d/s rack end, it remains positive. For $\beta = 90^\circ$, the more pronounced upstream flow deflection leads to negative transverse flow velocities of up to $-1.23 \cdot U_o$, $-0.8 \cdot U_o$ and $-0.44 \cdot U_o$ for $\alpha = 45^\circ, 30^\circ, 15^\circ$, respectively, and highly asymmetric flow distribution with a return flow zone downstream of the rack, which extends up to the end of the experimental flume (Figure 4.11b,d,f). The more mildly curved bars $\beta = 45^\circ$ cause a strong flow straightening effect resulting in a quasi-symmetrical velocity distribution downstream of the rack with only a slight decrease of velocities close to the right channel wall (Figure 4.11a,c,e). The effect of α , β and overlays on the admission flow is further discussed in Section 4.2.4 and shown in Table 4.1.

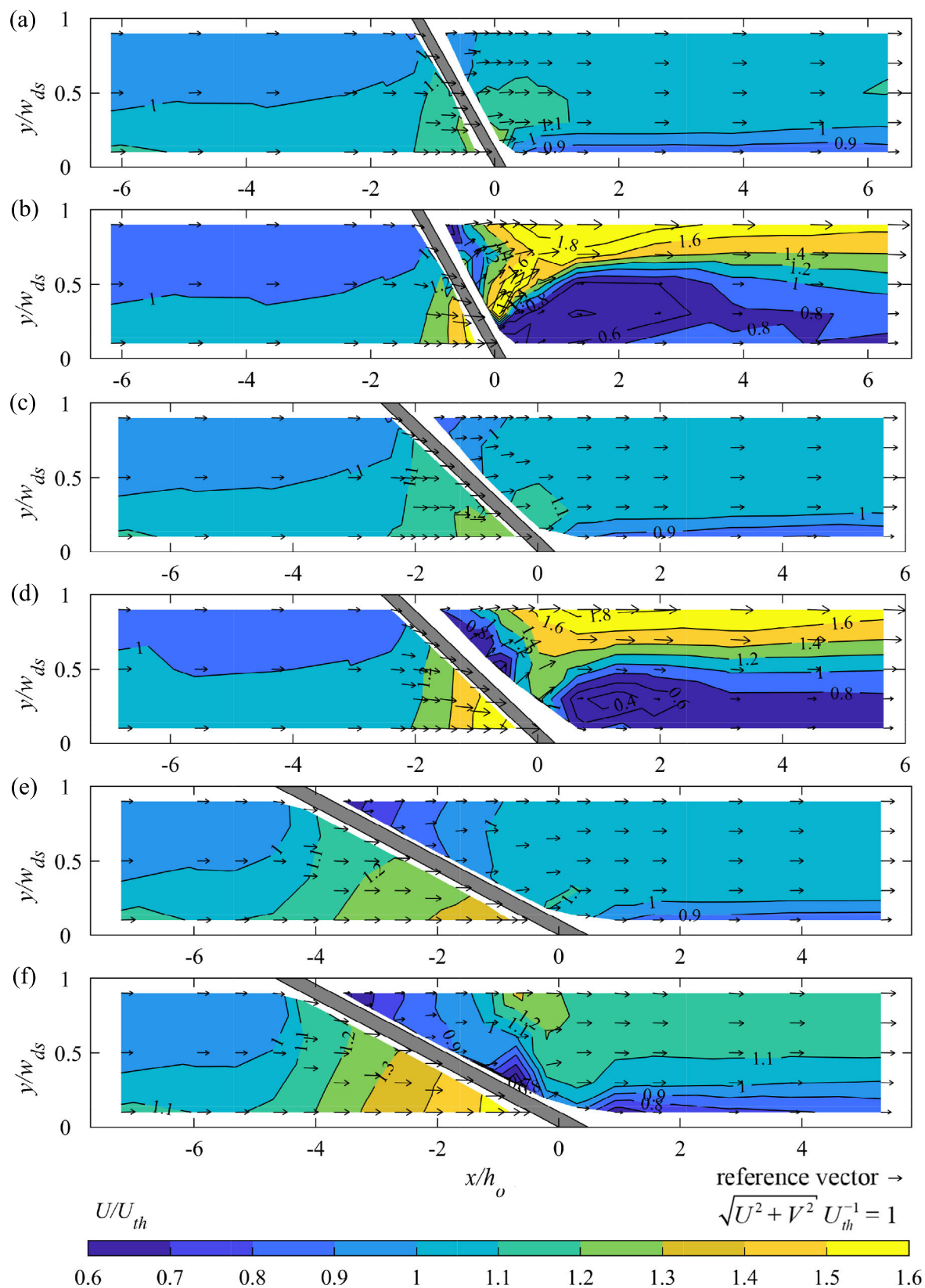


Figure 4.10 Longitudinal flow velocities U/U_{th} of CBR configurations A1-A6 (a)-(f) measured at $z/h_o = 0.5$; the direction of the resulting velocity vector at each measurement point and the contour values are indicated

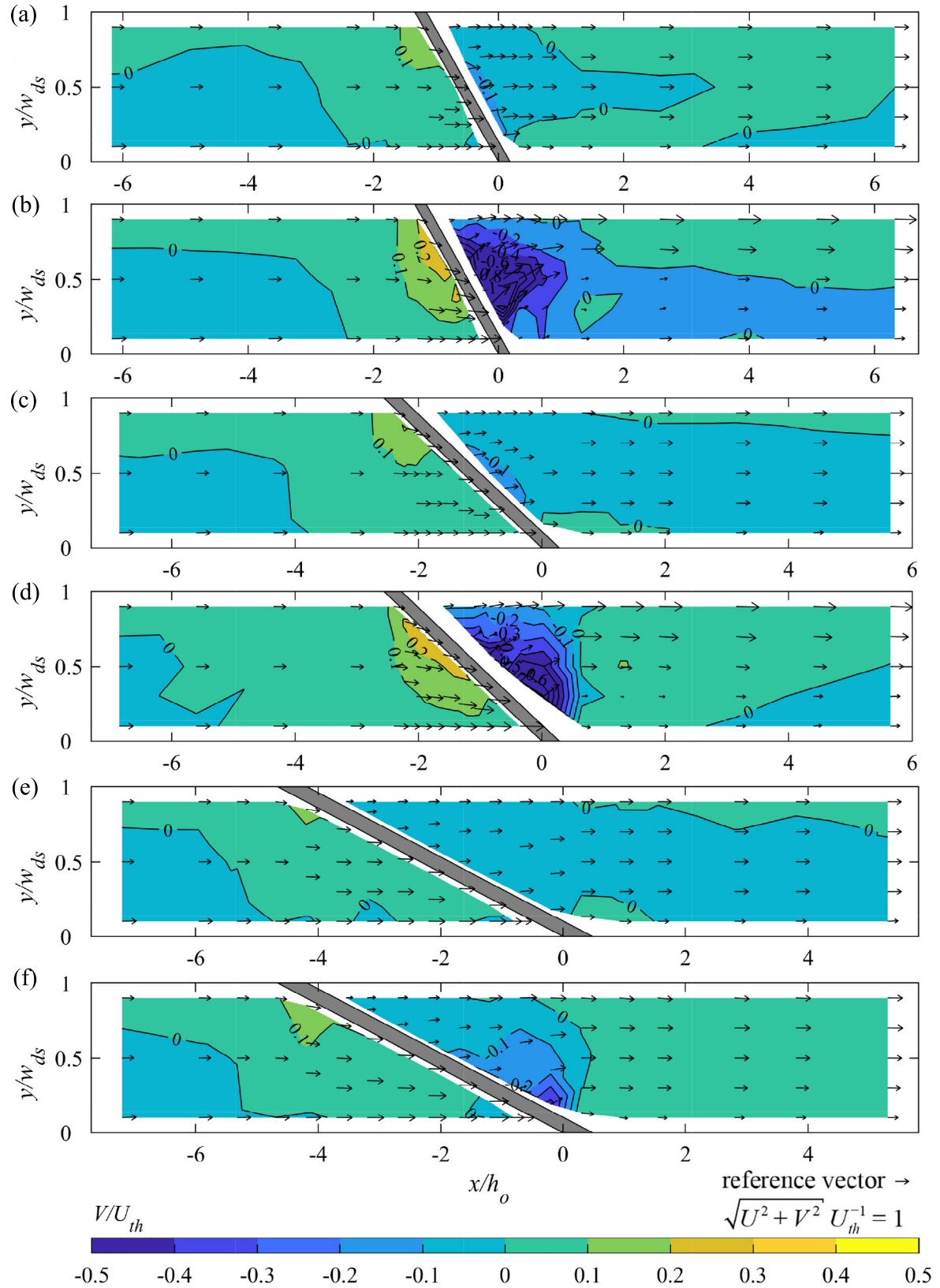


Figure 4.11 Transversal flow velocities V/U_{th} of CBR configurations A1-A6 (a)-(f) measured at $z/h_o = 0.5$; the direction of the resulting velocity vector at each measurement point and the contour values are indicated

4.2.2 Flow field in the rack-parallel cross section

Figure 4.12 shows the velocity components V_n , V_p and V_z normalized with $U_{th} = 0.5$ m/s (model value) measured at a perpendicular u/s distance of 50 mm (prototype value) along the rack for A1-A6. The u/s rack end is located at $y'/l_R = 1$, the d/s rack end at $y'/l_R = 0$. Since the trends are similar at different measuring planes, only the results at $z/h_o = 0.5$ are shown in Figure 4.12. The V_n/U_{th} and V_p/U_{th} values increase along the rack for all CBRs with the highest values at the d/s rack end ($y'/l_R = 0.1$), and V_p being the dominant component. The streamwise velocity increase towards the d/s rack end is less pronounced for lower α values leading to lower V_n/U_{th} values. The increase rate of V_n/U_{th} along the rack also becomes significantly lower with decreasing α and β values (Figure 4.12a) indicating less flow deflection towards the d/s rack end and a more uniform flow distribution along the rack for lower α and β values. The dashed line in Figure 4.12a marks the criterion $V_n \leq 0.5$ m/s for $U_{th} = 0.5$ m/s, hence this threshold is only exceeded at the d/s rack end for A2. For higher U_{th} values, the dashed line is shifted to the left. The parallel velocity components V_p/U_{th} generally increase with decreasing α values. The highest V_p/U_{th} values are measured for A4 (Figure 4.12b). The vertical velocity components V_z/U_{th} are almost zero along the rack. Slightly negative V_z/U_{th} values are measured at the d/s rack end. The fish guidance capacity $FGC = V_p/V_n$ is above 1 for all CBR configurations meeting the criterion $FGC \geq 1$ proposed by Courret and Larinier (2008) (Figure 4.12c). The FGC decreases along the rack indicating the strongest flow deflection towards the opposite channel wall at the u/s rack end and more flow being diverted through the rack to the downstream channel at the d/s rack end. Lower α values lead to a higher FGC due to the geometrical decomposition of V_p and V_n . Furthermore, stronger flow deflection towards the d/s rack end for higher α and β values leads to higher V_n values at the d/s rack end and hence lower V_p/V_n ratios.

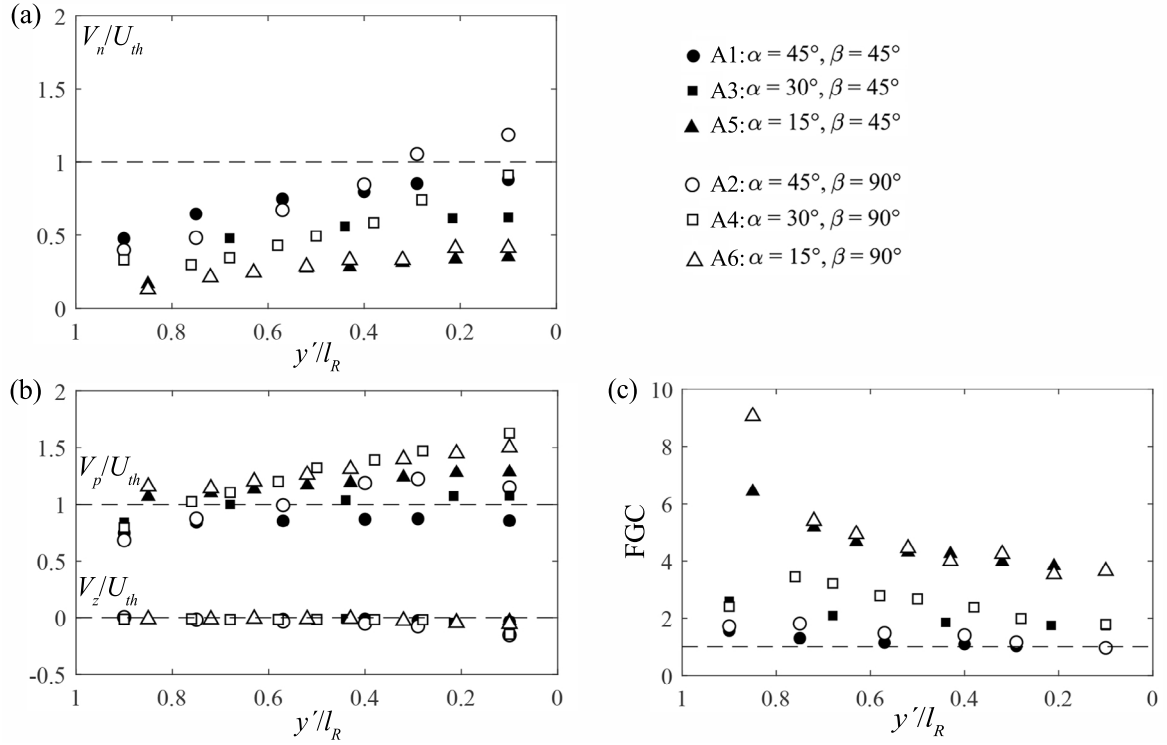


Figure 4.12 Comparison of velocity components (a) normal to the rack (V_n) normalized with U_{th} , (b) vertical (V_z) and parallel (V_p) to the rack normalized with U_{th} and (c) the $FGC = V_p/V_n$ for A1-A6 measured at $z/h_o = 0.5$

4.2.3 Hydraulics of CBRs with overlays

Different blockage ratios of top, top & bottom and bottom overlays were investigated for CBR configuration A3 (Tests B1- B6). Figure 4.13 shows the time-averaged longitudinal and transversal flow velocities U and V normalized by U_{th} for A3 without overlay and B6 (15% bottom overlay) measured close to the flume bottom at $z/h_o = 0.075$. The bottom overlay completely deflects the flow towards the d/s rack end leading to constant positive V values along the entire rack (Figure 4.13d) compared to the no-overlay configuration A3 (Figure 4.13c). At this flow depth, no flow diversion through the CBR occurs for B6 and hence the risk of fish entrainment near the bed is minimized. The downstream flow field is symmetric from $x/h_o \geq 0.2$ for A3 and from $x/h_o \geq 2$ for B6.

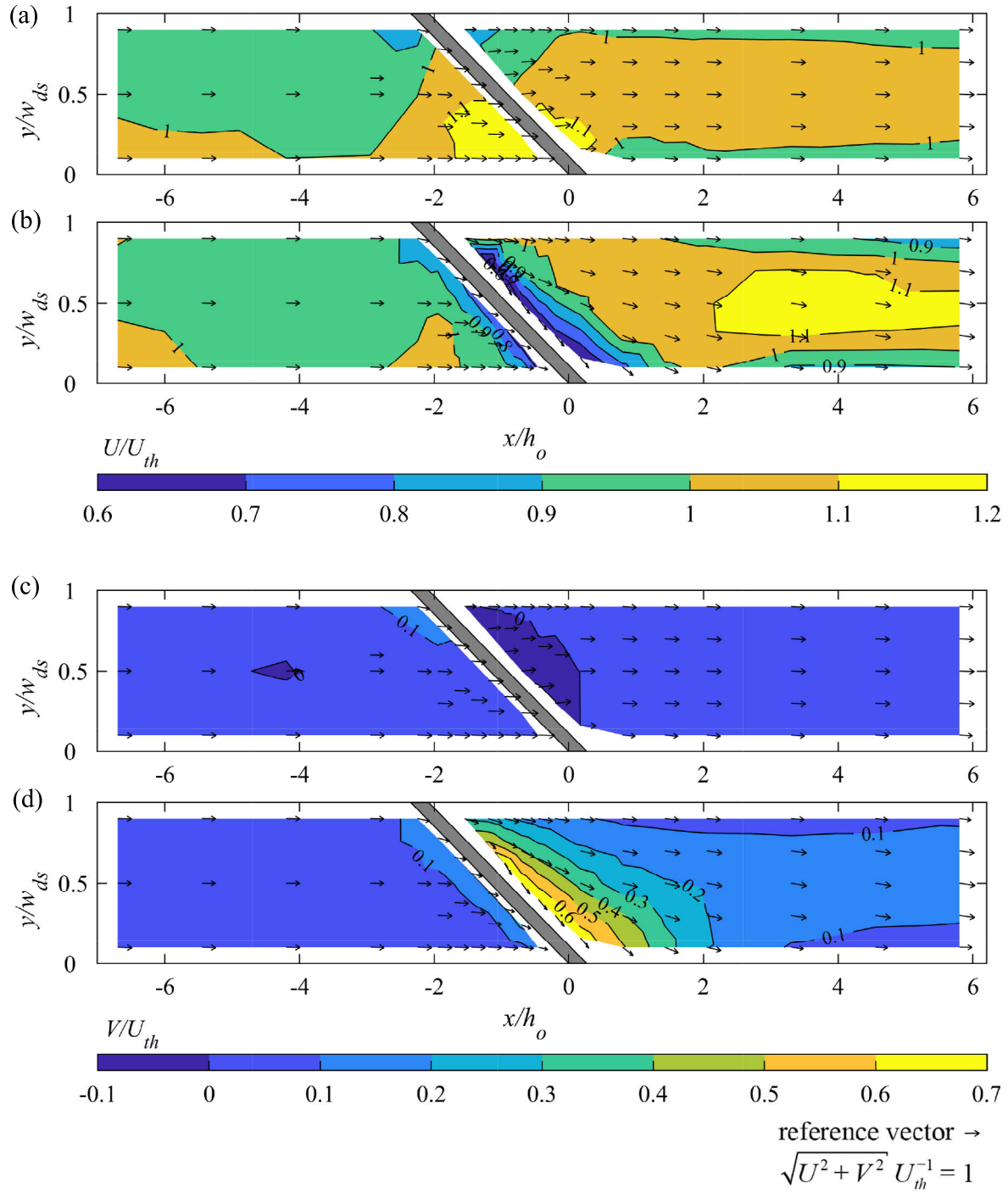


Figure 4.13 Flow field of CBR configuration with $\alpha = 30^\circ$, $\beta = 45^\circ$, $\sigma = 0.17$ (a), (c) without overlay (A3) and (b), (d) with a bottom overlay $h_{Bo} = 0.15 \cdot h_o$ (B6), measured at $z/h_o = 0.075$. The resulting velocity vector at each measurement point and the contour values are indicated for (a), (b) longitudinal velocities U/U_{th} and (c), (d) transversal velocities V/U_{th}

Figure 4.14 shows the contour plot of the FGC in the rack-parallel cross section with the resulting velocity vectors of parallel and vertical velocities $V_{p,z}/U_{th}$ for A3, B4, B5 and B6.

For A3, a gradual decrease of FGC along the rack is observed. With a top overlay (B4), the FGC is high in front of the overlay with a uniform distribution along the rack (Figure 4.14b). Minimum FGC values for B4 are lower compared to A3 and are shifted from the d/s rack end towards the rack centre. Analogous effects are observed for a bottom overlay (B6). With a top and a bottom overlay combined (B5), the FGC is highest in front of both overlays. The resulting velocity vectors $V_{p,z}/U_{th}$ are parallel for A3 indicating low V_z values. The $V_{p,z}/U_{th}$ vectors in front of top or bottom overlay show that the flow is diverted downwards or upwards, respectively, leading to higher velocities between the overlays, hence locally reducing the FGC. Despite this fact, the FGC is still higher than 1 for all rack configurations.

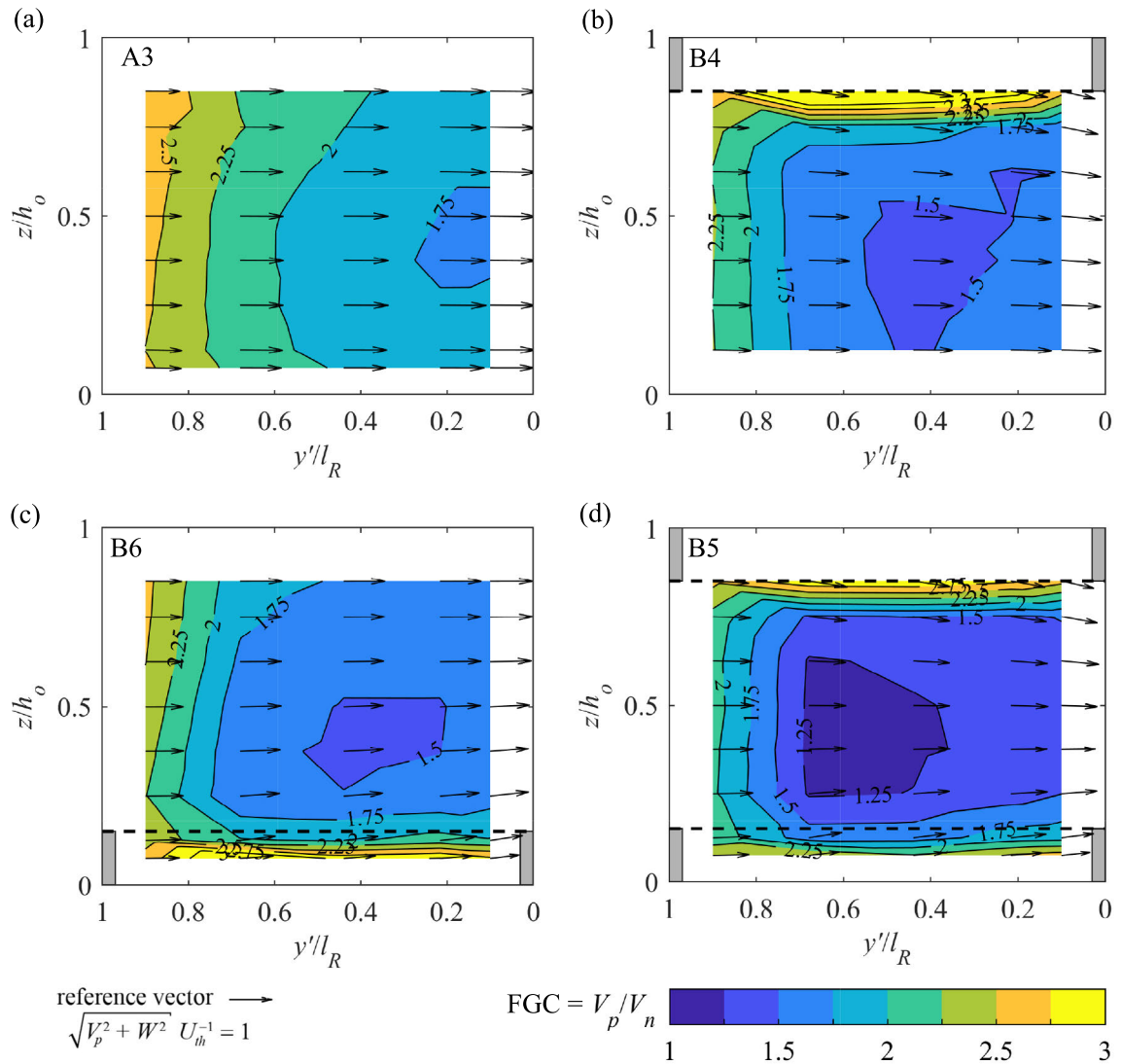


Figure 4.14 Contour plots of the FGC in the rack-parallel cross section for (a) A3: no overlay (b) B4: 15% top overlay, (c) B6: 15% bottom overlay and (d) B5: 15% top and 15% bottom overlay; the overlay dimensions are indicated; the positions $y'/l_R = 1.0$ and 0.0 mark the u/s rack end and the d/s rack end, respectively

4.2.4 Downstream flow field and turbine admission flow

Figure 4.15 shows the effect of β and top & bottom overlay on the flow distribution at $x/h_o = 3.5$ downstream of the CBR with contour plots of the longitudinal velocity U normalized with U_{th} for A3, B4, B5 and B6. Without overlays (A3), quasi-symmetrical downstream flow is seen and the admission discharge criteria by Godde (1994) is fulfilled (Figure 4.15a). Note that the velocity vectors are small, thus the flow is uniform, and transversal and vertical velocities are negligible.

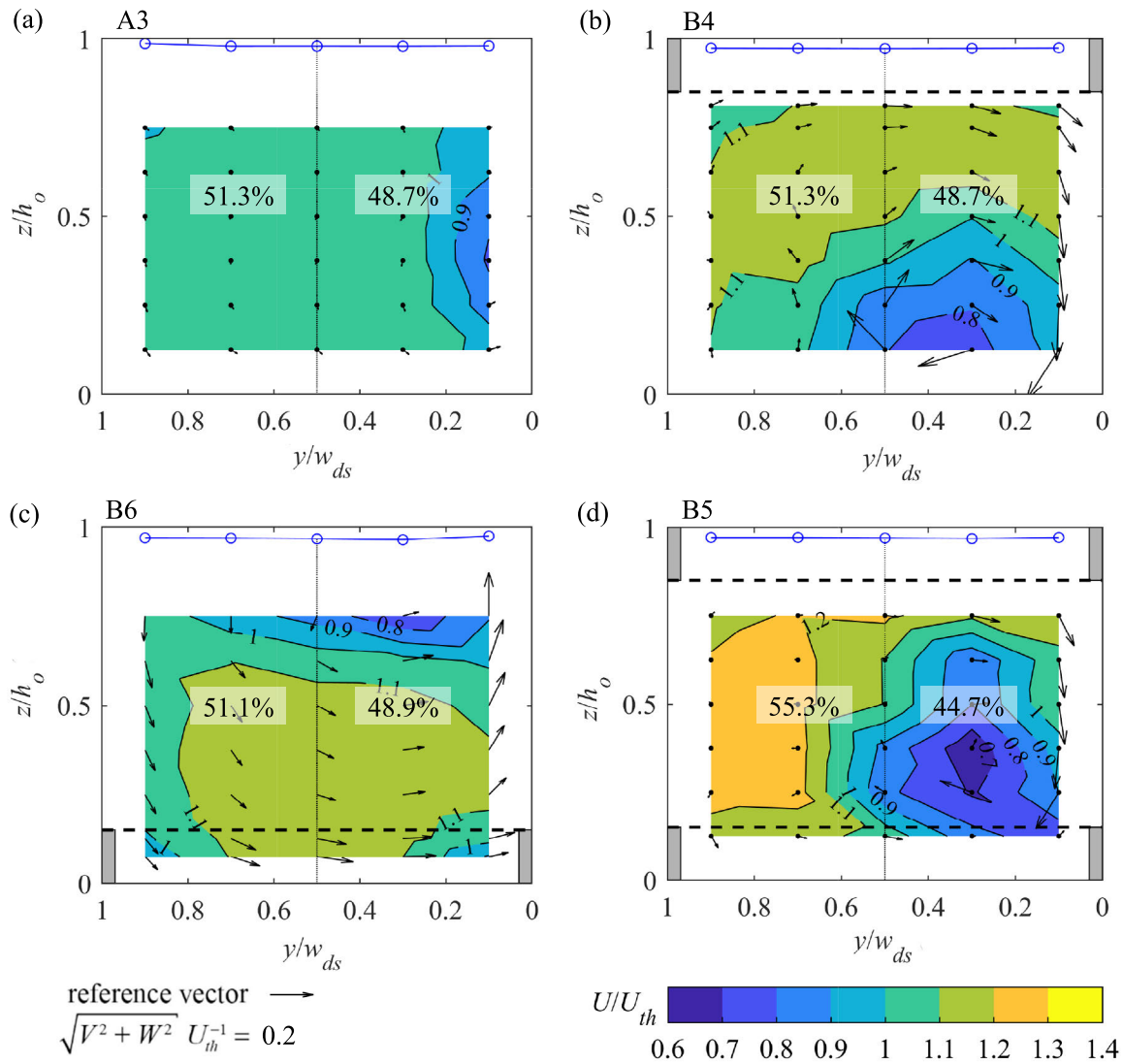


Figure 4.15 Contour plots of normalised flow velocities in the downstream cross section $x/h_o = 3.5$ for (a) A3: no overlay (b) B4: 15% top overlay, (c) B6: 15% bottom overlay and (d) B5: 15% top and 15% bottom overlay; the overlay dimensions and the flow depth are indicated; the discharge share is given in each channel half

The application of overlays leads to a flow diversion along the overlay with α and flow downwelling or upwelling under or over the overlay, respectively. This causes significant

spiral flow downstream of the CBR, which is indicated by the velocity vectors in Figures 4.15b-d. With a top overlay, a clockwise spiral flow develops with locally reduced flow velocities near the flume bottom at $x/h_o = 3.5$ (Figure 4.15b). Conversely, with a bottom overlay, a counter-clockwise spiral flow develops with locally reduced flow velocities near the water surface (Figure 4.15c). In both cases B4 and B6, the difference between the relative discharges in the left and the right channel half is far below 5% ($\Delta Q/Q_t = |Q_{\text{left}} - Q_{\text{right}}| / Q_t \leq 5\%$) with $\Delta Q/Q_t = 2.6\%$ and $\Delta Q/Q_t = 2.2\%$, respectively. With a combination of top and bottom overlay (B5), however, two counter-rotating vortices develop and the flow becomes more asymmetric with $\Delta Q/Q_t = 10.6\%$ (Figure 4.15d). The occurrence of a distinct spiral flow with the application of overlays was confirmed with a numerical simulation of this setup described in Chapter 5. Note that the difference between the downstream water levels of A3 and B4-B6 is small, indicating only a small increase of head losses with additional overlays. Table 4.1 lists the resulting head loss coefficients and the admission flow quality for all tested CBR configurations without overlays (A1-A6) and with overlays (B1-B6).

Table 4.1 Hydraulic parameters and turbine admission flow distribution measured at $x/h_o = 3.5$; it is indicated whether the criterion proposed by Godde (1994) is met (+) or not met (–)

Tests	α [°]	β [°]	ξ_R [–]	h_v [m]	U_{\max}/U_o [–]	Discharge per intake half [%]	$\Delta Q/Q_t$ [%]	
A1	45	45	0.70	0	1.25	52.1 / 47.9	4.2	+
A2		90	4.05	0	1.66	64.4 / 35.6	28.8	–
A3	30	45	0.57	0	1.27	51.3 / 48.7	2.6	+
A4		90	3.83	0	1.87	66.1 / 33.9	32.2	–
A5	15	45	0.80	0	1.36	50.5 / 49.5	1.0	+
A6		90	2.19	0	1.56	54.9 / 45.1	9.8	–
B1			0.55	$h_{To} = 0.10 \cdot h_o$	n/a	51.8 / 48.2	3.6	+
B2			0.58	$h_{To} = 0.10 \cdot h_o$ $h_{Bo} = 0.10 \cdot h_o$	n/a	53.6 / 46.4	7.2	–
B3	30	45	0.67	$h_{Bo} = 0.10 \cdot h_o$	n/a	50.3 / 49.7	0.6	+
B4			0.60	$h_{To} = 0.15 \cdot h_o$	1.13	51.3 / 48.7	2.6	+
B5			0.76	$h_{To} = 0.15 \cdot h_o$ $h_{Bo} = 0.15 \cdot h_o$	1.13	55.3 / 44.7	10.6	–
B6			0.64	$h_{Bo} = 0.15 \cdot h_o$	1.17	51.1 / 48.9	2.2	+

4.2.5 Effect of the HPP layout on the flow field

Figure 4.16 shows the time-averaged longitudinal velocities U normalized by U_{th} for the block-type HPP layout with $w_{ds}/w_o = 0.5$ without rack presence and with CBR configuration $\alpha = 30^\circ$, $\beta = 45^\circ$, $\sigma = 0.17$ (C3) measured at $z/h_o = 0.5$. Without a rack installed, the abrupt contraction leads to flow separation and asymmetrical downstream flow conditions (Figure 4.16a). This flow separation is suppressed when a CBR is installed due to the flow straightening effect of the curved bars, leading to a quasi-symmetric downstream flow field (Figure 4.16b). The weir blocking leads to a backwater rise and rotating flow in front of the closed weir. As a result, the approach flow angle changes along the CBR. At the u/s rack end, the flow is parallel to the channel walls, thus frontally approaching the rack. At the d/s rack end, however, the flow approaches the rack perpendicularly, which means that V_n values are increased compared to V_p values, decreasing the FGC. To mitigate this issue, a separation pier was installed to reorient the flow parallel to the channel walls (Figure 4.16c). The effect on the FGC is discussed further below and shown in Figure 4.18. Figure 4.16d shows the flow field of the same CBR configuration but with a bottom and a top overlay with $h_v = h_{To} + h_{Bo} = 0.15 \cdot h_o + 0.15 \cdot h_o = 0.30 \cdot h_o$. At $z/h_o = 0.5$, the upstream flow field remains the same as for C3. The flow field in the downstream channel, however, is asymmetric with increased flow velocities along the left channel wall due to the spiral flow caused by the overlays. Table 4.2 lists the resulting head loss coefficients and the admission flow quality for the CBR configurations tested at a block-type HPP layout.

The FGC is plotted for all basic rack configurations C1-C6 in Figure 4.17. The areas where $FGC = V_p/V_n < 1$ are plotted in greyscale colours. Since V_p and V_n are computed with the corresponding rack angle α , the FGC values are higher in the approach flow for $\alpha = 15^\circ$ than for $\alpha = 45^\circ$. Due to the rotating flow in front of the weir, the FGC is less than 1 at the d/s rack end for all rack configurations. Since the flow is diverted more strongly along the rack for $\beta = 90^\circ$ compared to $\beta = 45^\circ$, the FGC is larger than 1 further along the rack. At the d/s rack end, however, the flow diversion from the weir prevails and decreases the FGC.

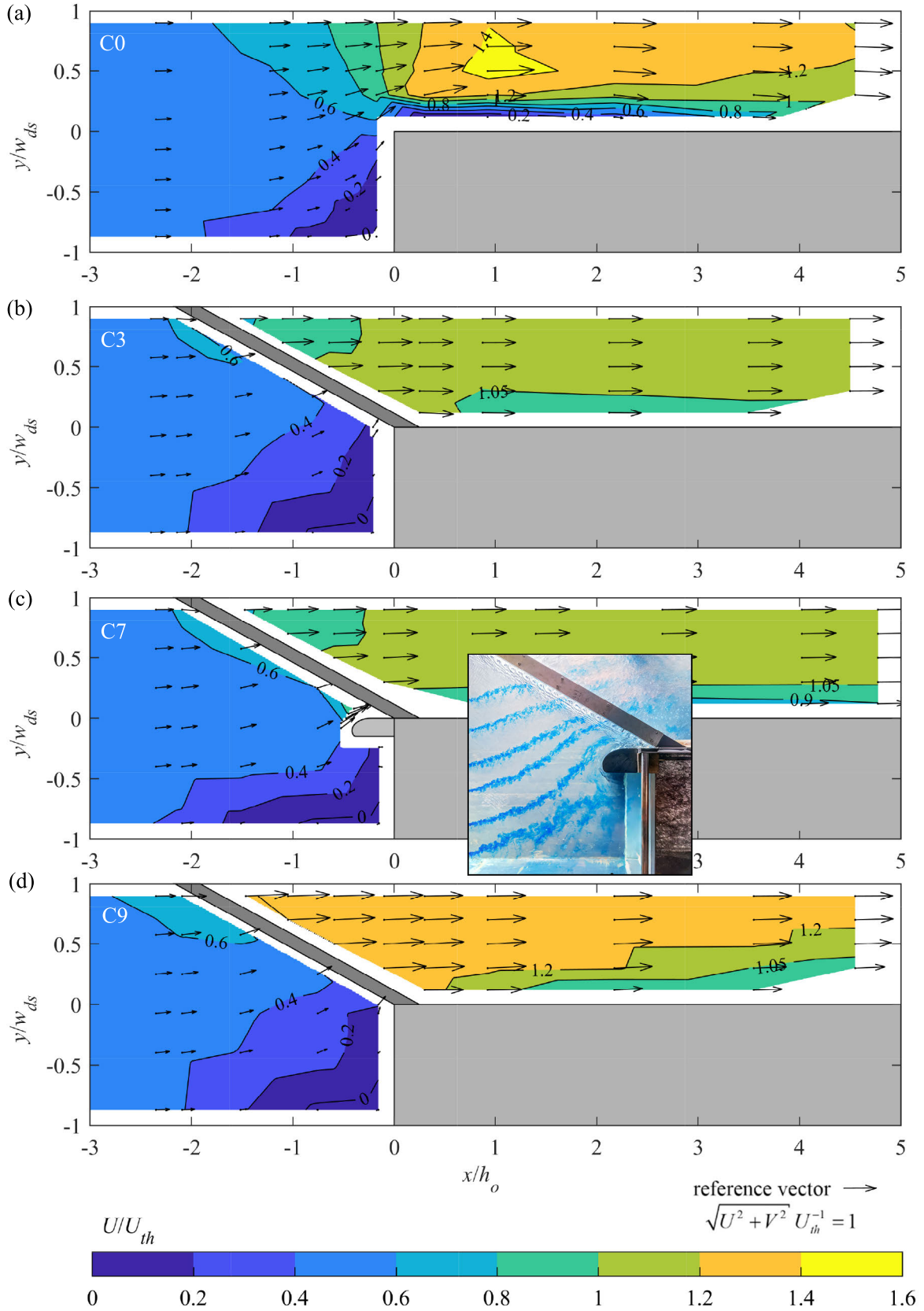


Figure 4.16 Longitudinal flow velocities U normalised with U_{th} for the block-type HPP layout with $w_{ds}/w_o = 0.5$ measured at $z/h_o = 0.5$; (a) C0: no rack (contraction head loss coefficient $\xi_c = 0.29$), (b) C3: CBR configuration with $\alpha = 30^\circ$, $\beta = 45^\circ$, $\sigma = 0.17$ ($\xi_R = 0.21$), (c) C7: CBR C3 and a separating pier, the flow field around the pier is visualised with blue dye, and (d) C9: C3 with $h_v = h_{To} + h_{Bo} = 0.3 \cdot h_o$ ($\xi_R = 0.56$)

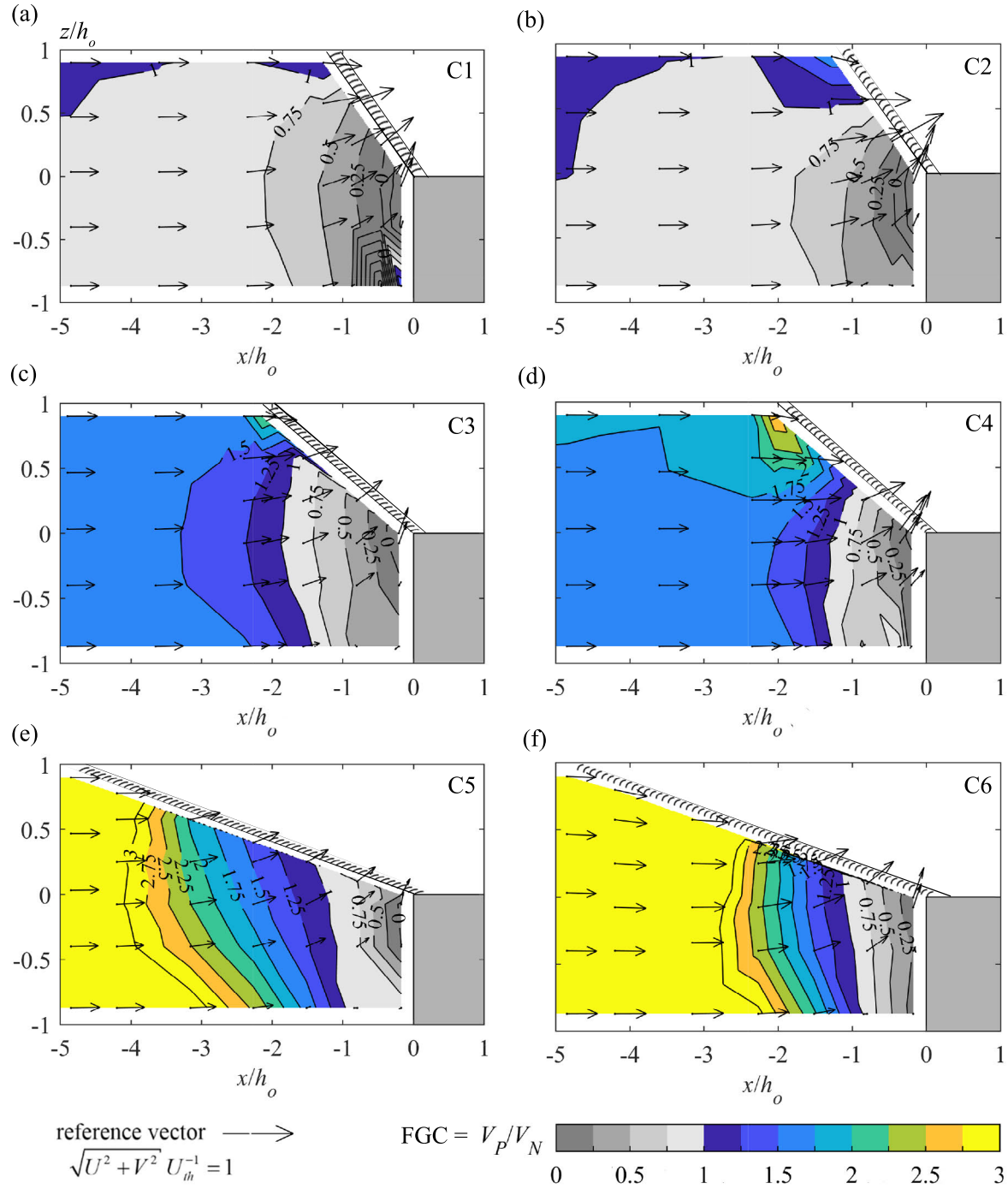


Figure 4.17 Fish guidance capacity (FGC) measured at $z/h_o = 0.5$ for the six basic rack configurations C1-C6 (a)-(f), grayscale colours mark the areas where the FGC is lower than 1

Three different mitigation measures were tested to improve the FGC for a block-type HPP layout: (I) the installation of top and bottom overlays (C9), (II) weir overflow of $Q_w = 0.4 \cdot Q_o$ (C8), and (III) the installation of a separating pier (C7). Figure 4.18 shows the flow field at the rack-parallel section 50 mm (prototype value) upstream of the CBR configuration C3 and the three mitigation measures (C7-C9). Although the FGC is high at the u/s rack end, it

decreases quickly for C3 and drops below 1 after one third of the rack length ($y'/l_R = 0.65$) (Figure 4.18a). The overlays do not improve the FGC in the area where measurements were possible. Conversely, the flow turning from the weir is guided along the bottom overlay in upstream direction, leading to negative V_p and thus negative FGC values (Figure 4.18b). If the weir is lowered and 40% of the total inflow is discharged over the weir, while 60% flow through the rack, the flow field along the rack is highly affected. As shown in Figure 4.18c, the flow component towards the weir V_p and thus the FGC increases and is above 1 for the upper half of the flow cross section. The FGC is low on the bottom of the d/s rack end, however. Finally, the installation of a separating pier improves the FGC compared to C3 with FGC values only slightly below 1 (Figure 4.18d). These results show that it is challenging to reach high FGC values at CBRs at block-type HPPs. Geometrical and operational aspects, which may both affect the approach flow towards a CBR, need to be carefully considered for the optimal CBR configuration and positioning choice. Feigenwinter *et al.* (2019) describe a possible method to approach this issue with CFD modelling.

Table 4.2 Hydraulic parameters and turbine admission flow distribution measured at $x/h_o = 3.5$ for the block-type HPP layout. It is indicated whether the criterion proposed by Godde (1994) is fully met (+) or not met (–)

Tests	α [°]	β [°]	ξ_R [–]	h_v [m]	Discharge per intake half [%]	$\Delta Q/Q_t$ [%]	
C0	no rack		0.29	–	56.6 / 43.4	13.2	–
C1	45	45	0.26	–	50.7 / 49.3	1.4	+
C2		90	1.50	–	54.6 / 45.4	9.2	–
C3	30	45	0.21	–	51.0 / 49.0	2.0	+
C4		90	0.77	–	59.4 / 40.6	18.8	–
C5	15	45	0.16	–	51.0 / 49.0	2.0	+
C6		90	0.30	–	51.9 / 48.1	3.8	+
C7	30	45	N/A	–	52.0 / 48.0	4.0	+
C9	30	45	0.56	$h_{To} = 0.15 \cdot h_o$ $h_{Bo} = 0.15 \cdot h_o$	55.7 / 44.3	11.4	–

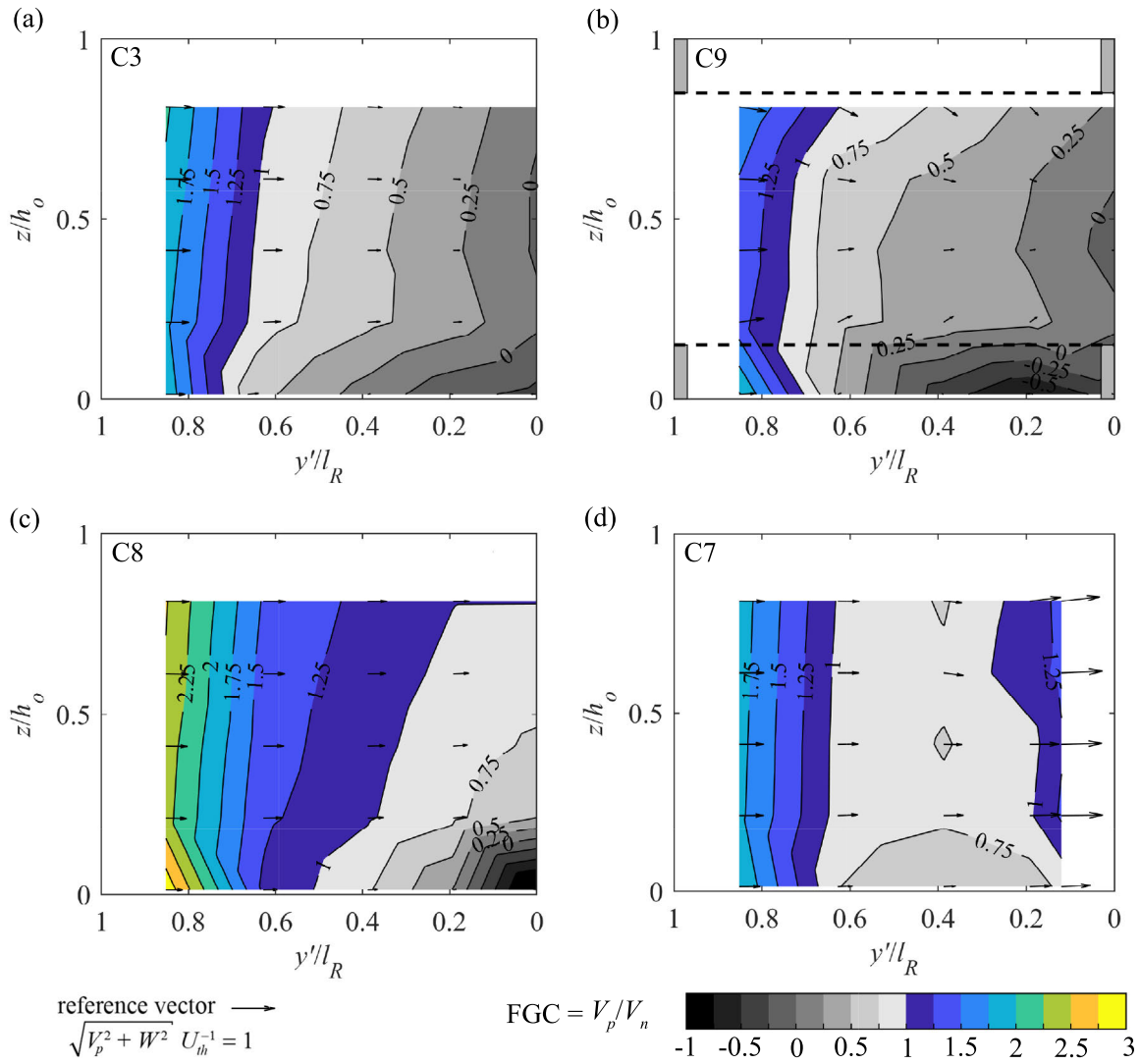


Figure 4.18 Fish guidance capacity (FGC) for the block-type HPP layout with $w_{ds}/w_o = 0.5$ measured in the rack-parallel cross section 50 mm upstream of the CBR for (a) C3: CBR with $\alpha = 30^\circ$, $\beta = 45^\circ$, $\sigma = 0.17$, (b) C9: C3 with overlays $h_v = h_{To} + h_{Bo} = 0.3 \cdot h_o$, (c) C8: C3 with weir discharge $Q_w = 0.4 \cdot Q_o$, and (d) C7: C3 and a separating pier, greyscale colours mark the areas where the FGC is lower than 1

4.2.6 Comparison to the flow fields of other mechanical behavioural FGSs

Kriewitz (2015) conducted PIV measurements assessing the flow field of louvers and MBRs. The comparison to the flow fields of CBRs with those of MBRs and louvers reveals that the curved bar shape leads to a significant reduction of U_{\max} compared to the equivalent rack configurations with straight bars from $1.75 \cdot U_o$ for the MBR to $1.25 \cdot U_o$ for the equivalent CBR A1 ($\alpha = 45^\circ$, $\beta = 45^\circ$), from $2.25 \cdot U_o$ to $1.66 \cdot U_o$ for A2 ($\alpha = 45^\circ$, $\beta = 90^\circ$), and from $1.70 \cdot U_o$ to $1.27 \cdot U_o$ for A3 ($\alpha = 30^\circ$, $\beta = 45^\circ$) (cf. Table 4.1). This comparison demonstrates that the curved bars reduce the flow deflection, leading to a more uniform

flow distribution along the rack, hence reducing U_{\max} compared to straight bars. Velocity components along the rack were studied for angled bar racks with $s_b = 10 - 30$ mm clear bar spacing by Raynal *et al.* (2013a). For $\alpha = 45^\circ$, angled bar racks are comparable to CBRs since β is 45° for both FGS-types. The V_p/U_{th} distributions are similar for angled bar racks with $s_b = 15$ mm and CBRs with $s_b = 50$ mm. The V_n values are similar at the u/s rack end, but increase more sharply for angled bar racks up to $1.2 \cdot U_o$ as compared to CBRs up to $0.8 \cdot U_o$. This comparison indicates that the narrow bar spacing of $s_b = 15$ mm increases the flow deflection toward the d/s rack end, hence increasing the normal velocities. Flow fields downstream of louvers and MBRs were studied by Kriewitz (2015) and Moretti (2015) for a similar parameter range as for CBRs in this study. Acceptable turbine admission flow conditions downstream of the rack were only met for the MBR configuration with $\alpha = 15^\circ$ and $\beta = 45^\circ$, but not for the other racks with $\alpha = 30^\circ$ or $\beta = 90^\circ$, indicating that the curved bars lead to a more sustainable hydropower production if the CBR is located closely upstream of the turbines.

5 Numerical modelling

A 2D numerical model was set up with OpenFOAM[®] to investigate the flow field in the vicinity and between the bars of CBR configurations with different bar shapes in detail. The model validation with regard to head losses and flow fields is described in Section 5.1. In Section 5.2, the detailed investigation of different bar shapes is presented and discussed.

5.1 Model validation

The numerical model validation was carried out by comparing the head loss coefficients and the flow fields from the numerical simulations and the physical model experiments. To this end, numerical simulations of the flow in the small flume were conducted for an MBR and a CBR, both with $\alpha = 30^\circ$, $\beta = 45^\circ$ and $s_b = 50$ mm, and compared to the experimental results from Kriewitz (2015) and from the present study, respectively. The ξ_R values from the simulations, the experiments and those computed with the empirical Eq. (4.1) are in good agreement for both CBR and MBR (Table 5.1). For the CBR, the numerical simulation reaches an even higher accuracy than the empirical equation.

The comparison of the streamwise velocities U normalised with $U_{th} = 0.5$ m/s resulting from the ADV measurements and the numerical simulation shown in Figure 5.1 confirms the good agreement. The velocity increase towards the d/s rack end to $U_{max}/U_o \approx 1.3$ corresponds to the value from the ADV measurements. The turbine admission flow criteria obtained from the ADV measurements in this study for the CBR configuration A3 (cf. Section 4.2.4) and in Moretti (2015) for the MBR are compared with the numerical data in Table 5.1, showing the percentage of discharge in each intake half at $x/h_o = 3.5$ downstream of the rack. The discharge distribution is accurately simulated with the numerical model for both rack types.

Table 5.1 Comparison of head loss coefficients ξ_R from the physical measurements, the empirical equation and the numerical simulations conducted by Leuch (2019) with the deviations to the measurements given in parentheses, and comparison of the turbine admission flow in each intake half from the physical measurements and the CFD simulations for a rack with curved (CBR) (Leuch, 2019) and with straight bars (MBR) (Moretti, 2015)

bar shape	measurement	Eq. (4.1) ξ_R [–]	CFD simulation	measurement	CFD simulation
				Q_{left}/Q_{right}	
CBR	0.57	0.67 (+17.5%)	0.62 (+7.6%)	51.3% / 48.7%	51.8% / 48.2%
MBR	2.56	2.83 (+10.7%)	2.25 (–12.1%)	63.2% / 36.8%	61.2% / 38.8%

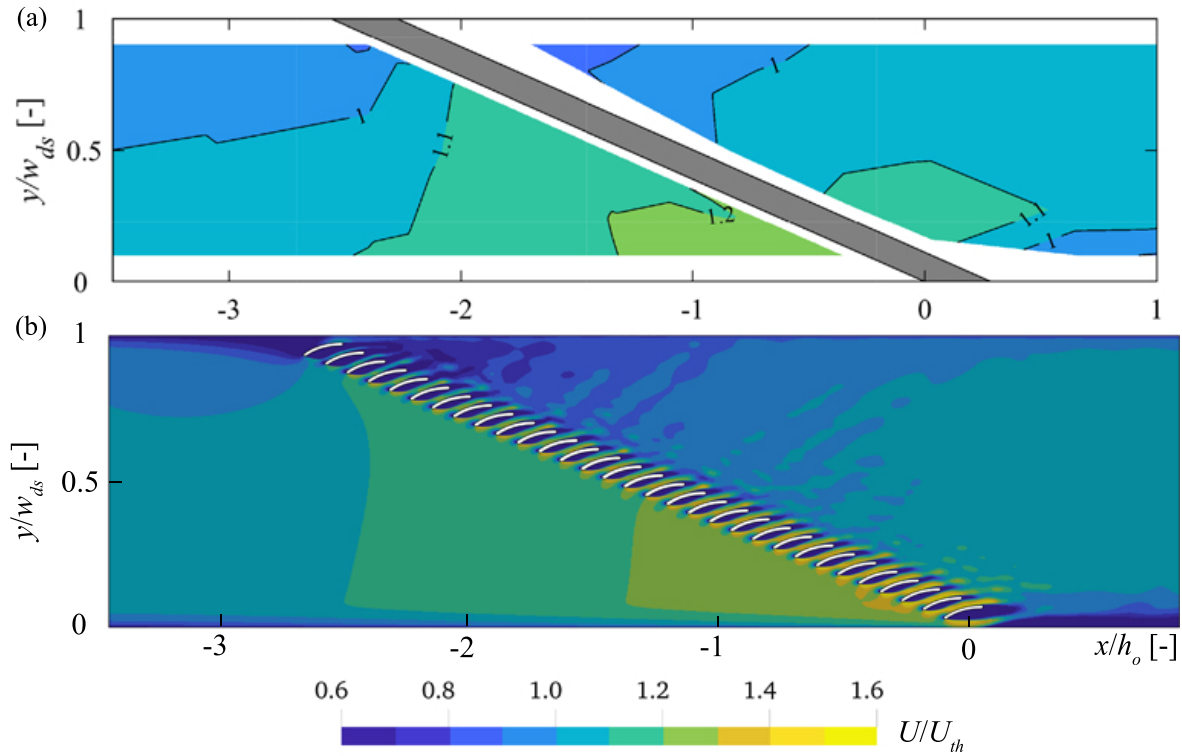


Figure 5.1 Normalised streamwise velocity distribution U/U_{th} at $z/h_o = 0.5$ resulting from (a) ADV measurements and (b) the numerical simulation of the flow in the small flume with CBR configuration A3 with $\alpha = 30^\circ$, $\beta = 45^\circ$, $s_b = 50$ mm ($\sigma = 0.17$)

The CBR configuration A3 was additionally simulated with a 3D numerical model with a top overlay, a bottom overlay and the combination of top and bottom overlays with $h_{To} = h_{Bo} = 0.15 \cdot h_o$ each, corresponding to the tests B4, B6, and B5, respectively (Table 3.4). The resulting normalised flow velocities in the cross section at $x/h_o = 3.5$ downstream of the CBR are shown in Figure 5.2. The numerical results show distinct spiral flows caused by the overlays and match well with the experimental results shown in Figures 4.15b-d. This comparison confirms that the numerical simulations accurately reproduce the experimental results. Although the discharge criteria by Godde are fulfilled for configurations B4 and B6 (cf. Table 4.1), the spiral flows are expected to lead to a decreased turbine efficiency. The numerical simulation of overlays in a large-scale model of a prototype CBR shows that spiral flow also occurs at prototype dimensions (VAW, 2020).

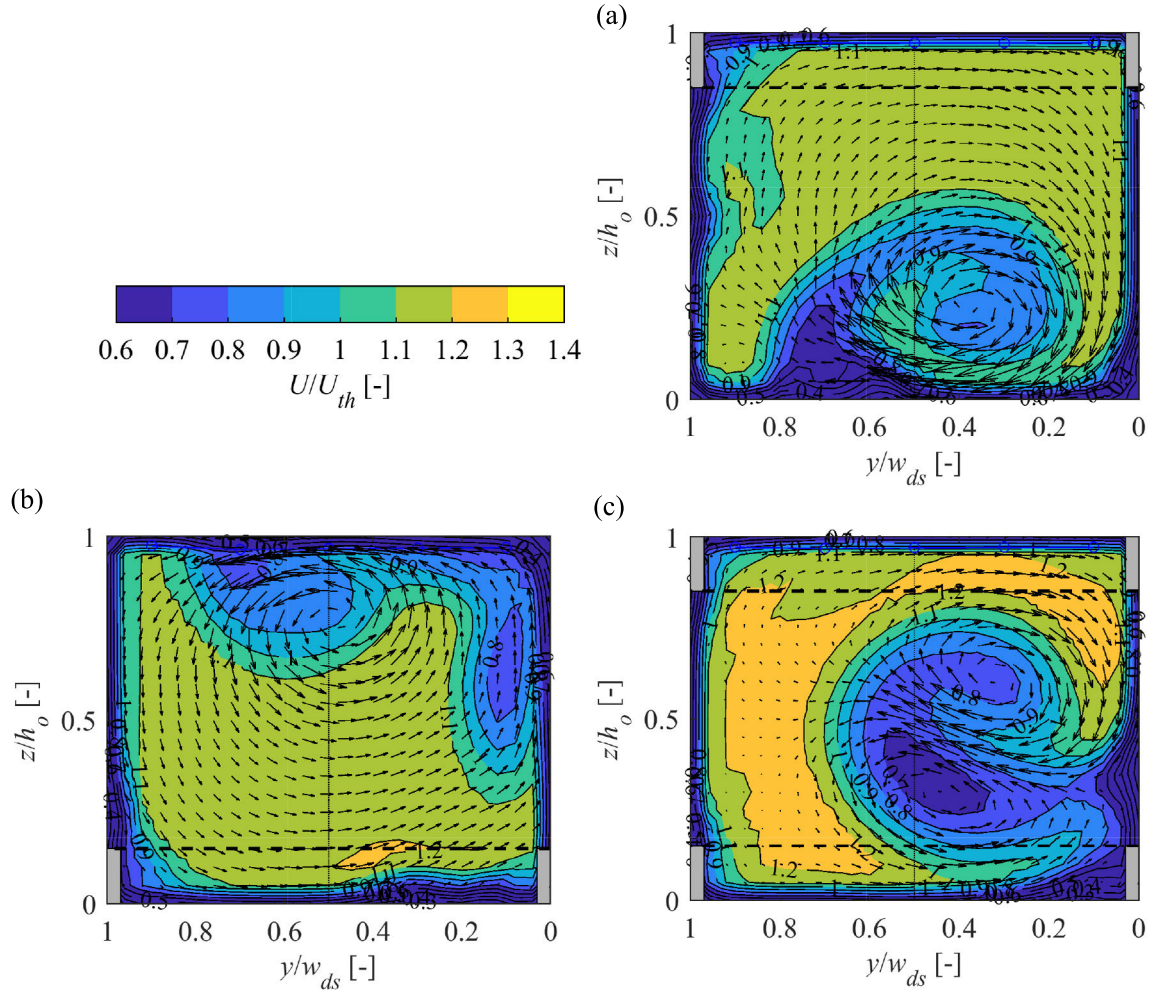


Figure 5.2 Numerical simulation of the normalised streamwise flow velocities in the downstream cross section $x/h_o = 3.5$ for (a) B4: 15% top overlay, (b) B6: 15% bottom overlay and (c) B5: 15% top and 15% bottom overlay; the overlay dimensions are indicated

5.2 Numerical simulations of different bar shapes

The requirements of a fish protection and guidance system are very site-specific with regard to geometrical, hydraulic and biological factors. It is therefore of great importance to optimise the bar rack geometry and in particular the bar shape to meet those requirements. Three different bar shapes were therefore numerically investigated with regard to their head losses and flow fields. The simulated rack head loss coefficients ξ_R of MBRs and CBRs were compared in Table 5.1. The numerical simulation of the f-CBR yields $\xi_R = 0.91$, which is 44% higher than for the CBR with $s_b = 50$ mm ($\sigma = 0.17$), but still 58% lower than for the MBR. To compare the resulting flow fields at the f-CBR with those at the CBR, the bar spacing was $s_b = 50$ mm in the simulations of both bar shapes. Due to the increased upstream bar tip thickness of the f-CBR of $t_b = 16$ mm compared to the CBR with $t_b = 10$ mm, the

bar blockage ratio is $\sigma = 0.24$ for the f-CBR, which is outside the range of tested σ values for the CBR (cf. Figure 9.1a). More simulations with different σ are needed to develop an additional bar shape head loss factor C_S for the f-CBR to apply Eq. (4.1).

The 2D numerical model further allows for a detailed simulation of the flow field in the vicinity of the rack and between the bars. Figure 5.3 shows the streamwise velocity field normalised with $U_{th} = 0.5$ m/s for the rack with $\alpha = 30^\circ$, $\beta = 45^\circ$, $s_b = 50$ mm and three different bar shapes. The MBR leads to a strong velocity increase towards the d/s rack end of $U_{max}/U_{th} = 1.6$, which agrees well with the ADV measurements reported by Kriewitz (2015). The CBR and the f-CBR lead to a similar velocity increase of $U_{max}/U_{th} \approx 1.3$. All three bar shapes lead to a flow separation at the upstream bar tip and a strong flow acceleration between the bars. The magnitude of the acceleration increases along the rack and reaches its maximum $U/U_{th} = 1.8$ between the bars at the d/s rack end for all bar shapes. A boundary layer separation forms at the downstream side of each bar, which is largest at the u/s rack end and decreases towards the d/s rack end.

Figure 5.4 shows the distribution of the spatial velocity gradients in streamwise direction ($SVG_x = \partial U / \partial x$) for the three bar shapes. The computation of SVG_x allows for the identification of acceleration as well as deceleration areas. Note that the scale only ranges from $-1 \text{ s}^{-1} < SVG_x < 1 \text{ s}^{-1}$, although SVG_x values between the bars are much higher with up to 45 s^{-1} , independent of the bar shape. This range was chosen since some species (e.g. salmonids) are known to react sensitively to velocity gradients larger than 1 s^{-1} (Enders *et al.*, 2012). Figure 5.4 therefore emphasises the regions, which are prone to elicit an avoidance reaction of fish. At the MBR with straight bars, SVG_x increases non-linearly from the u/s rack end towards the d/s rack end and reaches the maximum value of $SVG_x = 0.3 \text{ s}^{-1}$ due to the strong flow deflection along the rack towards the d/s rack end. On the contrary, at both CBR and f-CBR, the SVG_x is uniformly distributed in the upstream area of the rack with locally slightly lower and higher values at the upstream and downstream rack ends, respectively, indicating a quasi-linear streamwise velocity increase along the rack. Independent of the bar shape, $SVG_x \geq 1 \text{ s}^{-1}$ in a circular area upstream of the leading bar tip, while $SVG_x \leq -1 \text{ s}^{-1}$ between the bar tips. These alternating zones of high and low SVG_x extend up to a distance of approx. 40 mm upstream of the rack, and are responsible for the avoidance reaction of fish and thus for the behavioural barrier effect of all three FGS types.

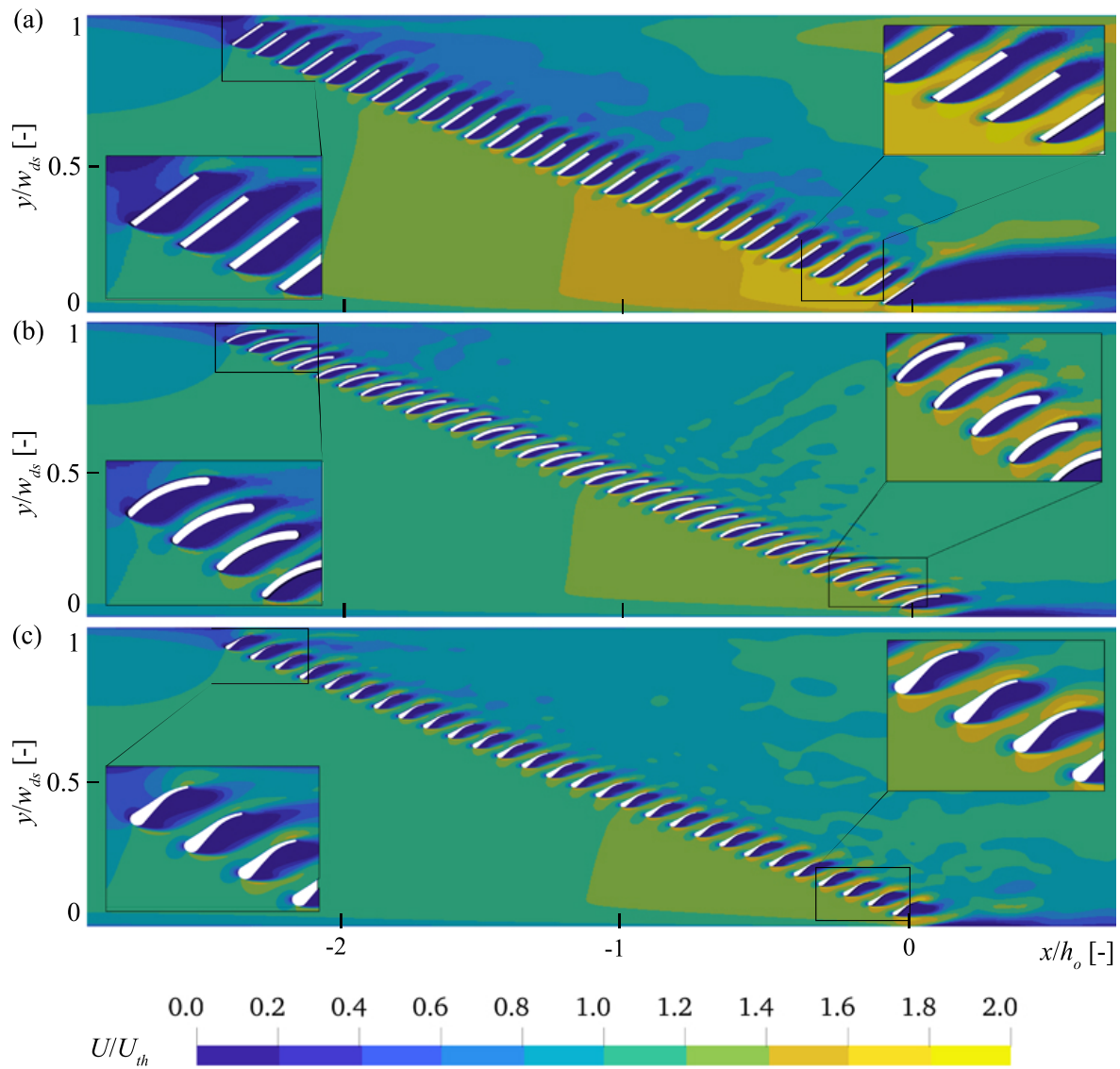


Figure 5.3 Normalised streamwise flow velocities in the vicinity of the rack for (a) MBR, (b) CBR and (c) f-CBR, all with $\alpha = 30^\circ$, $\beta = 45^\circ$, $s_b = 50$ mm, and $U_{th} = 0.5$ m/s

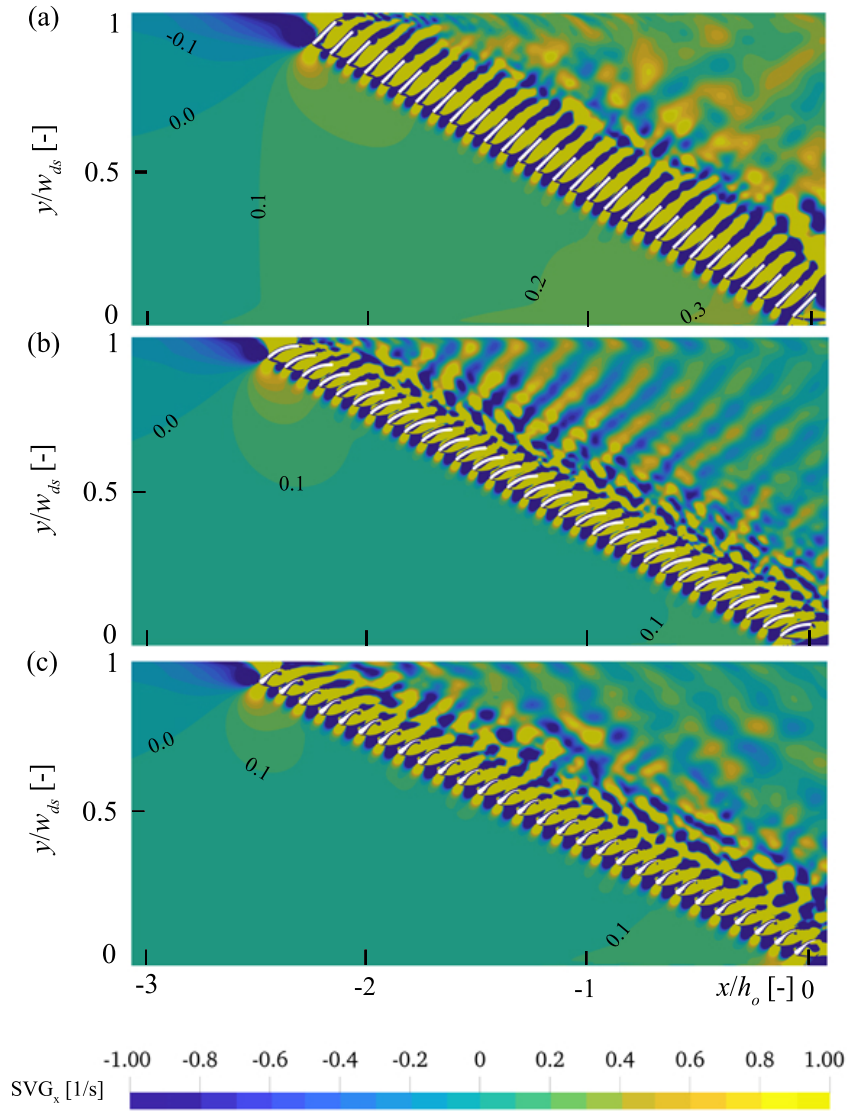


Figure 5.4 Spatial velocity gradients in streamwise direction (SVG_x) in the vicinity of the rack for (a) MBR, (b) CBR and (c) f-CBR, all with $\alpha = 30^\circ$, $\beta = 45^\circ$, $s_b = 50$ mm, and $U_{th} = 0.5$ m/s

The turbulent kinetic energy (TKE) is an important parameter affecting the fish behaviour (Liao *et al.*, 2003; Liao, 2007; Webb and Cotel, 2010). Figure 5.5 shows the TKE distribution calculated from the numerical simulations for the different bar shapes. The TKE is small with $TKE < 0.005 \text{ m}^2/\text{s}^2$ upstream of the rack independent of the bar shape, corresponding to the typical values of open channel flow (Nezu and Nakagawa, 1993). Figure 5.5 reveals high turbulence zones starting from the upstream bar tip, and increasing and enlarging along the outer edge of the recirculation zone along the bar and downstream for all bar shapes. The magnitude of the TKE between the bars increases along the rack and is highest at the d/s rack end. Due to the strong flow deflection with the straight bars, the highest turbulence levels occur downstream of the MBR (Figure 5.5a), followed by the f-CBR (Figure

5.5c) and the CBR (Figure 5.5b). This trend explains why the highest head losses and non-symmetric turbine admission flows occur for the MBR compared to the f-CBR and the CBR. The TKE is highest between the bars of the MBR with $TKE = 0.05 \text{ m}^2/\text{s}^2$, which is still an order of magnitude lower than $0.4 \text{ m}^2/\text{s}^2$ occurring in technical fish ladders for upstream fish movements (Quaranta *et al.*, 2017).

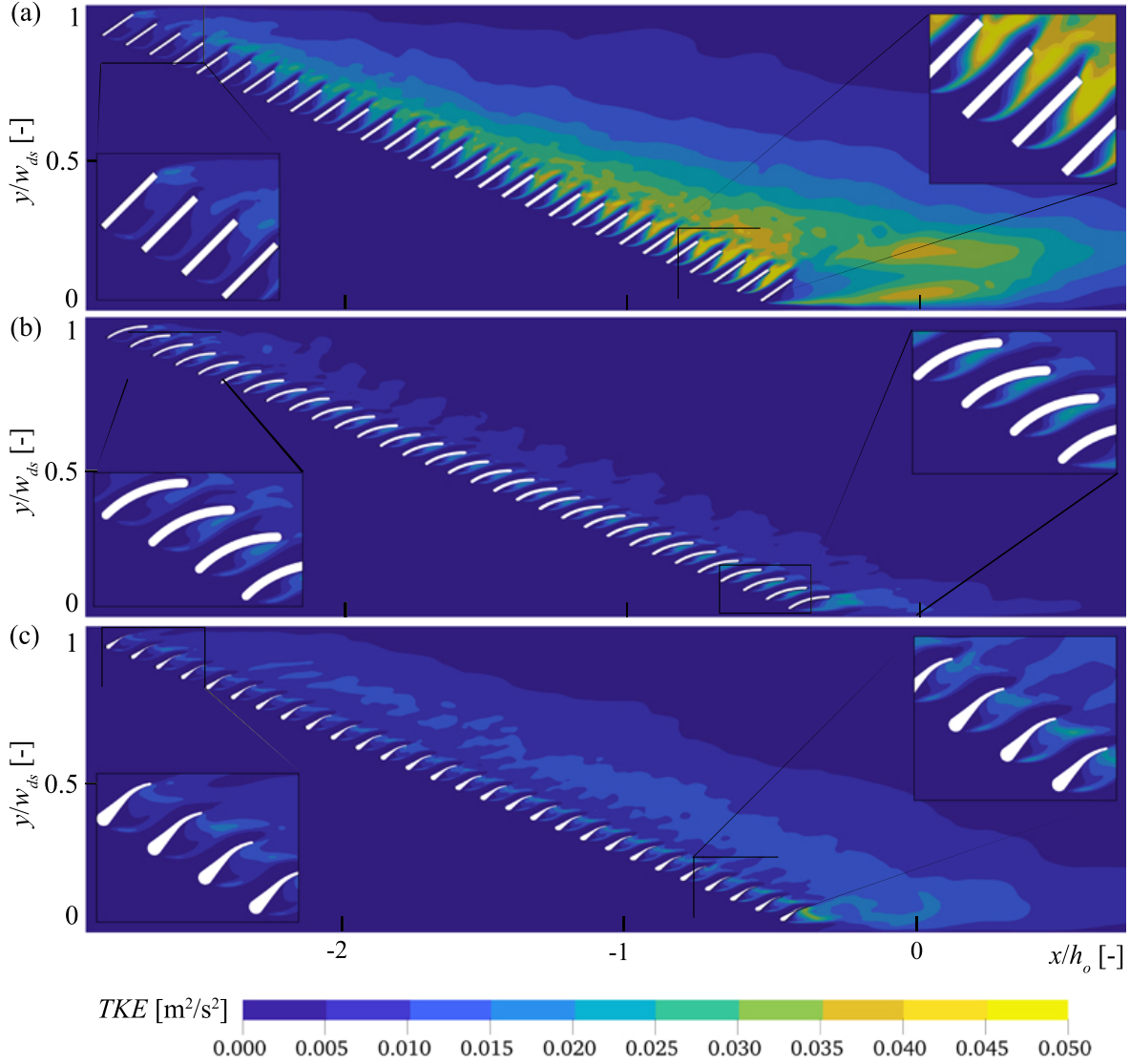


Figure 5.5 Turbulent kinetic energy (TKE) distribution in the vicinity of the rack for (a) MBR, (b) CBR and (c) f-CBR, all with $\alpha = 30^\circ$, $\beta = 45^\circ$, $s_b = 50 \text{ mm}$, and $U_{th} = 0.5 \text{ m/s}$

Overall, these results indicate that the SVG_x is a decisive parameter for the fish reaction and the rack guidance efficiency in front of all three tested FGS types compared to the TKE with no significant effect upstream of the rack (cf. Section 6.1.2). However, if the fish swim between the bars, the elevated turbulence might lead to disorientation and instability. This issue is strongest for the MBR, preventing small fish and weak swimmers in particular from

escaping back upstream once they have been entrained between the bars. In contrast, the high turbulence zones between the bars of the MBR might lead to an avoidance reaction for larger fish and strong swimmers, whereas the *TKE* between the bars of the CBR and the f-CBR is too low to elicit the same reaction.

The numerical model proved to be a powerful and reliable tool for the optimization of rack and bar geometry and the assessment of their hydraulic performance. Although the newly developed bar shape of the f-CBR creates slightly higher head losses than the simpler bar shape of the CBR, its head loss is still low and the up- and downstream flow fields are promising for fish guidance and energy production, respectively. In particular the f-CBR is less prone for clogging of floating debris and can be cleaned with a standard rack cleaning machine (Chapter 8).

6 Ethohydraulics of curved-bar rack bypass systems

This section displays the results of the numerical simulations, the ADV measurements and the live-fish tests conducted in the ethohydraulic flume with an optimised CBR configuration. The CBR with $\alpha = 30^\circ$, $\beta = 45^\circ$ and $s_b = 50$ mm ($\sigma = 0.17$) (A3 in Table 3.4) with an adjacent bypass of $w_{by} = 0.25$ m width was installed in the flume as a 1:1 Froude-scaled section model. This CBR configuration was chosen because it creates low head losses, quasi-symmetric turbine approach flow and it is more cost-effective with regard to the rack length compared to $\alpha = 15^\circ$ (cf. Chapter 4). The ratio of the bypass entrance velocity to the mean inflow velocity $U_{by,in}/U_o$ is introduced as a new parameter VR (bypass Velocity Ratio).

6.1 Hydraulics of curved-bar rack bypass systems

The CBR was tested with six different fish species under four main hydraulic conditions with two different U_o values (0.5 m/s and 0.7 m/s) and two different VR values (1.2 and 1.4) with a full depth open channel bypass. These flow fields were measured using an ADV probe and numerically simulated in detail and presented in Sections 6.1.1 and 6.1.2, respectively. The hydraulics of different bypass layouts and their effect on the fish behaviour are presented in Sections 6.1.3 and 6.1.4, respectively.

6.1.1 Velocity field for the live-fish tests with barbel, spirlin, nase and eel

Figure 6.1 shows the ADV measurement results of the streamwise flow velocities normalised with U_o for the ethohydraulic tests conducted in October and November 2018 with barbel, spirlin, nase and European eel. Since the fish tended to swim along the flume bed, the velocity fields are only shown for $z/h_o = 0.14$ (= 125 mm above the flume bed). At this horizontal plane, the normalised velocities U/U_o upstream of the CBR are slightly higher for $U_o = 0.5$ m/s (Figure 6.1a/b) than for $U_o = 0.7$ m/s (Figure 6.1c/d). The approach flow is slightly concentrated towards the right flume side due to the backwater caused by the fences of the starting compartment on the opposite flume side. The streamwise velocity U increases along the rack and reaches a maximum value of $VR = 1.2$ at the bypass entrance in Figure 6.1a/c and $VR = 1.4$ in Figure 6.1b/d. For $VR = 1.4$, the value of U starts increasing further upstream of the bypass entrance compared to $VR = 1.2$. The narrowly spaced contour lines indicate an increased SVG_x directly at the bypass entrance, which is higher for $VR = 1.4$.

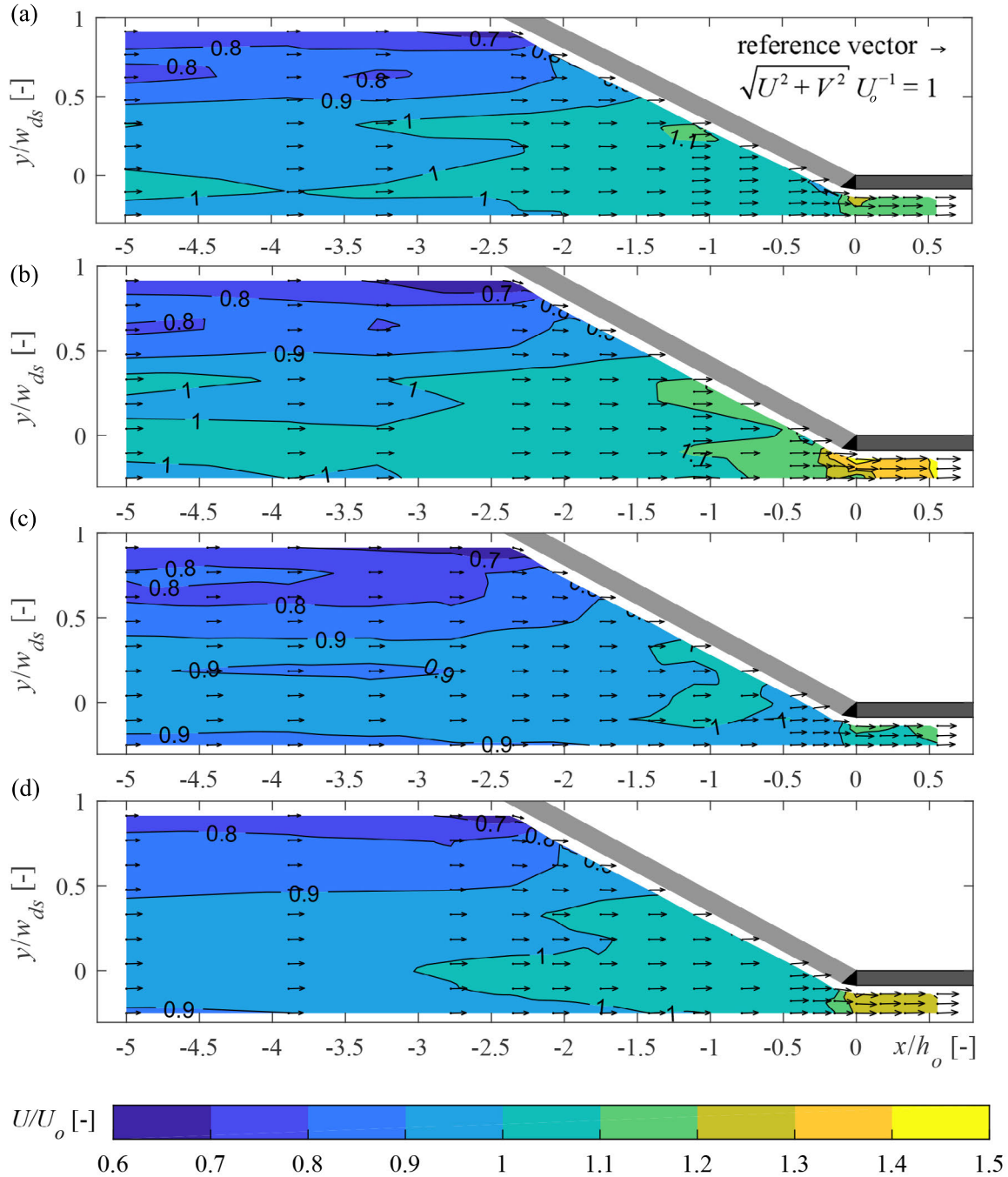


Figure 6.1 Streamwise normalised flow velocities U/U_o measured at $z/h_o = 0.14$ for (a) $U_o = 0.5$ m/s, $VR = 1.2$, (b) $U_o = 0.5$ m/s, $VR = 1.4$, (c) $U_o = 0.7$ m/s, $VR = 1.2$, and (d) $U_o = 0.7$ m/s, $VR = 1.4$; the direction of the resulting velocity vector at each measurement point and the contour values are indicated

The normalised transversal flow velocities V/U_o are depicted in Figure 6.2a/b for $U_o = 0.5$ m/s and in Figure 6.2c/d for $U_o = 0.7$ m/s. The CBR visibly starts affecting the flow field at $x/h_o = -3.25$ and diverts the flow towards the bypass. The transversal flow velocities are thus highest at the u/s rack end with $V \approx 0.2 \cdot U_o$ and decrease along the rack with minimum

values at the d/s rack end for all hydraulic conditions. Independent of U_o , $V = -0.075 \cdot U_o$ and $-0.025 \cdot U_o$ at the d/s rack end for $VR = 1.2$ and $VR = 1.4$, respectively, indicating an increased flow diversion through the rack in this area. Since these minimum values are much higher than $V = -0.2 \cdot U_o$ for the equivalent MBR configuration with a high fish guidance efficiency found by Albayrak *et al.* (2020a), fish are not expected to get entrained between the bars of the CBR, especially for $VR = 1.4$. At the bypass entrance ($x/h_o = 0$), V is positive with the highest values at the corner of the separation wall.

Figure 6.3 shows the velocity components in the rack-parallel cross section at a distance of 50 mm perpendicular to the upstream face of the rack. The upstream and the downstream rack end are located at $y'/l_R = 1$ and $y'/l_R = 0$, respectively. The V_n/U_o and the V_p/U_o values gradually increase along the rack for all flow conditions up to $y'/l_R = 0.35$ and then slightly decrease towards the d/s rack end with V_p/U_o being the dominant component. The criterion of $V_n \leq 0.5$ m/s is always met independent of U_o . The V_p/U_o values are slightly higher for $U_o = 0.7$ m/s compared to 0.5 m/s and for $VR = 1.4$ compared to $VR = 1.2$. The fish guidance capacity $FGC = V_p/V_n$ is highest at the u/s rack end and gradually decreases along the rack. It remains above the critical value of $V_p/V_n > 1$ proposed by Courret and Larinier (2008) for effective fish guidance. Except at the u/s rack end, the FGC values are almost identical for all flow conditions, but start to diverge near the bypass ($y'/l_R = 0.05$), where the FGC is slightly higher for $VR = 1.4$ compared to $VR = 1.2$.

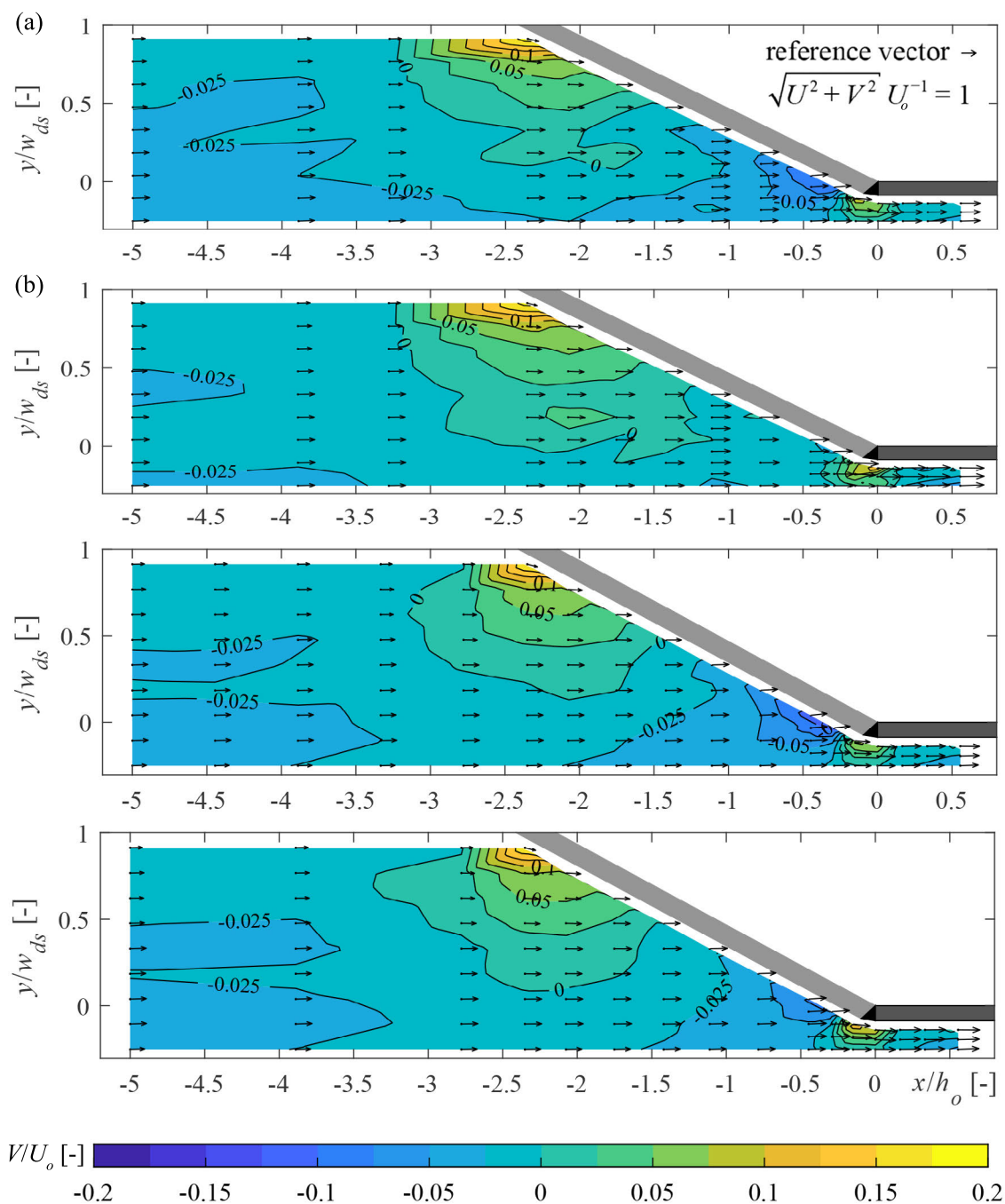


Figure 6.2 Transversal flow velocities V/U_o for $U_o = 0.5$ m/s and CBR configuration A3 measured at $z/h_o = 0.14$ for (a) $U_o = 0.5$ m/s, $VR = 1.2$, (b) $U_o = 0.5$ m/s, $VR = 1.4$, (c) $U_o = 0.7$ m/s, $VR = 1.2$, and (d) $U_o = 0.7$ m/s, $VR = 1.4$; the direction of the resulting velocity vector at each measurement point and the contour values are indicated

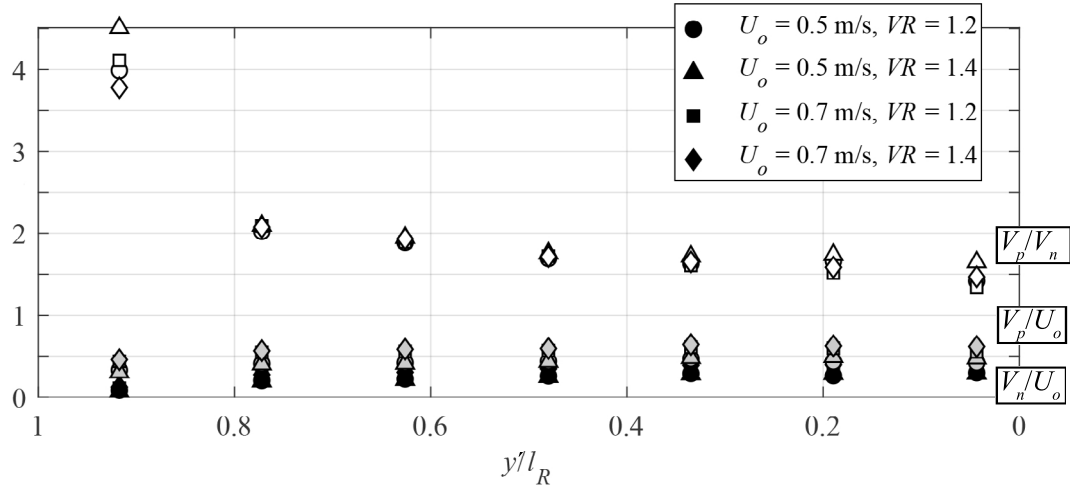


Figure 6.3 Velocity components $FGC = V_p/V_n$ (white markers), V_p/U_o (grey markers), and V_n/U_o (black markers) in the rack-parallel cross section of 50 mm distance for the four hydraulic conditions, measured with ADV at $z/h_o = 0.14$

6.1.2 Velocity field for the live-fish tests with salmon parr and trout

For the ethohydraulic tests in April and May 2019 with brown trout and salmon parr, an additional fence was installed on the right flume side to avoid the lower flow velocities on the left flume side shown in Figure 6.1. The resulting 3D flow fields were simulated with the numerical model (cf. Chapter 5) and validated with ADV measurements, which showed that a more symmetrical inflow profile was achieved with the additional fence. All following figures therefore show the results from the numerical simulations. Figure 6.4 shows the stream-wise velocity field normalised with $U_o = 0.5$ m/s for $VR = 1.2$ at different horizontal planes $z = 0.14 \cdot h_o$, $0.50 \cdot h_o$, and $0.86 \cdot h_o$, which correspond to the flow depths of $z = 0.125$ m, 0.45 m and 0.775 m, respectively. 3D flow develops due to the typical cross sectional inflow profile of a narrow open channel flow ($w_o/h_o = 1.67 < 4 - 5$; Auel, 2014). Since most fish swam along the flume bed during the live-fish tests, only the results at $z/h_o = 0.14$ are shown in the further analysis of the flow fields.

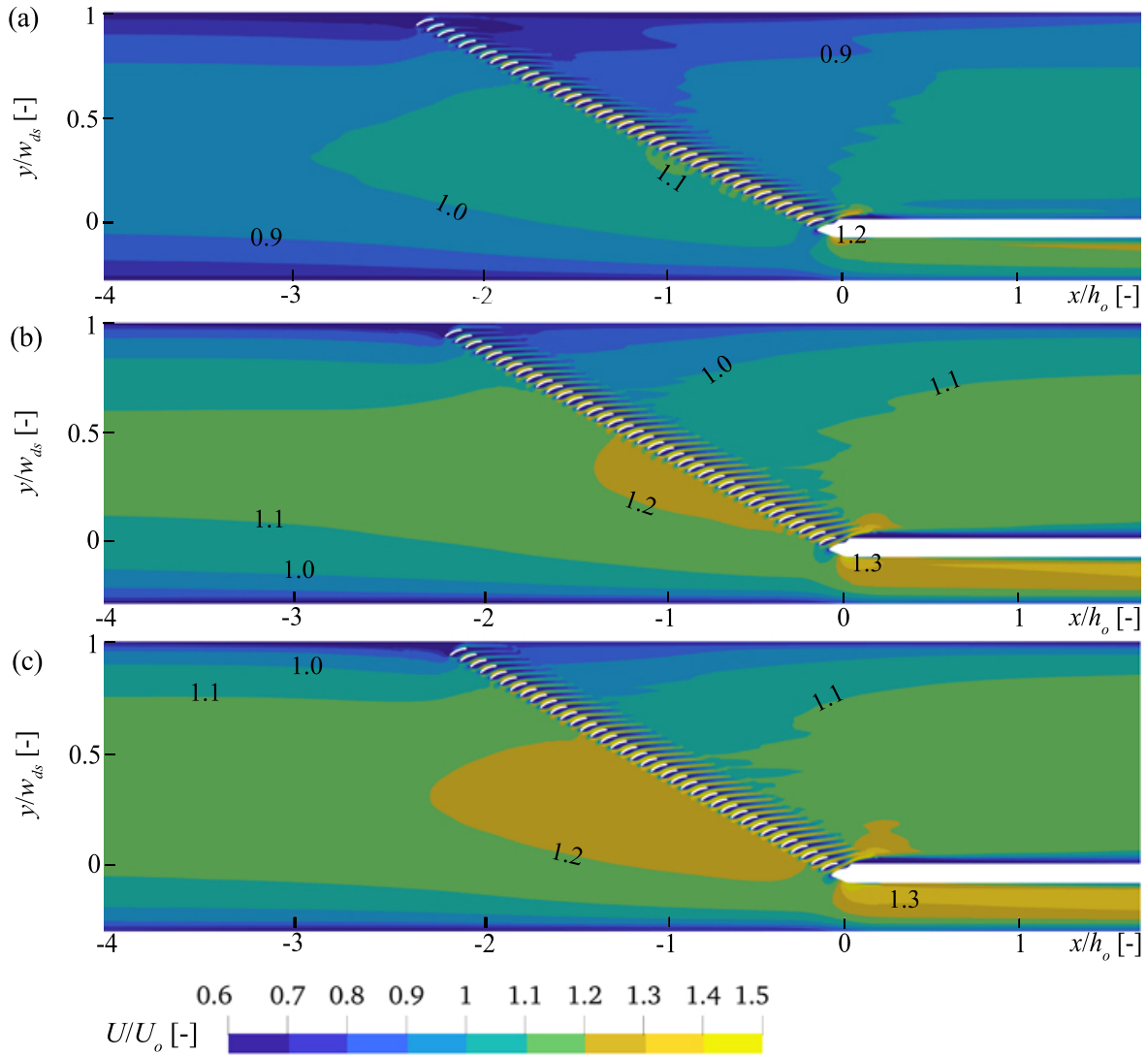


Figure 6.4 Streamwise flow velocities U/U_o from the numerical simulation for $U_o = 0.5$ m/s, $VR = 1.2$ and CBR configuration A3 extracted at (a) $z/h_o = 0.14$, (b) $z/h_o = 0.50$ and (c) $z/h_o = 0.86$; the contour values are indicated

Figure 6.5 and Figure 6.6 show the contour plots of the streamwise and transversal flow fields, respectively, normalised with U_o for the four main hydraulic conditions. A detailed view on the flow conditions at the bypass entrance is given for each flow condition. Figure 6.5 demonstrates that the flow field upstream of the rack and along the rack is quasi-identical, independent of U_o or VR . The rack starts visibly affecting the flow field from approx. $x/h_o = -2.5$, where the low flow velocity region along the right channel wall decreases and the transversal flow velocities V/U_o towards the bypass increase (Figure 6.6). Expectedly, the streamwise velocities are higher in the vicinity of and inside the bypass for $VR = 1.4$ compared to $VR = 1.2$. The relative bypass discharges were $Q_{by} = 0.17 \cdot Q_o$, $0.19 \cdot Q_o$, $0.20 \cdot Q_o$, and $0.22 \cdot Q_o$ for the Figures 6.5a-d, respectively. The flow field at dif-

ferent horizontal planes (Figure 6.4) and the detailed view of the flow field at the bypass entrance in Figure 6.5 demonstrate that the specification of VR of 1.2 or 1.4 is a mean value, which can deviate locally. The U/U_o values are thus highest at higher flow depths, along the separation wall directly at the bypass entrance ($x/h_o = 0$) and between the bars. Between the bars, the maximum values are $U/U_o = 1.5$ independent of U_o resulting in maximum absolute velocities $U_r = 0.75$ m/s and $U_r = 1.05$ m/s at $U_o = 0.5$ m/s and $U_o = 0.7$ m/s, respectively.

The effect of VR is visible in Figure 6.6, where positive V/U_o values extend further upstream of the rack for $VR = 1.4$ compared to $VR = 1.2$. At the d/s rack end, V/U_o increases towards the bypass and no negative V/U_o values occur, indicating a better fish guidance efficiency for the CBR than for the similar MBR configuration. Albayrak *et al.* (2020a) reported negative V/U_o values at the d/s rack end of an MBR with $\alpha = 30^\circ$, which led to an increased number of fish passing the rack at the d/s rack end. The negative V/U_o values are related to the fact that Albayrak *et al.* (2020a) did not regulate the bypass to achieve gradually increasing flow velocities towards the bypass. The comparison of their results with the present findings thus emphasises the importance of regulating the bypass accordingly.

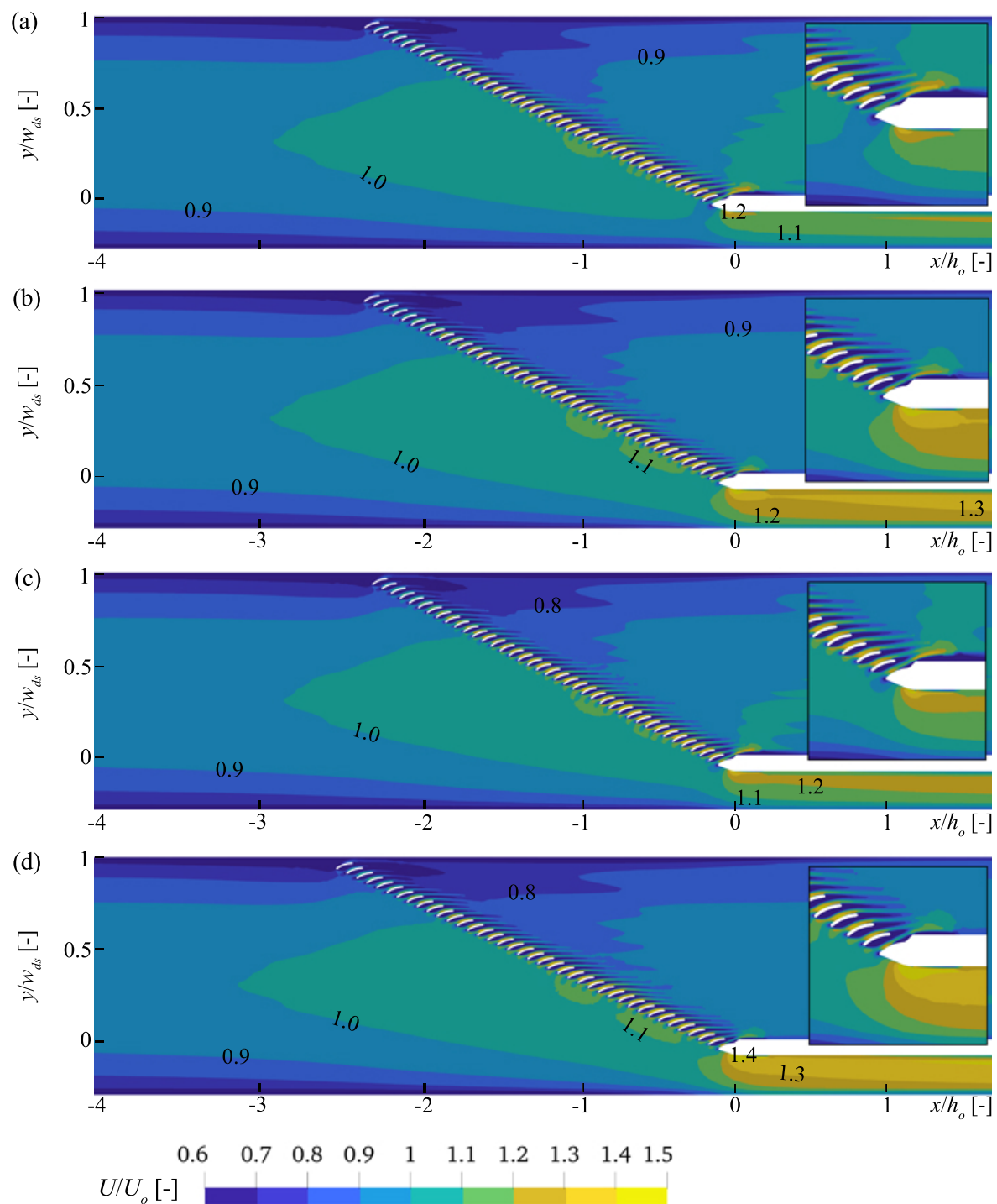


Figure 6.5 Streamwise flow velocities U/U_o from the numerical simulation at $z/h_o = 0.14$ for (a) $U_o = 0.5$ m/s, $VR = 1.2$, (b) $U_o = 0.5$ m/s, $VR = 1.4$, (c) $U_o = 0.7$ m/s, $VR = 1.2$, and (d) $U_o = 0.7$ m/s, $VR = 1.4$, the flow field at the bypass entrance is shown in detail

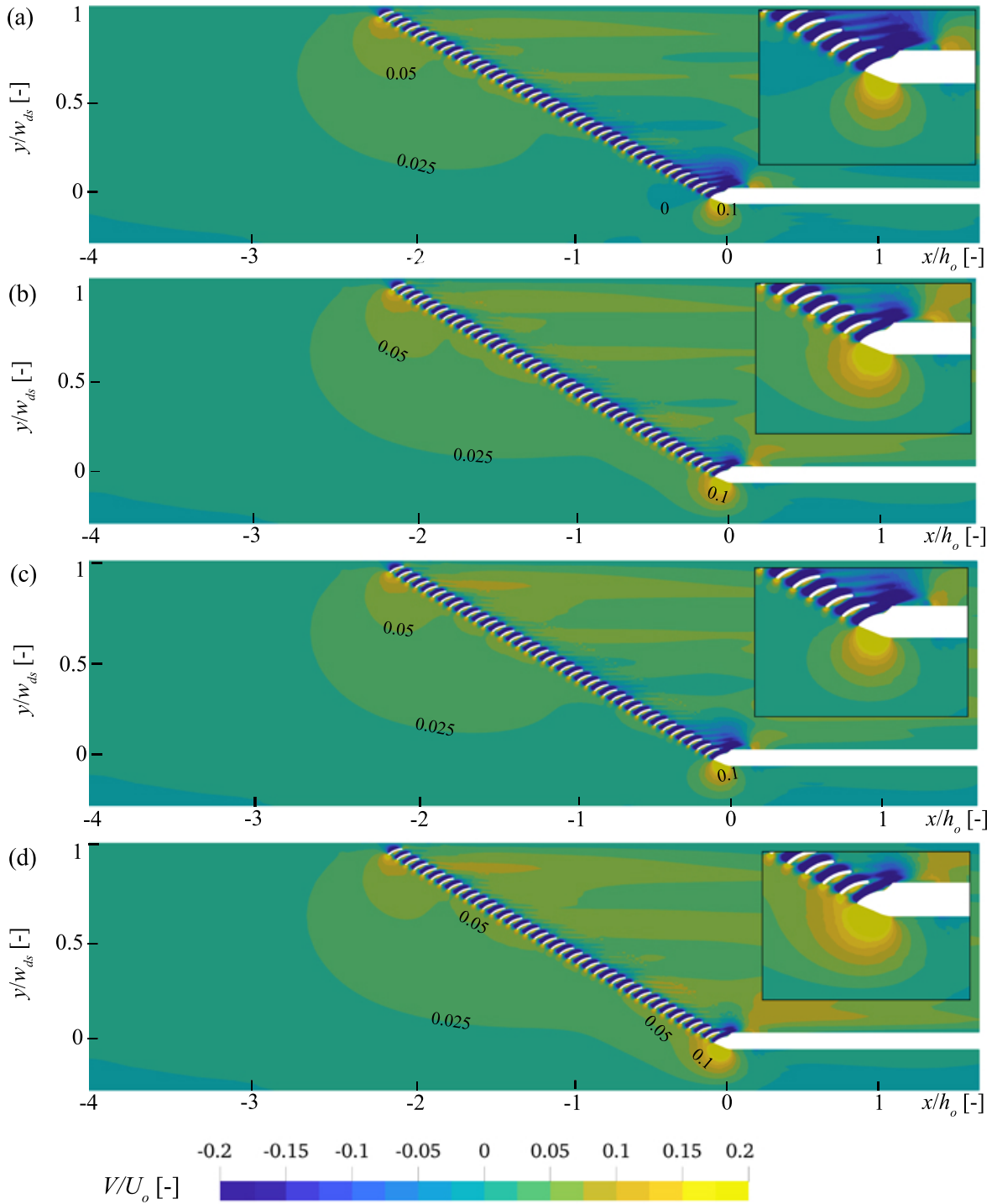


Figure 6.6 Transversal flow velocities V/U_o from the numerical simulation at $z/h_o = 0.14$ for (a) $U_o = 0.5$ m/s, $VR = 1.2$, (b) $U_o = 0.5$ m/s, $VR = 1.4$, (c) $U_o = 0.7$ m/s, $VR = 1.2$, and (d) $U_o = 0.7$ m/s, $VR = 1.4$, the flow field at the bypass entrance is shown in detail

The spatial velocity gradients in streamwise direction ($SVG_x = \partial U / \partial x$) in the vicinity of the d/s rack end and at the bypass entrance are shown in Figure 6.7 for the four main flow conditions. The computation of SVG_x allows for the identification of areas of acceleration as well

as deceleration. The cut-off value of $|SVG_x| = 1$ is chosen since values equal to or above this value are known to trigger an avoidance reaction in salmonid species (Enders *et al.*, 2012). Due to flow separation at the upstream bar tips, the SVG_x values are high between the bars and approx. 40 mm in front of the bars with values $SVG_x > 1$ and $SVG_x < -1$ indicating regions of a strong velocity increase and a strong velocity decrease, respectively. The alternating regions of high positive and negative SVG_x values contribute to the behavioural barrier effect of the CBR as a FGS.

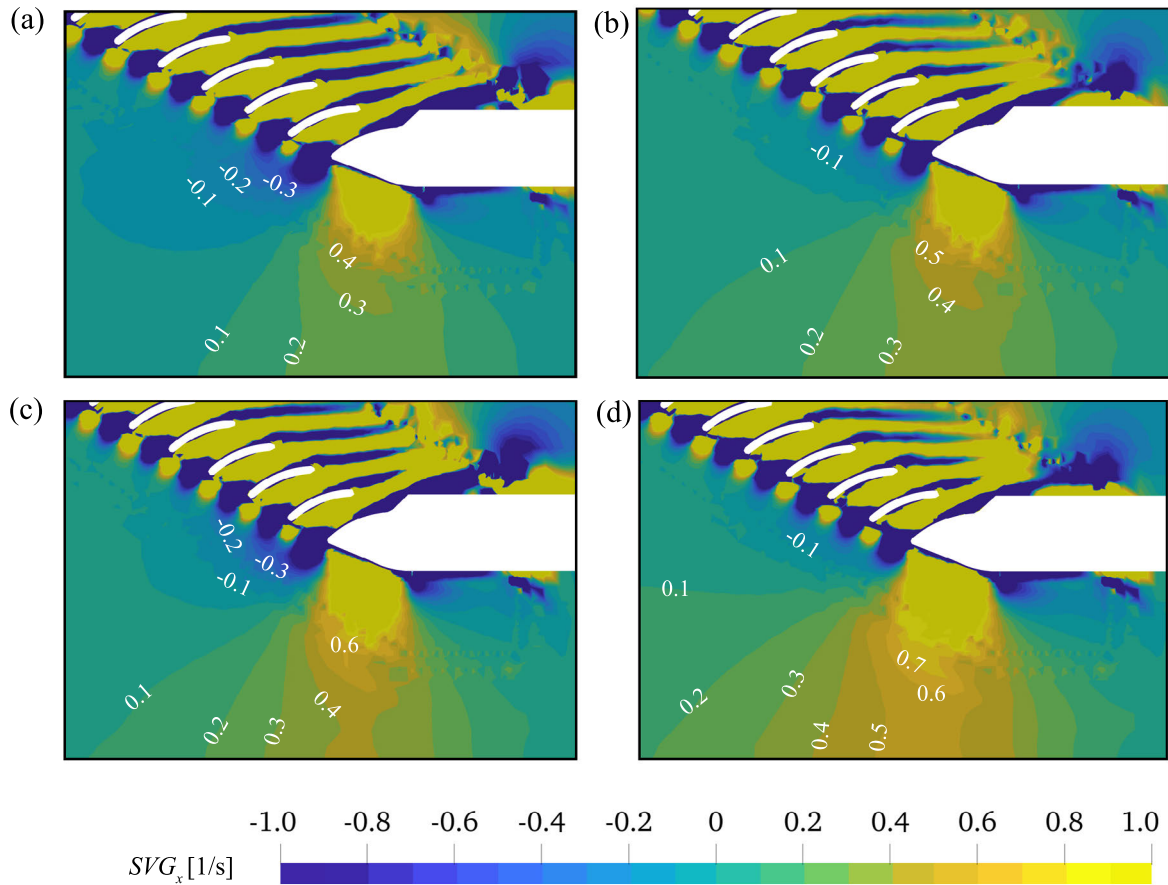


Figure 6.7 Spatial velocity gradients in streamwise direction (SVG_x) near the bypass entrance resulting from the numerical simulation at $z/h_o = 0.14$ for (a) $U_o = 0.5$ m/s, $VR = 1.2$, (b) $U_o = 0.5$ m/s, $VR = 1.4$, (c) $U_o = 0.7$ m/s, $VR = 1.2$, and (d) $U_o = 0.7$ m/s, $VR = 1.4$

A foam spacerholder was placed between the last bar of the CBR and the separation wall dividing the bypass from the main channel to avoid large separation zones and to ensure a gradual velocity increase from the d/s rack end into the bypass. Nevertheless, a flow deceleration with values down to $SVG_x = -0.3 \text{ s}^{-1}$ is observed at the d/s rack end caused by the separation wall. This deceleration is strongest for $U_o = 0.5$ m/s and $VR = 1.2$ (Figure 6.7a) and decreases at higher U_o and higher VR . High $SVG_x > 1$ are observed directly at the

bypass entrance close to the separation wall due to the arrangement of the bypass parallel to the downstream channel for all flow conditions. This leads to a reduction of the available flow cross section with $SVG_x < 1$. A different bypass arrangement with an outflow in line with the rack angle α might mitigate this issue, which is observed in particular for laboratory studies, where the available bypass width is often limited. Downstream of the transition from the foam spaceholder to the separation wall, a small separation zone with negative SVG_x values occurs. Otherwise, SVG_x remains positive inside the bypass indicating that there are no areas of flow deceleration. The different flow conditions lead to slightly different SVG_x distributions near the bypass entrance. Figure 6.7 shows that the velocity increase starts further upstream and reaches higher SVG_x values over the entire bypass width at higher VR and higher U_o . This means that the same VR values can lead to different SVG_x values at different U_o , thus triggering a different avoidance reaction of fish, which are sensitive to velocity gradients.

The total absolute spatial velocity gradients SVG between the bars in the middle of the CBR are shown at $U_o = 0.5$ m/s in Figure 6.8a and at $U_o = 0.7$ m/s in Figure 6.8b. Since the SVG values at this location are similar for $VR = 1.2$ and 1.4 , they are only shown for $VR = 1.2$. The SVG sharply increase at a distance of about 40 mm upstream of the CBR to $SVG \geq 5$ s⁻¹ at both tested U_o values. In contrast, SVG values are higher between the bars at $U_o = 0.7$ m/s compared to $U_o = 0.5$ m/s with values up to $SVG = 75$ s⁻¹ and $SVG = 50$ s⁻¹, respectively, which is much higher than the threshold value of $SVG_x = 1$ s⁻¹ found by Haro *et al.* (1998) and Enders *et al.* (2012).

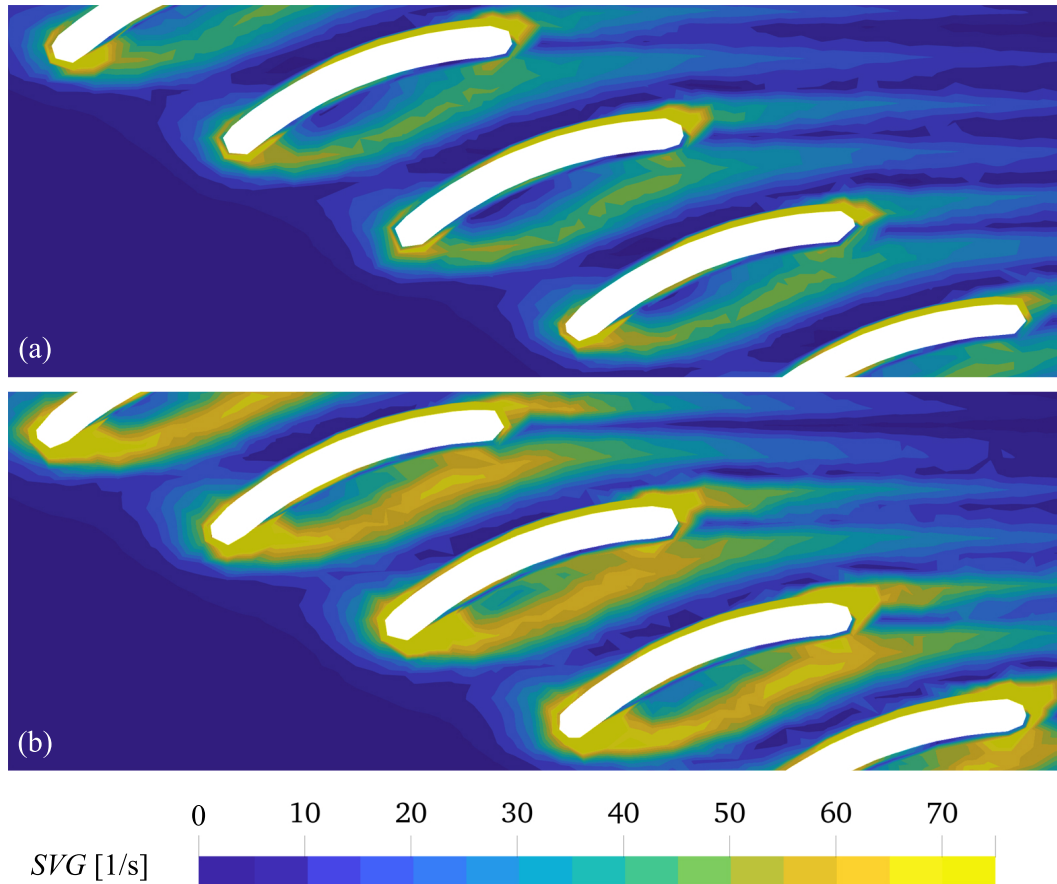


Figure 6.8 Total spatial velocity gradient (SVG) between the bars of the CBR at $z/h_o = 0.14$ for $VR = 1.2$ and (a) $U_o = 0.5$ m/s, (b) $U_o = 0.7$ m/s

The distribution of the spatial pressure gradients SPG in [Pa/cm] at the bypass entrance depicted in Figure 6.9 looks very similar to the distribution of SVG_x in Figure 6.7 with values of $SPG \leq 5$ Pa/cm in the right bypass half. The separation zone at the foam spacerholder leads to increased SPG values at the left side of the bypass entrance. Fish are known to perceive pressure gradients with their lateral line organs (Venturelli *et al.*, 2012; Ristroph *et al.*, 2015). However, no threshold values for SPG triggering an avoidance reaction were found in the literature. Figure 6.9 shows that the pressure increase starts further upstream and reaches higher SPG values over the entire bypass width at higher VR and higher U_o . This means that the same VR values can lead to different SPG values at different U_o , thus triggering a different avoidance reaction of fish, which are sensitive to pressure gradients.

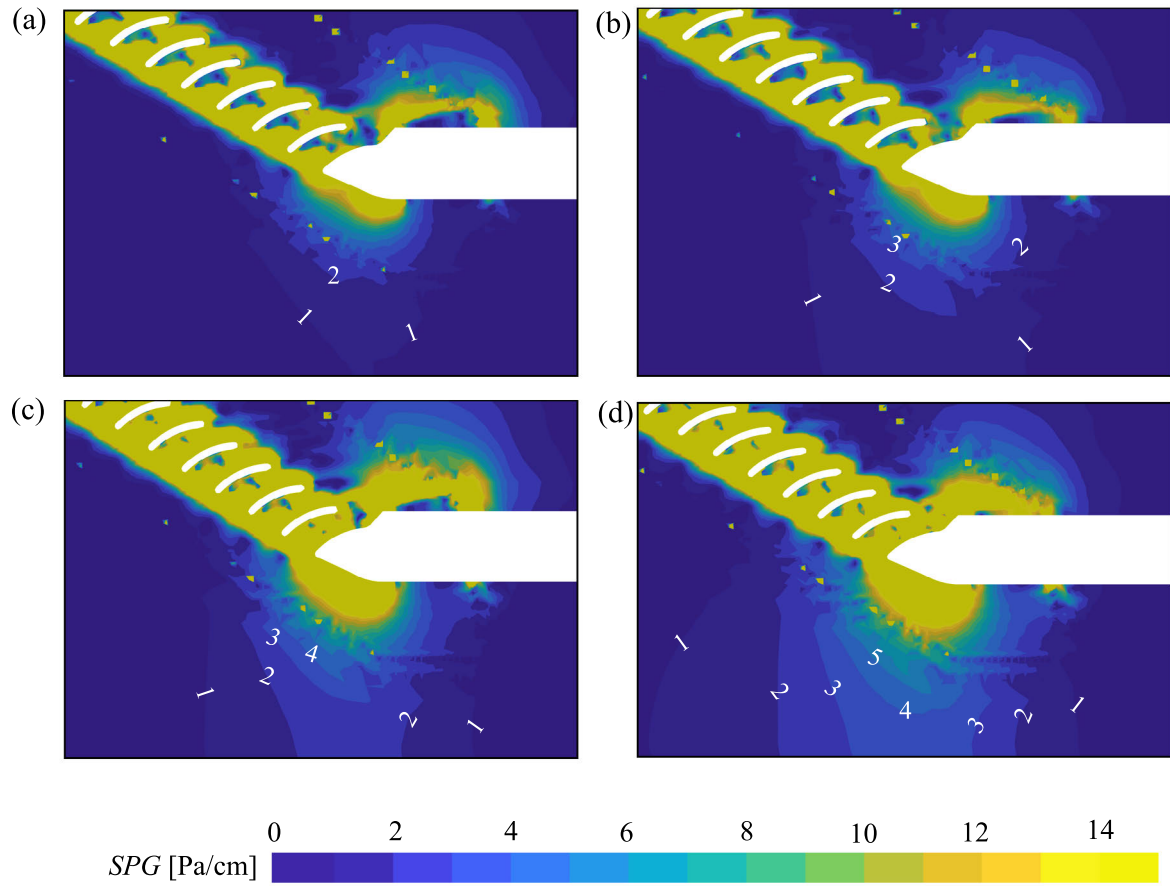


Figure 6.9 Spatial pressure gradients (*SPG*) near the bypass entrance resulting from the numerical simulation at $z/h_o = 0.14$ for (a) $U_o = 0.5$ m/s, $VR = 1.2$, (b) $U_o = 0.5$ m/s, $VR = 1.4$, (c) $U_o = 0.7$ m/s, $VR = 1.2$, and (d) $U_o = 0.7$ m/s, $VR = 1.4$

The *SPG* values between the bars in the middle of the CBR are shown for $U_o = 0.5$ m/s in Figure 6.10a and for $U_o = 0.7$ m/s in Figure 6.10b. Note that the range of the colour scale is an order of magnitude higher than in the previous Figure 6.9 to better visualise the *SPG* distribution between the bars. Similar to the *SVG*, the pressure gradient sharply increases from 40 mm away from the bars up to the bar tips at both U_o values but reaches higher values at $U_o = 0.7$ m/s compared to $U_o = 0.5$ m/s with maximum values up to $SPG = 150$ Pa/cm around the upstream bar tips. Between the upstream bar tips, the minimum *SPG* values are around 40 Pa/cm and 80 Pa/cm at $U_o = 0.5$ m/s and at $U_o = 0.7$ m/s, respectively.

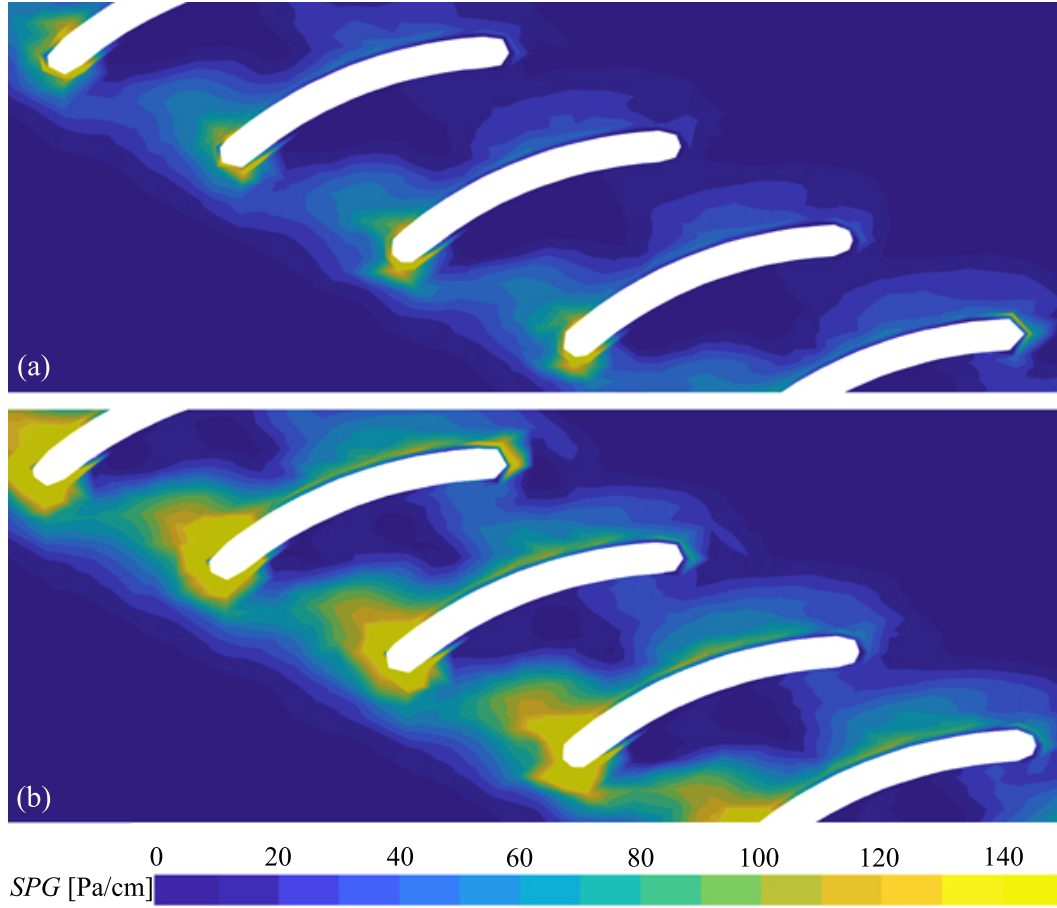


Figure 6.10 Spatial pressure gradient SPG between the bars of the CBR at $z/h_o = 0.14$ for $VR = 1.2$ and (a) $U_o = 0.5$ m/s, (b) $U_o = 0.7$ m/s

Figure 6.11 shows the velocity components in the rack-parallel cross section at a distance of 50 mm perpendicular to the rack. The rack normal V_n/U_o , and the rack parallel V_p/U_o normalised velocities gradually increase along the rack for all flow conditions along the upper rack part up to $y'/l_R \approx 0.5$ and remain almost constant along the lower rack part, which indicates a quasi-uniform flow distribution along the rack. The V_n/U_o values are slightly higher at $U_o = 0.7$ m/s compared to $U_o = 0.5$ m/s. The criterion of $V_n \leq 0.5$ m/s is always met at $U_o = 0.5$ m/s ($V_n/U_o \leq 1$) but is slightly exceeded at $U_o = 0.7$ m/s ($V_n/U_o \leq 0.71$) for $y'/l_R < 0.5$. The V_p/U_o values are clearly higher at $U_o = 0.7$ m/s compared to $U_o = 0.5$ m/s. The $FGC = V_p/V_n$ slightly decreases along the rack but remains above the critical value of $V_p/V_n > 1$ proposed by Courret and Larinier (2008) for effective fish guidance and is particularly high at the u/s rack end ($y'/l_R = 0.9$) due to the strong flow deflection towards the bypass. The FGC values are almost identical for all flow conditions, but start to diverge near the bypass ($y'/l_R = 0$), where the FGC is slightly higher for $VR = 1.4$ compared to $VR = 1.2$.

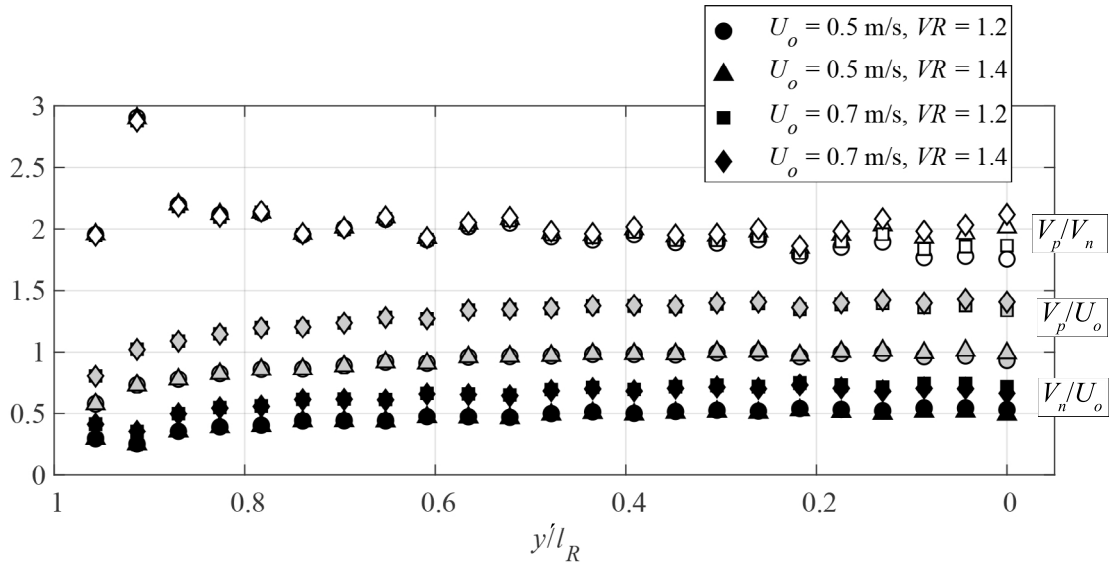


Figure 6.11 Velocity components $FGC = V_p/V_n$ (white markers), V_p/U_o (grey markers), and V_n/U_o (black markers) in the rack-parallel cross section of 50 mm distance for the four hydraulic conditions, simulated at $z/h_o = 0.14$

The comparison of the flow fields presented in Sections 6.1.1 and 6.1.2 demonstrates that already small changes in the approach flow field can affect the velocity field along the rack and at the bypass entrance. It is therefore of great importance to quantify the detailed flow field at a specific site to assess its impact on the fish guidance capacity of a planned FGS. Since the ethohydraulic tests were conducted in a 1.5 m wide flume, the model CBR only represented the last part of a prototype CBR. To achieve flow velocities favourable for a fast bypass acceptance, the bypass discharges in this laboratory study were $Q_{by} = (0.17...0.22) \cdot Q_o$ and thus disproportionately high compared to prototype conditions with $Q_{by} = (0.02...0.10) \cdot Q_o$ (Ebel, 2016). The flow field in the laboratory is therefore further affected by the high bypass discharge. The flow fields without a bypass presented in Section 4.2 thus roughly correspond to the flow fields at a prototype site, where the effect of the bypass on the flow field is expected to be only local. However, the velocity components along the CBR are very similar for both laboratory studies with and without bypass (compare Figure 4.12 with Figure 6.11) and hence expected to be similar at prototype scale.

6.1.3 Bypass hydraulics

Velocity measurements were conducted along the red line shown in Figure 6.12 for four different bypass layouts L1-L4 (Figure 3.9). The velocity components in the x , y and z directions (U , V , W) were measured 125 mm above the flume bed ($z = 0.14 \cdot h_o$) with an ADV probe.

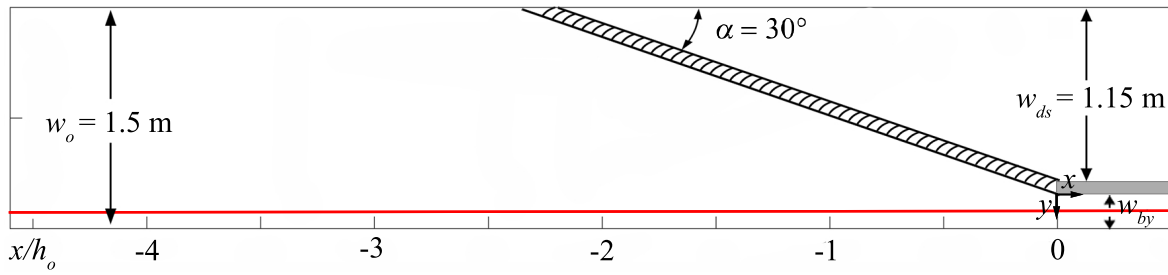


Figure 6.12 Schematic representation of the ethohydraulic flume with the installed CBR; the velocity profiles were measured close to the wall along the red line

Figure 6.13a shows the velocity profiles for the full-depth open channel bypass without a ramp (L1), with a 12° vertically inclined ramp (L2), and with a restrictor creating top and bottom openings (L3). The corresponding spatial velocity gradients in streamwise direction ($SVG_x = \partial u / \partial x$) are shown in Figure 6.13b. For L1, the velocity profiles were measured for different approach flow velocities $U_o = 0.3, 0.5, 0.7$ and 0.9 m/s, leading to different bypass discharge ratios $Q_{by}/Q_o = 17\ldots 23\%$. The bypass entrance velocity to the approach flow velocity ratio was kept at $VR = 1.4$. L1 leads to a gradual velocity increase towards the bypass from $x/h_o \approx -4$ up to -0.25 and a stronger increase directly at the inlet. The normalised velocities match well, whereas the SVG_x profiles differ particularly near and at the bypass by attaining the highest value of $SVG_{x,max} = 0.9 \text{ s}^{-1}$ at $U_o = 0.90$ m/s and the lowest value of $SVG_{x,min} = 0.25 \text{ s}^{-1}$ at $U_o = 0.30$ m/s (Figure 6.13b). Inside the bypass, the SVG_x rapidly decrease again, similar as shown in Figure 6.7. The installation of an inclined ramp in the bypass L2 creates a backwater effect so that the normalised velocities become lower compared to L1, and $SVG_{x,max} = 0.4 \text{ s}^{-1}$. The SVG_x values decrease downstream of the bypass entrance and gradually increase again over the inclined ramp. Due to the locally pressurised flow along the bottom opening of the restrictor (L3), the highest velocity gradients among the bypass layouts occur with $SVG_{x,max} = 1.2 \text{ s}^{-1}$.

The design of the pipe bypass (L4) leads to a strong backwater effect, resulting in an opposite trend for the velocity profiles compared to L1, L2 and L3, with decreasing velocities near the bypass inlet. From $x/h_o = -0.25$ up to the bypass inlet, the velocities sharply increase (Figure 6.14a). Increasing the bypass discharge Q_{by} reduces the velocity decrease at $x/h_o = -0.25$, but causes a strong increase in velocity and SVG_x between $x/h_o = -0.25$ and 0 (Figure 6.14b). The effect of the different bypass layouts on the fish behaviour are presented in Section 6.1.4.

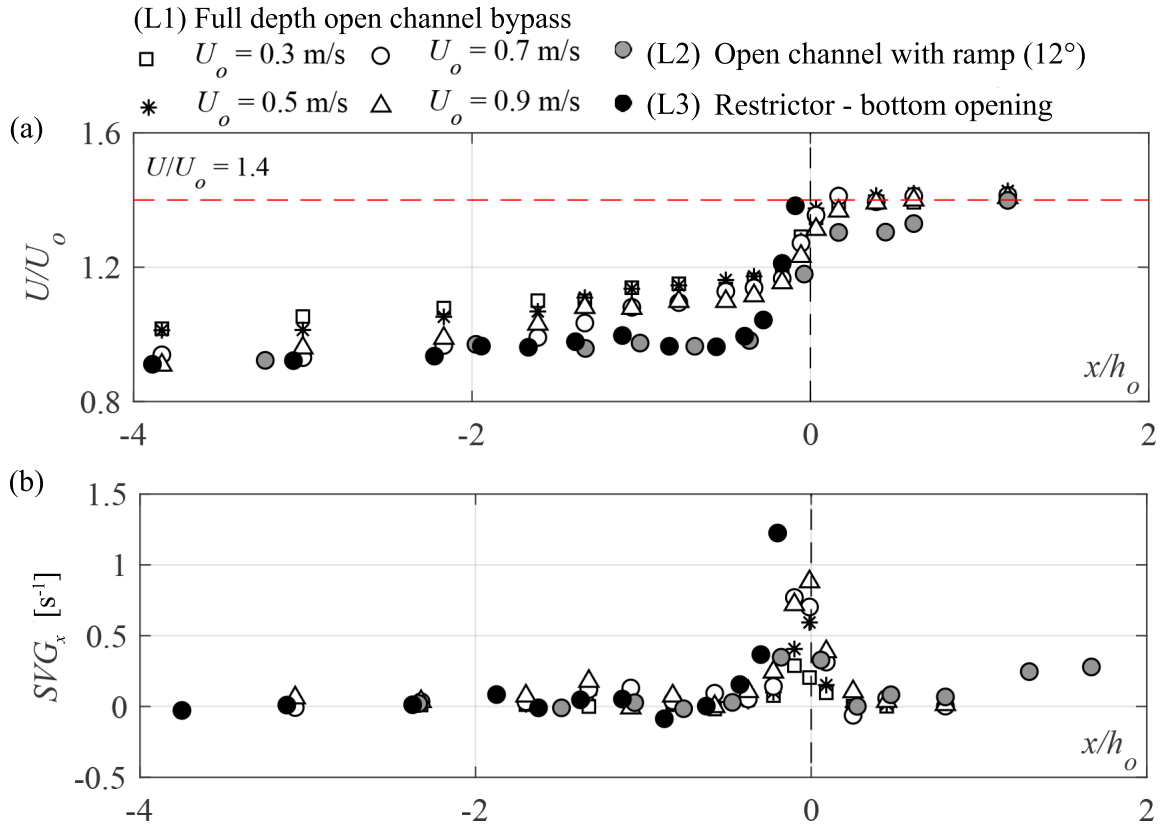


Figure 6.13 (a) velocity profile U/U_o and (b) spatial velocity gradient (SVG_x) for the bypass layouts L1-L3 (L2, L3 were only measured at $U_o = 0.7$ m/s), the bypass entrance is at $x/h_o = 0$

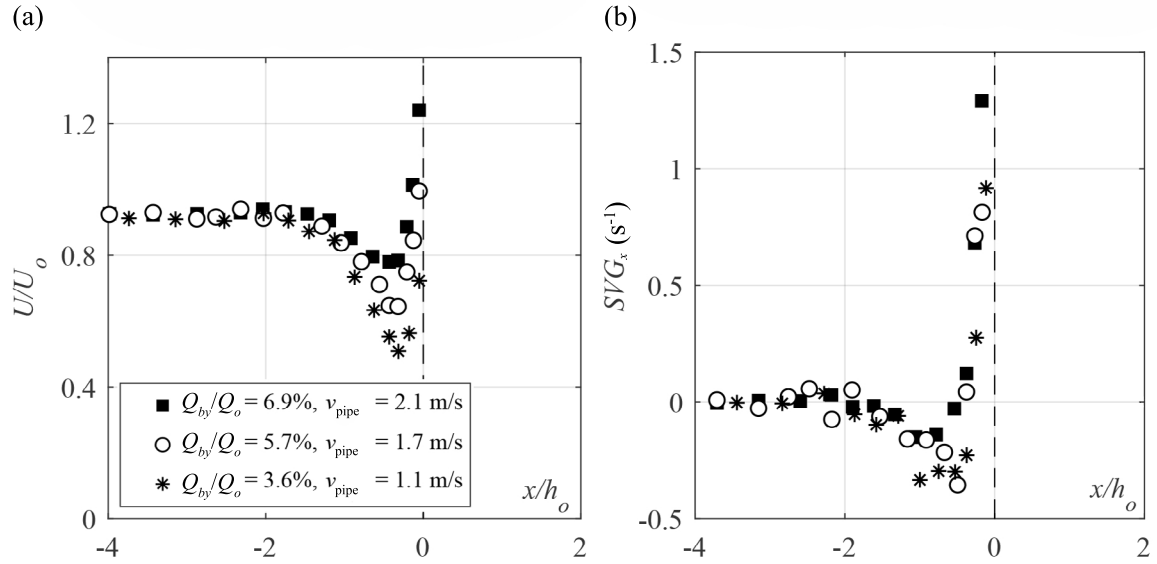


Figure 6.14 (a) velocity profile U/U_o with v_{pipe} = mean flow velocity inside the pipe, and (b) SVG_x upstream and directly in front of the pipe bypass (L4) for U_o , measured for different values of Q_{by}/Q_o

6.1.4 Effect of different bypass layouts on fish behaviour and guidance

Due to the unfavourable velocity profiles of the pipe bypass, the live-fish tests were only carried out for the bypass layouts L1-L3. Figure 6.15 shows the number of bypass passages and refusals for the tests with spiralin. Since no rack passages were observed, the fish protection efficiency (FPE) of the CBR-BS L1-L3 was 100% for all live-fish tests with spiralin. Even at $U_o = 0.7$ m/s (L1b) the fish were actively drifting to the rack with a positive rheotaxis and guided to the bypass. The comparison of the two test series with the full depth open channel bypass (L1a with $U_o = 0.5$ m/s, L1b with $U_o = 0.7$ m/s) shows that a higher SVG_x in case of L1b led to more refusals. Furthermore, lower SVG_x (L1a) resulted in a faster bypass acceptance (on average, 95 s for L1a and 225 s for L1b). The open channel bypass with the 12° inclined ramp (L2) led to more refusals. For this configuration ($U_o = 0.5$ m/s, $VR = 1.4$) the velocity profile was not measured, so that $SVG_{x,\max}$ is not known. It was observed that the fish hesitated not only at $x/h_o = 0$, but also at the transition region between $x/h_o = 0$ and 0.56, and along the ramp. In order to link such hesitant behaviour of the fish to the hydraulics, more detailed velocity measurements are needed for bypass layout L2. The velocity gradient in front of the bottom opening of the restrictor (L3) was the highest for $VR = 1.4$ (cf. Figure 6.13). To reduce the SVG_x , the bypass discharge was regulated, so that VR and the velocity v_{by} at the narrowest point of the bottom opening reduced to $VR = 1.0$ and $v_{by} = 0.75$ m/s, respectively. This regulation thus resulted in $v_{by}/U_o = 1.5$ and $SVG_{x,\max} \approx 0.55 \text{ s}^{-1}$, and the bypass acceptance of all tested fish (Figure 6.15). Baumgartner (2020) conducted a visual analysis of these ethohydraulic tests in the frame of a Bachelor's thesis and counted how many times on average the spiralin hesitated at the bypass entrance. Hesitation was thereby defined as an upstream swimming movement of at least one fish length. She found that fish hesitated on average 14.7 and 11.5 times for L2 and L3, respectively. In contrast, the fish only hesitated 0.7 times on average at the full depth open channel bypass (L1), which indicates that some fish entered this bypass type without any hesitation.

These results confirm that an unfavourably designed or unfavourably regulated bypass can lead to more refusals or reduce the bypass acceptance of fish. This in turn leads to a delayed downstream movement and increases the risk of a rack passage. Due to limited geometrical conditions in the laboratory, not all bypass layouts could be optimally regulated. The live-fish tests with spiralin showed that these fish react very sensitively to spatial velocity gradients, whereby the bypass was accepted by all spiralin up to $SVG_x \approx 0.6 \text{ s}^{-1}$. The high velocity gradients at the inlet of the pipe bypass might trigger an avoidance reaction if it was tested. In addition, HPP operators' experience has shown that this type of bypass quickly clogs with floating and submerged debris or sediment and is difficult to clean. In order to

achieve high acceptance, a bellmouth inlet (similar to L3) should be designed in such a way that the velocity gradients remain small. To confirm these findings, more detailed velocity measurements are necessary.

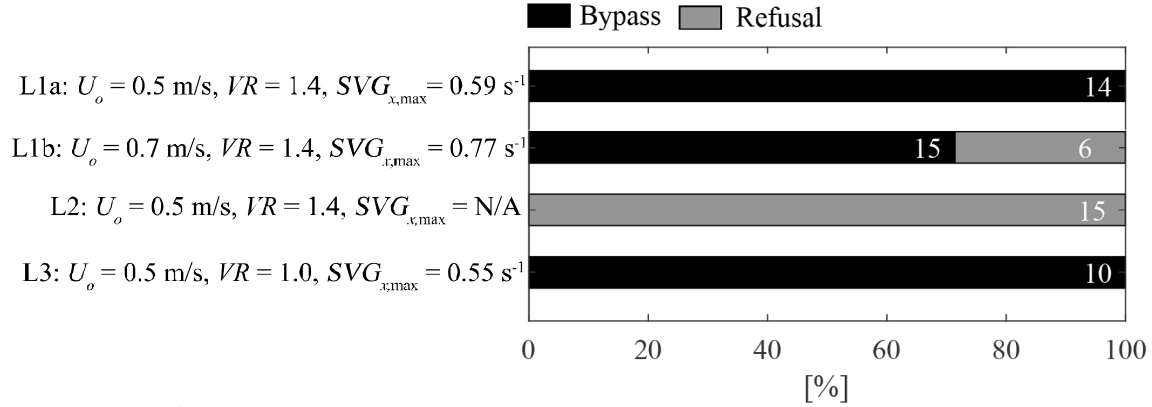


Figure 6.15 Bypass passages and refusals for spiralin (absolute numbers of fish given in white) with $U_o = 0.5$ m/s and 0.7 m/s for bypass layout L1 and $U_o = 0.5$ m/s for L2 and L3

The tested CBR in the ethohydraulic flume only represents the most downstream section of a prototype rack. Consequently, the relative bypass flow Q_{by}/Q_o in the laboratory is significantly higher than in prototype. However, the parameters VR and SVG_x , which are relevant for the fish behaviour and the bypass efficiency, are modelled correctly and can thus be compared to prototype conditions. Although most available guidelines recommend a bypass discharge as a percentage of the approach flow discharge, the presented results indicate that the SVG_x in front of the bypass is the decisive parameter for an efficient bypass design, which is quickly accepted by fish (Figure 6.15). For spiralin, acceptance was faster at low SVG_x . The comparison with the recommendations for salmonids shows that spiralin are more sensitive to velocity gradients and prefer lower SVG_x . Further experiments with different fish species are therefore needed to improve the knowledge on the interactions between fish behaviour and bypass hydraulics and hence to optimise bypass designs.

6.2 Protection and guidance efficiencies of curved-bar rack bypass systems

In this section, the fish protection and guidance efficiencies of the optimised CBR-BS and the general swimming behaviour of the tested fish species are analysed and discussed for each fish species separately. The tested CBR-BS featured $\alpha = 30^\circ$, $\beta = 45^\circ$, $\sigma = 0.17$ ($s_b = 50$ mm) and a full depth open channel bypass. The parameters significantly affecting the fish's reactions to the CBR-BS are identified with a logistic regression model. The tested

fish species are spirlin, barbel, nase, European eel, Atlantic salmon parr and brown trout. The swimming behaviour of these fish species is cross-compared in detail by introducing a so-called residence coefficient. The rack passage locations along the rack are compared. The absolute swimming velocities and locations of rheotaxis changes determined from the individual fish swimming paths are presented. Finally, the fish protection and guidance efficiencies of the CBR-BS are compared to other FGSs.

6.2.1 Spirlin

Spirlin showed an active swimming behaviour during all tests. Shortly after the test start, they left the starting compartment and swam downstream with positive rheotaxis in a zig-zag movement. The three fish tested per experiment showed a strong schooling behaviour. Spirlin generally avoided direct contact with all structures, i.e. the flume bed and walls, or the rack. When first approaching the CBR, the spirlin swam at a distance of approx. 15–30 cm to the rack and were guided quickly to the bypass. In section 3.6, the rack interaction was defined with the fish swimming into a 15 cm wide rack-parallel area (sector 5) during the test. Figure 6.16 shows the FGE at the end of the green bar (percentage of bypass passages with rack interaction) and FPE at the end of the yellow bar (percentages of bypass passages plus refusals) for spirlin. Because the spirlin tended to keep a distance of more than 15 cm to the rack, only a small number of fish swam into sector 5 and therefore the number of fish swimming into the bypass with rack interaction is small. None of the tested spirlin passed the CBR. The FPE was therefore 100% at all tested flow conditions.

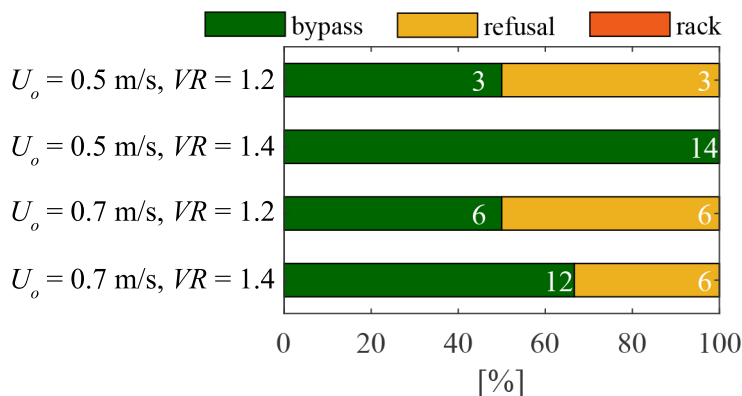


Figure 6.16 Bypass passages with rack interaction (for a 15 cm wide rack-parallel sector 5) and refusals for spirlin (absolute numbers of fish given in white) (Tests E4, E10, E18, E21)

The visual observation during the tests indicated, however, that the spirlin still perceived the installed CBR as an obstacle because of the positive transverse velocities towards the bypass

(Figure 6.2) and were guided by it. For this fish species, the sector 5 was therefore extended to a 30 cm wide rack-parallel area and the definition of a bypass passage with rack interaction adjusted accordingly. Figure 6.17a shows the FGE (percent of bypass passages with rack interaction = fish swimming into the 30 cm wide sector 5) and FPE (percent of bypass passages plus refusals) for spirlin. Figure 6.17b shows the FGE* and the FPE* (including all bypass passages both with and without rack interaction). The absolute numbers of fish are given in white colour for each configuration. In addition to the tests with four different hydraulic conditions, some spirlin were also tested without a CBR installed in the flume (no rack). For the no-rack-configuration, the distinction between FGE and FGE* is not made. Without a CBR installed, the FGE = 14%, i.e. 86% of the spirlin swam into the downstream channel, which roughly corresponds to the discharge distribution between the bypass and the downstream channel. The installation of the CBR resulted in significantly higher FGEs with 63–100% ($FGE_{\text{mean}} = 79\%$) ($\chi^2 = 26.649$, $p < 0.001$), which demonstrates that the CBR functions as a mechanical behavioural barrier. The FGE is significantly higher and the refusal rate is hence significantly lower at $U_o = 0.5$ m/s compared to $U_o = 0.7$ m/s ($\chi^2 = 4.595$, $p = 0.032$). Furthermore, the spirlin needed more time to find and accept the bypass at $U_o = 0.7$ m/s compared to $U_o = 0.5$ m/s (cf. Figure 6.29d), indicating a significant effect of U_o on the FGE for spirlin. These results are in good agreement with the observations reported by Flügel *et al.* (2015), where more refusals of spirlin at the MBR were observed at $U_o = 0.6$ m/s compared to 0.3 m/s. Independent of the flow conditions, no spirlin passed the rack, resulting in FPE = 100% for all tests with the CBR. Spirlin reacted sensitively to the spatial velocity gradient at the entrance of different bypass layouts and showed an avoidance reaction for $SVG_x > 0.6 \text{ s}^{-1}$ (cf. Figure 6.15). Figure 6.7 indicates that a corridor into the bypass with $SVG_x < 0.6 \text{ s}^{-1}$ is available for each of the four main flow conditions and thus no significant difference is observed in the FGE for different VR values ($\chi^2 = 0.271$, $p = 0.603$). However, this corridor is considerably narrower at $U_o = 0.7$ m/s compared to $U_o = 0.5$ m/s, which could explain the significantly increased number of refusals at $U_o = 0.7$ m/s.

The $FGE^* = 78 - 100\%$ without rack interaction is higher than the FGE with rack interaction. The absolute number of bypass passages considered in this analysis almost doubles indicating that many fish swam into the bypass without rack interaction. While Figure 6.17a shows the protection and guidance efficiency of the entire CBR-BS with rack interaction, Figure 6.17b also includes those fish without rack interaction and can therefore be used as an indicator for the bypass acceptance. The effect of U_o on the bypass acceptance in Figure 6.17b is significant ($\chi^2 = 5.023$, $p = 0.025$), while the effect of VR is not significant ($\chi^2 = 0.060$, $p = 0.807$). This confirms that the narrower corridor of $SVG_x < 0.6 \text{ s}^{-1}$ for

$U_o = 0.7$ m/s compared to $U_o = 0.5$ m/s leads to a significantly decreased bypass acceptance rate and thus to more refusals.

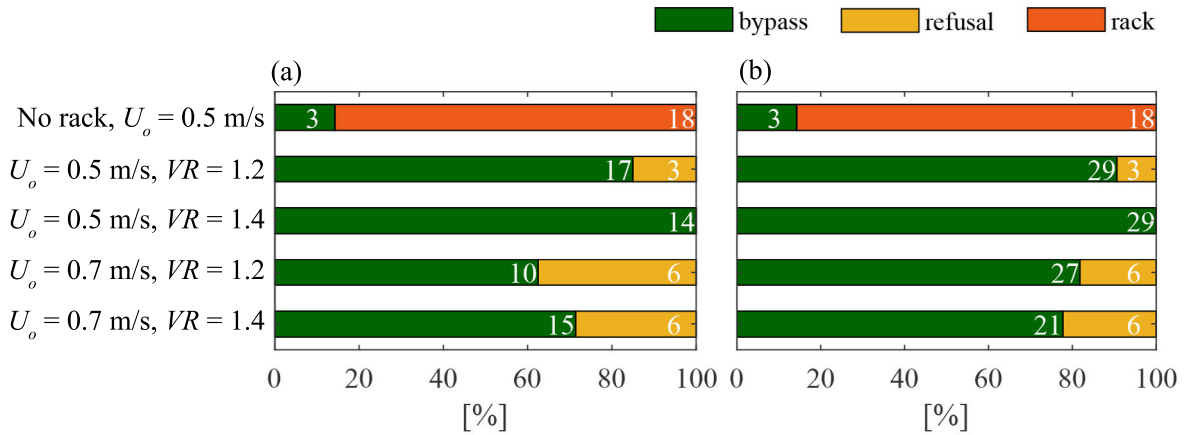


Figure 6.17 Rack passages, refusals, and (a) bypass passages with rack interaction for a 30 cm wide rack-parallel sector 5 (FGE) and (b) all bypass passages (FGE*) for spiralin (absolute numbers of fish given in white) (Tests E4, E10, E18, E21)

Figure 6.18 shows the normalised residence coefficient $R_{c,norm}$ for each sector (see Figure 3.12 for the definition of the different sectors). $R_{c,norm}$ is used as a measure to quantify the preference of the fish for each sector. The sectors 1-3 thereby describe the areas further upstream of the rack, which are mostly unaffected by the rack, whereas sectors 4-7 define the area just upstream of the rack, where the rack strongly affects the flow field (cf. Figures 6.2 and 6.6). Without the CBR installed, the fish spent more time in the sectors along the upstream walls (Sec1, Sec2), preferring both walls equally, than in the upstream centre sector (Sec3). With a CBR installed, however, they clearly preferred the right wall leading to the bypass (Sec2, Sec7) to the opposite, left flume wall (Sec1). This comparison between the tests without a rack and with a CBR installed demonstrates, that even though many fish entered the bypass without direct rack interaction (Figure 6.17), these fish reacted sensitively to changes in the flow field, and were guided towards the right flume wall and the bypass by the positive transverse velocities caused by the CBR (Figure 6.2). The most interesting finding is the residence time in the 15 cm wide rack-parallel sector 5. The spiralin spent much more time close to the rack (Sec5) for $VR = 1.4$ compared to $VR = 1.2$. This result is unexpected, since VR did not have a statistically significant effect on the FGE. Furthermore, the number of attempts to swim into the bypass was not significantly different for $VR = 1.2$ or $VR = 1.4$ (Baumgartner, 2020). At $U_o = 0.7$ m/s, however, the spiralin needed less time to find the bypass for $VR = 1.4$ compared to $VR = 1.2$ (cf. Figure 6.29b). If the bypass was not accepted in the first attempt, the spiralin swam back upstream along the right flume wall (Sec2, Sec7) for $VR = 1.2$, while they swam upstream along the rack (Sec5) for $VR = 1.4$. It

is possible that the negative transverse velocities at the d/s rack end at $VR = 1.2$ (Figure 6.2) led to an increased avoidance of this area by the spirlin. This behaviour did not lead to a rack passage in the laboratory tests (cf. Figure 6.17), however. At a prototype CBR, however, the risk of a rack passage for spirlin is expected to be higher if the bypass is not accepted quickly because the fish will search for alternative passages along a longer rack.

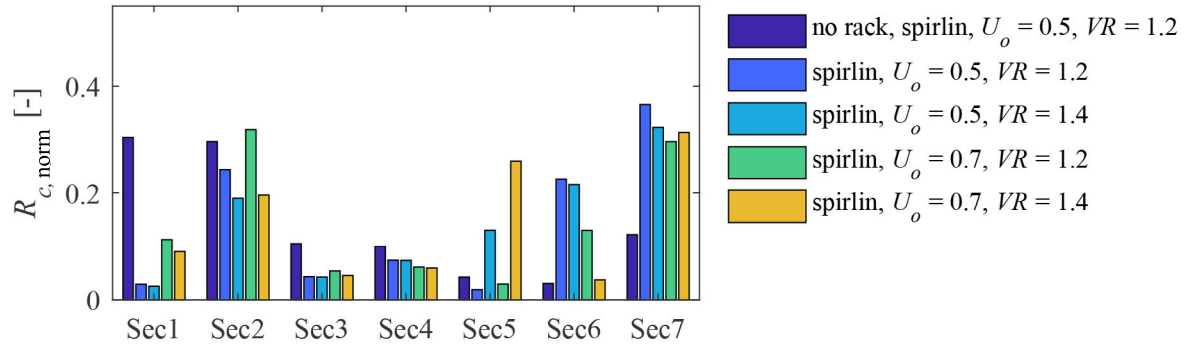


Figure 6.18 Normalised residence coefficient of spirlin in each sector without a CBR installed (no rack) and with the CBR for different flow conditions

6.2.2 Barbel

Barbel showed a different swimming behaviour compared to spirlin. Although also mostly swimming in positive rheotaxis, the barbel were more passive, spending more time in the starting compartment on the one hand and preferring the low velocity regions of the flume on the other hand. Because of their ability to rest their bodies on the flume bed by putting down their pectoral fins, they could stay in the flume corners along the walls or just in front of the rack for longer periods of time with minimum energy expenditure. Furthermore, they showed a strong thigmotactic behaviour, i.e. moving closely along the flume walls and exploring the rack with their tail fins. This behaviour of barbel was also observed by Clough *et al.* (2004) and Albayrak *et al.* (2020a). The barbel were rarely swimming actively against the current, and mostly let themselves drift passively downstream between longer resting periods. In contrast to the swimming behaviour during the rack passages described in Albayrak *et al.* (2020a), the barbel in the present study never lost control due to the more favourable flow conditions along the CBR as compared to the flow fields of louvers and MBRs with strong flow deflection towards the downstream channel at the d/s rack end (cf. Section 6.1.1).

Figure 6.19a shows the FGE and FPE for barbel. The FGE is slightly lower than for spirlin with a range of 54-89% ($FGE_{\text{mean}} = 76\%$). Although the FGE for barbel was higher at $U_o = 0.7$ m/s than at $U_o = 0.5$ m/s, the effect of U_o on the bypass passages, i.e. the FGE, was not statistically significant ($\chi^2 = 2.727$, $p = 0.099$, Table 6.1). Increasing U_o caused less rack passages and more refusals leading to $FPE = 100\%$ at $U_o = 0.7$ m/s and a significant effect

on the rack passages ($\chi^2 = 10.417$, $p = 0.001$). The barbel could maintain their sustained swimming speed for all tested flow conditions (cf. Table 6.6). However, the maximum absolute flow velocity between the bars of $U_r = 1.05$ m/s at $U_o = 0.7$ m/s exceeds the prolonged swimming speed of most tested barbel, which might trigger an increased avoidance reaction compared to $U_o = 0.5$ m/s. The spatial velocity and pressure gradients between the bars are higher at $U_o = 0.7$ m/s compared to $U_o = 0.5$ m/s (Figure 6.8 and Figure 6.10), possibly leading to a stronger avoidance behaviour and therefore to less rack passages at $U_o = 0.7$ m/s for the barbel. At $U_o = 0.5$ m/s, more rack passages were observed for $VR = 1.4$ than for the lower $VR = 1.2$. The effects of VR on the fish reaction or the bypass acceptance were not significant, however (Table 6.1).

Figure 6.19b shows the FGE* and the FPE* for barbel. The FGE* and thus the bypass acceptance is 74-91% and is therefore higher than the FGE. Since barbel preferred to swim or drift along the right flume wall in front of the bypass, many fish entered the bypass without rack interaction.

Table 6.1 Result of the χ^2 test for barbel including only the bypass passages with rack interaction, and including all bypass passages with and without rack interaction, data taken from Figure 6.19

		bypass		rack passage		refusal	
		<i>p</i> -value	χ^2	<i>p</i> -value	χ^2	<i>p</i> -value	χ^2
with rack	$U_o : 0.5/0.7$	0.099	2.727	0.001	10.417	0.169	1.890
interaction only	$VR: 1.2/1.4$	0.912	0.012	0.838	0.042	0.797	0.066
including all	$U_o : 0.5/0.7$	0.353	0.863	0.009	6.770	0.092	2.849
bypass passages	$VR: 1.2/1.4$	0.817	0.053	0.757	0.096	0.750	0.102

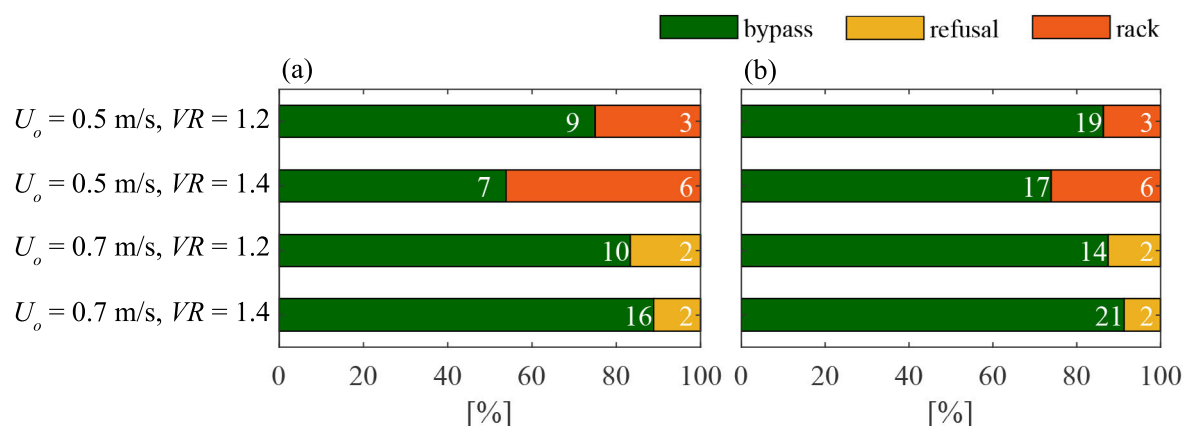


Figure 6.19 Rack passages, refusals, and (a) bypass passages with rack interaction (FGE) and (b) all bypass passages (FGE*) for barbel (absolute numbers of fish given in white) (Tests E5, E11, E19, E22)

The analysis of $R_{c,norm}$ for each sector confirms the observation that barbel preferred the low velocity regions (Figure 6.20). For the majority of the time, they swam along the walls or close to the rack (Sec1, Sec2, Sec5, Sec7) and only rarely in the flume centre (Sec3, Sec4). The barbel often swam to the right flume wall shortly after leaving the starting compartment, which led to a higher $R_{c,norm}$ for Sec2 compared to Sec1 and to many bypass passages without rack interaction (Figure 6.19). Since the flow is expected to be unaffected by the CBR this far upstream of the rack, the reason for this preference is unclear. A possible explanation could be the asymmetry of the inflow (Figure 6.1). No tests were conducted with barbel without a rack installed or during the second test phase, where the inflow was more symmetric. The barbel spent the least amount of time in the rack-parallel Sector 5 at $U_o = 0.5$ m/s and $VR = 1.2$. This result is attributed to the increased velocity gradients at the bypass entrance for higher U_o and higher VR leading to more hesitation at the bypass (cf. Section 6.1.1). Although the barbel interacted more with the rack at $U_o = 0.7$ m/s, more rack passages occurred at $U_o = 0.5$ m/s, which indicates that the behavioural barrier effect of the CBR is stronger at $U_o = 0.7$ m/s compared to $U_o = 0.5$ m/s.

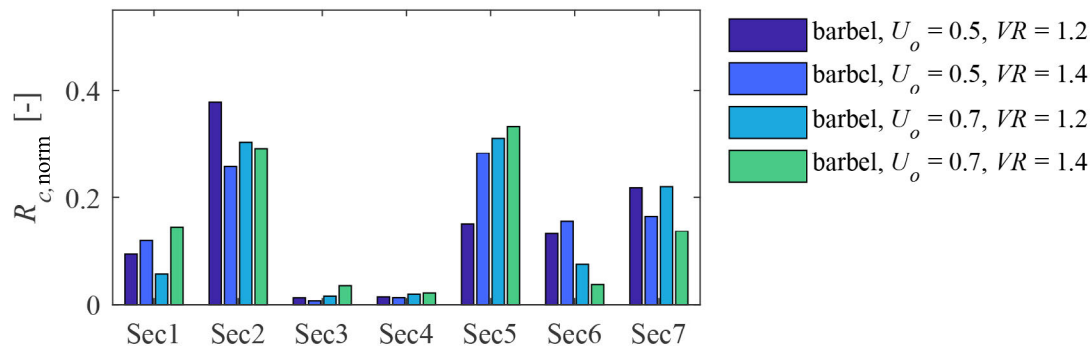


Figure 6.20 Normalised residence coefficient of barbel in each sector for different flow conditions

6.2.3 Nase

Nase showed a similar swimming behaviour as the spirlin. They exited the starting compartment quickly and actively swam downstream with positive rheotaxis using the entire flume width. Similar to the spirlin, the nase did not touch the rack, but perceived the CBR as an obstacle due to the increased velocity and pressure gradients upstream of the rack (Figure 6.8 and Figure 6.10). When approaching the CBR, the nase searched actively in the 15 cm wide rack parallel area (Sec5). All tested fish interacted with the rack, i.e. swam into sector 5, and no refusals occurred, thus $FGE = FPE = FGE^* = FPE^*$ in Figure 6.21 for both flow conditions. Since some of the nase hesitated to use the bypass and hence ended up passing the rack at $VR = 1.2$, the bypass flow was reduced to $VR = 1.1$ (Figure 6.21). The flow fields were not measured or simulated for $VR = 1.1$, however. Although the number of fish

tested for the latter was small and the effect of VR on the FGE is not significant ($\chi^2 = 0.886$, $p = 0.347$), visual observations indicated, that the nose hesitated less at the bypass and accepted it quickly (cf. Figure 6.29b). Figure 6.22 confirms this observation. The $R_{c, \text{norm}}$ of Sec5 is considerably higher for $VR = 1.2$ than for $VR = 1.1$ indicating that nose spent more time searching along the rack when the bypass was not quickly accepted. The mean total length of the nose was 7.2 cm while it was 10 cm for the spiralin. It is therefore possible that the stronger hesitation reaction of the nose compared to the spiralin is related to their smaller total length and lower swimming capacities (cf. Table 6.6). Although the nose were swimming at their prolonged swimming speed at $U_o = 0.5$ m/s according to Ebel (2016), they did not prefer the low velocity regions along the flume walls.

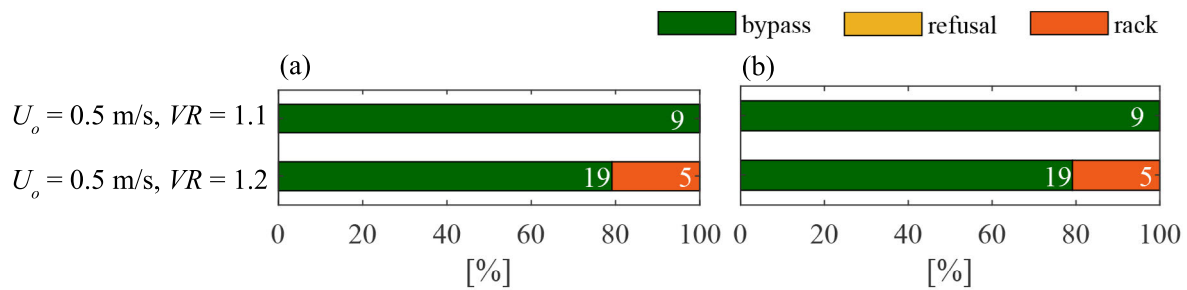


Figure 6.21 Rack passages and (a) bypass passages with rack interaction (FGE) and (b) all bypass passages (FGE*) for nose (absolute numbers of fish given in white) (Tests E3, E8)

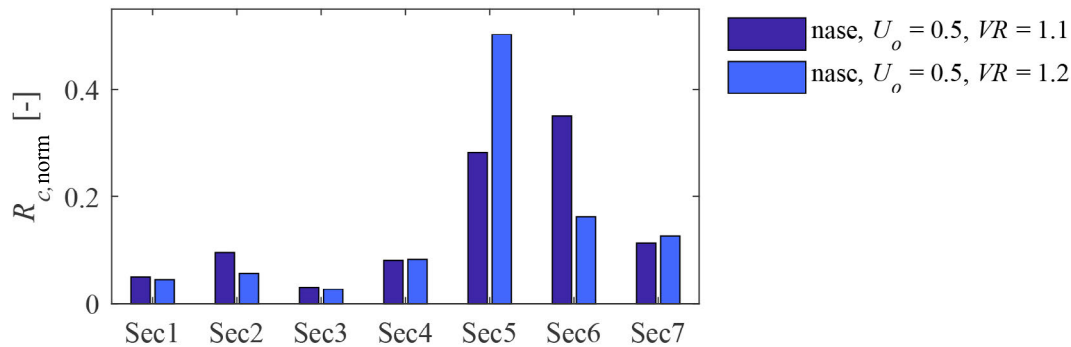


Figure 6.22 Normalised residence coefficient of nose in each sector for $U_o = 0.5$ m/s, $VR = 1.1, 1.2$

6.2.4 European Eel

The swimming behaviour of European eel was completely different compared to the other tested fish species. In most of the tests, the eel approached the CBR with negative rheotaxis, collided with the rack and passed it without hesitation. This swimming behaviour is similar as described in Silva *et al.* (2016), and Schwevers and Adam (2019). The eel were insensitive to the hydrodynamic cues created by the CBR, which led to a low FGE and FPE of

27% (Figure 6.23a). Since they preferred to swim along the wall and were thus guided to the bypass without rack interaction, the $FGE^* = FPE^*$ is higher with 43% (Figure 6.23b). The $R_{c,norm}$ values for the eel are shown in Figure 6.24. Only one hydraulic condition with $U_o = 0.5$ m/s and $VR = 1.2$ was tested with eel. The $R_{c,norm}$ values are higher along the walls and at the rack, because the eel preferred to swim along the structures and interact with them. Note that the total number of experiments conducted with eel is small due to limited catch rate of these fish at the time of the live-fish tests. Since the eel did not react to the physical or behavioural barrier effects of the CBR, increasing the number of tested individuals might not change the resulting FGE and FPE. However, more tests with European eel are recommended for a larger range of hydraulic conditions. Moreover, different monitoring studies have shown that European eel prefer migrating at night (e.g. Adam *et al.*, 2018; Adam, 2018). Since their swimming behaviour can be considerably different in the dark, night experiments are recommended.

Because of the low resulting FGE with the CBR for European eel, the CBR was equipped with a low-voltage electric field to increase the protection and guidance of these fish. The results of the live-fish tests with eel at the e-CBR are presented in Chapter 7.

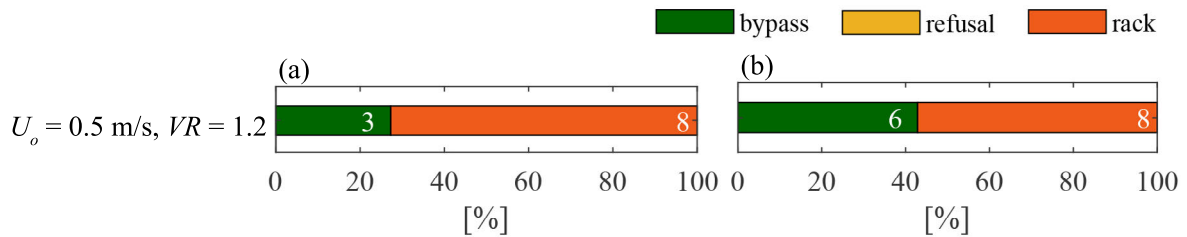


Figure 6.23 Rack passages and (a) bypass passages with rack interaction (FGE) and (b) all bypass passages (FGE*) for the European eel (absolute numbers of fish given in white) (Test E9)

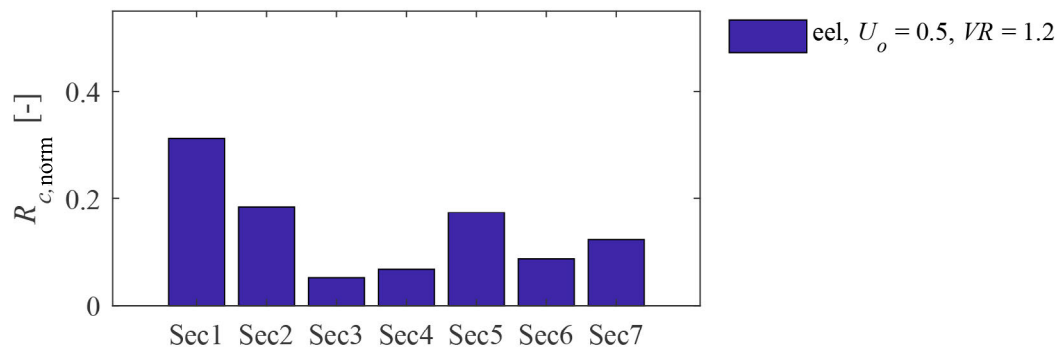


Figure 6.24 Normalised residence coefficient of the European eel in each sector for $U_o = 0.5$ m/s and $VR = 1.2$

6.2.5 Atlantic salmon parr

The salmon parr left the starting compartment quickly and actively swam downstream in positive rheotaxis. The three fish of each test often swam together in a school. Due to the limited number of fish available for the experiments, the salmon parr were only tested at $U_o = 0.5$ m/s. The FGE was high with 88% and 79% for $VR = 1.2$ and $VR = 1.4$, respectively (Figure 6.25a). The effect of VR on the FGE is not significant ($\chi^2 = 0.238$, $p = 0.625$). More rack passages were observed for $VR = 1.4$ compared to $VR = 1.2$, although this difference is not significant ($\chi^2 = 0.855$, $p = 0.355$). Due to the close interaction of the fish with the CBR, the values for FGE* and FPE* are only marginally higher (Figure 6.25b). These results are confirmed in Figure 6.26 showing similar residence times for all sectors for both VR values and only slightly higher $R_{c,norm}$ values in Sec5 for $VR = 1.4$, reflecting the increased number of rack passages. The $R_{c,norm}$ values are clearly higher for sectors 5 and 6 than for the other sectors, which can be attributed to a high willingness of the fish to move downstream and thus actively exploring the available passage options of the CBR and the bypass. The salmon parr generally swam close to the rack with a distance of a few centimetres. The behaviour described by Bates and Vinsonhaler (1957) shown in Figure 2.11b was often observed during the present live-fish tests, where fish repeatedly moved away from the rack, approached it again and were thereby guided to the bypass. Sometimes they interacted with the CBR and explored the spaces between two bars with their caudal fins. The visual observations indicated that the fish reacted with burst swimming against the flow between the bars. The flow fields around the CBR and between the bars are shown and discussed in detail in Section 6.1.2, where they are simulated with a numerical model. The flow detachment at the upstream bar tips leads to a distinct shear layer and high velocity and pressure gradients, which are perceived and avoided by the fish. These results therefore confirm the findings of Haro *et al.* (1998) and Enders *et al.* (2012), stating that SVG_x values much higher than 1.0 s^{-1} lead to a hesitation reaction for Atlantic salmon parr. Although the salmon parr were not tested at $U_o = 0.7$ m/s (because of the limited catch rate of these fish), the FGE and FPE could be similarly high or even higher at $U_o = 0.7$ m/s compared to $U_o = 0.5$ m/s because of the higher velocity and pressure gradients between the bars.

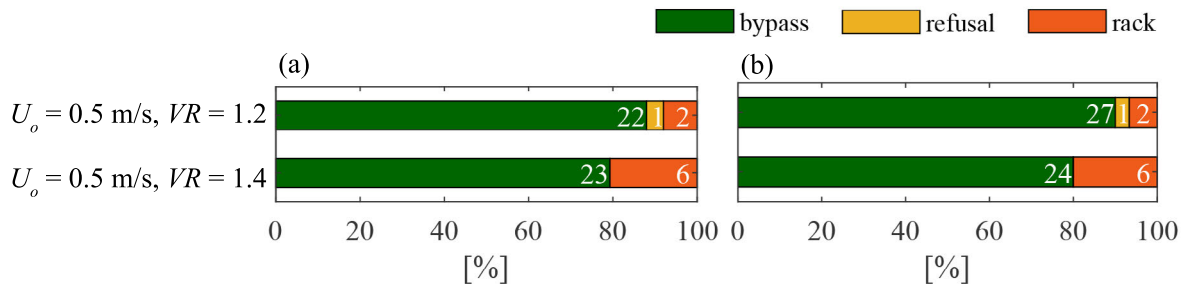


Figure 6.25 Rack passages, refusals and (a) bypass passages with rack interaction (FGE) and (b) all bypass passages (FGE*) for Atlantic salmon parr (absolute numbers of fish given in white) (Tests E7, E13)

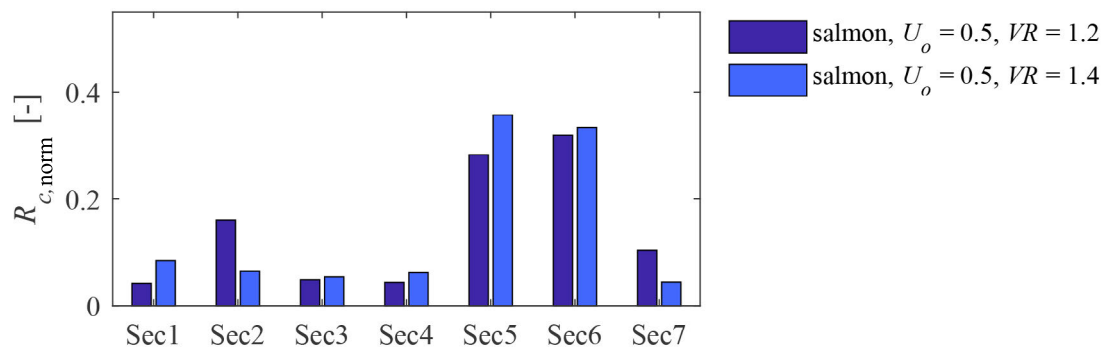


Figure 6.26 Normalised residence coefficient of Atlantic salmon parr in each sector for $U_o = 0.5 \text{ m/s}$, $VR = 1.2$ and 1.4

6.2.6 Brown trout

The brown trout were the most inactive among all tested fish species, i.e. they left the starting compartment only after a few minutes or did not exit it at all. Once the trout left the starting compartment, however, they swam actively in mostly positive rheotaxis, showing only a weak schooling behaviour. The trout explored the flow between the bars with their caudal fin, often reacting with swimming upstream for a few fish lengths, rheotaxis changes along the rack as described by Anderson *et al.* (1998) and illustrated in Figure 2.11c, or with a rack passage. It was often observed that the fish swam halfway between two bars with positive rheotaxis, were guided along a few bars, thereby touching each bar, but finally turned around and passed the rack with negative rheotaxis. This strong thigmotactic behaviour was observed in the majority of the tests. The FGE for brown trout was low with 30% and 43% for $U_o = 0.5 \text{ m/s}$ and 0.7 m/s , respectively, and significantly higher with 79% for $U_o = 0.3 \text{ m/s}$ ($\chi^2 = 4.361$, $p = 0.037$, Figure 6.27a, Table 6.2). This result is surprising, since the spatial velocity and pressure gradients between the bars increase at higher U_o . Since the flow field was not measured or simulated for $U_o = 0.3 \text{ m/s}$, it remains unclear why the FGE was much higher for this flow condition. Compared to the FGE, the FPE was higher with 59-79%.

The FPE was higher for $VR = 1.2$ compared to $VR = 1.4$ at each approach flow velocity, indicating that lower bypass flows with lower SVG_x values are more favourable for trout. This effect was not statistically significant, however ($\chi^2 = 0.676$, $p = 0.411$). Due to the close interaction with the CBR, the values for FGE^* and FPE^* are only marginally higher (Figure 6.27b).

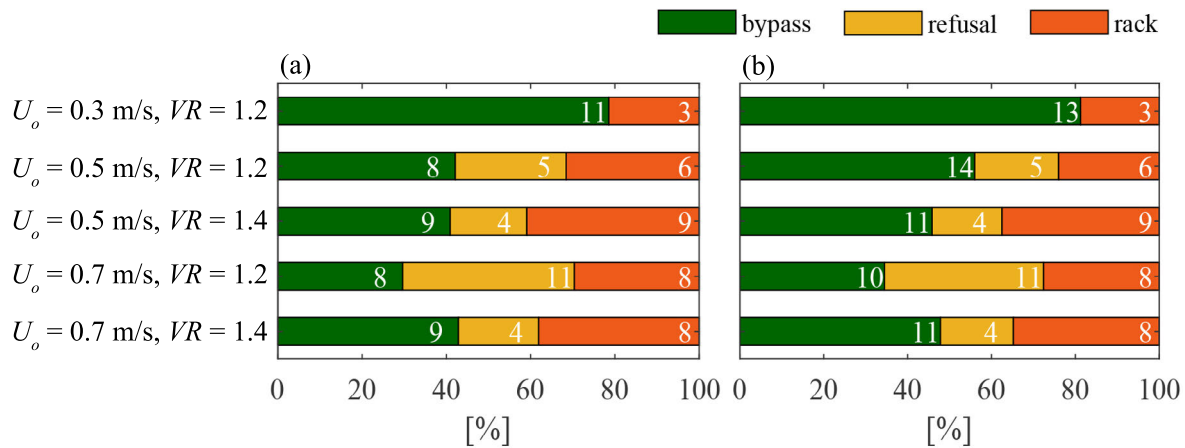


Figure 6.27 Rack passages, refusals and (a) bypass passages with rack interaction (FGE) and (b) all bypass passages (FGE^*) for brown trout (absolute numbers of fish given in white) (Tests E2, E6, E12, E20, E23)

Table 6.2 Result of the χ^2 test for brown trout, data taken from Figure 6.27a, the FPE represents the sum of bypass passages and refusals

	bypass		rack passage		refusal		FPE	
	<i>p</i> -value	χ^2	<i>p</i> -value	χ^2	<i>p</i> -value	χ^2	<i>p</i> -value	χ^2
$U_o : 0.3/0.5$	0.037	4.361	0.475	0.509	0.134	2.246	0.475	0.509
$U_o : 0.5/0.7$	0.714	0.134	0.922	0.010	0.456	0.556	0.922	0.010
$VR: 1.2/1.4$	0.991	0.000	0.286	1.138	0.512	0.430	0.411	0.676

Figure 6.28 depicts that the residence time was similar along the walls (Sec1, Sec2) or in the flume centre (Sec3) further upstream of the CBR. Higher $R_{c,norm}$ values in Sec5 do not correlate with a lower FPE, which indicates that these fish were not sensitive to VR or U_o in the tested range.

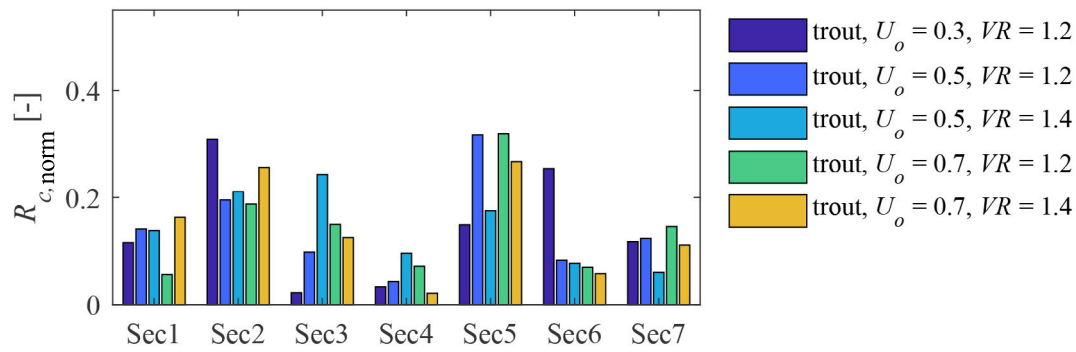


Figure 6.28 Normalised residence coefficient of brown trout in each sector for different flow conditions

6.2.7 Cross-comparison of the tested fish species

In Figure 6.29a, the normalised residence coefficients $R_{c,norm}$ in sector 5 of different fish species are compared for the range of tested VR values. The results demonstrate that the time the fish spent in sector 5 substantially increases with increasing VR for all fish species except for the brown trout. Figure 6.29c shows the $R_{c,norm}$ values versus U_o for the different fish species. The time spent in sector 5 increases with increasing U_o and its magnitude depends on the fish species. The comparison of Figures 6.29a and 6.29c reveals that the effect of VR on $R_{c,norm}$ of sector 5 is larger than the effect of U_o . The nase spent most of the time in sector 5 among all fish species with some 50% for $VR = 1.2$. Although higher $R_{c,norm}$ values were not always correlated with a lower FGE or FPE, they are still an important indicator for the transferability of the results to prototype dimensions, because they increase the risk of a rack passage for longer CBRs. Based on these results, lower values of $VR \leq 1.2$ are recommended for most species, whereas it is recommended to test $VR \geq 1.4$ for brown trout.

Figures 6.29b and 6.29d show how much time on average the fish spent to swim from line 1 into the bypass versus VR and U_o , respectively. No clear trend is visible for VR . In contrast, increasing U_o increased the time for fish to find and accept the bypass (Figure 6.29d). This result indicates that the higher energy expenditure of the fish at $U_o = 0.7$ m/s might decrease their sensitivity to the hydrodynamic cues leading to the bypass. Among the tested fish species, the salmon parr and the barbel needed the least amount of time to find and accept the bypass. Although the Atlantic salmon parr and the brown trout both belong to the salmonid species and their swimming behaviour at the rack was similar, the resulting FGE and FPE values are considerably different. Furthermore, the salmon parr quickly found and accepted the bypass (88-100 s), whereas the brown trout were searching much longer (256-405 s). This result indicates that the bypass attraction was not high enough for the brown trout with the maximum value of $VR = 1.4$ and that these fish might prefer higher velocity gradients.

Figure 6.30 shows $R_{c,norm}$ for all sectors and all six tested fish species at $U_o = 0.5$ m/s and $VR = 1.2$. In general, all fish equally used the low velocity regions along the flume walls (Sec1 and Sec2), with some exceptions (e.g. the nase). barbel and spirlin particularly preferred the glass wall on the right flume side leading into the bypass (Sec2, Sec7) to the mortar wall on the left flume side (Sec1). The most interesting result are the $R_{c,norm}$ values of the 15 cm wide, rack-parallel sector 5. Among the tested fish species, the spirlin spent the least amount of time in sector 5, which coincides with the result that no rack passage was observed for this fish species.

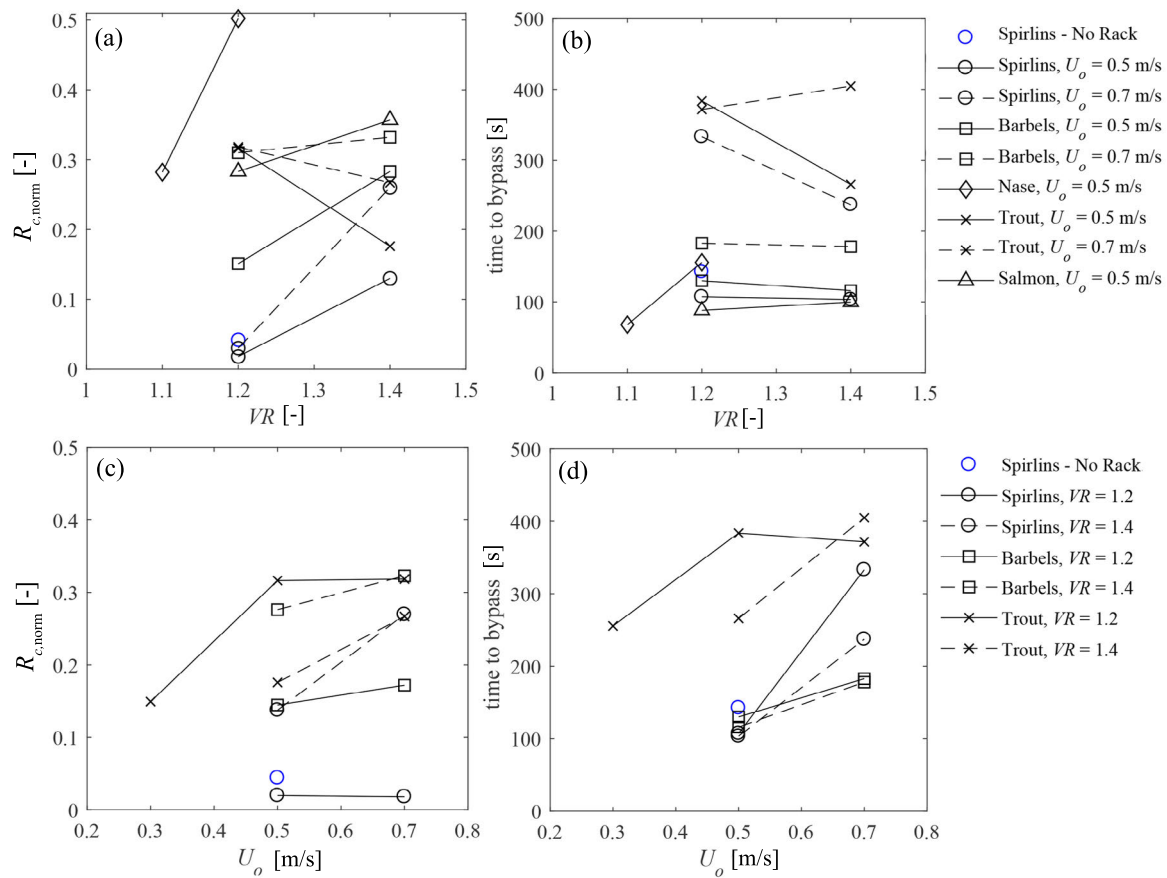


Figure 6.29 Normalised residence coefficient $R_{c,norm}$ of sector 5 for different fish species (a) versus VR for $U_o = 0.5$ m/s (solid lines), $U_o = 0.7$ m/s (dashed lines) and (c) versus U_o for $VR = 1.2$ (solid lines), $VR = 1.4$ (dashed lines), and time to bypass (b) versus VR and (d) versus U_o , respectively

Barbel, salmon parr, and brown trout all explored the flow fields near the CBR and between the bars with their caudal fins and often stayed in direct contact with the rack. These fish-rack interactions did not lead to a high rack passage rate for the barbel and the salmon parr. Conversely, many brown trout passed the rack, indicating less or no avoidance reaction to the high velocity and pressure gradients. Eel showed a completely different behaviour overall,

often approaching the CBR with a negative rheotaxis and passing the rack without reacting to any hydrodynamic cues. For the flow conditions shown in Figure 6.30, the nase spent the most time in the vicinity of the CBR. This behaviour is related to their sensitive reaction to $VR = 1.2$, which led to exploratory movements to find an alternative route along the rack. Nevertheless, the number of rack passages for nase was small.

Overall, these results demonstrate that the CBR functioned as a behavioural barrier for spirlin, barbel, nase and salmon parr with high FGE and FPE, whereas it had low or no behavioural effect for brown trout and European eel for the tested parameter range. Smaller bar spacings, lower rack angles, a bottom overlay, or the electrification of the rack, which will be discussed in Chapter 7, might be solutions to achieve higher FGE and FPE for these fish species.

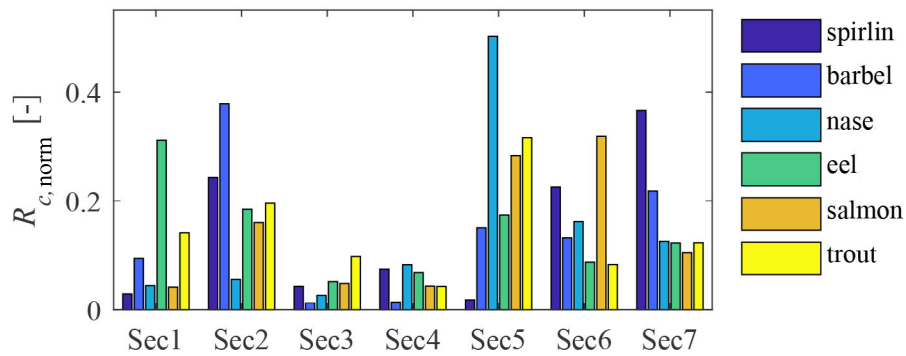


Figure 6.30 Normalised residence coefficient of all tested fish species in each sector for $U_o = 0.5$ m/s and $VR = 1.2$

6.3 Logistic regression model

Three separate binary logistic regression models were set up to investigate the extent to which various factors affect the likelihood of each dependent response variable: (i) bypass passage, (ii) rack passage or (iii) refusal (cf. Section 3.6.3). The model included all fish species and the main hydraulic conditions ($U_o = 0.5$ m/s and 0.7 m/s, and $VR = 1.2$ and 1.4), and both rack types CBR and HBR (data from Meister, 2020). A species-specific model setup was not possible due to the small number of observations per species and the large number of empty entries for the output variables (e.g. no rack passage for the spirlin with the CBR). The following analysis is therefore limited to the effects of the independent variables rack type, U_o , VR , usage, and time of day. The reference configuration to which all outputs of the model are compared is the CBR, $U_o = 0.5$ m/s, and $VR = 1.2$. The variable *usage* was used to compare whether fish, which were used for the second or the third time in an experiment, reacted differently than fish, which were used in an experiment for the first time. Finally, the

variable *time of day* is divided into the two categories morning and afternoon. Fish used in the afternoon are thus compared to the reference category of fish used in the morning.

In the following sections, the output of the logistic regression models with the dependent variables of bypass passage (Section 6.3.1), rack passage (Section 6.3.2) and refusal (Section 6.3.3) are given. The odds ratio, i.e. $\exp(\beta)$, refers to the odds that a fish showed the reaction of the dependent variable compared to an alternative reaction. As an example, an odds ratio of $\exp(\beta_{X_i}) = 1$ means that the independent parameter X_i does not change the odds of the specific outcome. An odds ratio of $\exp(\beta_{X_i}) = 0.5$ with the bypass passage as the dependent variable means that for one bypass passage, two alternative reactions occurred (rack passage or refusal). In this case, the probability of a bypass passage is $P = \exp(\beta)/(1 + \exp(\beta)) = 0.5/(1 + 0.5) = 33\%$, whereas the probability of an alternative reaction is $1 - P = 67\%$. The odds therefore describe the rate of change of the probability of a specific outcome if the value of an independent parameter is changed.

6.3.1 Model 1: Regression with bypass passage as the dependent variable

Table 6.3 shows the results of the binary logistic regression model with the *bypass passage* as the dependent variable. A calculation example for the corresponding probabilities is given in the following for the intercept X_0 . For the reference configuration (CBR, $U_o = 0.5$ m/s, $VR = 1.2$, usage = 1, time of day = morning), the odds of a bypass passage were $\exp(\beta_0) = 3.666$ times higher than those for the other reactions (rack passage and refusal). This means that 3.666 bypass passages occurred for every rack passage or refusal. The probability of a bypass passage can thus be calculated to $P_0 = 3.666/(1 + 3.666) = 0.79$ compared to the significantly lower probability of an alternative reaction $P_1 = 1/(1 + 3.666) = 0.21$ for the reference configuration (Table 6.3). Changing the rack from the CBR to the HBR, while maintaining the reference values for the other parameters, decreases the odds of a bypass passage by $1 - 0.575 = 0.425$, i.e. $\exp(\beta_{0:HBR}) = 3.666 \cdot 0.575 = 2.108$. The probability of a bypass passage with the HBR ($U_o = 0.5$ m/s, $VR = 1.2$, usage = 1, time of day = morning) is therefore $P_{0:HBR} = 2.108/(1 + 2.108) = 0.68$ compared to the probability of an alternative reaction $P_{1:HBR} = 1/(1 + 2.108) = 0.32$. This means that changing the rack from the CBR to the HBR while maintaining all other parameters reduces the probability of a bypass passage from 79% to 68%. The rack type has the most significant effect on the bypass passages among all modelled parameters ($p < 0.001$). With this procedure, the effect of every parameter on the probability of a specific outcome compared to the reference configuration can be computed separately. The corresponding probabilities $P_{0;i}$ are given in Table 6.3. If the values of two independent parameters are changed compared to the reference configuration, all odds have to be multiplied. As an example, for the configuration

with a CBR, $U_o = 0.7$ m/s and $VR = 1.4$, usage = 1, time of day = morning, the odds ratio is computed to $\exp(\beta_{0:U_o:VR}) = 3.666 \cdot 0.854 \cdot 0.721 = 2.257$.

The model further shows that VR has a significant effect on the odds of a bypass passage ($p = 0.048$), although the χ^2 -test yielded no significance of VR for each individual fish species. The logistic regression model integrates all fish species, however, resulting in a much larger sample size. This result coincides with the observation that many fish quickly accepted the bypass for $VR = 1.2$, but showed hesitation or avoidance for $VR = 1.4$ taking more time to accept the bypass. The odds of a bypass passage for $VR = 1.4$ are thus only 0.721 times the odds for $VR = 1.2$, i.e. $\exp(\beta_{0:VR}) = 3.666 \cdot 0.721 = 2.643$ and the probability of a bypass passage reduces from 79% to 73%. The approach flow velocity U_o and the usage did not have a significant effect on the bypass passages. However, the higher value of $U_o = 0.7$ m/s was only tested for three out of the six fish species, i.e. spirlin, barbel and brown trout, with different effects on the behaviour for the tested species (cf. Section 6.2). The odds for the variable usage is nearly 1, which indicates that this variable has a negligible effect on the bypass passages, i.e. there is no learning or habituation effect. The time of day a fish was used in the experiment shows a significant effect on the bypass passages ($p = 0.002$). The odds of a bypass passage for fish used in the afternoon were only 0.583 times those for fish used in the morning. The effect of the rack type and time of day on the probability of a bypass passage was thus similarly high. However, according to the model 1, the reference configuration, i.e. the CBR, $U_o = 0.5$ m/s and $VR = 1.2$, leads to the highest probability ($P_0 = 78.6\%$) of a bypass passage over all ethohydraulic tests conducted in this study and in Meister (2020), whereas the HBR, $U_o = 0.7$ m/s and $VR = 1.4$ leads to the lowest probability ($P_{0:HBR:U_o:VR} = 56.5\%$) of a bypass passage.

Table 6.3 Output of the logistic regression model with bypass passage as the dependent variable, n = number of fish included in the model, BIC = Bayesian Information Criterion, AIC = Akaike Information Criterion; significance levels are denoted with * $p < 0.05$, ** $p < 0.01$, *** $p < 0.001$

	Intercept	rack type: HBR	U_o : 0.7 m/s	VR: 1.4	usage	time of day: afternoon
coefficient β	1.299***	-0.553***	-0.158	-0.327*	-0.077	-0.539**
$\exp(\beta)$	3.666	0.575	0.854	0.721	0.926	0.583
std.error	0.281	0.168	0.176	0.165	0.083	0.170
p -value	3.719e-06	9.775e-04	0.367	0.048	0.354	0.002
$P_{0:i}$	0.786	0.678	0.758	0.726	0.772	0.681
n	639					
log-likelihood	-417.687					
BIC	874.134					
AIC	847.370					

6.3.2 Model 2: Regression with rack passage as the dependent variable

Table 6.4 shows the results of the binary logistic regression model with *rack passage* as the dependent variable. The odds of a rack passage are $\exp(\beta_0) = 0.104$, meaning that for every alternative reaction (bypass passage and refusal), 0.104 rack passages occur. The probability of a rack passage is thus $P_0 = 0.104 / (1 + 0.104) = 0.094$ for the reference configuration. The rack type has the most significant effect on the odds of a rack passage ($p < 0.001$). Changing the rack from the CBR to the HBR increases the odds of a rack passage 2.303 times, i.e. $\exp(\beta_{0:\text{HBR}}) = 0.104 \cdot 2.303 = 0.240$. This means that if only the rack is changed from the CBR to the HBR, the probability of a rack passage increases from 9.4% to 19.3%. U_o also has a significant effect on the odds of a rack passage ($p = 0.018$). The odds of a rack passage with the CBR are reduced by $1 - 0.621 = 38\%$ for $U_o = 0.7$ m/s compared to $U_o = 0.5$ m/s, resulting in the probability of a rack passage of $P_{0:U_o} = 6.1\%$ for $U_o = 0.7$ m/s. The model further shows that VR also has a significant effect on the odds of a rack passage ($p = 0.037$), which coincides with the result that fish spent more time in the rack parallel sector 5 for $VR = 1.4$ compared to $VR = 1.2$ (cf. Section 6.2.7). The odds of a rack passage for $VR = 1.4$ are thus 46% higher compared to $VR = 1.2$ resulting in a probability of a rack passage of $P_{0:VR} = 13.2\%$ for $VR = 1.4$ if all other parameters maintain their reference values. The effect of the usage is significant for the rack passages ($p < 0.001$). The $\exp(\beta_{\text{usage}}) = 1.370$ indicates that the odds of a rack passage increase by 37% with each time the fish was used in an experiment. This result suggests that the fish adapted to the rack and showed a decreased avoidance behaviour when used for a second or a third time within the same week. The time

of day does not have a significant effect on the rack passages ($p = 0.237$).

In conclusion, according to the model 2 and neglecting the secondary parameters *usage* and *time of day*, the probability of a rack passage is lowest with $P_{0:U_o} = 6.1\%$ for the CBR, $U_o = 0.7$ m/s and $VR = 1.2$, whereas it is highest with $P_{0:HBR:VR} = 25.9\%$ for the HBR, $U_o = 0.5$ m/s and $VR = 1.4$. Note that the logistic regression model includes all fish species. The result can therefore differ considerably for individual fish species like the European eel (cf. Section 6.7).

Table 6.4 Output of the logistic regression model with rack passage as the dependent variable, n = number of fish included in the model, BIC = Bayesian Information Criterion, AIC = Akaike Information Criterion; significance levels are denoted with * $p < 0.05$, ** $p < 0.01$, *** $p < 0.001$

	Intercept	rack type	U_o : 0.7 m/s	VR : 1.4	usage	time of day
coefficient β	-2.262***	0.834***	-0.477*	0.380*	0.315***	0.223
$\exp(\beta)$	0.104	2.303	0.621	1.462	1.370	1.250
std.error	0.317	0.187	0.201	0.182	0.091	0.189
p -value	9.290e-13	8.311e-06	0.018	0.037	5.438e-04	0.237
$P_{0:i}$	0.094	0.193	0.061	0.132	0.125	0.11
n	639					
Log-Likelihood	-361.048					
BIC	760.855					
AIC	734.100					

6.3.3 Model 3: Regression with refusal as the dependent variable

Table 6.5 shows the results of the binary logistic regression model with *refusal* as the dependent variable. The odds of a refusal are $\exp(\beta_0) = 0.273$, i.e. 0.273 refusals occur for every alternative reaction (bypass and rack passage). The probability of a refusal is thus $P_0 = 21.4\%$ for the reference configuration. U_o has the most significant effect on the odds of a refusal ($p < 0.001$). The odds of a refusal at the CBR are 4.000 times higher for $U_o = 0.7$ m/s compared to $U_o = 0.5$ m/s. This means that the odds of a refusal with $U_o = 0.7$ m/s are $\exp(\beta_{0:U_o}) = 0.273 \cdot 4.000 = 1.092$. The probability of a refusal therefore increases from $P_0 = 21.4\%$ to $P_{0:U_o} = 52.1\%$ if U_o is increased from 0.5 m/s to 0.7 m/s while all other parameters maintain their reference values (Table 6.5). The rack type also has a significant effect on the odds of a refusal ($p = 0.019$). Changing the rack from the CBR to the HBR decreases the odds of a refusal by 49.6% and thus reduces the probability of a refusal to $P_{0:HBR} = 12.1\%$. VR does not have a significant effect on the odds of a refusal ($p = 0.602$).

The effect of the usage is significant for the odds of a refusal ($p < 0.001$). The $\exp(\beta_{\text{usage}}) = 0.436$ indicates that the odds of a refusal decrease by 83% with each time the fish were re-used for an experiment. The probability of a refusal with the reference configuration is $P_{0:\text{usage}} = 10.6\%$ if a fish is used for the second time in an experiment compared to $P_0 = 21.4\%$ if it is used for the first time. This result coincides with the increased odds of a rack passage for multiple usage and suggests that the fish show a decreased avoidance behaviour when used for a second or a third time within the same week. Furthermore, the time of day also has a significant effect on the odds of a refusal ($p < 0.001$). The $\exp(\beta_{\text{time}}) = 2.959$ indicates that the odds of a refusal for fish used in an experiment in the afternoon are 2.959 times the odds if it is used in the morning. The probability of a refusal for the reference configuration is therefore $P_{0:\text{time}} = 44.6\%$ for fish used in the afternoon compared to $P_0 = 21.4\%$ for fish used in the morning.

In conclusion, according to the model 3 and neglecting the secondary parameters *usage* and *time of day*, the probability of a refusal is lowest with $P_{0:\text{HBR}} = 12.1\%$ for the HBR, $U_o = 0.5$ m/s and $VR = 1.2$, whereas it is highest with $P_{0:U_o:VR} = 55.8\%$ for the CBR, $U_o = 0.7$ m/s and $VR = 1.4$.

Table 6.5 Output of the logistic regression model with refusal as the dependent variable, n = number of fish included in the model, BIC = Bayesian Information Criterion, AIC = Akaike Information Criterion; significance levels are denoted with * $p < 0.05$, ** $p < 0.01$, *** $p < 0.001$

	Intercept	rack type	U_o : 0.7 m/s	VR : 1.4	usage	time of day
coefficient β	−1.300**	−0.682*	1.386***	0.145	−0.831***	1.085***
$\exp(\beta)$	0.273	0.506	4.000	1.156	0.436	2.959
std.error	0.472	0.291	0.285	0.277	0.175	0.283
p -value	0.006	0.019	1.106e-06	0.602	1.956e-06	1.225e-04
$P_{0:i}$	0.214	0.121	0.521	0.240	0.106	0.446
n	639					
Log-Likelihood	−179.417					
BIC	397.595					
AIC	370.840					

6.3.4 Effects of the main parameters on the fish behaviour and the guidance efficiency

While the χ^2 tests give important implications on the effects of U_o and VR on the behaviour of each individual fish species, the logistic regression model including all data yields the conclusions on the effects of U_o and VR on the behaviour of the entity of all tested fish

species. The most important outputs of the logistic regression model are summarised in the following:

- U_o did not have a significant effect on the number of bypass passages, i.e. the FGE, in the tested range. It significantly affected the refusal and the rack passage rates, however. Increasing U_o from 0.5 m/s to 0.7 m/s thus significantly increased the number of refusals and significantly decreased the number of rack passages.
- Increasing VR from 1.2 to 1.4 significantly decreased the number of bypass passages and significantly increased the number of rack passages. In the tested range, VR did not have a significant effect on the number of refusals.
- The rack type had the most significant effect on the FGE. With the CBR ($s_b = 50$ mm), significantly more bypass passages occurred than with the HBR ($s_b = 20$ mm). Changing the CBR to the HBR significantly increased the number of rack passages and significantly decreased the number of refusals.
- The above stated findings imply that the CBR with $VR = 1.2$ yielded the highest fish guidance efficiency with $FGE = 79\%$ for $U_o = 0.5$ m/s and $FGE = 76\%$ for $U_o = 0.7$ m/s, if all the tested fish species are included in the analysis. Because a binary regression model was used, the FPE, which is computed with the number of bypass passages plus the number of refusals, cannot be directly quantified with the model outputs. However, the FPE is expected to be highest with the CBR, $U_o = 0.7$ m/s and $VR = 1.2$ because of the significantly increased refusals and decreased rack passages. Note that these results can vary considerably for the individual fish species. Furthermore, some fish species, i.e. the juvenile nase, were not tested at $U_o = 0.7$ m/s.

6.4 Average fish protection and guidance efficiencies

Figure 6.31 shows the average, minimum, and maximum fish protection and guidance efficiencies considering only the bypass passages with rack interaction (FGE, FPE) and considering all bypass passages (FGE^* , FPE^*) resulting from the live-fish tests. The values are computed by taking the average efficiencies over all tested flow conditions for each fish species. No minimum or maximum values are shown for the eel, since they were only tested with one flow condition. The average FGEs and FPEs are higher than 75% and 80%, respectively, for spiralin, barbel, nase and salmon parr, while they are below 75% and 80%, respectively, for brown trout and European eel. The FPEs are only slightly higher than the FGEs for nase, eel and salmon parr, indicating that these fish species did not refuse the CBR-BS but swam either into the bypass or through the CBR. In contrast, the average FPE is considerably higher than the FGE for spiralin, barbel and brown trout because these fish

refused the CBR-BS and swam back upstream more often. The average FGE* and FPE* are mostly only slightly higher than the average FGE and FPE, which indicates that considering the rack interaction does not greatly affect the resulting protection and guidance efficiencies for most of the tested fish species.

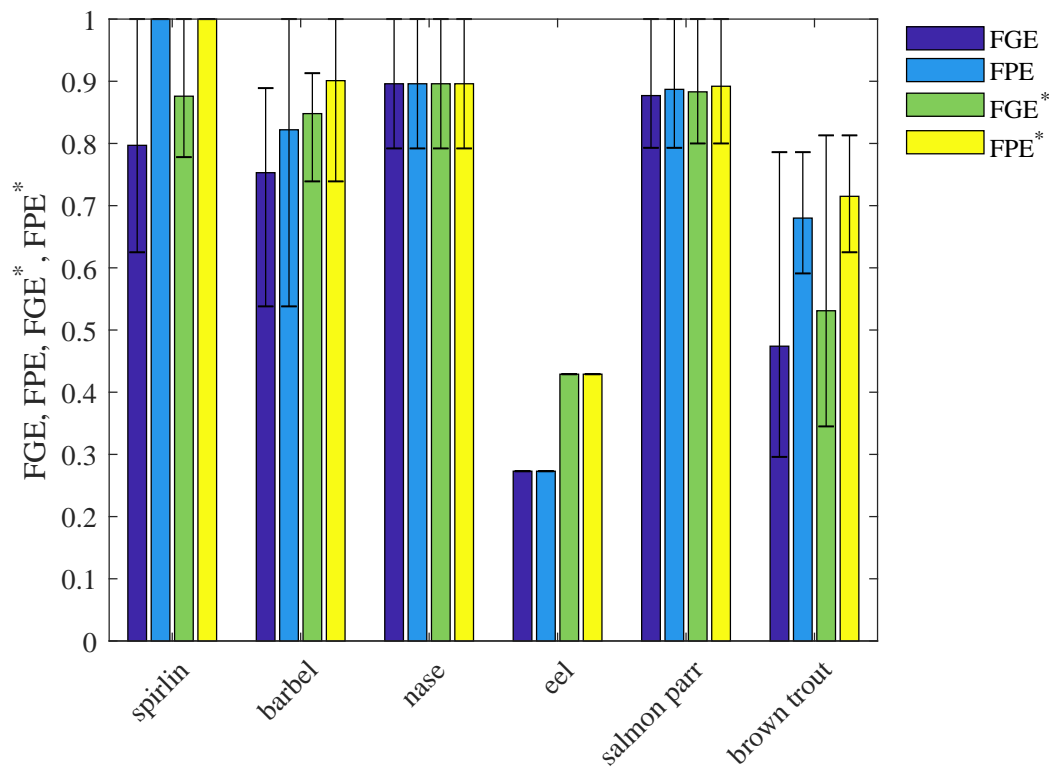


Figure 6.31 Average fish protection and guidance efficiencies considering only the bypass passages with rack interaction (FPE, FGE) and considering all bypass passages (FPE*, FGE*); the minimum and maximum values are indicated with horizontal bars

6.5 Rack passage locations

The exact location of each rack passage was determined from a visual assessment of the videos recorded during the live-fish tests for all six tested fish species in the scope of a Bachelor's Thesis. The results show that the rack passage locations are generally evenly distributed along the CBR (Figure 6.32). The slightly increased transversal flow velocities towards the rack measured at the d/s rack end (cf. Figure 6.2) did therefore not lead to an increased fish entrainment. The number of tested European eel was small, so that no final conclusion about the passage locations can be made. No rack passage was observed for spirlin (Figure 6.32d) and only few rack passages occurred with nase (Figure 6.32c). Note that the number of tested fish was different for each fish species (cf. Table 3.7), and Figure 6.32 therefore gives no indication on the fish guidance efficiency.

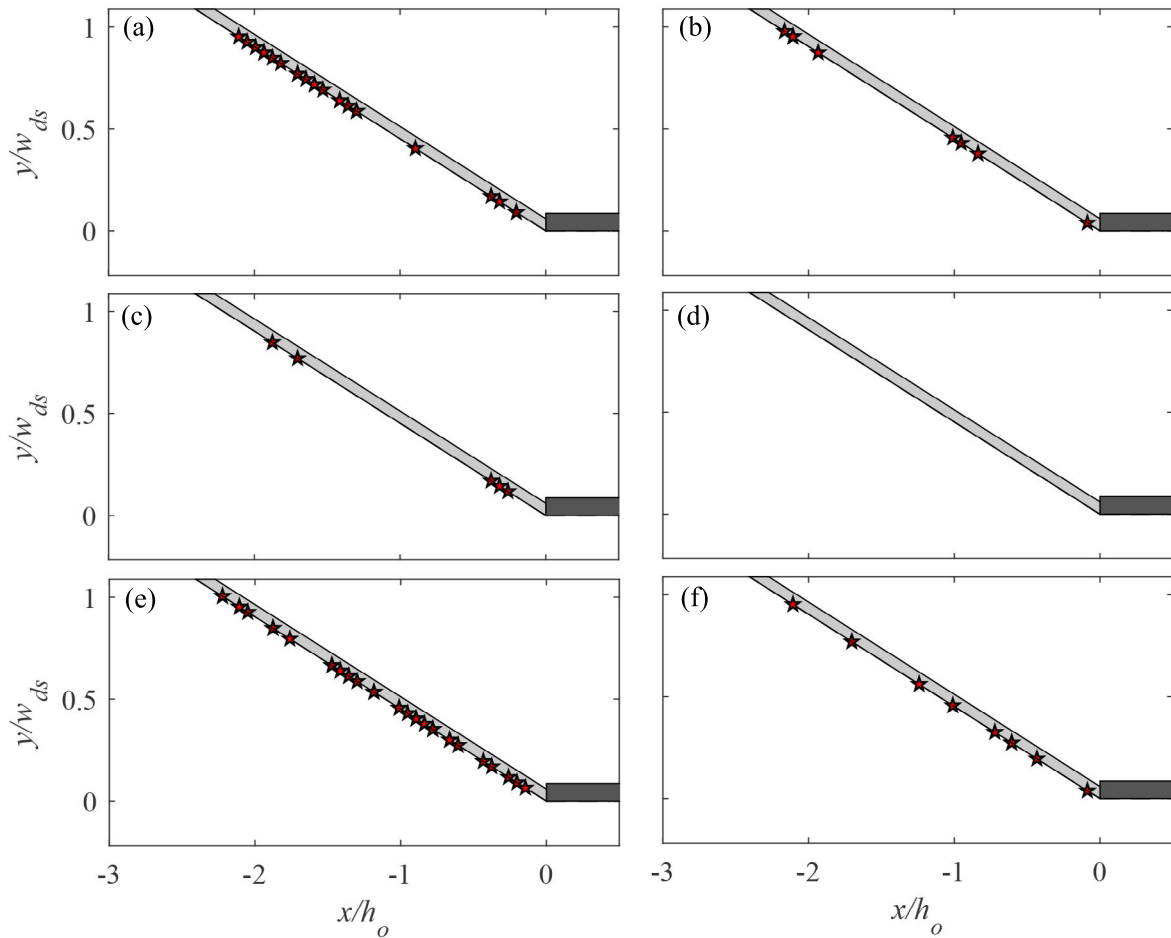


Figure 6.32 Locations of rack passages along the CBR for (a) barbel, (b) European eel, (c) nase, (d) spirlin, (e) brown trout, and (f) Atlantic salmon parr

6.6 Fish swimming velocities and behaviour

The absolute fish swimming velocities were computed from the digitised individual fish swimming paths and the flow velocities from the ADV measurements or the numerical simulation (cf. Section 3.6.2). In this section, exemplary typical fish swimming paths and velocities, and the rheotaxis behaviour are presented and discussed. The swimming paths and velocities of all live-fish tests can be found in the digital repository of the supplement material of this study under: <https://doi.org/10.3929/ethz-b-000438798>.

6.6.1 Fish swimming paths

Figure 6.33 shows the swimming paths of a single live-fish test with three spirlin at $U_o = 0.5$ m/s (a,b) and $U_o = 0.7$ m/s (c,d). Figures 6.33a,c show the paths for a selected test with $VR = 1.2$, while Figures 6.33b,d show the paths for a test with $VR = 1.4$. These plots were generated for each live-fish test separately. The plots shown in this section thus only

represent a selection of some typical swimming paths for each fish species. The absolute fish swimming velocities v_{fish} are represented with colour. The blue colours ($v_{\text{fish}} < 0$) represent positive rheotaxis, i.e. the fish swimming downstream with their head against the current or swimming upstream if $v_{\text{fish}} < -U_o$, whereas the red colour ($v_{\text{fish}} > 0$) represents negative rheotaxis, i.e. the fish actively swimming downstream with their head first (cf. Table 3.9). A change from $v_{\text{fish}} < 0$ to $v_{\text{fish}} > 0$ or vice versa thus shows a rheotaxis change from positive to negative rheotaxis or negative to positive rheotaxis, respectively.

Figure 6.33a shows the typical zig-zag movement of three spirlin swimming closely together in a school exploring the flume over its entire width. They approached the CBR once but hesitated and avoided it at a distance of approx. 15 cm. They were directly guided to the bypass with $VR = 1.2$ and quickly accepted it. Figure 6.33b shows the swimming behaviour for $VR = 1.4$. The stronger velocity increase, i.e. higher SVG_x , at the bypass entrance led to hesitation in the area in front of the bypass and a searching swimming behaviour along the rack. This coincides with the observations that the spirlin spent more time in the rack-parallel sector 5 at $VR = 1.4$ compared to $VR = 1.2$ (cf. Figure 6.29a). At $U_o = 0.7$ m/s, the spirlin had to maintain a higher v_{fish} corresponding to their prolonged swimming speed to actively drift downstream (6.33c/d, Table 6.6). They needed more time and attempts to find and accept the bypass at $U_o = 0.7$ m/s compared to $U_o = 0.5$ m/s (Figure 6.29d) leading to a higher refusal rate at $U_o = 0.7$ m/s (cf. Figure 6.17a). None of the spirlin performed a rheotaxis change in the experiments shown in Figure 6.33.

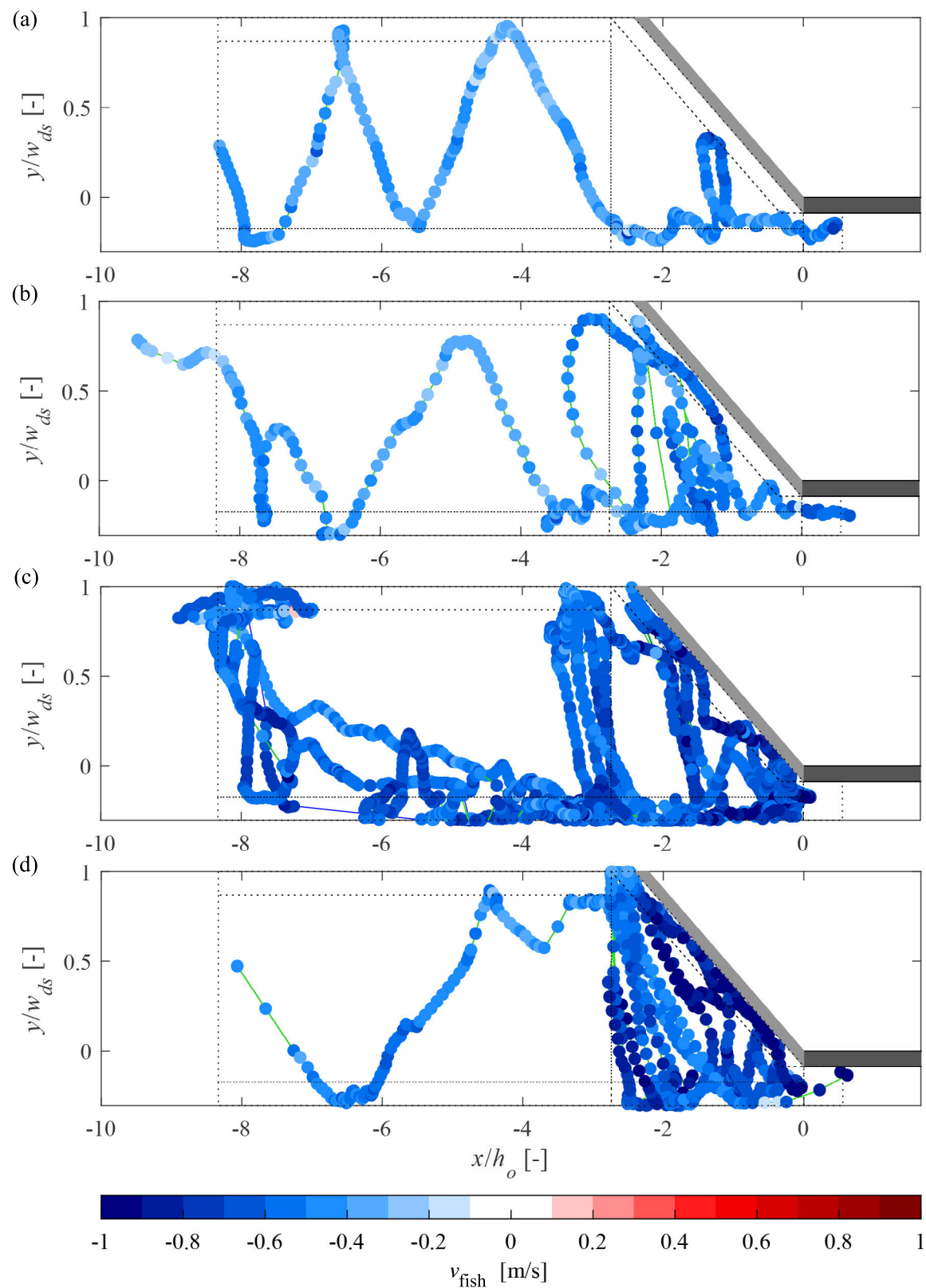


Figure 6.33 Swimming paths of three spiralin for (a) $U_o = 0.5$ m/s, $VR = 1.2$, (b) $U_o = 0.5$ m/s, $VR = 1.4$, (c) $U_o = 0.7$ m/s, $VR = 1.2$, and (d) $U_o = 0.7$ m/s, $VR = 1.4$

As described in Section 6.2.2, barbel exhibited a different swimming behaviour compared to spiralin. They often preferred to stay in the low flow velocity regions along the flume walls as shown in Figure 6.34b, where three barbel swam closely together and finally passed the rack. The three barbel in 6.34a showed a more exploratory behaviour, but still mostly swam along the right flume side. A short change to negative rheotaxis was performed in the vicinity of the CBR indicated by the positive fish swimming speeds. In this test, two barbel passed the rack and one swam into the bypass. Although the barbel had to maintain a higher v_{fish} at $U_o = 0.7$ m/s compared to 0.5 m/s, the swimming patterns look similar and are therefore only shown for $U_o = 0.5$ m/s in Figure 6.34.

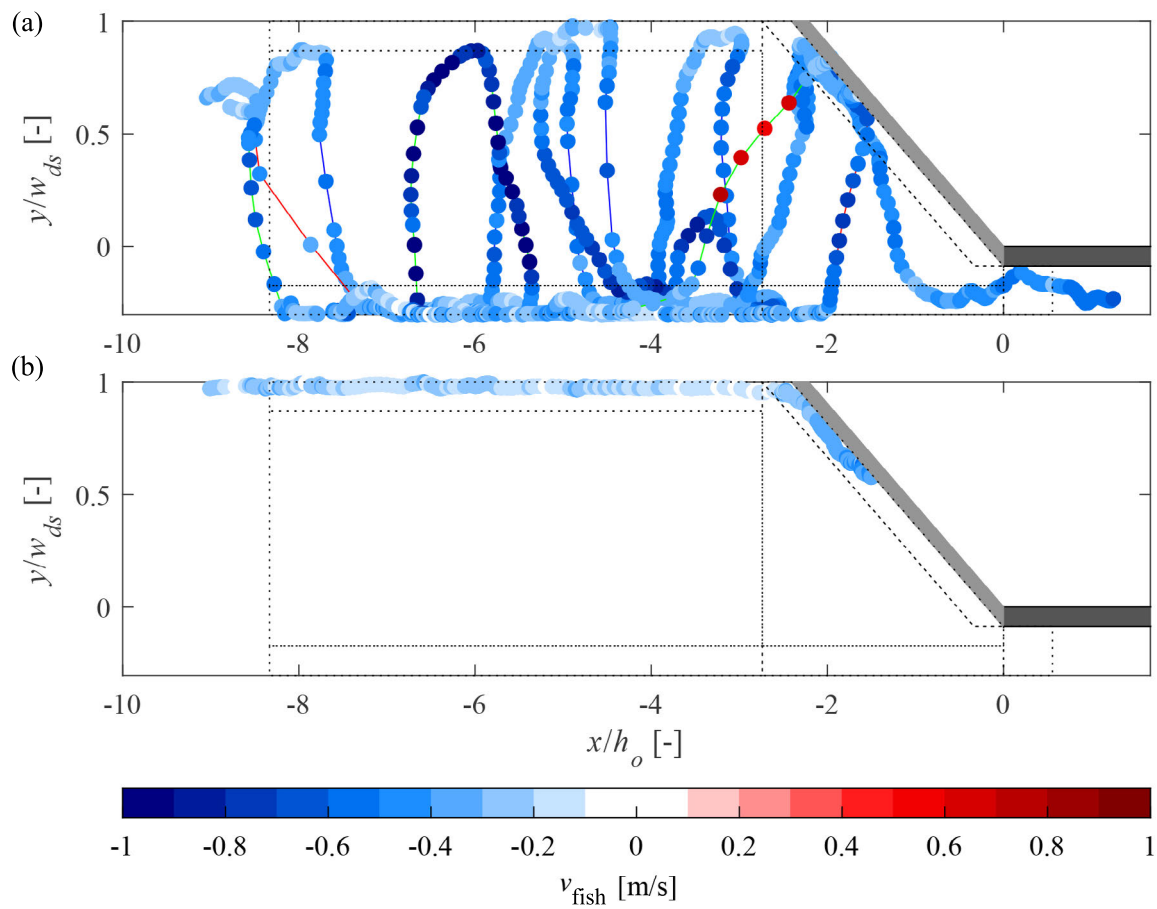


Figure 6.34 Swimming paths of three barbel for $U_o = 0.5$ m/s and (a) $VR = 1.2$, (b) $VR = 1.4$

During the live-fish tests with $U_o = 0.5$ m/s, it was often observed that the nose approached the CBR in a negative rheotaxis, but changed to positive rheotaxis directly in front of the rack, where the velocity and pressure gradients are high (Figure 6.8 and 6.10). Figure 6.35a shows this behaviour for three nase swimming closely together in a school. The fish actively swam downstream in negative rheotaxis, changed to positive rheotaxis in front of the CBR and were successfully guided to the bypass. Figure 6.35b shows a different behaviour, also

typical for the nose and similar to that of spirlin. While the fish accepted the bypass quickly for $VR = 1.1$ (Figure 6.35a), they searched along the CBR, refusing to enter the bypass with $VR = 1.2$ several times leading to more rack passages (Figure 6.35b). According to Ebel (2016), the prolonged swimming speed for nose with a total body length of 6.0-8.9 cm for the maximum duration of an experiment (45 min) lies between 0.39-0.53 m/s (cf. Table 3.10). This explains why the nose accepted the bypass quicker for $VR = 1.1$ than for $VR = 1.2$. The CBR generally functions as a behavioural barrier for juvenile nose. If they have to search for a long time at their prolonged swimming speed, however, they get exhausted, which increases the risk of a rack passage.

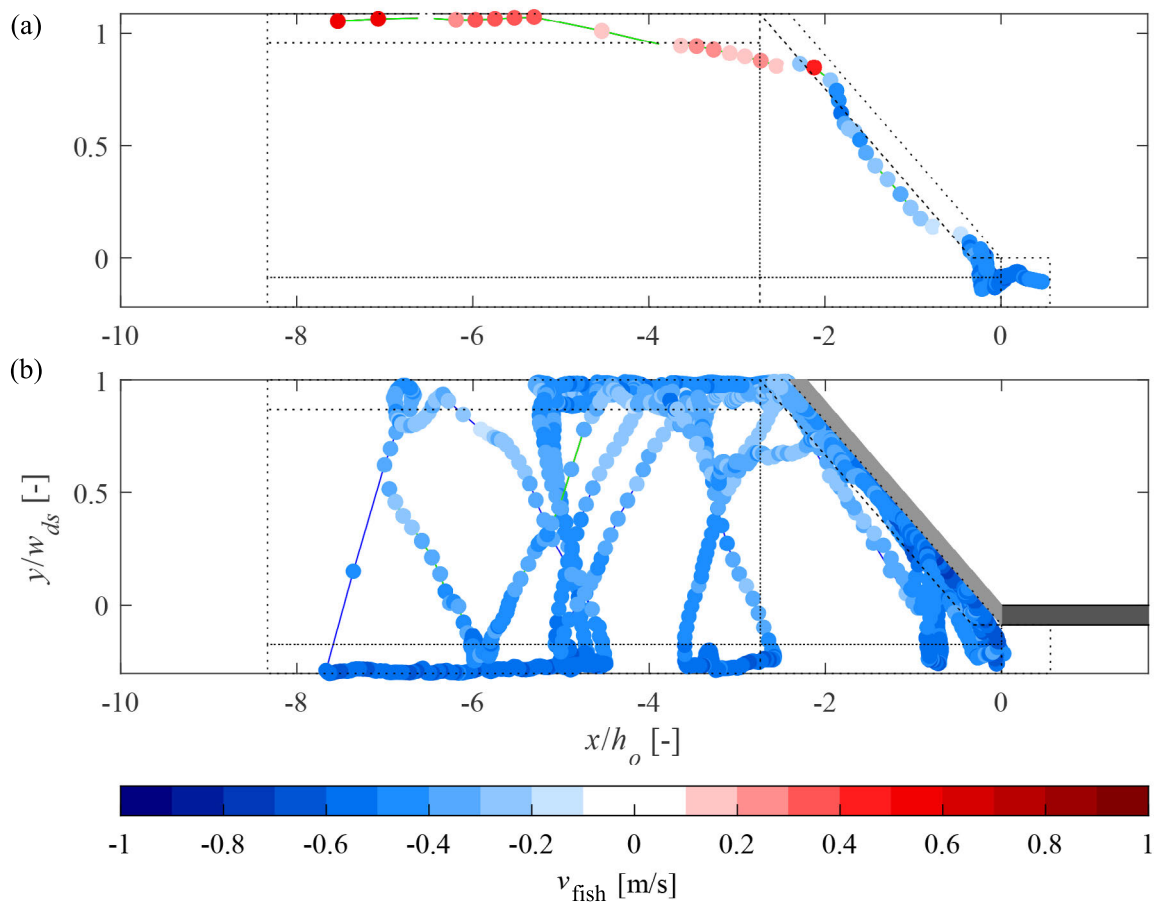


Figure 6.35 Swimming paths of three nose for $U_o = 0.5$ m/s and (a) $VR = 1.1$ leading to three bypass passages, and (b) $VR = 1.2$ leading to two rack passages and a bypass passage

Brown trout and Atlantic salmon parr generally showed a similar swimming behaviour characterised by short rheotaxis changes and burst swimming as an avoidance reaction at the CBR. Figure 6.36a shows the swimming path of a single brown trout with a very short change to negative rheotaxis. The trout was guided by the CBR towards the bypass at a distance of about one body length ($TL_{mean} = 14.4$ cm) of the rack. Similarly, Figure 6.36b

shows the swimming paths of three salmon parr with slightly longer rheotaxis changes. The parr searched along the rack, the dark blue coloured circles thus represent short but fast up-stream movements close to the rack. Lemasson *et al.* (2008) report a similar behaviour for the reaction of rainbow trout to a louver with $\alpha = 15^\circ$ in a laboratory study. In the present study, however, the FGE for brown trout was clearly lower for the brown trout than for the salmon parr (cf. Figures 6.27 and 6.25). Some brown trout individuals swam closer to the rack exploring the space between the bars and actively drifting through the rack.

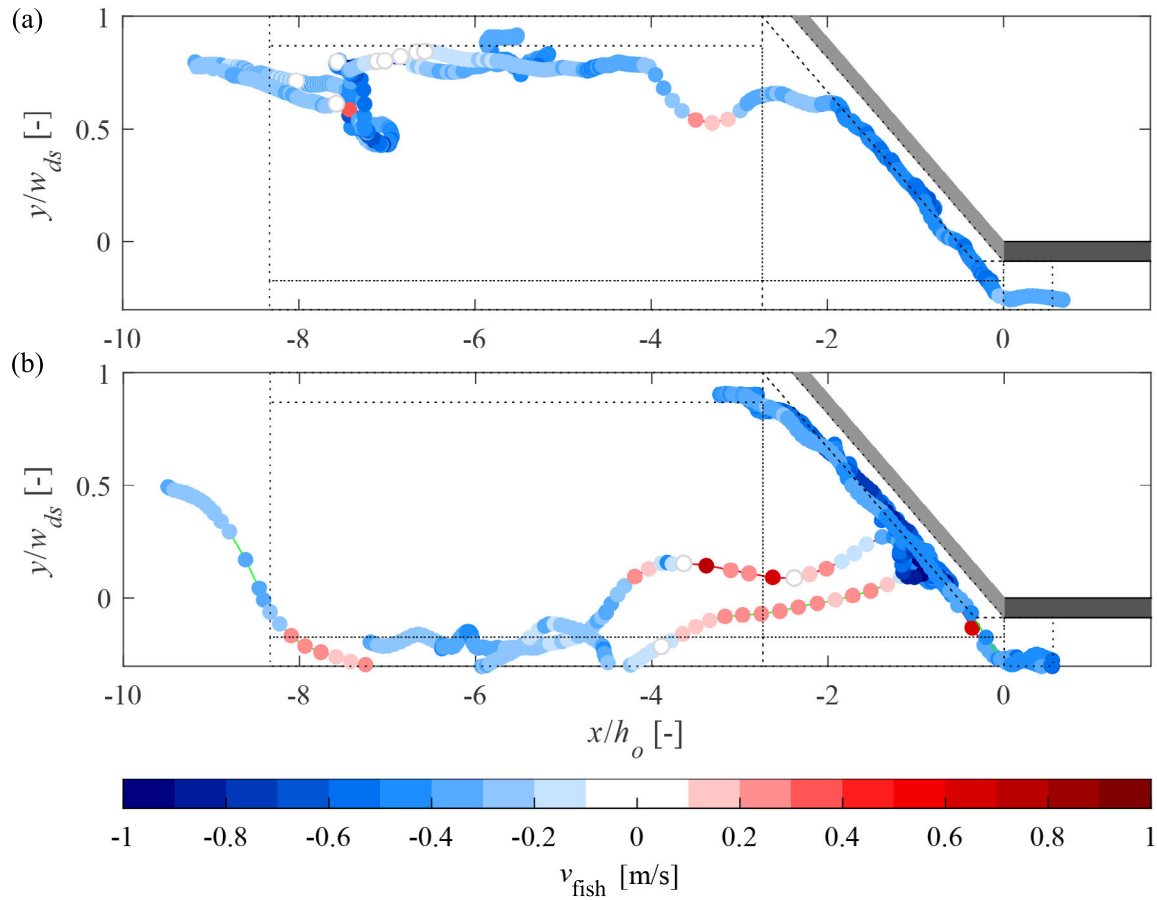


Figure 6.36 Swimming paths of (a) a bypass passage of a single brown trout for $U_o = 0.5$ m/s, $VR = 1.2$ and (b) a bypass passage of three salmon parr for $U_o = 0.5$ m/s, $VR = 1.4$

Figure 6.37 shows the swimming paths of three eel. Eel (1) actively drifted downstream along the left flume wall. At $x/h_o \approx -6.5$ it started turning around, passively drifting downstream with the flow velocity until it reached the CBR head first and passed it. Eel (2) changed to negative rheotaxis at $x/h_o \approx -7.5$ and actively swam downstream until it hit the CBR, shortly swam backwards with a snake-like motion until it finally passed the rack. Eel (3) swam from the starting compartment toward the right flume wall and passively drifted downstream and into the bypass without rack interaction.

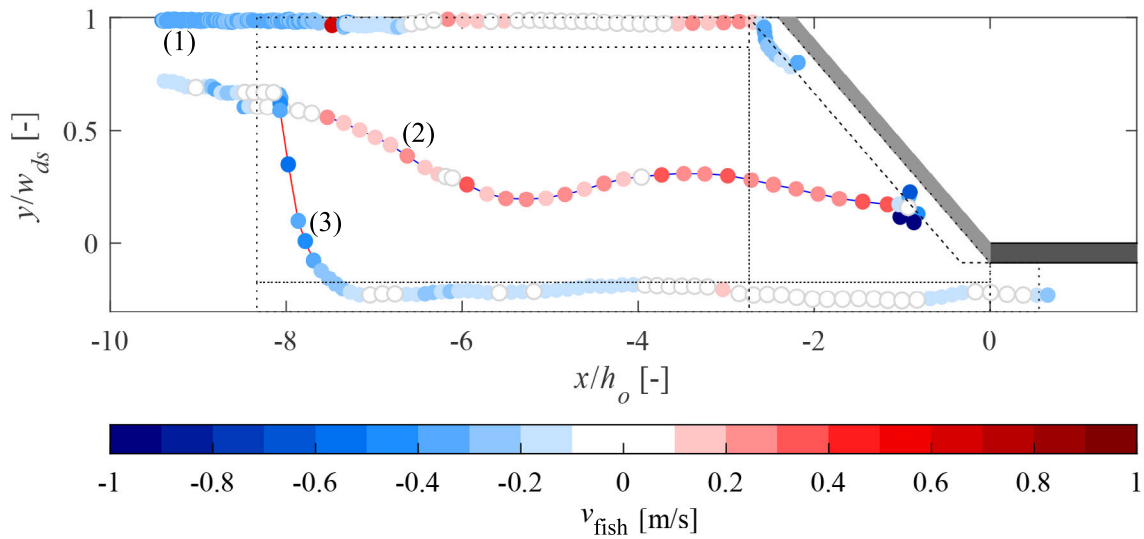


Figure 6.37 Typical swimming paths of three eel for $U_o = 0.5$ m/s, $VR = 1.2$; the raw data of these particular swimming paths is shown in Figure 3.11

6.6.2 Statistical analysis of fish swimming speeds

The mean swimming speeds of the tested fish species are listed in Table 6.6 for the four main tested flow conditions. According to this analysis, the spirlin and the eel exhibited the highest and the lowest mean swimming speeds, respectively. As expected, $v_{\text{fish,mean}}$ for all fish was higher at $U_o = 0.7$ m/s than at $U_o = 0.5$ m/s. Generally, $v_{\text{fish,mean}}$ was almost identical at $VR = 1.4$ and at $VR = 1.2$ at the same U_o , except for the salmon parr where it was clearly higher for $VR = 1.4$. The comparison with the sustained and the prolonged swimming speeds of the tested fish given in Table 3.10 shows that the nase were swimming at their prolonged swimming speed at $U_o = 0.5$ m/s. The spirlin were swimming at their sustained swimming speed at $U_o = 0.5$ m/s but switched to their prolonged swimming speed at $U_o = 0.7$ m/s. The higher energy expenditure of the spirlin at $U_o = 0.7$ m/s is a possible explanation for the increased number of refusals at $U_o = 0.7$ m/s compared to $U_o = 0.5$ m/s (cf. Section 6.2.1). The CBR led to a high FGE and FPE for spirlin at both tested U_o and for nase at $U_o = 0.5$ m/s (cf. Figures 6.17 and 6.21). The nase were not tested at $U_o = 0.7$ m/s, however. In contrast, barbel, eel, salmon parr and brown trout swam below their mean sustained swimming speed $\bar{v}_{\text{sustained}}$ in all experiments (Table 6.6).

The maximum swimming speed observed during the live-fish tests is given with the 99% quantile. This excludes outliers, which were produced during the tracking process and its data analysis. The maximum swimming speeds can be compared with the burst swimming speeds given in Table 3.10 for the largest individual of each fish species $v_{\text{burst,max}}$. Spirlin and nase exhibited a higher maximum swimming speed in the tests with $VR = 1.2$ than those

estimated with the empirical model by Ebel (2016). This trend is opposite for barbel, eel, trout and salmon parr, which indicates that these fish did not have to apply burst swimming to avoid the CBR. In particular, the measured swimming speeds of the tested eel are much lower than their estimated burst speeds, confirming the observations from the tests that the eel did not react to the hydraulic cues or the physical barrier with fast avoidance reactions or flight.

Table 6.6 Calculated values for the mean sustained and maximum burst swimming speed; mean values, standard deviations, and 99.0% quantile of the swimming speeds for the fish species tested in the ethohydraulic tests

U_o [m/s]	VR	statistics	spirlin	barbel	nase	eel	salmon parr	trout
Calculated values		$\bar{v}_{\text{sustained}}$ [m/s]	0.51	0.69	0.39	0.61	0.55	0.69
(cf. Table 3.10)		$v_{\text{burst,max}}$ [m/s]	1.11	1.70	0.83	1.58	1.25	1.60
0.5	1.2	$v_{\text{fish,mean}}$ [m/s]	0.46	0.43	0.46	0.36	0.34	0.42
		std-dev [m/s]	0.20	0.22	0.16	0.18	0.11	0.14
		99.0% [m/s]	1.31	1.09	0.91	0.75	0.63	0.77
0.5	1.4	$v_{\text{fish,mean}}$ [m/s]	0.47	0.41			0.43	0.42
		std-dev [m/s]	0.18	0.20			0.16	0.14
		99.0% [m/s]	1.06	1.02			0.86	0.81
0.7	1.2	$v_{\text{fish,mean}}$ [m/s]	0.60	0.53				0.57
		std-dev [m/s]	0.22	0.15				0.13
		99.0% [m/s]	1.57	0.93				0.94
0.7	1.4	$v_{\text{fish,mean}}$ [m/s]	0.62	0.55				0.59
		std-dev [m/s]	0.21	0.16				0.15
		99.0% [m/s]	1.36	0.97				0.94

6.6.3 Rheotaxis changes

The majority of the tested fish generally explored the flume with positive rheotaxis independent of the flow conditions. However, rheotaxis changes were more frequently observed for some flow conditions and fish species than for others. Figure 6.38 shows the locations of rheotaxis changes from negative to positive rheotaxis for the different flow conditions and the different fish species. A rheotaxis change was defined as the change of swimming direction for at least 0.75 s, which corresponds to 15 video frames with 1/20 s each. Note that for nase, only the flow condition with $U_o = 0.5$ m/s and $VR = 1.2$ was tested. For salmon parr, only $U_o = 0.5$ m/s, and $VR = 1.2$ and 1.4 were tested. Since eel are able to swim backwards, a change of the swimming direction does not necessarily indicate a rheotaxis change. The rheotaxis changes of eel can therefore not be directly extracted from the absolute fish swimming speeds as for the other fish species, so that they are not shown in Figure 6.38.

In most cases, the tested fish only shortly changed to negative rheotaxis, i.e. for 1-2 s, before changing back to positive rheotaxis. In a few cases, the fish exited the starting compartment and approached the CBR in negative rheotaxis, but changed to positive rheotaxis just in front of the rack. This change was most likely caused by the high SVG_x and SPG values or by the visual barrier effect of the rack. While rheotaxis changes were observed for all fish species at $U_o = 0.5$ m/s, only few rheotaxis changes occurred at $U_o = 0.7$ m/s. This indicates that the tested fish species showed a bolder, more exploratory swimming behaviour at the lower approach flow velocity. The two tested salmonid species, i.e. brown trout and Atlantic salmon parr, performed a particularly high number of rheotaxis changes at $U_o = 0.5$ m/s compared to spirlin, barbel and nase, for which only few rheotaxis changes were observed. While the brown trout used the entire flume for this exploratory behaviour (Figure 6.38d), the salmon parr often changed to positive rheotaxis in the vicinity of the CBR where the highest and the lowest SVG_x values occurred in front of the bars along the CBR (cf. Figure 6.7). The salmon parr reacted sensitively to the CBR as a behavioural barrier, which is reflected by the high FGE for this fish species (cf. Section 6.2.5). Few rheotaxis changes were observed in the bypass for $VR = 1.4$, whereas none were observed for $VR = 1.2$.

The prolonged swimming speed for 45 min for TL_{mean} lies between 0.5 m/s and 0.7 m/s for the tested spirlin and the salmon parr, whereas it is lower than 0.5 m/s for the nase and higher than 0.7 m/s for the barbel and the brown trout (cf. Table 3.10). This could explain why only the brown trout exhibited several rheotaxis changes at $U_o = 0.7$ m/s. Although swimming at their prolonged swimming speed (cf. Section 6.6.2), the nase still performed some rheotaxis changes at $U_o = 0.5$ m/s.

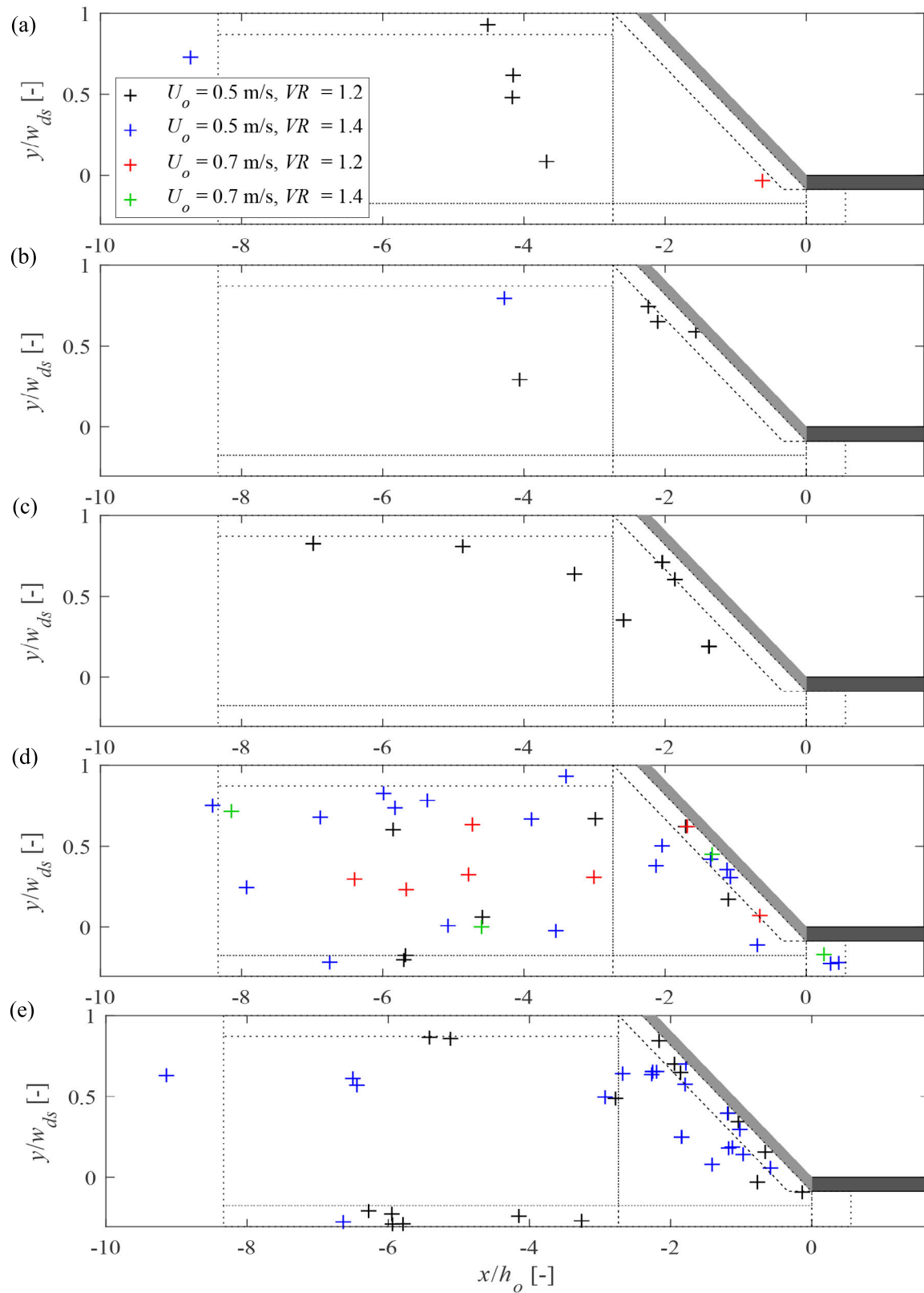


Figure 6.38 Locations of rheotaxis changes from negative to positive rheotaxis for different flow conditions for (a) spirlin, (b) barbel, (c) nase, (d) brown trout and (e) Atlantic salmon parr; the legend shown in (a) is valid for all plots

6.7 Comparison of fish protection and guidance efficiencies of the CBR to other fish guidance structures

Kriewitz (2015) and Albayrak *et al.* (2020a) conducted similar ethohydraulic experiments with MBRs and louvers in 2014 in the same laboratory flume as for the present study. In their data analysis, they did not distinguish between bypass passages with and without rack interaction, therefore only the FGE^* and the FPE^* can be compared between their and the present study. Table 6.7 lists the FGE^* and the FPE^* for the CBR with $\alpha = 30^\circ$ and a clear bar spacing of $s_b = 50$ mm (this study), the HBR with $\alpha = 30^\circ$ and $s_b = 20$ mm (Meister, 2020), two MBR configurations with $\alpha = 15^\circ$, 30° and $s_b = 50$ mm, and the louver with $\alpha = 15^\circ$ and $s_b = 50$ mm (Kriewitz, 2015; Albayrak *et al.*, 2020a). The HBR and the CBR were tested at $U_o = 0.5$ m/s with all fish species and $U_o = 0.7$ m/s with spirlin, barbel and brown trout, and the bypass was regulated to obtain $VR = 1.2$ and 1.4 . The MBRs and the louver were tested at $U_o = 0.6$ m/s with all fish species, at $U_o = 0.3$ m/s with spirlin and barbel, and at $U_o = 0.8$ m/s with barbel. The bypass was not regulated, so that VR was different for each MBR and louver, and for different U_o values. The live-fish test results of the CBR and the HBR shown in Table 6.7 were conducted in the same time period with the same fish and the same flume setup.

For spirlin, nase and salmon parr, the FGE^* and the FPE^* are considerably higher with the CBR compared to the HBR. The FGE^* of the CBR and the HBR are similar for barbel and brown trout. However, trout are not sufficiently guided or protected by neither the CBR nor the HBR in these laboratory studies. For the European eel, the FGE^* and the FPE^* are both substantially higher for the HBR compared to the CBR.

The MBRs and the louver were partly tested with the same fish species by Kriewitz (2015) and Albayrak *et al.* (2020a). They did not test nase or salmon parr in their study, but the European grayling. Table 6.7 indicates that the FGE^* and the FPE^* are similar for the MBRs and the CBR for spirlin, barbel and brown trout, whereas they are considerably lower with the louver in particular for the spirlin due to the unfavourable flow field at the louver (Albayrak *et al.*, 2020a). The MBR with $\alpha = 15^\circ$ leads to a much higher FGE^* and FPE^* for European eel and the brown trout than the CBR with $\alpha = 30^\circ$. No tests were conducted with the MBR with $\alpha = 30^\circ$, however. The higher FGE^* and FPE^* are therefore possibly a result of the lower rack angle or the larger body size of brown trout tested with the MBR. Since the FGE , i.e. the number of bypass passages with rack interaction, is unknown for the MBRs and the louver, it is not possible to know, whether the brown trout and the eel did have any rack interaction or were just swimming along the flume wall into the bypass. The numerical

model study presented in Chapter 5 shows that SVG_x values in front of the bars are similar for the CBR and the MBR. Therefore, it is expected that the CBR with $\alpha = 15^\circ$ leads to a similarly high FGE for the brown trout and the European eel as the MBR with the same rack angle. Furthermore, Kriewitz (2015) and Albayrak *et al.* (2020a) report considerably higher FGE^* and FPE^* with a bottom overlay of $h_{Bo} = 0.11 \cdot h_o$ in particular for barbel, brown trout and European eel (Table 6.7). In the present study, no overlays were tested in the ethohydraulic experiments with the CBR. Since most fish swam along the flume bottom, however, the FGE^* and FPE^* are expected to increase with a bottom overlay. For the louver, the FGE^* and FPE^* were considerably higher at $U_o = 0.3$ m/s compared to $U_o = 0.6$ m/s for both the spiralin and the barbel, whereas no clear effect of U_o on the FGE^* was observed for the MBRs. The FPE^* was slightly higher at $U_o = 0.6$ m/s compared to $U_o = 0.3$ m/s for the MBR with $\alpha = 30^\circ$. This result matches well with the higher FPE^* of the CBR for barbel at $U_o = 0.7$ m/s compared to $U_o = 0.5$ m/s. The CBR with $\alpha = 30^\circ$ and $\beta = 45^\circ$ and the MBR with $\alpha = 15^\circ$ and $\beta = 45^\circ$ both resulted in $FPE^* = 100\%$ for the spiralin, independent of U_o .

The range of total fish lengths in Kriewitz (2015) and Albayrak *et al.* (2020a) was much wider than in the present study. Their bypass was only 20 cm wide compared to 25 cm for the HBR-BS in Meister (2020) and the CBR-BS in the present study. In the present study and Meister (2020), i.e. for the CBR and the HBR, the fish had to swim 1.5 m into the bypass (crossing line 3 in Figure 3.12) to count as a successful bypass passage, whereas it was counted differently in Kriewitz (2015) and Albayrak *et al.* (2020a) for the MBR and the louver. In the latter two studies it was considered a bypass passage as soon as the fish entered the bypass, even if it left the bypass again shortly afterwards. The assessment of FGE^* and FPE^* for the CBR and the HBR is therefore more conservative than that for the MBR and the louver. The results shown in Table 6.7 therefore need to be compared by considering these differences.

The results listed in Table 6.7 confirm the findings by Enders *et al.* (2012) that fish react sensitively to high SVG values and avoid sudden velocity changes. The CBRs and MBRs leading to milder velocity gradients along the rack resulted in substantially higher FGE^* as compared to louvers. Enders *et al.* (2012) found that salmon smolts started showing avoidance reactions for spatial velocity gradients $SVG \approx 1.0 \dots 1.2 \text{ s}^{-1}$ and proposed that this threshold is associated with the energetically optimum swimming speed of fish, which corresponds to about 1 body length per second. Similar threshold values for salmonids were found by Haro *et al.* (1998) and Goodwin *et al.* (2007). No definite threshold values are reported for potamodromous fish species, however. The present findings indicate that CBRs leading to SVG_x towards the bypass lower than 1.0 s^{-1} therefore have the potential to guide

even fish with weaker swimming capacities.

Table 6.7 FGE* and FPE* for different FGSs and different fish species tested in the same etho-hydraulic flume at VAW of ETH Zurich, the data for the MBRs and the louver are taken from Kriewitz (2015) and Albayrak *et al.* (2020a) (Bo = bottom overlay with $h_{Bo} = 0.11 \cdot h_o$), the data for the HBR from Meister (2020)

FGS (α, β)	U_o [m/s]	FGE*[%]					
		spirlin	barbel	trout	eel	nase	salmon parr
CBR (30°, 45°)	0.5, 0.7	78-100	74-91	34-81	43	79-100	80-90
HBR (30°, 45°)	0.5, 0.7	45-100	71-91	38-64	75-100	0	29-46
MBR (30°, 45°)	0.3/0.6	75/75	86/100	–	–	–	–
MBR & Bo (30°, 45°)	0.6	76.2	100	96.3	94.7	–	–
MBR (15°, 45°)	0.3/0.6/0.8	100/85/–	95/83/100	–/78/–	–/73/–	–	–
MBR & Bo (15°, 45°)	0.6	–	100	85.2	90.5	–	–
louver (15°, 90°)	0.3/0.6	81/10	79/65	–	–	–	–
FGS (α, β)	U_o [m/s]	FPE* [%]					
		spirlin	barbel	trout	eel	nase	salmon parr
CBR (30°, 45°)	0.5, 0.7	100	74-100	63-81	43	79-100	80-93
HBR (30°, 45°)	0.5, 0.7	82-100	85-96	46-68	88-100	0-5	29-46
MBR (30°, 45°)	0.3/0.6	80/95	86/100	–	–	–	–
MBR & Bo (30°, 45°)	0.6	100	100	100	94.7	–	–
MBR (15°, 45°)	0.3/0.6	100/100	100/100	–/95.7	–/95.5	–	–
MBR & Bo (15°, 45°)	0.6	–	100	100	95.3	–	–
louver (15°, 90°)	0.3/0.6	90/75	79/65	–	–	–	–

6.8 Transferability of the results from laboratory to prototype

Laboratory experiments offer great possibilities to study detailed hydraulic phenomena and fish behavioural traits under controlled conditions, but they are always subject to limitations regarding the available space and resources. This section therefore aims at disclosing and critically discussing the limitations of the present laboratory study and the transferability of the results to prototype sites.

While the behaviour of salmonid species to accelerating and decelerating flows has been the subject of many studies, the knowledge about the behaviour of cyprinids to these hydrodynamic stimuli is limited. The present study therefore partly fills this research gap by providing detailed information on the avoidance reaction of spirlin, barbel and nase to the hydrodynamic cues created by CBR-BS. The present results indicate that the spatial velocity gradient (SVG) is a decisive factor for the guidance efficiency of the CBR as a mechanical behavioural barrier and for a fast bypass acceptance rate. However, the tested fish species reacted differently to this particular hydraulic stimulus. While some species, i.e. the spirlin, reacted sensitively and avoided areas with $SVG > 0.6 \text{ s}^{-1}$, other species, i.e. brown trout

or eel, were mostly insensitive even to the high *SVG* between the bars of the CBR. These observations suggest large interspecies differences in the behaviour at CBR-BS, which is supported by the findings of Kemp *et al.* (2006), who observed different avoidance reactions for different species of Pacific salmon (Steelhead, Chinook, Sockeye) at two weirs of different slope. They further reported that total fish length and the lighting conditions also affected the behaviour. Silva *et al.* (2016) reported a similarly insensitive behaviour of European eel to strongly decelerating or accelerating flows, which the authors ascribe to the thigmotactic nature of eel. The presented results therefore imply that downstream passage facilities and bypass systems in particular need to offer several paths with various hydrodynamic cues to attract all species and sizes in order to avoid a system-induced selection.

Migrating and non-migrating fish react differently to changing water flows and hydrodynamic stimuli. Long-distance migrators in particular, i.e. Atlantic salmon and European eel, optimise their downstream migration to arrive at optimal conditions. Therefore, the migratory time window of anadromous and catadromous fish is oftentimes quite short. For this study, it was impossible to catch actively migrating wild Atlantic salmon smolts and silver eel. The reactions of these fish species to the CBR-BS might therefore differ from what was observed in the ethohydraulic tests for Atlantic salmon parr and yellow eel. Furthermore, several studies point out that fish and in particularly European eel move downstream at dusk or during the night (Adam, 2018; Adam *et al.*, 2018; Zaugg and Mendez, 2018). Since infrared light is considered to be outside the visible range of fish, Kemp and Williams (2009), Vowles and Kemp (2012), and Vowles *et al.* (2014) conducted live-fish experiments under daylight conditions as well as in dark conditions with infrared lighting, and showed that the behaviour of juvenile Pacific and Chinook salmon can be considerably different in light and dark conditions. In the present study it was not possible to conduct the live-fish tests at night. The size of the study area, i.e. flume width and flow depth of 1.5 m and 0.9 m, respectively, prevented the application of infrared lighting and video recording. The absorption of infrared light by water was too strong to detect the fish swimming along the flume bed with the available camera equipment. Since the avoidance behaviour at the CBR-BS could significantly differ at night, it is recommended to adapt the laboratory setup (e.g. by decreasing the flow depth) to enable night experiments in the future.

For each live-fish test, only three fish were simultaneously released. This way, it was possible to distinguish each individual fish with visual observation during the tests and with the tracking software during the data post-processing. However, some of the tested fish species (e.g. spirlin, brown trout) can form large schools under natural conditions, which might affect their behaviour on encountering a behavioural FGS. In the present study, the spirlin

swam in a close school. If one fish accepted the bypass, the other two often followed quickly, which led to a high FGE.

Since laboratory space was limited, the dimensions of the CBR-BS in the laboratory setup are distorted compared to prototype dimensions. The laboratory CBR with $\alpha = 30^\circ$ has a length of $l_R = 2.3$ m and therefore represents only the last section of a longer rack. Furthermore, the bypass width of $w_{by} = 0.25$ m is smaller than recommended by Ebel (2016) for most of the tested fish. As shown in Section 6.1.2 (Figure 6.7), the SVG_x values are locally increased at the bypass entrance, which possibly masks the gradual velocity increase into the bypass leading to more hesitation in the laboratory tests.

Nevertheless, the ethohydraulic tests conducted in this study give important implications on the behaviour of the six tested fish species on encountering a mechanical behavioural barrier. The test setup and the usage of the fish-tracking software allowed for a detailed observation of the fish behaviour at a high resolution, which is not possible in field studies. Especially in case of the tested cyprinid species, almost no literature on their reactions to changing flows is available. As a next step to further develop and optimize CBR-BS, the prototype testing of the recommended CBR-BS at a HPP is proposed. An extensive monitoring over at least one migratory cycle is necessary to conclusively evaluate the effectiveness and efficiency of the system. It is recommended to use stow nets at the turbine and bypass outlets to assess passage rates or to tag and release individual fish in the upstream reach.

7 Electrified curved-bar rack

The CBR was equipped with a low-voltage electric field (e-CBR) to further increase the fish protection and guidance efficiency of European eel. Furthermore, it was tested whether the protection and guidance can be maintained for the spiralin, which were guided well without the electrification. This chapter reports the protection and guidance efficiencies for both tested fish species, discusses the reaction of the fish to the electric stimuli and demonstrates the importance of the e-CBR setup to avoid fish injuries.

Parts of this section have been published in Meister et al. (2020c): EthoMoSt, Ethohydraulische Modellversuche an elektrifizierten Fischleitrechen (Ethohydraulic model study on electrified fish guidance structures), Swiss Federal Office of Energy, SI/501758-01

7.1 Fish protection and guidance efficiencies

The European eel started to perceive the electric field only a few centimetres upstream of the e-CBR or upon direct contact, which generally led to a strong avoidance reaction. The majority of the eel approached the rack with negative rheotaxis, i.e. with their head first, and reacted stressed with fast movements as soon as they perceived the electric field. They swam backwards in sigmoidal movements before turning around and fleeing back upstream or in the direction of the bypass, which coincides with the behaviour described by Berger (2017). Figure 7.1a/b shows the FGE, FPE and the FGE*, FPE*, respectively, of the live-fish tests with the CBR ($\alpha = 30^\circ$, $s_b = 50$ mm) without electrification and the e-CBR with electrification. The e-CBR was equipped with different pulse settings (cf. Table 3.8). However, only two different pulse settings resulting in a duty cycle of 0.2% (Test F2: $L_{\text{pulse}} = 0.2$ ms, $L_{\text{gap}} = 0$ ms, $N_{\text{pulse}} = 1$, $t_{\text{rep}} = 100$ ms) and 0.75% (Test F4: $L_{\text{pulse}} = 0.3$ ms, $L_{\text{gap}} = 7$ ms, $N_{\text{pulse}} = 5$, $t_{\text{rep}} = 200$ ms) led to controlled fish reactions. As shown and discussed in Section 6.2.4, the FGE and FPE of the CBR without electrification were low for eel. With electrification, the FGE increased from 27% to 67% for F2 and to 75% for F4. Due to the small number of observations with rack interaction, the significance for the increase of bypass passages from the CBR to the e-CBR could not be proven (F2: $\chi^2 = 2.165$, $P = 0.141$; F4: $\chi^2 = 2.534$, $P = 0.111$). The FPE significantly increased from FPE = 27% with the CBR to FPE = 100% with the e-CBR independent of the pulse parameters (F2: $\chi^2 = 10.368$, $P = 0.001$; F4: $\chi^2 = 7.288$, $P = 0.007$).

The pulse pattern (cf. Table 3.8) with a duty cycle of 0.93% in test F5 triggered a violent and sometimes uncontrolled escape reaction and scared the eel away from the rack and the bypass instead of guiding them. Since only the pulse parameters were changed for F5 compared to

the configurations shown in Figure 7.1, the higher duty cycle of 0.93% must be decisive for the more violent reaction. The configuration F5 was finally aborted after four tests, because black spots were found on the skin of an eel after contact with the rack (cf. section 7.3). The Centre for Fish and Wildlife Medicine (FIWI) found internal bleeding in this eel.

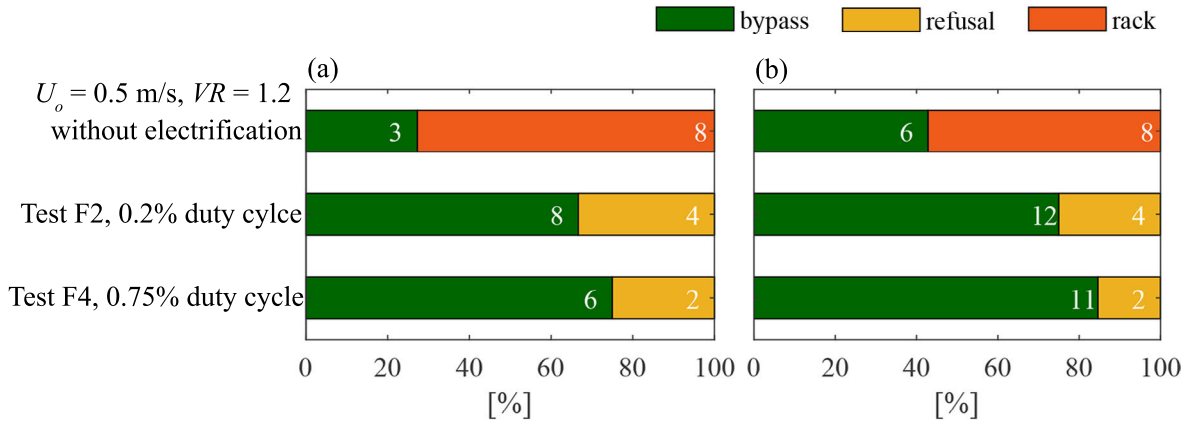


Figure 7.1 Rack passages, refusals and (a) bypass passages with rack interaction (FGE) and (b) all bypass passages (FGE*) for European eel (absolute numbers of fish given in white) at the CBR without electrification and at the e-CBR (both with $s_b = 50$ mm) for two different pulse settings (Tests E9, F2, F4)

The two pulse settings that led to favourable results for European eel were also tested with spiralin (Tests F1 and F3). The spiralin mostly approached the e-CBR with positive rheotaxis and perceived the electric field approximately 10 cm upstream of the e-CBR. In general, the CBR without electrification successfully guided spiralin to the bypass without any rack passages (Figure 6.17). As a result, $FPE = 100\%$ and $FGE = 85\%$ with 15% refusals (cf. Section 6.2.1). The FPE of the e-CBR remained the same with 100%, but resulted in significantly higher refusals compared to the non-electrified CBR (Figure 7.2). The FGE therefore decreased from $FGE = 85\%$ without electrification to $FGE = 47 - 60\%$ for the e-CBR depending on the pulse parameters (F1: $\chi^2 = 4.631$, $P = 0.031$; F3: $\chi^2 = 1.648$, $P = 0.199$). It was observed, however, that the spiralin were guided well by the e-CBR in the tests F1 and F3, but often hesitated at the bypass entrance. To isolate the bypass from the electric field of the CBR, a 20 mm thick wooden plate was fastened to the bypass wall closer to the CBR. This might have led to an increased flow separation at the bypass entrance and thus to the increased avoidance behaviour of the spiralin, which react sensitively to hydrodynamic cues (cf. Section 6.1.4).

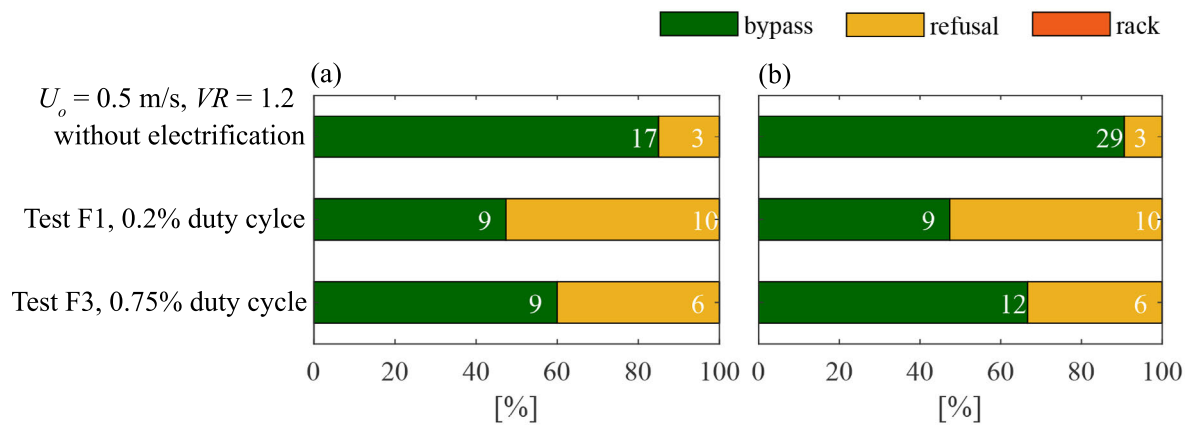


Figure 7.2 Rack passages, refusals and (a) bypass passages with rack interaction (FGE) and (b) all bypass passages (FGE*) for spiralin (absolute numbers of fish given in white) with the CBR and the e-CBR (both with $s_b = 50$ mm) for two different pulse settings (Tests E4, F1, F3)

7.2 Fish reaction to electric stimuli

The fish protection and guidance of the CBR with $s_b = 50$ mm for eel was significantly increased with the e-CBR, whereas the fish guidance for spiralin significantly decreased. The latter is attributed to the sensitive reaction of spiralin to electrical stimuli. For larger bar spacings ($s_b = 110$ mm) all tested pulse parameters led to uncontrolled reactions, increased rack passages and/or fish injuries. With $s_b = 110$ mm, the hydraulic guidance effect of the CBR was expected to reduce compared to the CBR with $s_b = 50$ mm, which consequently did not trigger the same avoidance reaction of spiralin as for $s_b = 50$ mm. Furthermore, the CBR with $s_b = 50$ mm functions only as a weak physical barrier for eel, but not as a behavioural barrier (cf. Section 6.2.4). Therefore, increasing the bar spacing to 110 mm further reduces the physical barrier effect with the result that the eel could easily pass between the bars.

The current lines in Figure 7.3a illustrate the flow from the anode (+) to the cathode (-). The voltage lines, i.e. lines of equal potential, are oriented orthogonally to the current lines. The voltage gradient in [V/cm] is defined as the voltage change over a specific length. The fish perceive the electric field as the voltage change over their body length, width or height. Figure 7.3b schematically illustrates the current lines around and between the bars of a fish guidance structure. At the e-CBR, the anode and cathode are separated by the distance between the bars, which at 38 V results in a voltage gradient of 7.6 V/cm for $s_b = 50$ mm and 3.5 V/cm for $s_b = 110$ mm. When fish approach the rack orthogonally to the current lines, i.e. parallel to the voltage lines, they feel the electric potential across their lateral body width (blue fish in Figure 7.3b). In this case, the potential difference perceived by the fish is small and a controlled reaction is possible. However, if the fish passes between the bars and aligns

itself normal to the bars and parallel to the current lines, it perceives the maximum potential difference over the entire body length (red fish in Figure 7.3b). In this case, the voltage gradient is high and a controlled reaction is no longer possible, the fish escapes or undergoes galvanotaxis, i.e. the current triggers a muscle reaction guiding the fish to the anode or even anaesthetises it for a short time (galvanonarcosis, cf. Section 7.3).

The e-CBR setup means that the orientation of the fish to the rack and thus towards the current lines is decisive for the fish reaction. Therefore, the reaction takes place earlier and in a more controlled manner if the fish is oriented orthogonally to the rack plane either with negative rheotaxis like the eel or with positive rheotaxis like the spiralin. However, eel in particular often aligned themselves parallel to the rack, so that they come into contact with the bars of the CBR more easily. Furthermore, with larger bar spacings, both spiralin and eel are more prone to a rack passage because of the reduced hydraulic and physical barrier effect of the rack and are hence prone to be exposed to high voltage gradients depending on their orientation. The present results clearly show that increasing the bar spacing increases the risk of uncontrolled fish reaction and hence injuries (Section 7.3).

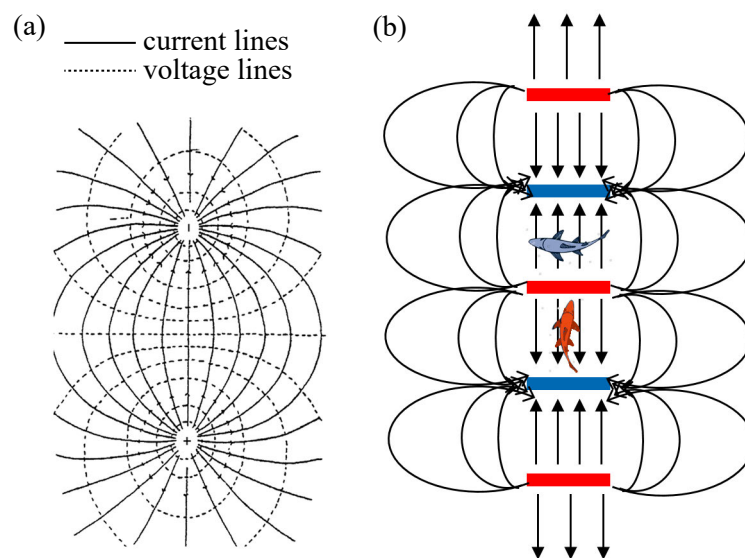


Figure 7.3 (a) Electric field between a circular anode and cathode, and (b) simplified representation (top view) of the electric field, i.e. current lines, at a row of plate capacitors; the electric field at the CBR is thus strongest between the bars

7.3 Fish injuries

None of the reference projects and literature studies presented in Section 2.8 addressed any fish injuries caused by electrified FGSs. According to Tutzer *et al.* (2019), low voltages are harmless to living organisms. It is known from electrofishing, however, that not the absolute

voltages but the respective voltage gradients are decisive for fish reactions and ultimately for fish injuries. Pulsed direct current (pDC) is more harmful than direct current (DC). As a general rule, the voltage gradient for pDC in electrofishing should be between 0.1 and 1.0 V/cm, with the exact value depending on the conductivity of the water and the pulse parameters (Beaumont, 2016). Starting from a voltage gradient of about 0.1 V/cm, fish swim towards the anode, which is forced by muscle contraction. Tetany can occur from voltage gradients as low as 0.5 V/cm (Beaumont, 2016), which severely limits the fish swimming capacity. As a result, in the present study a passive rack passage can occur, during which the fish are exposed to an even higher voltage gradient between the anode and the cathode (cf. Figure 7.3b). The resulting voltage gradients between the bars of the CBR at 38 V are 7.6 V/cm for $s_b = 50$ mm and 3.5 V/cm for $s_b = 110$ mm, and are thus substantially higher compared to the values for incipient reaction found by Beaumont (2016).

In the present study, black marks on the skin of the eel and the spiralin were observed after some experiments, especially when the fish were in contact with the bars (Figure 7.4). The marks occurred independent of bar spacing, voltage or applied pulse patterns for the e-CBR tests F5, F7 and F8 (Table 3.8). The marks did not disappear even after several days in the laboratory, which is an indication for internal bleeding. Figure 7.4 shows the eel described in section 7.1, which was aligned parallel to the rack and touched the electrified aluminium bars during test F5. In order to determine whether these injuries were only superficial or serious, the eel was examined by FIWI. They did not detect any internal injuries directly beneath the black marks. However, bleeding in the spinal cord, spinal column and ventral fin was diagnosed. The fish were examined for external injuries before each live-fish test. However, it could not be determined whether these internal injuries were caused by the electrification during the ethohydraulic test or whether the fish had internal injuries on arrival at the laboratory (e.g from electrofishing). A spiralin passed the e-CBR with $s_b = 110$ mm in test F7. The observed behaviour was similar as described in Section 7.2. Due to the large bar spacing, the fish swam up to 1-2 cm close to the rack, where it suddenly lost control and drifted passively through the rack. After this test, the swimming behaviour of this spiralin was restricted indicating a rupture of the spinal canal (Meister, 2020).



Figure 7.4 External injuries of an eel after direct contact of the e-CBR in test F5

8 Operational aspects of curved-bar rack bypass systems

8.1 Clogging probability by organic fine material

Physical model experiments with organic fine material were conducted for the CBR configurations with $\alpha = 15^\circ, 30^\circ, 45^\circ$, $\beta = 45^\circ$ and $\sigma = 0.17$ ($s_b = 50$ mm) at a diversion-type HPP setup. Two types of leaves, i.e. the common beech and the common hazel, were tested, representing two different leaf sizes (Table 3.5). The ratio of the leaf length to clear bar spacing L_L/s_b is 2.3 for the hazel leaves and 1.5 for the beech leaves.

The statistical analysis by means of χ^2 -tests indicates that the approach flow velocity U_o has no significant effect on the clogging probability (CP) neither for the beech ($p = 0.464$) nor for the hazel ($p = 0.283$). The effect of α on the CP of hazel and beech are shown in Figure 8.1a for $U_o = 0.71$ m/s (prototype value). The CP is significantly different for the two leaf types ($p < 0.001$). The high hazel leaf length to bar spacing ratio $L_L/s_b = 2.3$ leads to a high $CP > 80\%$ independent of the rack angle ($p = 0.168$). For the smaller beech leaves, however, decreasing α from 30° to 15° significantly increases CP ($p < 0.001$), whereas the increase of CP when decreasing α from 45° to 30° is not significant ($p = 0.203$). The curved bar shape leads to a reduced bar opening in flow direction for smaller rack angles, thus increasing the probability of a single leaf getting stuck. Increasing the rack angle increases the bar opening in flow direction, allowing small leaves to pass between the bars.

The CP of hazel leaves at an HBR with $s_b = 20$ mm clear bar spacing is similar to the one of the CBR for $\alpha = 30^\circ, 45^\circ$. The HBR leads to higher CP for beech leaves, however, with $CP \approx 80\%$ and 70% for $\alpha = 30^\circ$ and 45° , respectively (Ganzmann, 2019). While most leaves are small enough to wrap around a single bar at the CBR (Figure 8.1b), they can stretch across two bars at the HBR, thereby reducing the available flow cross section and initialising further clogging.

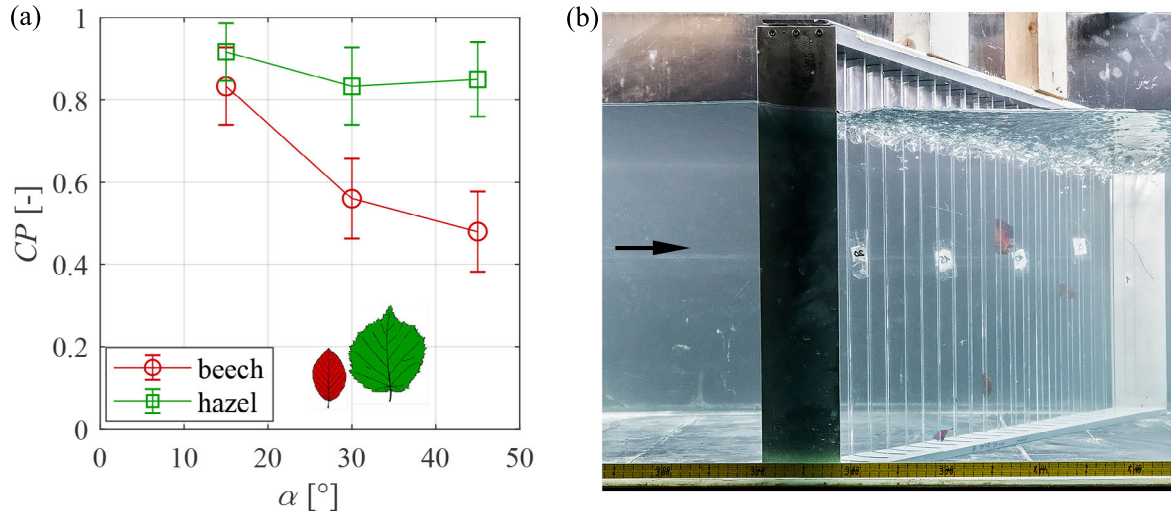


Figure 8.1 (a) Clogging probability (CP) of beech and hazel as a function of the rack angle α for $U_o = 0.71$ m/s, (b) photo of the CBR with hazel leaves wrapped around single bars, adapted from Ganzmann (2019)

8.2 Clogging probability by floating debris

Physical model experiments with driftwood were conducted for the CBR configuration with $\alpha = 30^\circ$, $\beta = 45^\circ$ and $\sigma = 0.17$ ($s_b = 50$ mm) at a diversion-type and a block-type HPP layout. Two different log diameters $d_L = 10$ mm and 40 mm (prototype values), corresponding to $d_L/s_b = 0.2$ and 0.8, respectively, and three different log lengths $d_L = 40$ mm, 100 mm and 200 mm (prototype values), corresponding to $L_L/s_{b,eff} = 1.29$, 3.23 and 6.45, respectively, were used (Table 3.6).

The CP of the logs with $d_L = 40$ mm was 100% for all experiments. Although all logs could fit between two bars on the upstream rack side, they got stuck at the downstream end of the bars due to the narrowing distance between the bars in streamwise direction (Figure 8.3). The smallest distance between two bars for this particular CBR configuration is $s_{b,eff} = 31$ mm (Figure 8.5b).

Figure 8.2a shows the CP of single logs as a function of the approach flow velocity U_o for different log length to minimum effective clear bar spacing ratios $L_L/s_{b,eff}$ and $d_L = 10$ mm for both HPP types. The majority of the logs, which are shorter than the upstream clear bar spacing ($L_L/s_b < 1$), passed the rack, leading to a low CP . Due to the narrowing distance between the bars, however, some logs still got stuck between the bars for low U_o . The CP strongly increases with increasing log length, i.e. $L_L/s_{b,eff} > 1.3$. Thereby, increasing the approach flow velocities decreases the CP because approaching logs are reoriented parallel to the flow and thus transported through the CBR more easily at higher U_o . It was also observed that a log hits the CBR and got stuck but was reoriented and transported through

the rack shortly afterwards. The block-type HPP layout leads to lower CP s compared to the diversion-type HPP. At the block-type HPP, the flow towards the rack is reoriented due to the presence of a closed weir. The transported logs are similarly reoriented parallel to the flow and thus easily transported through the rack.

To model congested driftwood transport, a mix of all log types was simultaneously added to the flow upstream of the CBR. As for the single log experiments, all logs with $d_L = 40$ mm accumulated at the rack ($CP = 100\%$). Therefore, only the CP of logs with $d_L = 10$ mm is shown in Figure 8.2b. The CP for congested transport is higher than for single logs, since the logs accumulate at already clogged logs. The logs interact during transport and are not reoriented parallel to the flow as easily as single logs. Once again, the CP is lower for the block-type HPP, particularly for small U_o compared to the diversion-type HPP. Independent of the HPP geometry, the CP decreases with increasing U_o and decreasing log lengths. This effect of U_o on the CP was also observed by Gudde (2016) and Schalko (2018).

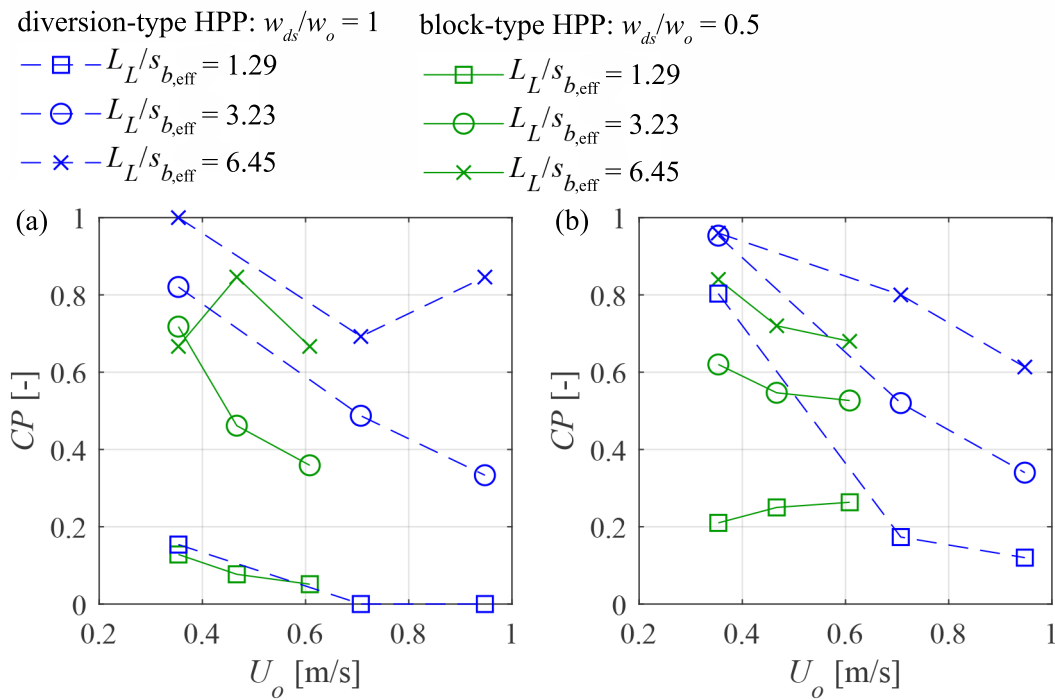


Figure 8.2 Clogging probability (CP) of (a) logs within single log transport and (b) logs within congested wood transport with $d_L = 10$ mm at the CBR configuration with $\alpha = 30^\circ$, $\beta = 45^\circ$, $\sigma = 0.17$ for a diversion- (blue data) and a block-type HPP layout (green data)

The different approach flow conditions to the CBR for the diversion- and the block-type HPP layout led to different main clogging locations. At the diversion-type HPP, the logs were often transported along the CBR towards the d/s rack end after the first rack contact and accumulated there, leading to the accumulation pattern shown in Figure 8.3a. There was

no bypass in this model study, but a properly designed and located bypass at a prototype HPP could facilitate the transport of driftwood to the downstream reach. At a block-type HPP, however, the logs mainly accumulate at the rack centre (Figure 8.3b), because the flow rotating in front of the weir decreases the rack parallel flow component (cf. section 4.2.5).

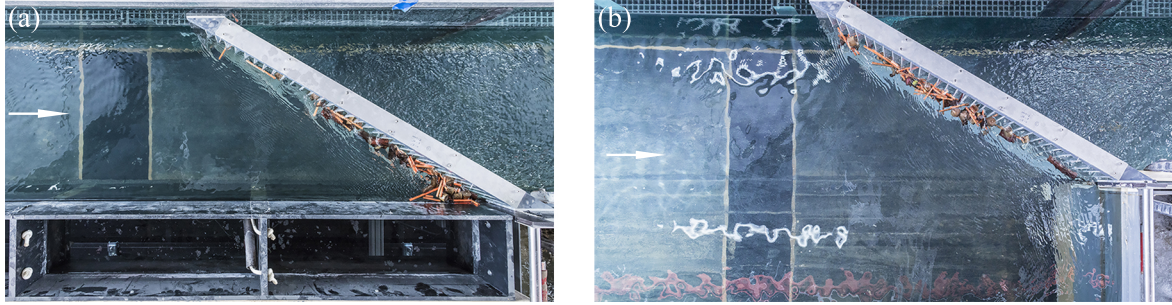


Figure 8.3 Top view on the driftwood accumulation at the CBR for (a) diversion-type HPP and (b) block-type HPP

Since the CP of the model driftwood was highest at low approach flow velocities, the application of a top overlay ($h_{To} = 0.15 \cdot h_o$) and simultaneous weir discharge of $Q_w = 0.07 \cdot Q_o$ was tested as a mitigation measure for the block-type HPP at $U_o = 0.35$ m/s. Figure 8.4a shows the CP as a function of $L_L/s_{b,eff}$ for the two different log diameters $d_L/s_{b,eff} = 0.32$ and 1.29 with and without the mitigation measures. The CP was considerably reduced with the mitigation measures. The logs, which were mostly transported on the water surface, were guided along the top overlay to the weir, where they first accumulated, and finally were spilled over the weir. Nevertheless, the CP for $L_L/s_{b,eff} > 1.29$ and $d_L/s_{b,eff} = 1.29$ remained high and increased up to almost 90% for $L_L/s_{b,eff} = 6.45$. Figure 8.4b shows the percentage of logs, which clogged at the CBR, passed the weir or passed the rack when the mitigation measures were applied. The top overlay did not only lead to an increased rack-parallel, but also to a vertical flow component (cf. Figure 4.18). While for $d_L/s_{b,eff} = 1.29$, none of the logs passed the rack due to their size, for $d_L/s_{b,eff} = 0.32$ up to 46% of the logs passed the CBR by diving underneath the top overlay.

These experiments show that the application of a top overlay in combination with weir discharge or a regulated bypass is an efficient measure to reduce driftwood accumulations. However, the layout of the curved bars narrowing in flow direction will inevitably lead to clogging (Figure 8.5). The presented experimental results showed that the majority of the logs remained clogged at the water surface in a horizontal position. Some logs with a higher density accumulated below the water surface. At higher flow velocities, i.e. $U_o > 0.5$ m/s, about 50% of the logs with $d_L = 40$ mm were clogged vertically between two bars (Figure 8.5a). The question then arises, whether the rack cleaning machine is able to remove those

logs or whether they get pushed further inside the rack, where they can no longer be removed. The latter might ultimately lead to a high blockage by driftwood and thus to increased hydraulic losses. For this reason, alternative curved bar designs (f-CBR) were developed and investigated in a numerical model study presented in Chapter 5.

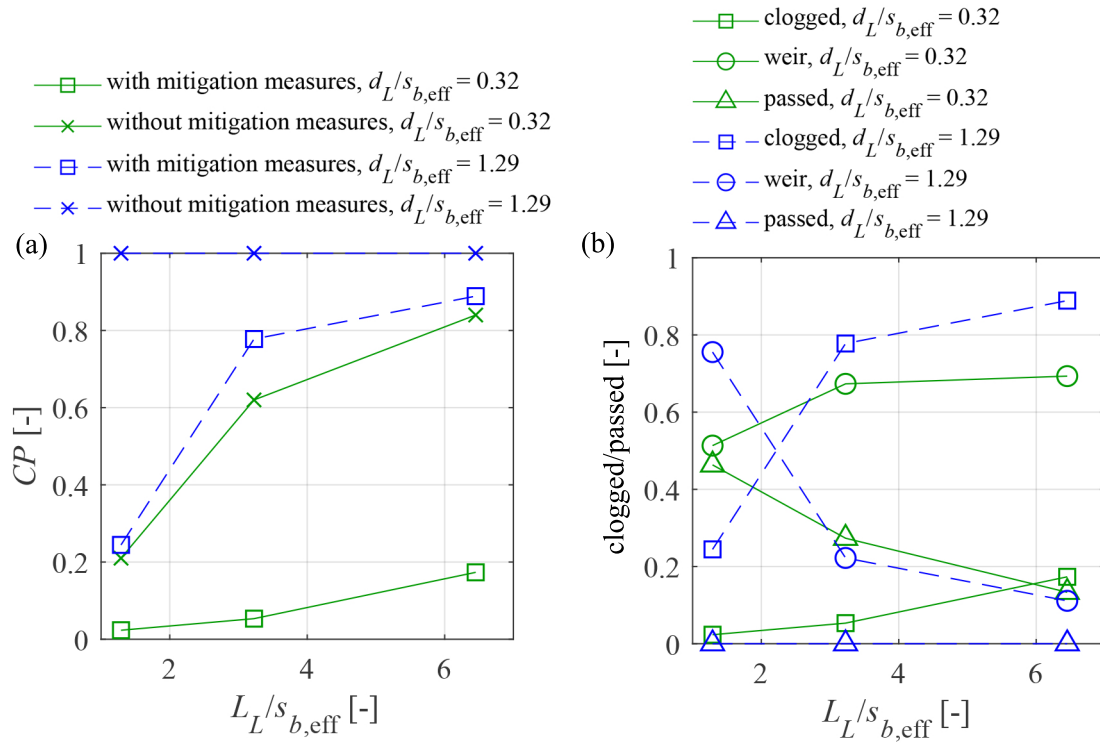


Figure 8.4 (a) Clogging probability (CP) of congested wood transport at a block-type HPP with and without mitigation measures and (b) percentage of clogged or passed logs with the mitigation measures, $U_o = 0.35$ m/s

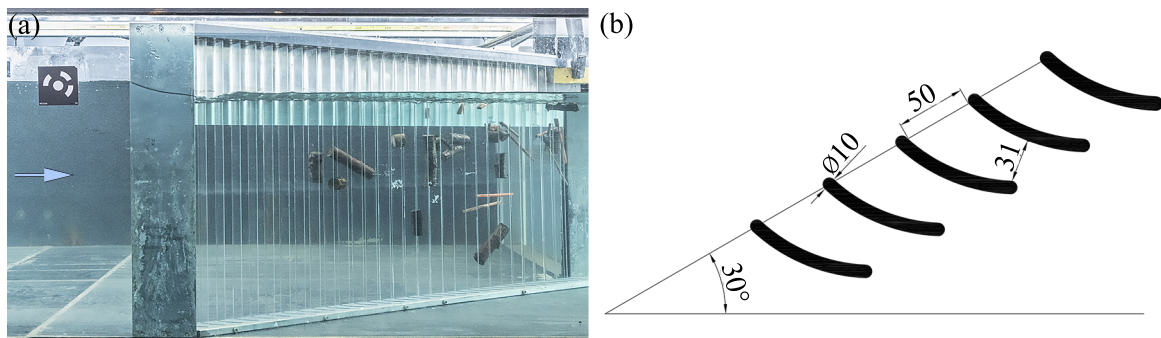


Figure 8.5 (a) Some logs remain clogged during the experiment with the mitigation measures (overlay and weir discharge) and (b) detail of the CBR configuration with $\alpha = 30^\circ$, $\beta = 45^\circ$, $\sigma = 0.17$ ($s_b = 50$ mm, $s_{b,eff} = 31$ mm)

In addition to the alternative bar shape, shutting down turbine operation during a flood event with major driftwood transport is also recommended to increase the guidance of the logs to

the weir (Kriewitz, 2015).

8.3 Rack cleaning machine

Currently, there are several different types of rack cleaning machines being used at trash racks of run-of-river HPPs. These trash racks are typically inclined with a vertical angle of $\gamma = 75^\circ$ (Meusburger, 2002), so that a cable operated cleaning machine can be used (Figure 8.6a). In contrast, the CBR is placed at a vertical angle of $\gamma = 90^\circ$. For this application, a hydraulic cleaning machine with a flexible, tilting arm is suitable (Figure 8.6b). Note that the arm needs space to swing out, typically in the range of 1-2 m. Several manufacturers of rack cleaning machines based in Switzerland, Germany or Austria have confirmed that the rake of standard cleaning machines can be adjusted for the use at the CBR or the f-CBR with costs in the same range as for standard rack cleaning machines (via personal communication).



Figure 8.6 (a) Cable operated rack cleaning machine, (b) hydraulic cleaning machine with a flexible, tilting arm (photos by kuenz GmbH)

9 Engineering application and design guideline

The hydraulic head losses, the flow fields and the fish guidance efficiency of curved-bar rack bypass systems (CBR-BS) are affected by a large number of parameters. In Section 9.1, each parameter is analysed for an adequate engineering application and design of a CBR-BS with regard to the hydraulic performance, efficient fish guidance as well as operational and economic issues. A step-by-step guideline for the design of a CBR-BS is presented in Section 9.2.

9.1 Effect of design parameters on the hydraulic and fish-biological performance of CBR-BS

Bar attack angle β

Among the three main rack parameters, i.e. rack angle α , bar angle β and bar blockage ratio σ , β has the most significant impact on the hydraulic head loss coefficient ξ_R of CBRs. For the smallest tested bar spacing of $s_b = 50$ mm ($\sigma = 0.17$), ξ_R decreases about six times from $\beta = 90^\circ$ to $\beta = 45^\circ$ (Figure 4.1b). Similarly, β has the most significant impact on the velocity distribution up- and downstream of the CBRs. The curved bars of CBRs with $\beta = 45^\circ$ cause a flow straightening effect resulting in a quasi-symmetrical flow distribution downstream of the rack. In the present study, the fish guidance efficiency (FGE) was only evaluated for a CBR with $\beta = 45^\circ$. According to Kriewitz (2015) and Albayrak *et al.* (2020a), the FGEs in ethohydraulic laboratory tests for five European fish species, namely spirlin, European grayling, common barbel, brown trout and European eel, are significantly higher for MBRs with $\beta = 45^\circ$ than for louvers with $\beta = 90^\circ$. Similar trends are expected for the CBR since the velocity gradients upstream of the CBR are more gradual and the maximum velocities at the d/s rack end are decreased for $\beta = 45^\circ$ compared to $\beta = 90^\circ$. Since the upstream velocity gradients are decreased, the downstream flow distribution is improved, the head losses are significantly lower, and the FGE for most tested fish species is high, CBRs with $\beta = 45^\circ$ are recommended over those with $\beta = 90^\circ$.

Clear bar spacing s_b

The second most influencing factor on ξ_R is the non-dimensional bar spacing, i.e. the blockage ratio of the vertical bars $\sigma = t_b/(s_b + t_b)$. For $\beta = 45^\circ$, however, the effect of σ is relatively small (Figure 4.1a) and therefore, the bar spacing should be selected mainly based on the size of the target fish species or operational aspects. In the present study, the effect of different bar spacings on the velocity distribution up- and downstream of the CBR or on

the FGE was not investigated. The FGE was tested for $\sigma = 0.17$, which corresponds to $s_b = 50$ mm clear bar spacing and $t_b = 10$ mm bar thickness at prototype scale. In addition to $s_b = 50$ mm, Kriewitz (2015) conducted live-fish tests with barbel and spirlin at MBRs and louvers with larger bar spacings of $s_b = 110$ mm and reported that the FGE significantly decreased for $s_b = 110$ mm compared to $s_b = 50$ mm. EPRI and DML (2001) investigated angled bar racks with $\alpha = 45^\circ$, and with $s_b = 25$ mm and 50 mm. At $U_o = 0.6$ m/s, the FGEs were considerably higher for $s_b = 25$ mm for the riverine species (bass, walleye, shiner and catfish), whereas s_b did not have an effect on the FGE of American eel.

It is expected that the physical and the behavioural barrier effect of the CBR decreases with increasing s_b . To ensure a high degree of fish guidance, clear bar spacings of $s_b \leq 50$ mm are therefore recommended.

Rack angle α

Although α has the least impact on ξ_R , it strongly affects other parameters. Based on Figure 4.5a, α should not be larger than 45° , since the application of overlays significantly increases ξ_R . Furthermore, α should not be smaller than 15° due to the high cost of excessive structural length. For $\beta = 45^\circ$, the rack angle α has a minor effect on the flow fields up- and downstream of the CBR. For $\beta = 90^\circ$, however, flow conditions improve for $\alpha = 15^\circ$ as compared to $\alpha = 30^\circ$ or 45° . Furthermore, the ratios of parallel to normal velocity components V_p/V_n are more favourable for fish guidance with decreasing α . At a diversion-type HPP setup, the criterion for the fish guidance capacity (FGC) $V_p/V_n > 1$ proposed by Courret and Larinier (2008) is fulfilled for all tested CBR configurations (Figure 4.12c). At a block-type HPP setup, the $FGC < 1$ at the d/s rack end for all CBR configurations (Figure 4.17). However, V_p/V_n values are higher for $\alpha = 15^\circ$ than for $\alpha = 45^\circ$. The installation of a separating pier was tested for the CBR with $\alpha = 30^\circ$, $\beta = 45^\circ$, $\sigma = 0.17$ and improved the FGC with values only slightly below 1 (Figure 4.18d). For CBRs with a clear bar spacing $s_b = 50$ mm, the criterion $V_n \leq v_{\text{sustained}}$ (Ebel, 2016) might be particularly critical for small fish due to their reduced sustained swimming speed. Small fish might get entrained between the bars if V_n values are high. For CBRs, the V_n values decrease with decreasing rack angle α with $V_n \approx U_o \cdot \sin(\alpha)$. Consequently, a smaller rack angle might be suitable for HPPs with higher approach flow velocities U_o in order to decrease V_n .

In the present study, the FGE was only evaluated for a CBR with $\alpha = 30^\circ$. The live-fish test results reported by Kriewitz (2015) and Albayrak *et al.* (2020a) reveal similar FGEs for MBRs with $\alpha = 15^\circ$ or 30° and a bottom overlay for five European fish species, namely spirlin, European grayling, common barbel, brown trout and European eel. The MBR with $\alpha = 15^\circ$ (with or without bottom overlay) and the MBR with $\alpha = 30^\circ$, which was only tested

with a bottom overlay, led to a much higher FGE* and FPE* for European eel and brown trout than the CBR with $\alpha = 30^\circ$. The higher FGE* and FPE* of these two fish species are therefore possibly a result of the lower rack angle and/or the application of a bottom overlay (cf. Table 6.7). EPRI and DML (2001) showed high FGE for milder rack angles, i.e. $\alpha = 15^\circ$, for the tested North American fish species. Similar or even higher FGEs for CBRs than for louvers and MBRs can be expected for $\alpha < 30^\circ$ because of the improved flow fields and are therefore recommended to improve the FPE and FGE for European eel and brown trout.

The curved bar shape of the CBR leads to a reduced bar opening in flow direction for smaller rack angles, thus increasing the clogging probability by floating debris and fine organic material for smaller rack angles α (Figure 8.1a). Increasing the rack angle increases the bar opening in flow direction allowing small leaves to pass between the bars. Considering these issues, CBRs with $\alpha = 15^\circ \dots 30^\circ$ are recommended by considering site-specific parameters, i.e. U_o or geometric restrictions.

Bar depth ε

Different dimensionless bar depths $\varepsilon = d_b/D_b$ were tested only with regard to their effect on the head losses. The reference bar depth in the present study was $D_b = 100$ mm. It is expected that ε does not have a significant impact on the FGE in the range of $0.7 \leq \varepsilon \leq 1.25$. If structural rigidity and large wood and sediment accumulations are no issues, a shorter relative bar depth of $\varepsilon = 0.70$ ($d_b = 70$ mm) is therefore recommended due to reduced head losses and cost compared to $\varepsilon = 1.0$. Otherwise, the bar depth has to be increased accordingly.

Bottom and top overlays

The effect of a top and/or bottom overlay on ξ_R strongly depends on the basic parameters α , β , and σ . If $\sigma = 0.17$, additional overlay blockage has only a small effect on ξ_R . Top and bottom overlays not only provide a physical barrier for fish, they also increase the guidance effect for fish swimming close to the water surface or the channel bed, respectively. Although overlays were not tested with fish in the present study, it is expected that fish guidance increases similarly as seen for louvers and MBRs with overlays (Table 6.7) (Odeh and Orvis, 1998; EPRI and DML, 2001; Amaral, 2003; Albayrak *et al.*, 2020a). The parallel velocity components V_p increase while the normal velocity components V_n decrease in front of the overlays, reducing the risk of fish entrainment through the CBR. It was shown in Section 8.2 that a top overlay further guides large wood along the CBR preventing wood accumulations at the rack, while a bottom overlay may promote the guidance of sediments

to the bypass. Between the overlays, however, V_p/V_n values are decreased, which locally reduces the guidance effect. Additional overlay blockage slightly deteriorates the turbine admission flow distribution and causes spiral flow but only marginally increases the head loss (Table 4.1). The live-fish test results reported by Kriewitz (2015) and Albayrak *et al.* (2020a) reveal higher FGE* for European eel and brown trout with an MBR equipped with a bottom overlay with $h_{Bo} = 0.11 \cdot h_o$ compared to the same MBR configuration without a bottom overlay. Ebel (2016) proposes a minimum height for top and bottom overlay of $h_{To} = 1.0$ m and $h_{Bo} = 0.5$ m, respectively. Based on the results of this study, a maximum total overlay height of $h_v = (0.20 \dots 0.30) \cdot h_o$ is recommended for a high fish guidance efficiency and the mitigation of operational issues by considering site-specific geometrical (e.g. flow depth), fish-biological and operational conditions. For approach flow depths $h_o > 5$ m, the recommendation by Ebel (2016) can be applied at CBRs. For $h_o < 5$ m, however, it is recommended to apply $h_v \leq (0.20 \dots 0.30) \cdot h_o$ to minimise the hydraulic head losses.

Bar shape

As shown in Section 4.1, the impacts of the primary parameters of rack angle α , bar attack angle β and bar-blockage ratio σ on the hydraulic head loss coefficient ξ_R are similar for both CBRs and MBRs described by Albayrak *et al.* (2018). However, the curved bar shape of the CBR leads on average to 4.2-fold lower head losses than the straight, rectangular bars of the MBR (Figure 4.3). In Figure 9.1a, the hydraulic head losses of CBRs are compared with other FGS types and conventional trash racks. The ξ_R values of CBRs and MBRs with $\alpha = 30^\circ$ and $\beta = 45^\circ$ were calculated with Eq. (4.1) in combination with Eq. (4.3) or $C_s = 1$, respectively. The ξ_R values of horizontal bar racks (HBR) with $\alpha = 30^\circ$ and of conventional trash racks placed perpendicular to the approach flow were computed for hydrodynamic bars with the equations proposed by Meister *et al.* (2020b) and Meusburger (2002), respectively. In Figure 9.1a, all equations were used in their respective limitations for the tested rack and hydraulic configurations. Increasing σ (= decreasing the clear bar spacing s_b) results in increasing ξ_R for conventional trash racks and all FGSs. Blockage ratios between $0.17 \leq \sigma \leq 0.33$ lie outside the limits of the FGS equations. Only one f-CBR configuration with $\sigma = 0.24$ was investigated with the numerical model. Its head loss was computed to $\xi_R = 0.91$. The ξ_R values of CBRs are in the lower range of ξ_R values of conventional trash racks used at Swiss run-of-river HPPs (Meusburger, 2002) and of HBRs. The recommended MBR (Albayrak *et al.*, 2018), HBR (Meister *et al.*, 2020b), and CBR configurations are compared in Figure 9.1b showing the rack head loss measured in the respective laboratory study ($\xi_{R,m}$) and predicted with the empirical equation ($\xi_{R,p}$). Additionally, the head losses for the CBR configuration with $\alpha = 30^\circ$ and top, bottom, and top & bottom overlay are illustrated.

Although the hydraulic performance of the CBR with curved bars was greatly improved compared to the MBR with straight bars, the CBR is disadvantageous with regard to the accumulation of large wood and organic fine material (Chapter 8). The narrowing cross section in streamwise direction of the curved bars are difficult to reach by the rack cleaning machine, which can lead to high clogging of the CBR. For this reason, the curved bar shape was further optimized and a foil-shaped bar (f-CBR) was developed. The narrowest cross section is located at the upstream bar tips of the f-CBR (Figure 3.15c), which facilitates the cleaning process and thus mitigates the clogging problem of the CBR. The ξ_R of the f-CBR is only slightly higher than for the CBR (Figure 9.1) and the hydraulic performance is similar to the CBR with regard to a quasi-linear velocity increase along the rack towards the d/s rack end and a quasi-symmetrical flow downstream of the rack (Section 5.2). Therefore, the f-CBR is expected to have a similarly high fish protection and guidance efficiency as the CBR and the application of the f-CBR is recommended.

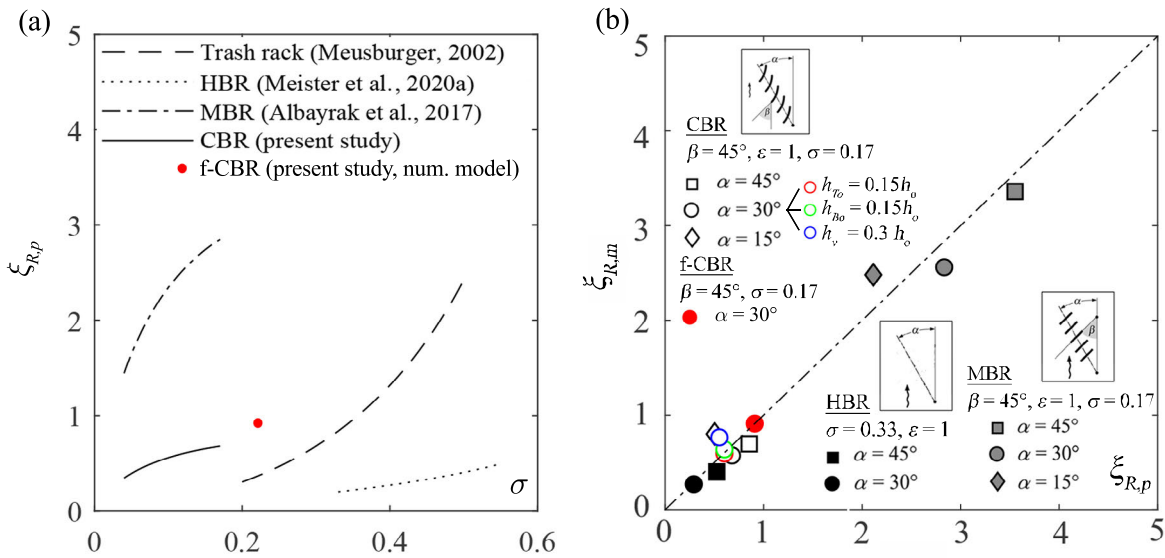


Figure 9.1 (a) Comparison of predicted ξ_R values versus σ for trash racks and different FGSs, namely HBR, MBR, CBR, and f-CBR with a rack angle $\alpha = 30^\circ$ (b) Overview of predicted versus measured head loss coefficients of recommended rack configurations: MBR and CBR with $\alpha = 15^\circ, 30^\circ$ & 45° , $\beta = 45^\circ$, $\sigma = 0.17$ and $\varepsilon = 1$, HBR with $\alpha = 30^\circ$ & 45° , blockage ratio $\sigma = 0.33$ ($s_b = 20$ mm) and $\varepsilon = 1$, and ξ_R value for the f-CBR with $\alpha = 30^\circ$ from the numerical model study

Approach flow velocity U_o

According to the logistic regression model including all fish species, the approach flow velocity U_o did not have a significant effect on the number of bypass passages, i.e. the fish guidance efficiency, of the CBR-bypass system (CBR-BS) in the tested range. In contrast, the fish spent more time in the vicinity of the rack and took more time to find and accept the

bypass, hence the number of refusals significantly increased and the rack passages significantly decreased, resulting in a higher fish protection efficiency for $U_o = 0.7$ m/s compared to $U_o = 0.5$ m/s (Figure 6.29). The lower approach flow velocity $U_o = 0.3$ m/s was only tested with brown trout and led to a significant increase of the FGE for these fish. The live-fish tests were conducted with a CBR with $\alpha = 30^\circ$ and a maximum U_o of 0.7 m/s, resulting in $V_n \leq 0.5$ m/s (Figures 6.3 and 6.11). The smallest fish tested at this velocity, i.e. the spiralin with a minimum body length of 8.4 cm, navigated along the flume and in front of the CBR in a controlled manner and without obvious exhaustion for the duration of the experiment of 45 minutes. The impingement of a fish to the CBR was not observed in any of the conducted tests. Ebel (2016) suggests $V_n \leq v_{\text{sustained}}$ for HBR-BS to avoid the impingement of fish to racks with such small bar spacings. This recommendation leads to lower rack angles α for higher approach flow velocities U_o , since $V_n \approx U_o \cdot \sin(\alpha)$. BAFU (2012) gives a more conservative recommendation of $U_o \leq 0.5$ m/s for physical barriers, i.e. vertical or horizontal bar racks with clear bar spacings $s_b \leq 20$ mm. The USBR (2006) recommends maximum approach flow velocities of $U_o = 0.30 \dots 0.61$ m/s for weak and $U_o = 0.83 \dots 1.37$ m/s for strong swimmers at louvers. Based on the results of this study, it is recommended to select the rack angle α to comply with the criteria $V_n \leq v_{\text{sustained}}$ proposed by Turnpenny and O’Keeffe (2005) and Ebel (2016) to enable fish of all sizes to react to the hydrodynamic cues of the mechanical behavioural barrier and avoid exhaustion.

Bypass design and operation

Velocity measurements were conducted at four different bypass layouts. The pipe bypass led to decreasing velocities near the bypass inlet followed by a sharp velocity increase directly at the entrance, which could trigger an avoidance reaction of the fish. For this reason and due to the high risk of clogging, this bypass layout is not recommended. Generally, gradual geometrical transitions are recommended to obtain a gradual velocity increase with little turbulence.

Contrary to U_o , the ratio of the bypass entrance velocity to the approach flow velocity $VR = U_{\text{by,in}}/U_o$ did have a significant effect on the fish guidance efficiency in the tested range. The total number of bypass passages significantly decreased, while the number of rack passages increased for $VR = 1.4$ compared to $VR = 1.2$ (section 6.3). Some fish species like the spiralin or the nase reacted more sensitively to VR than others like the barbel, the brown trout, the salmon parr or the European eel.

Although most available practice guidelines recommend a bypass discharge as a percentage of the approach flow discharge (DWA, 2005; BAFU, 2012; Ebel, 2016), the presented results indicate that the VR and the spatial velocity gradient SVG_x at the bypass entrance are the

decisive parameters for an efficient bypass design, which is quickly accepted by fish (Figure 6.15). The comparison with the recommendations for salmonids of $SVG_x = 1.0 \dots 1.2 \text{ s}^{-1}$ (Haro *et al.*, 1998; Enders *et al.*, 2012) shows that the spirlin tested in the present study were more sensitive to velocity gradients and prefer lower values of $SVG_x \leq 0.6 \text{ s}^{-1}$ resulting in a lower bypass discharge. The discharge of the bypass system Q_{by} at existing FGSs mostly installed at HPP with $Q_d < 100 \text{ m}^3/\text{s}$ amounts to 2 - 10% of the design discharge (Odeh and Orvis, 1998; Larinier and Travade, 1999; Ebel, 2016). For large run-of-river HPPs with $Q_d > 100 \text{ m}^3/\text{s}$, however, $Q_{by} < 0.02 \cdot Q_d$ might be practical to reach the ideal velocity gradients for efficient fish guidance and a fast bypass acceptance.

The findings of this study therefore support the recommendation by Ebel (2016) for a full-depth open channel bypass including an axial flap gate with bottom and top openings at the entrance and an inclined ramp for discharge control. This design allows for velocity regulation and intermittent flushing of floating debris. An alternative solution for surface oriented species is the NU-Alden weir proposed by Haro *et al.* (1998) in combination with a full-depth open channel bypass, which also allows for velocity regulation and continuous transport of floating debris. The ratio of bypass entrance to approach flow velocity VR is an important design criteria independent of the bypass design. Ebel (2016) recommends $VR = 1.0 \dots 2.0$ for all fish species, while USBR (2006) proposes $VR = 1.1 \dots 1.5$ for American fish species. To protect and guide fish of all species, life stages and sizes, $VR = 1.1 \dots 1.2$ are recommended according to the findings of this study.

9.2 Guideline for the design of a prototype CBR

For the positioning and the design of the optimum CBR configuration for effective fish protection and guidance, and low impacts on hydropower production at a specific HPP site, the following workflow adapted from Ebel (2016) and Feigenwinter *et al.* (2019) is proposed by considering the recommendations in the previous Section 9.1:

1. Identification of one or several target fish species and their main migration and movement corridors by taking advantage of the experience of the local fisheries manager and telemetry data if available. Knowledge on the fish sizes, their main migration and movement times and preferred habitats further improve the assessment of the swimming capacities.
2. Mapping of the site-specific hydraulic conditions by means of in-situ measurements (e.g. with an Acoustic Doppler Current Profiler - ADCP) and/or large-scale CFD simulations for different flow regimes (e.g. $Q_{30} - Q_{330}$).
3. Conducting a variant study of different CBR locations and rack angles considering the movement corridors, the swimming capacities and the seasonal behaviour patterns of the target fish species, and the following design criteria:
 - Fish guidance capacity (FGC): $V_p/V_n > 1$ along the entire rack to ensure efficient fish guidance towards the bypass (Courret and Larinier, 2008)
 - $V_n \leq v_{\text{sustained}}$ along the entire rack to ensure that the fish can actively swim against a rack without exhaustion (Turnpenny and O’Keeffe, 2005). Thereby, $v_{\text{sustained}}$ is computed with $t \geq 200 \cdot 60$ s, and Eq. (9.1) for rheophile fish species and Eq. (9.2) for eel for different fish lengths TL (Ebel, 2016)

$$\log(v_{\text{fish}}) = 0.546 + 0.7937 \cdot \log(TL) - 0.0902 \cdot \log(t) + 0.2813 \cdot \log(T), \quad (9.1)$$

$$\log(v_{\text{eel}}) = 0.425 + 0.567 \cdot \log(TL) - 0.133 \cdot \log(t), \text{ for } T > 10^\circ\text{C} . \quad (9.2)$$

The simplified relation $V_n \approx U_o \cdot \sin(\alpha)$ gives a rough estimate of the cross-sectional mean V_n at the CBR. A CFD model allows for a more detailed modelling of V_n at the entire rack, however, which might be particularly useful for intakes without a frontal approach flow (e.g. block-type HPP). The sustained swimming speed of fish $v_{\text{sustained}}$ increases with increasing fish length. See point 7 for a discussion on the fish guidance efficiency if $V_n \geq v_{\text{sustained}}$ for some fish.

- Symmetrical turbine admission flow: $\Delta Q/Q_t = |Q_{\text{left}} - Q_{\text{right}}| / Q_t \leq 5\%$ (Godde,

1994)

- Geometrical or constructional constraints for the bypass routing

A detailed example for the assessment of the optimal FGS position using a CFD model is given in Feigenwinter *et al.* (2019).

4. Consideration of top and bottom overlays for the guidance of floating debris and sediments, respectively, and to increase fish guidance. While the absolute overlay heights proposed by Ebel (2016) for top and bottom overlay of $h_{To} = 1.0$ m and $h_{Bo} = 0.5$ m, respectively, are practical for deep approach flow depths, the relative overlay heights of $h_v = (0.20...0.30) \cdot h_o$ are recommended for smaller flow depths. An additional flushing channel or a vortex tube in front of the CBR-BS can increase the intermittent sediment flushing efficiency and provides shelter with low flow velocities for fish.
5. Selection of the bar shape based on operational and structural boundary conditions. The f-CBR is recommended due to the low head losses, symmetrical flow downstream of the rack, expected high fish guidance, and low clogging probability. The presented shape of the f-CBR can be applied for $\alpha \geq 30^\circ$ and has to be adapted for $\alpha < 30^\circ$ to minimise the clogging probability.
6. Head loss assessment
 - The head losses can be estimated with Table 9.1 for the following limitations: $\alpha = 15^\circ...45^\circ$, $\beta = 45^\circ...90^\circ$, $\sigma = 0.04...0.17$ with $\sigma = t_b/(s_b + t_b)$, $\varepsilon = 0.7...1.25$ with $\varepsilon = d_b/D_b$ corresponding to $d_b = 70$ mm...125 mm, $V_{1,3} = 0...0.25$ and $V_2 = 0...0.30$ with $V_i = h_v/h_o$, and $w_{ds}/w_o = 0.5...1.0$.
 - The total head loss includes the head loss caused by the vertical bars (Eq. 4.1) and the head loss caused by horizontal spacers and tie bars (subscript sp). The latter was not investigated in this study but can be estimated with the empirical equation proposed in Raynal *et al.* (2013b) developed for angled trash racks and listed in Table 9.1 with $\sigma_{sp} = t_{sp}/(s_{sp} + t_{sp})$. The bar shape coefficient K_i for the horizontal spacers can be taken from Kirschmer (1926) and is $K_i = 2.24, 1.67, 1.04$ for rectangular, rounded, and foil-shaped spacers, respectively.
 - The f-CBR was not systematically investigated for a wide parameter range. The head loss coefficient for the f-CBR with $\alpha = 30^\circ$, $\beta = 45^\circ$, $\delta = 10^\circ$, $s_b = 50$ mm and $t_b = 16$ mm leading to $\sigma = t_b/(s_b + t_b) = 0.24$ was assessed with the numerical model to $\xi_R = 0.91$. The numerical model can be used to assess the head losses and the flow fields for any f-CBR configuration.

Table 9.1 Empirical equations for the head loss assessment of CBRs

Parameter	Equation
Total head loss coefficient ξ_{CBR}	$\xi_{\text{CBR}} = \xi_R + \xi_{sp}$
head loss coefficient ξ_R Eq. (4.1)	$\xi_R = \xi_B \cdot C_S \cdot C_L \cdot C_{V,i} \cdot C_w$
Basic head loss coefficient ξ_B Albayrak <i>et al.</i> (2018), Eq. (4.2)	$\xi_B = 245 \left[0.0275 + (\sigma - 0.0815) \left(\frac{\alpha}{90^\circ} \right) \right] \cdot \left(\frac{\beta}{90^\circ} \right)^{5\sigma^{0.44}}$
Bar shape factor C_S Eq. (4.3)	$C_{S,\text{curved}} = \left(\frac{1}{4.2} \right) \approx 0.24$
Bar depth factor C_L Eq. (4.4)	$C_L = \left[1 + 3.3 (1 - \varepsilon) \left(\frac{\alpha}{90^\circ} \right) \right] \sigma^{2(1-\varepsilon) \left(\frac{\alpha}{90^\circ} \right)}$
Overlay factor $C_{V,i}$ Top or bottom overlay Eqs. (4.5) and (4.6)	$C_{V,1,3} = 1 + \left[10 \left(\frac{90^\circ}{\beta} \right) \left(\frac{V_{1,3}}{1-V_{1,3}} \right)^{4.3\sigma^{0.75 \left(\frac{\alpha}{90^\circ} \right)}} \right] - 5.3 \left(\frac{V_{1,3}}{1-V_{1,3}} \right)^{1.7}$
Top and bottom overlay Eqs. (4.5) and (4.7)	$C_{V,2} = 1 + \left[7 \left(\frac{90^\circ}{\beta} \right) \left(\frac{V_2}{1-V_2} \right)^{9.5\sigma^{1.2 \left(\frac{\alpha}{90^\circ} \right)}} \right] - 1.5 \left(\frac{V_2}{1-V_2} \right)^{1.4}$
HPP layout factor C_w Eq. (4.8)	$C_w = \left(\frac{w_{ds}}{w_o} \right)^{2.3 \left(1 - \frac{\alpha}{90^\circ} - V_i \right)}$
Head loss coefficient of spacers ξ_{sp} Raynal <i>et al.</i> (2013b)	$\xi_{sp} = K_i \left(\frac{\sigma_{sp}}{1-\sigma_{sp}} \right)^{0.77}$

- Errors of $\pm 50\%$, 30% and 15% should be considered for the predicted head loss coefficients $\xi_R < 2$, < 4 and > 4 , respectively.
- According to Table 9.1, the head loss coefficient for the recommended CBR with $\alpha = 30^\circ$, $\beta = 45^\circ$, $\sigma = 0.17$, $\varepsilon = 1$ without overlays is calculated to $\xi_R = 0.68$. Horizontal foil-shaped spacers with $t_{sp} = 0.02$ m and a spacing of $s_{sp} = 0.8$ m result in a spacer head loss coefficient of $\xi_{sp} = 0.06$, which corresponds to 8.9% of ξ_R . The total head loss of this CBR is thus $\xi_{\text{CBR}} = \xi_R + \xi_{sp} = 0.74$.
- The absolute head losses in [m] are calculated to

$$\Delta h_{\text{CBR}} = \xi_{\text{CBR}} \cdot \frac{U_{th}^2}{2g}, \quad \text{with } U_{th} = \frac{Q_t}{h_o \cdot w_{ds}}, \quad (9.3)$$

with U_{th} = theoretical flow velocity in the downstream or the admission flow

channel without rack presence. $U_{th} = U_o$ at diversion-type HPPs with $w_{ds} = w_o$. By using U_{th} instead of U_o or U_{ds} , the assessment is independent of potential weir and bypass discharge in the case of a block-type HPP, but still accounts for Δh_{CBR} .

7. Evaluation of the mitigation potential of a CBR by computing the total fish survival rate of the HPP (S_{HPP}). Currently, no concrete target survival rate for a single movement barrier or river reach has been specified in most countries. Depending on the size of the HPP, its location within the fish passage route and the number of consecutive HPPs, different survival rates might be practical. If a FGS is installed, S_{HPP} is herein defined as the sum of the FGE and the percentage of fish surviving the turbine passage S_t :

$$S_{HPP} = FGE + (1 - FGE) \cdot S_t, \quad (9.4)$$

i.e. weir passage survival rates are not considered in Eq. (9.4). S_t is a function of turbine type, turbine size and rotating speed, and the fish length. The total HPP survival rate S_{HPP} versus TL is computed with S_t according to Monten (1985) and illustrated in Figure 9.2a for a large Kaplan turbine and $Q_d = 400 \text{ m}^3/\text{s}$ ($d_{\max} = 5.9 \text{ m}$, $d_{\min} = 1.0 \text{ m}$, 64 rpm, 4 blades), and in 9.2b for a small Kaplan turbine and $Q_d = 50 \text{ m}^3/\text{s}$ ($d_{\max} = 2.9 \text{ m}$, $d_{\min} = 0.7 \text{ m}$, 215 rpm, 6 blades) without any FGS installed ($S_{HPP} = S_t$) and with a CBR-BS with either low FGE (50%), medium FGE (75%), or high FGE (90%). The total survival rate generally decreases with fish length and is substantially lower for the small compared to the large turbine type.

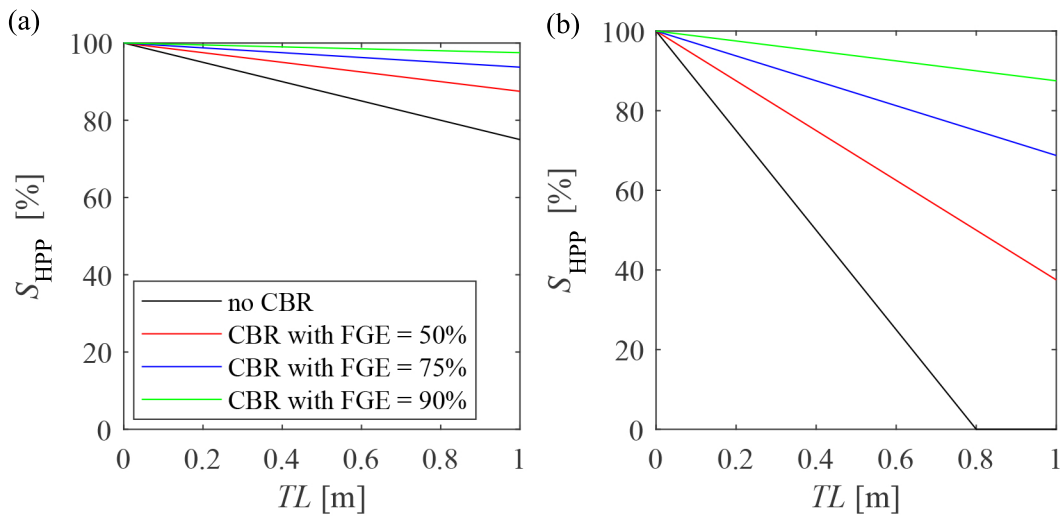


Figure 9.2 Total HPP survival rates S_{HPP} versus fish total length TL for a (a) large Kaplan turbine and $Q_d = 400 \text{ m}^3/\text{s}$, and (b) small Kaplan turbine and $Q_d = 50 \text{ m}^3/\text{s}$

The criterion $V_n \leq v_{\text{sustained}}$ can lead to small rack angles and hence to long structures and high cost for large HPPs with high approach flow velocities. Since V_n depends on the approach flow velocity with $V_n \approx U_o \cdot \sin(\alpha)$, the entire flow duration curve at a HPP site should be considered. As an example, Figure 9.3 shows a fictitious flow duration curve for a HPP with a design discharge $Q_D = 280 \text{ m}^3/\text{s}$. If a CBR with an angle of $\alpha = 35^\circ$ is selected to minimise structural cost, the TL_{crit} of the fish for $V_n = v_{\text{sustained}}$ can be derived with Eq. (9.1) for the entire flow duration curve. It can be assumed that the FGE of the CBR will be compromised for fish with $TL < TL_{\text{crit}}$, because $V_n > v_{\text{sustained}}$ for these fish. Figure 9.3 further shows the theoretical total HPP survival rates, S_{HPP} , for fish with $TL < TL_{\text{crit}}$ in case a large or a small Kaplan turbine is installed, which runs in full-load operation (Monten, 1985). These survival rates result from Eq. (9.4) assuming that $\text{FGE} = 100\%$ for fish with $TL \geq TL_{\text{crit}}$ and $\text{FGE} = 0\%$ for fish with $TL < TL_{\text{crit}}$. As an example, the FGE is assumed here to be zero for fish with $TL < 0.12 \text{ m}$ at Q_{30} , although the real fish guidance is likely not binary at the theoretical total length threshold value. At a HPP with a large Kaplan turbine, the turbine survival rate is still $S_{\text{HPP}} \geq 97\%$ for these fish, whereas it is considerably smaller with $S_{\text{HPP}} \geq 85\%$ at a HPP with a small Kaplan turbine. Note that the fish survival rates can significantly decrease in case of partial load operation. In Figure 9.3, TL_{crit} was computed with Eq. (9.1) assuming a constant water temperature of 15°C . Depending on the HPP site, however, the water temperatures can vary considerably throughout the year. Since the swimming capacity of fish decreases with decreasing water temperatures, the water temperature should be taken into account if this data is available.

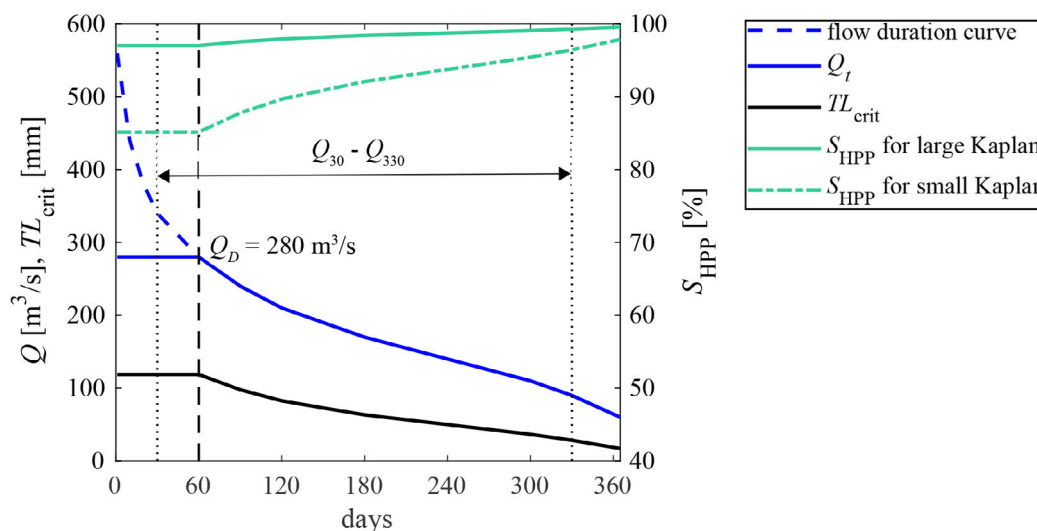


Figure 9.3 Flow duration curve, turbine discharge Q_t , TL_{crit} for $V_n = v_{\text{sustained}}$ with a CBR with $\alpha = 35^\circ$, and turbine survival rates at a large or a small Kaplan turbine for fish with TL_{crit}

Furthermore, the number of consecutive HPPs within a fish movement route is decisive to compute the species survival rate of an entire catchment. Depending on the necessary survival rate for species preservation, the total target survival rate of a single HPP (S_{HPP}) can be specified. As an example, Table 9.2 lists the survival rates of fish with $TL = 0.2$ m at a single HPP and for 10 consecutive HPPs without and with a CBR with different levels of FGE.

Table 9.2 Survival rates of fish with $TL = 0.2$ m at a single HPP and for 10 consecutive HPPs according to Eq. (9.4)

Turbine type		no FGS	CBR (FGE = 50%)	CBR (FGE = 75%)	CBR (FGE = 90%)
large Kaplan	1 HPP	95.0%	97.5%	98.8%	99.5%
	10 HPPs	59.9%	77.6%	88.6%	95.1%
small Kaplan	1 HPP	75.0%	87.5%	93.8%	97.5%
	10 HPPs	5.6%	26.3%	52.7%	77.6%

Note that the survival rate can be further decreased by delay, predation or mortality in the bypass system. Moreover, weir passage during surplus flows exceeding the turbine design discharge have not been accounted for in Eq. (9.4). The fish survival rates at weirs and stilling basins are currently largely unknown, but could be substantial due to the high turbulence, pressure changes, solid obstacles or oxygen supersaturation. If alternative solutions for the fish downstream passage (e.g. weir passage) are considered, the estimation of fish survival rate has to be adapted accordingly. The effective fish guidance efficiency should be evaluated with a thorough monitoring campaign.

10 Conclusions and outlook

10.1 Conclusions

The overarching goal of this research study was to improve the sustainable and efficient use of hydropower by providing a technical solution for the safe downstream fish movement at run-of-river hydropower plants (HPPs) with a minimal impact on hydropower production and operation. The focus was put on the development of mechanical behavioural fish guidance structures (FGSs) with vertical bars. To this end, innovative curved bar shapes for the application at these FGSs were developed, herein called curved-bar racks (CBRs). The hydraulic performance of various CBR configurations, the fish guidance efficiency, four different bypass systems (BS) and the option of electrifying the CBR were systematically investigated in two different laboratory flumes and with a numerical simulation in OpenFOAM[®]. The conclusions drawn from the results of these investigations are presented within the following topics: (1) hydraulic performance of CBRs, (2) fish guidance and fish swimming behaviour at CBR-BS, (3) fish swimming behaviour at electrified CBRs, and (4) operational aspects of CBR-BSs. A practical guide for the engineering application of CBR-BSs and design recommendations are presented in Chapter 9.

(1) Hydraulic performance of curved-bar racks

The hydraulics of selected CBR configurations without a bypass were systematically investigated at 1:2 Froude-scaled detail models in a laboratory flume. The objective of these tests was to find optimal CBR configurations with minimal head losses and favourable flow fields for fish guidance and energy production. The studied primary parameters are the rack angle, the bar angle, and the dimensionless bar spacing characterising the basic geometric properties of a CBR and the secondary parameters are the bar shape, the bar depth, various overlay combinations, and the HPP layout. The main findings on the hydraulics of CBRs are:

- The curved bar shapes promote a flow straightening effect resulting in a quasi-symmetric downstream flow field and favourable turbine admission. The maximum velocities and velocity gradients at the downstream rack end of CBRs are significantly lower as compared to the equivalent rack configurations with straight bars, leading to a more uniform flow distribution along the rack, which is advantageous for fish guidance.
- Due to the flow straightening effect, the hydraulic head losses of CBRs are on average 4.2 times lower as compared to the equivalent fish guidance structures with straight bars and are thus in the same range as for conventional trash racks used at Swiss run-of-river hydropower plants. The existing head loss formula developed for louvers

and modified angled bar racks (MBRs) was extended with a constant shape factor of $C_S = 1/4.2 \approx 0.24$ accounting for curved bars.

- The application of top and/or bottom overlays only slightly deteriorates the downstream flow fields (and hence turbine admission flow if the CBR is placed closely to the power intake) but potentially improves fish guidance as well as drift wood and sediment transport. An overlay factor for the application of top, top & bottom, and bottom overlays C_V was developed.
- The hydraulics of CBRs were investigated for two different HPP layouts, i.e. a diversion-type HPP and a block-type HPP. For the former, the approach flow to the CBR is uniform, whereas the approach flow angle changes along the rack for the latter. This leads to lower head losses for the same CBR configuration at a block-type HPP compared to the diversion-type HPP, which is accounted for with a newly developed head loss factor for HPP layout geometry C_w . However, the block-type HPP layout leads to unfavourable flow conditions for fish guidance, i.e. normal to parallel velocity components at the rack lower than 1. The installation of a separation pier between the weir and the turbine intake greatly improved the flow fields.
- A detailed computational fluid dynamics (CFD) model of the CBRs was set up and validated with the results from the physical model study. The model allows for the computation of the flow conditions between the bars of the CBR and in close vicinity of the rack, where ADV measurements were not possible. Since the distance between two bars decreases in streamwise direction leading to a high clogging probability for floating debris (see (4) further below), the curved bar shape was further optimised and a more foil-shaped curved bar (f-CBR) was developed and investigated with the CFD model. The smallest distance between two bars of the f-CBR is located at the upstream rack angle, which is advantageous for the rack cleaning process with only slightly higher head losses than the CBR. The f-CBR is therefore recommended over the CBR.
- The recommended CBR and f-CBR configurations have a rack angle of $\alpha = 30^\circ$, a bar attack angle of $\beta = 45^\circ$ and a clear bar spacing of $s_b = 50$ mm. The head loss coefficient for this CBR configuration is $\xi_R = 0.57$. With additional top and bottom overlays of 15% each, the head loss coefficient increases to $\xi_R = 0.76$. The head loss coefficient for the recommended f-CBR configuration is $\xi_R = 0.91$. Overlays were not investigated at the f-CBR. However, the head losses are expected to increase similarly as for the CBR with overlays.

(2) Fish guidance and fish swimming behaviour at CBR-BSs

The objective of this part was to determine the fish protection and fish guidance efficiency of the recommended CBR configuration with a rack angle of $\alpha = 30^\circ$, a bar angle of $\beta = 45^\circ$ and a clear bar spacing of $s_b = 50$ mm, guiding the fish to a full-depth open channel bypass, and to link the fish swimming behaviour to the hydrodynamic cues created by the curved-bar rack bypass system (CBR-BS). To this end, live-fish tests with six endemic fish species, namely barbel (*Barbus barbus*), spirlin (*Alburnoides bipunctatus*), nase (*Chondrostoma nasus*), European eel (*Anguilla anguilla*), brown trout (*Salmo trutta*), and Atlantic salmon parr (*Salmo salar*), were conducted in a large ethohydraulic flume for different approach flow and bypass entrance velocities at a water temperature of 12–16°C. The swimming behaviour was investigated with a fish-tracking software, and the flow fields were measured with an ADV probe and simulated with a 3D CFD model in OpenFOAM. The main findings of these tests are:

- Four main hydraulic conditions were investigated in the live-fish tests with the approach flow velocities $U_o = 0.5$ m/s and 0.7 m/s, and bypass entrance to approach flow velocity ratios $U_{by,in}/U_o = VR = 1.2$ and 1.4 by regulating the bypass discharge. These flow conditions were expected to be favourable for fish guidance because of the low transverse velocities towards the rack and high ratios of parallel to normal velocity components V_p/V_n . The CFD simulation showed that the different flow conditions led to different spatial velocity gradients (SVG_x) at the bypass entrance. The velocity and pressure gradients between the bars of the CBR and up to ~ 40 mm upstream of the rack are particularly high, triggering an avoidance reaction of the fish and confirming the behavioural barrier effect of the CBR.
- The live-fish tests resulted in three possible fish reactions: bypass passages (= successful guidance), rack passages (= unsuccessful guidance), and refusals (= fish refused bypass and rack, and swam back upstream). The number of bypass passages defines the fish guidance efficiency, whereas the sum of bypass passages and refusals defines the fish protection efficiency. To evaluate the guidance effect of the CBR-BS, a distinction was made between fish that swam close to the rack and those that swam into the bypass without rack interaction.
- The CBR functioned as a mechanical, behavioural barrier for spirlin, barbel, nase and Atlantic salmon parr with high fish protection and guidance efficiencies ($> 75\%$), whereas it had low or no behavioural effect for brown trout and European eel (guidance efficiency $< 75\%$), respectively. The protection efficiency was 100% for the spirlin in all tests, i.e. no rack passage was observed for these fish. The CBR-BS leads to sim-

ilar protection and guidance efficiencies as the comparable bar rack configuration with straight bars.

- The live-fish tests including all fish species were evaluated with a logistic regression model including the data from Meister (2020) for the horizontal bar rack bypass system (HBR-BS) with $s_b = 20$ mm, yielding the following findings:
 - Among the tested parameters, the rack type had the most significant effect on the fish guidance efficiency, which was significantly higher with the CBR-BS than with the HBR-BS.
 - The approach flow velocity U_o did not have a significant effect on the fish guidance efficiency in the tested range. It significantly affected the fish protection efficiency, however. Increasing U_o from 0.5 m/s to 0.7 m/s significantly increased the number of refusals and significantly decreased the number of rack passages, thus increasing the fish protection efficiency.
 - Increasing VR from 1.2 to 1.4 significantly decreased the fish guidance efficiency. Hence, a mild velocity increase into the bypass is a key design parameter for efficient fish guidance and fast bypass acceptance, which underlines the importance of a bypass regulation.
 - The above stated findings imply that the CBR with $U_o = 0.7$ m/s and $VR = 1.2$ yielded the highest fish protection and guidance efficiencies if all the tested fish species are included in the analysis. However, these results varied considerably for the individual fish species. Furthermore, some fish species (e.g. the juvenile nase) were not tested at $U_o = 0.7$ m/s or $VR = 1.4$.
- The hydraulics of four different bypass layouts were determined. The pipe bypass led to high SVG_x values unfavourable for fish guidance. The pipe bypass was therefore not further investigated with live-fish tests. The full-depth open channel bypass was investigated with and without a 12° inclined ramp and with a restrictor leading to top and bottom openings. These bypass layouts led to $SVG_x < 1$ s⁻¹. The live-fish tests with spiralin showed that these fish react very sensitively to spatial velocity gradients, whereby the bypass was quickly accepted up to $SVG_x \approx 0.6$ s⁻¹.
- The fish tracking-software was a useful tool for the semi-automated determination of individual fish swimming paths, which were used to compute the fish swimming velocities and the locations of rheotaxis changes. Barbel, brown trout, salmon parr and European eel were in constant contact with the flume bed and the rack, whereas the spiralin and the nase avoided contact to any structures.

(3) Fish swimming behaviour at an electrified CBR

To further improve the protection and guidance of the European eel, an additional live-fish test series with an electrified CBR (e-CBR) was conducted. To this end, the CBR was connected to a power supply and the curved bars were alternatively wired as cathodes and anodes with 38 V. Pulsed direct current was applied with different pulse parameters. Spirlin were tested in addition to eel, to evaluate whether the e-CBR leads to a similarly high protection and guidance efficiency for these fish as the CBR without electrification. Furthermore, larger clear bar spacings of $s_b = 110$ mm were tested since this would further mitigate operational issues. The findings can be summarised as follows:

- The tested fish species European eel and spirlin reacted with a pronounced avoidance reaction to the electric field around the e-CBR, which shows the great potential of the electrified CBR as a fish protection measure. It was shown that fish can be efficiently prevented from swimming through the e-CBR leading to a high fish protection efficiency for $s_b = 50$ mm. While the protection efficiency of eel was as low as 27% without electrification, it increased to 100% with the e-CBR. The guidance efficiency was increased from 27% to 75%. The protection and guidance efficiency of the CBR without electrification for the spirlin were 85% and 100%, respectively. With the e-CBR, the protection efficiency was still 100% for the spirlin, but the guidance efficiency decreased to 60%. The spirlin were guided well along the e-CBR, but often hesitated at the bypass entrance due to the high voltage gradients at the downstream rack end.
- The electric stimuli that the fish perceive is equal to the voltage potential over their body width or their body length. Therefore, the fish perceive the maximum electric stimuli over their body length when they are oriented orthogonally to the voltage lines. The larger bar spacing of $s_b = 110$ mm led to a reduced physical and behavioural barrier effect for both the European eel and the spirlin. As a result, the fish swam closer to the rack. When they were aligned parallel to the voltage lines, the perceived electric stimuli were low and they swam even closer to the rack, where the electric field was stronger. In this case, if they rotated their body orthogonal to the voltage lines, the perceived voltage potential suddenly increased leading to uncontrolled reactions, rack contact and increased rack passages, which increased the risk of fish injuries. Tests with $s_b = 110$ mm had to be aborted because of severe fish injuries.
- The challenge is to set up the electric field in such a way that the fish are not only protected from a rack passage but are also successfully guided into the bypass to avoid a delay. In order for the bypass to be accepted by the fish, the electric potential at

the bypass entrance and inside the bypass must be minimised. Furthermore, the fish behaviour strongly depends on the pulse parameters. Two promising pulse parameter settings were found for the European eel and spirlin.

- Since the CBR without electrification showed a high protection and guidance efficiency for fish species that react sensitively to hydrodynamic cues, the electrification represents a promising additional protection, especially for eel. Since the downstream migration of eel is closely linked to a seasonal timing, one possible solution could be to electrify the CBR only for a few days or weeks per year. This would also minimise erosion of the rack due to oxidation.
- The electrification prevents the eel from staying in contact with the rack for a longer time period and impingement is avoided, so that the mortality caused by the rack cleaning machine is minimised.

(4) Operational aspects of curved-bar racks

The objective of this part was to determine the driving factors for the transport and clogging processes of organic fine material and floating debris at CBRs. Small scale laboratory tests at 1:2 Froude scale were conducted to evaluate the clogging probability of leaves and driftwood for a wide range of rack and approach flow parameters. The main findings are:

- The clogging probability of single leaves was not affected by the approach flow velocity U_o . The curved bar shape leads to a reduced bar opening in flow direction for smaller rack angles and thus increased the clogging probability of a single leaf with decreasing rack angle. The leaves wrapped around a single bar and therefore did not increase the blockage ratio, even though the clogging probability was high with 50-90%.
- The clogging probability of logs with a log diameter $d_L = 40$ mm was 100%, even though the upstream clear bar spacing was higher with $s_b = 50$ mm. Although all logs could fit between the bars on the upstream rack side, they got stuck at the downstream end of the bars due to the narrowing distance between the bars in streamwise direction. For smaller logs, increasing the approach flow velocities decreased the clogging probability because approaching logs are reoriented parallel to the flow and thus transported through the CBR more easily at higher U_o .
- The application of a top overlay in combination with weir discharge was an effective mitigation measure to reduce the clogging probability of congested driftwood at a block-type HPP. In practice, the bypass can be used for intermittent flushing of driftwood.
- The layout of the curved bars narrowing in flow direction will inevitably lead to clog-

ging. Therefore, an alternative foil-shaped curved bar design (f-CBR) was developed to mitigate this issue.

Given the highly reduced head losses, improved up- and downstream hydraulic conditions, and high fish protection and guidance efficiencies, CBRs and in particular the f-CBR present a promising potential for fish protection and guidance at small-to-large hydropower plants and water intakes, minimising economic and operational impacts.

10.2 Outlook

In addition to the findings presented in this study, the following topics still comprise knowledge gaps for future investigations, which could further improve the understanding of the fish behaviour at fish guidance structure bypass systems:

- Investigation of the behaviour of cyprinids to accelerating and decelerating flow at different bypass layouts by regulating the bypass discharge in 1:1 scaled models. Since the present study demonstrated, that the flow conditions at the bypass entrance are a key parameter for effective fish guidance, different bypass layouts should be systematically investigated with regard to hydraulic, fish-biological, structural and operational aspects.
- Investigation of the fish behaviour at the CBR-BS in dark lighting conditions. Many fish species and in particular European eel are known to perform their active downstream movements at night, which could affect their swimming behaviour at the CBR-BS.
- Systematic investigation of the f-CBR with the high-resolution 3D CFD model to assess the effect of different bar shapes and rack parameters on the head losses and the flow fields to evaluate the sensitivity of each parameter with regard to the hydraulic and fish biological performance of the f-CBR.
- Installation of an f-CBR at a HPP with a thorough monitoring study evaluating the hydraulic and fish-biological performance of the f-CBR in the field and at prototype conditions.
- Due to the promising results with the e-CBR in the present study, electrified CBRs should be further investigated with a focus on measurements and simulations of the electric field to increase the understanding of fish reactions. Electrical (voltage, pulse pattern) and geometric parameters (electrode arrangement) should be determined, which can guarantee an avoidance effect and an efficient fish guidance independent of the fish orientation and without the risk of major injuries. Safety issues for humans and animals during the operation of an e-CBR at a prototype site should be considered.

Notation

Abbreviations

ADV	acousting Doppler velocimetry
AIC	Akaike information criterion
BIC	Bayesian information criterion
bl	body length
BS	bypass system
CBR	curved-bar rack
cDC	constant direct current
CFD	computational fluid dynamics
e-CBR	electrified curved-bar rack
f-CBR	foil-shaped curved-bar rack
FGC	fish guidance capacity
FGE	fish guidance efficiency
FGS	fish guidance structure
FIThydro	Fishfriendly Innovative Technologies for hydropower
FIWI	Swiss Federal Centre for Fish and Wildlife Medicine
FPE	fish protection efficiency
gpDC	pulsed direct current with gated bursts
HBR	horizontal bar rack
HPP	hydropower plant
LW	large wood
MBR	modified angled bar rack
pDC	pulsed direct current
UDS	ultrasonic distance sensor
VAW	Laboratory of hydraulics, hydrology and glaciology of ETH Zurich
VBR	vertically inclined bar rack

WFD	Water Framework Directive
WPA	Waters Protection Act
WPO	Waters Protection Ordinance

Greek Symbols

α	horizontal approach flow angle	[°]
β	bar attack angle of flow	[°]
β_i	output coefficient of logistic regression model	[-]
δ	downstream bar angle with respect to turbine admission channel	[°]
Δh_f	friction head loss	[m]
Δh_R	rack head loss	[m]
ε	relative bar depth	[-]
ε_t	turbulent dissipation	[m ² /s ²]
η_k	Kolmogorov microscale	[m]
γ	vertical rack inclination	[°]
κ	von Kármán constant	[-]
κ_s	relative submergence	[-]
λ	scale factor	[-]
ν	kinematic viscosity	[m ² /s]
ω	specific rate of dissipation	[1/s]
π_k	probability of response variable Y taking category k	[-]
ρ	density	[kg/m ³]
σ	blockage ratio of vertical bars	[-]
σ_{tot}	total rack blockage ratio including bars and spacers	[-]
σ_{sp}	blockage ratio of spacers	[-]
τ	shear stress	[N/m ²]
τ_{bed}	bed shear stress	[N/m ²]

ξ_B	basic head loss coefficient	[-]
ξ_R	rack head loss coefficient not including spacers	[-]
ξ_c	head loss coefficient of a sudden contraction	[-]
$\xi_{R,m}$	measured rack head loss coefficient	[-]
$\xi_{R,p}$	predicted rack head loss coefficient	[-]
ξ_{sp}	head loss coefficient of tie bars and spacers	[-]

Roman Symbols

A_i	sector area	[m ²]
A_o	area of upstream flow cross section	[m ²]
A_{tot}	sum of all sector areas	[m ²]
A_{ds}	area of downstream flow cross section	[m ²]
C_L	head loss factor of bar depth	[-]
C_S	head loss factor of bar shape	[-]
C_w	head loss factor of HPP layout geometry	[-]
C_K	head loss factor of bar submergence depth	[-]
C_{Bo}	head loss factor of bottom overlay	[-]
$C_{V,i}$	head loss factor of overlays	[-]
CP	clogging probability	[-]
d	diameter	[m]
D_b	standard bar depth of 0.1 m	[m]
d_b	bar depth	[m]
d_L	log diameter	[m]
e_X	total error of target value	[unit of the respective variable]
e_x	total error	[unit of the respective variable]
e_{x_n}	total error of measured parameter x_n	[unit of the respective variable]
F	Froude number	[-]
g	gravitational acceleration	[m/s ²]

h_o	inflow water depth	[m]
h_s	submergence depth	[m]
h_v	total overlay height	[m]
h_{Bo}	bottom overlay height	[m]
h_{by}	bypass flow depth	[m]
h_{ds}	water depth downstream of the rack	[m]
h_{To}	top overlay height	[m]
K	bar shape	[–]
k	response category	[–]
K_i	bar shape factor	[–]
k_i	bar shape factor	[–]
K_α	rack angle factor	[–]
$K_{V,i}$	overlay factor	[–]
L	length	[m]
L_L	leaf or log length	[m]
L_M	model length	[m]
L_P	prototype length	[m]
l_R	rack length	[m]
L_{gap}	gap length between two pulses	[ms]
L_{pier}	pier length	[m]
L_{pulse}	pulse length	[ms]
N	total number of fish	[–]
n	number of active fish used in the analysis	[–]
N_{pulse}	number of pulses	[–]
N_{rack}	number of rack passages	[–]
N_{refusal}	number of refusals	[–]
$N_{\text{by,all}}$	total number of bypass passages	[–]
$N_{\text{by,red}}$	number of bypass passages with rack interaction	[–]

P	probability	[-]
p	p-value	[-]
PE	prediction error	[-]
Q	discharge	[m ³ /s]
Q_d	design discharge	[m ³ /s]
Q_o	inflow discharge	[m ³ /s]
Q_t	turbine admission flow discharge	[m ³ /s]
Q_w	weir discharge	[m ³ /s]
Q_{left}	discharge in the left turbine intake half	[m ³ /s]
Q_{right}	discharge in the right turbine intake half	[m ³ /s]
Q_{by}	bypass discharge	[m ³ /s]
r	radius	[m]
R	Reynolds number	[-]
R_b	bar Reynolds number	[-]
R_h	hydraulic radius	[m]
$R_{c,i,\text{norm}}$	normalised sector residence coefficient	[-]
$R_{c,i}$	sector residence coefficient	[m]
s_b	clear bar spacing	[m]
S_e	energy slope	[-]
S_t	fish turbine survival rate	[-]
S_{HPP}	total HPP fish survival rate	[-]
$s_{b,\text{eff}}$	smallest clear bar spacing between two curved bars	[m]
SPG	spatial pressure gradient	[Pa/cm]
SVG	spatial velocity gradient	[1/s]
SVG_x	spatial velocity gradient in streamwise direction	[1/s]
T	temperature	[°C]
t	time step	[s]
t_b	bar thickness	[m]

t_{rep}	repetition time	[ms]
t_{tot}	total swimming time during a live-fish test	[s]
$T_{i,j}$	residence time of fish j in sector i	[s/m ²]
$t_{i,j}$	time of fish j in sector i	[s]
TKE	turbulent kinetic energy	[m ² /s ²]
TL_{max}	maximum fish length	[m]
TL_{mean}	mean fish length	[m]
TL_{min}	minimum fish length	[m]
U	local mean streamwise flow velocity	[m/s]
\hat{U}	depth averaged flow velocity	[m/s]
U^+	flow velocity normalised with the friction velocity	[m/s]
u', v', w'	velocity fluctuations in x -, y -, z -direction	[m/s]
u, v, w	local, instantaneous velocity components in x -, y -, z -direction	[m/s]
U_g	fish ground streamwise velocity	[m/s]
U_o	mean inflow velocity from continuity	[m/s]
u_*	friction velocity	[m/s]
U_{fish}	fish swimming velocity in streamwise direction	[m/s]
U_{max}	maximum resulting velocity at the d/s rack end	[m/s]
$U_{\text{by,in}}$	flow velocity at the bypass entrance	[m/s]
U_{ds}	mean flow velocity downstream of the rack from continuity	[m/s]
$u_{rms}, v_{rms}, w_{rms}$	turbulence intensity in x -, y -, z -direction	[m/s]
U_r	resulting flow velocity	[m/s]
U_{th}	theoretical downstream flow velocity without rack presence	[m/s]
V	local mean transverse flow velocity	[m/s]
v	flow velocity	[m/s]
V_1	top overlay blockage ratio	[–]
V_2	top and bottom overlay blockage ratio	[–]
V_3	bottom overlay blockage ratio	[–]

V_g	fish ground transverse velocity	[m/s]
V_n	normal velocity component	[m/s]
V_p	rack-parallel velocity component	[m/s]
V_z	vertical velocity component at the rack	[m/s]
v_{burst}	burst swimming speed of fish	[m/s]
V_{fish}	fish swimming velocity in transverse direction	[m/s]
v_{fish}	absolute fish swimming speed	[m/s]
v_{pipe}	flow velocity in the pipe bypass	[m/s]
$v_{prolonged}$	prolonged swimming speed of fish	[m/s]
$v_{sustained}$	sustained swimming speed of fish	[m/s]
VR	bypass entrance to mean approach flow velocity ratio	[-]
W	local mean flow velocity in z-direction	[m/s]
w_o	inflow flume width	[m]
w_{pier}	pier width	[m]
w_{by}	bypass width	[m]
w_{ds}	downstream flume width	[m]
X	target value	[unit of the respective variable]
\bar{x}	mean or expected value	[unit of the respective variable]
x', y'	directions normal and parallel to the rack	[m]
x, y, z	local coordinates	[m]
X_n	independent parameter	[unit of the respective variable]
x_n	measured quantity	[unit of the respective variable]
Y	response variable	[-]
FGE	fish guidance efficiency with rack interaction	[-]
FGE*	total fish guidance efficiency	[-]
FPE	fish protection efficiency with rack interaction	[-]
FPE*	total fish protection efficiency	[-]

Subscripts

<i>b</i>	bar
<i>Bo</i>	bottom overlay
<i>by</i>	bypass
<i>by, all</i>	all bypass passage with and without rack interaction
<i>by, red</i>	bypass passage with rack interaction
<i>by, in</i>	bypass entrance
<i>c</i>	coefficient
<i>d</i>	design
<i>ds</i>	downstream
<i>e</i>	energy
<i>g</i>	ground
<i>h</i>	hydraulic
<i>i</i>	certain quantity
<i>j</i>	fish index
<i>L</i>	leaf or log
<i>m</i>	measured
<i>n</i>	sample
<i>o</i>	approach flow
<i>p</i>	predicted
<i>R</i>	rack
<i>r</i>	resulting
<i>S</i>	bar shape
<i>sp</i>	spacers and tie bars
<i>t</i>	turbine
<i>th</i>	theoretical
<i>To</i>	top overlay
<i>V</i>	overlay blockage

w	weir
X	target value
crit	critical
eff	effective
max	maximum
mean	mean value
min	minimum
red	reduced
tot	total

Bibliography

- Abernethy, C.S.; Amidan, B.G.; Cada, G.F. (2001). Laboratory studies of the effects of pressure and dissolved gas supersaturation on turbine-passed fish. *Technical Report PNNL-13470*, Pacific Northwest National Laboratory, Richland (WA), USA.
- Achord, S.; Eppard, M.; Hockersmith, E.; Sandford, B.; Matthews, G. (1997). Monitoring the migrations of wild Snake River spring/summer chinook salmon smolts, 1996. *Report of the National Marine Fisheries Service to the Bonneville Power Administration*, Portland, Oregon.
- Adam, B. (2018). Mit dem Frühwarnsystem Migromat abwandernde Aale schützen ('Protecting downstream migrating eels with the early warning system Migromat'). *zekHydro*, 15(3): 68–70 (in German).
- Adam, B.; Engler, O.; Schwevers, U. (2018). HDX-Monitoring Wupper: Projektendbericht ('HDX-monitoring Wupper: final project report'). *Technical Report*, Institut für angewandte Ökologie, Kirtorf-Wahlen, Germany (in German).
- Adam, B.; Lehmann, B. (2011). Ethohydraulik: Grundlagen, Methoden und Erkenntnisse (Ethohydraulics: Basics, methods and insights). ISBN 3642172105. *Springer-Verlag* (in German).
- Adam, B.; Schwevers, U.; Dumont, U. (2002). Rechen- und Bypassanordnungen zum Schutz abwandernder Aale (Rack and bypass layout for the protection of downstream migrating eels). *Wasserwirtschaft*, 4-5: 43–46 (in German).
- Albayrak, I.; Boes, R.M.; Kriewitz-Byun, C.R.; Peter, A.; Tullis, B.P. (2020a). Fish guidance structures: hydraulic performance and fish guidance efficiencies. *Journal of Ecohydraulics*.
- Albayrak, I.; Kriewitz, C.R.; Hager, W.; Boes, R.M. (2018). An experimental investigation on louvres and angled bar racks. *Journal of Hydraulic Research*, 56(1): 59–75.
- Albayrak, I.; Maager, F.; Boes, R.M. (2020b). An experimental investigation on fish guidance structures with horizontal bars. *Journal of Hydraulic Research*, 58(3): 516–530.
- Amaral, S.V. (2003). Use of angled bar racks and louvers for guiding fish at FERC-licensed projects. *Proc. FERC Fish Passage Workshop*. Holden, USA.
- Anderson, W.G.; Shepherd, D.; Katopodis, C.; McKinley, R.S.; Rajaratnam, N. (1998). Laboratory and field testing of a louver array for the guidance of juvenile rainbow trout. *Technical Report*, Applied Biometrics Inc., Waterloo, Ontario and Department of Civil Engineering, University of Alberta, Edmonton, Canada.

- Arenas, A.; Politano, M.; Weber, L.; Timko, M. (2015). Analysis of movements and behavior of smolts swimming in hydropower reservoirs. *Ecological Modelling*, 312: 292–307.
- Auel, C. (2014). Flow characteristics, particle motion and invert abrasion in sediment bypass tunnels. *VAW-Mitteilung 229* (R.M. Boes, ed.). VAW, ETH Zurich, Switzerland.
- BAFU (2012). Wiederherstellung der Fischauf- und abwanderung bei Wasserkraftwerken, Check-list best practice (Restoration of the fish up- and downstream migration at hydropower plants). *Technical Report*, Swiss Federal Office of the Environment (FOEN) (in German).
- BAFU (2016). Fischpassage durch die Turbinen (Fish passage through turbines). *Technical Report*, Swiss Federal Office of the Environment (FOEN) (in German).
- Bates, D.W.; Vinsonhaler, R. (1957). Use of louvers for guiding fish. *Transactions of the American Fisheries Society*, 86(1).
- Baumgartner, T. (2020). Schwimmverhalten von Fischen an Fischleitrechen-Bypasssystemen (Fish swimming behaviour at bar rack bypass systems). *Bachelor's Thesis*, VAW, ETH Zurich, Switzerland (in German).
- Beamish, F.W.H. (1978). Chap. Swimming capacity: 101–187. In: W.S. Hoar; D.J. Randall (eds.) *Fish physiology*, Bd. VII. *New York (Academic Press)*.
- Beaumont, W.R.C. (2016). *Electricity in fish research and management - Theory and practice*. 2nd edn. *Wiley Blackwell*.
- Beck, C.; Albayrak, I.; Meister, J.; Boes, R. M. (2019a). Hydraulic performance of fish guidance structures with curved bars - Part 1: head loss assessment. *Journal of Hydraulic Research*.
- Beck, C.; Albayrak, I.; Meister, J.; Boes, R. M. (2019b). Hydraulic performance of fish guidance structures with curved bars - Part 2: flow fields. *Journal of Hydraulic Research*.
- Berger, C. (2017). Rechenverluste und Auslegung von (elektrifizierten) Schrägrechen anhand ethohydraulischer Studien (Rack head losses and design of (electrified) angled racks with ethohydraulic studies). *PhD Thesis*, Technical University Darmstadt, Germany (in German).
- Blaxter, J.H.S. (1969). Swimming speeds of fish. *FAO Fisheries and Aquaculture Report*. 2070-6987.
- Blevins, R.D. (1984). *Applied fluid dynamics handbook*. *New York, Van Nostrand Reinhold Co.*

- Boes, R.B.; Albayrak, I. (2017). Fish guidance structures: New head loss formula and fish guidance efficiencies. *Proc. Proceedings of the 37th IAHR World Congress, Kuala Lumpur, Malaysia*.
- Bollrich, G. (2013). Technische Hydromechanik 1 – Grundlagen (Technical hydromechanics 1 – Fundamentals). *Beuth Verlag GmbH* (in German).
- Brinkmeier, B.; Boetticher, H.; Tutzer, R.; Aufleger, M. (2017). Fish protection using electric flexible fish fences. *Proc. Proceedings of the Hydro 2017 conference*. Sevilla, Spain.
- Brown, L.; Haro, A.; Castro-Santos, T. (2009). Three-dimensional movement of silver-phase American eels in the forebay of a small hydroelectric facility. *Proc. Eels at the edge: science, status, and conservation concerns. American Fisheries Society, Symposium*: 277–291.
- Bühler, F. (2019). Driftwood clogging at fish guidance structures with vertical curved bars. *Project Thesis*, VAW, ETH Zurich, Switzerland.
- Cada, G.F.; Coutant, C.C.; Whitney, R.R. (1997). Development of biological criteria for the design of advanced hydropower turbines. *Technical Report*, EERE Publication and Product Library, Washington, DC, United States.
- Calles, O.; Olsson, I.C.; Comoglio, C.; Kemp, P.S.; Blunden, L.; Schmitz, M.; Greenberg, L.A. (2010). Applied Issues: Size-dependent mortality of migratory silver eels at a hydropower plant, and implications for escapement to the sea. *Freshwater Biology*, 55(10).
- Chatellier, L.; Wang, R.-W.; David, L.; Courret, D.; Larinier, M. (2011). Experimental characterization of the flow across fish-friendly angled trashrack models. *Proc. Proceedings of the 34th World Congress of the International Association for Hydro-Environment Research and Engineering: 33rd Hydrology and Water Resources Symposium and 10th Conference on Hydraulics in Water Engineering*.
- Clark, S.P.; Tsikata, J.M.; Haresign, M. (2010). Experimental study of energy loss through submerged trashracks. *Journal of Hydraulic Research*, 48(1): 113–118.
- Clough, S.; Lee-Elliott, I.; Turnpenny, A.; Holden, S.; Hinks, C. (2004). Swimming speeds in fish: phase 2. *R&D Technical Report W2-049/TR1*, Fawley Aquatic Research Laboratories Ltd.
- Courret, D.; Larinier, M. (2008). Guide pour la conception de prises d'eau 'ichthyocompatibles' pour les petites centrales hydroélectriques (Guide for the design of fish-friendly intakes for small hydropower plants). *Agence de l'Environnement et de la Maîtrise de l'Energie (ADEME)* (in French).

- Coutant, C.C.; Whitney, R.R. (2000). Fish behavior in relation to passage through hydro-power turbines: A review. *Transactions of the American Fisheries Society*, 129(2).
- Deng, Z.; Carlson, T.J.; Dauble, D.D.; Ploskey, G.R. (2011). Fish passage assessment of an advanced hydropower turbine and conventional turbine using blade-strike modeling. *Energies*, 4: 57–67.
- Dönni, W.; Spalinger, L.; Knutti, A. (2017). Erhaltung und Förderung der Wanderfische in der Schweiz — Zielarten, Einzugsgebiete, Aufgaben (Preservation and promotion of migratory fish in Switzerland — target species, catchments, tasks). *Technical Report*, Bundesamt für Umwelt (BAFU) (in German).
- Ducharme, L.J.A. (1972). Application of louver deflectors for guiding Atlantic salmon. *Journal of the Fisheries Research Board of Canada*, 29(10): 1397–1404.
- Durif, C.; Elie, P. (2008). Predicting downstream migration of silver eels in a large river catchment based on commercial fishery data. *Fisheries Management and Ecology*, 15(2): 127–137.
- Durif, C.; Elie, P.; Gosset, C.; Rives, J.; Travade, F. (2002). Behavioral study of downstream migrating eels by radio-telemetry at a small hydroelectric power plant. *American Fisheries Society Symposium*.
- DWA (2005). Fischschutz- und Fischabstiegsanlagen — Bemessung, Gestaltung, Funktionskontrolle, 2. korrigierte Auflage (Fish protection and downstream migration facilities — Dimensioning, Design, Monitoring). *Deutsche Vereinigung für Wasserwirtschaft, Abwasser und Abfall* (in German).
- Ebel, G. (2008). Turbinen bedingte Schädigung des Aales (*Anguilla anguilla*) — Schädigungsraten an europäischen Wasserkraftanlagenstandorten und Möglichkeiten der Prognose (Turbine induced injuries of the European eel — Injury rates at European hydropower plants and possibility of forecasting). *Mitteilungen aus dem Büro für Gewässerökologie und Fischereibiologie Dr. Ebel* (in German).
- Ebel, G. (2016). Fischschutz und Fischabstieg an Wasserkraftanlagen – Handbuch Rechen- und Bypasssysteme. Ingenieurbiologische Grundlagen, Modellierung und Prognose, Bemessung und Gestaltung (Fish protection and fish downstream migration at hydropower plants – handbook for rack and bypass systems. Engineering basics, modelling and forecast, dimensioning and design). *Mitteilungen aus dem Büro für Gewässerökologie und Fischereibiologie, Band 4* (in German).
- Enders, E.C.; Boisclair, D.; Roy, A.G. (2003). The effect of turbulence on the cost of

- swimming for juvenile Atlantic salmon (*Salmo salar*). *Canadian Journal of Fisheries and Aquatic Sciences*, 60(9): 1149–1160. 0706-652.
- Enders, E.C.; Gessel, M.H.; Anderson, J.J.; Williams, J.G. (2012). Effects of decelerating and accelerating flows on juvenile salmonid behavior. *Transactions of the American Fisheries Society*, 141(2): 357–364.
- Engler, O.; Stöhr, V.; Defaweux, C.; Adam, B. (2016). HDX-Monitoring Wupper II – Untersuchung der Wanderung von Fischen (HDX-Monitoring Wupper II – Investigation of fish migration). *Technical Report*, Institut für angewandte Ökologie, Kirtorf-Wahlen (in German).
- EPRI (1998). Review of downstream fish passage and protection technology evaluations and effectiveness. *Technical Report 111517*, Electric Power Research Institute, Palo Alto, CA.
- EPRI; DML (2001). Evaluation of angled bar racks and louvers for guiding fish at water intakes. *Technical Report 1005193*, Electric Power Research Institute and Dominion Millstone Laboratories, Palo Alto, CA and Waterford, CT, USA.
- Feigenwinter, L.; Vetsch, D.F.; Kammerer, S.; Kriewitz, C.R.; Boes, R.M. (2019). Conceptual approach for positioning of fish guidance structures using CFD and expert knowledge. *Sustainability*, 11(6).
- Ferguson, J.W.; Absolon, R.F.; Carlson, T.J.; Sandford, B.P. (2006). Evidence of delayed mortality on juvenile pacific salmon passing through turbines at Columbia River dams. *Transactions of the American Fisheries Society*, 135(1).
- Flügel, D.; Börs, T.; Peter, A. (2015). Forschungsprojekt: Massnahmen zur Gewährleistung eines schonenden Fischabstiegs an grösseren mitteleuropäischen Flusskraftwerken – Ethohydraulische Untersuchungen zum Fischabstieg entlang eines vertikalen, schräg ausgerichteten Fischleitrechens (Investigation on downstream fish migration along vertical, angled fish guidance screens – Ethohydraulic investigations in a laboratory flume). *Technical Report*, Swiss Federal Institute of Aquatic Science and Technology (Eawag), Dübendorf, Switzerland (in German).
- Ganzmann, M. (2019). Model investigation of flow conditions and foliage clogging at fish guidance structures. *Master Thesis*, VAW, ETH Zurich, Switzerland.
- Godde, D. (1994). Experimentelle Untersuchung zur Anströmung von Rohrturbinen: Ein Beitrag zur Optimierung des Turbineneinlaufs (Experimental investigation on the approach flow of bulb turbines: Optimisation of the turbine intake). *Proc. Bericht Nr. 75. Versuchsanstalt Oberrach und Lehrstuhl für Wasserbau der TU München, Germany* (in

German).

Goodwin, R.A.; Nestler, J.M.; Anderson, J.J.; Weber, L.J. (2007). A new tool to forecast fish movement and passage. *Hydro Review*, 26(4): 58–71.

Goring, D.G.; Nikora, V.I. (2002). Despiking acoustic Doppler velocimeter data. *Journal of Hydraulic Engineering*, 128(1): 117–126.

Gudde, A. (2016). Experimentelle Untersuchungen zu Schwemmholz an Fischleitreechen (Experimental investigations on driftwood at fish guidance structures). *Master Thesis*, VAW, ETH Zurich, Switzerland (in German).

Guensch, G.R.; Müller, R.P.; McKinstry, C.A.; Dauble, D.D. (2002). Evaluation of fish-injury mechanisms during exposure to a high velocity jet. *Technical Report*, U.S. Department of Energy, Richland, Washington.

Haefner, J.W.; Bowen, M.D. (2002). Physical-based model of fish movement in fish extraction facilities. *Ecological Modelling*, 152(2-3): 227–245.

Halls, A.S.; Kshatriya, M. (2009). Modelling the cumulative barrier and passage effects of mainstream hydropower dams on migratory fish populations in the Lower Mekong Basin. *Mekong River Commission, MRC Technical Paper No. 25*.

Harby, A.; Charmosson, J.; Boavida, I.; Pinheiro, A.N.; Godinho, F.; Tuhtan, J.; Albayrak, I.; Detert, M.; Boes, R.M.; Schneider, M. (2019). Tools for fish behaviour assessment. *Deliverable 3.2, Fishfriendly Innovative Technologies for Hydropower*.

Haro, A.; Odeh, M.; Noreika, J.; Castro-Santos, T. (1998). Effect of water acceleration on downstream migratory behavior and passage of Atlantic salmon smolts and juvenile American shad at surface bypasses. *Transactions of the American Fisheries Society*, 127(1): 118–127. 0002-8487.

Hassinger, R.; Hübner, D. (2009). Entwicklung eines neuartigen Aal-Abstiegssystems mithilfe von Laborversuchen (Laboratory investigations on a novel downstream migration system for eels). *KW Korrespondenz Wasserwirtschaft*, 2(5): 276–281 (in German).

Heller, V. (2009). Beschreibung turbulenter Strömungen (Description of turbulent flows). *Wasser Energie Luft*, 4: 328–336 (in German).

Heller, V. (2011). Scale effects in physical hydraulic engineering models. *Journal of Hydraulic Research*, 49(3): 293–306.

Hendry, K.; Cragg-Hine, D. (2003). Ecology of the atlantic salmon. *Conserving Natura 2000 Rivers Ecology Series 7*: 32 P.

- Hsieh, T. (1964). Resistance of cylindrical piers in open-channel flow. *Proc. Proceedings of the Hydraulics Division, American Society of Civil Engineers*.
- Hughes, S.A. (2005). Physical models and laboratory techniques in coastal engineering. *Advanced Series on Ocean Engineering - Volume 7*.
- Idelcik, I.E. (2007). Handbook of hydraulic resistance. 4th ed. edn. *Hemisphere Publishing Corporation*.
- IEA (2018). Renewables 2018 - Analysis and forecasts to 2023. *Technical Report*, International Energy Agency (IEA).
- IMK (2011). Wanderfische in der Maas (Migratory fish in the River Maas). *Technical Report*, Internationale Maasskommission, Belgium (unpublished).
- Jirka, G.H.; Lang, C. (2009). Einführung in die Gerinnehydraulik (Introduction to open channel flow). *KIT Scientific Publishing* (in German).
- Kammerlander, H.; Schlosser, L.; Zeiringer, B.; Unfer, G.; Zeileis, A.; Aufleger, M. (2020). Downstream passage behavior of potamodromous fishes at the fish protection and guidance system "Flexible Fish Fence". *Ecological Engineering*, 143.
- Katopodis, C.; Ead, S.A.; Standen, G.; Rajaratnam, N. (2005). Structure of flow upstream of vertical angled screens. *Journal of Hydraulic Engineering*, 131(4): 294–304.
- Katopodis, C.; Gervais, R. (2016). Fish swimming performance database and analyses. *Research Document 2016/002*, Canadian Science Advisory Secretariat (CSAS).
- Kemp, P.; Gessel, M.; Sandford, B.; Williams, J. (2006). The behaviour of pacific salmonid smolts during passage over two experimental weirs under light and dark conditions. *River Research and Applications*, 22: 429–440.
- Kemp, P. S.; Williams, J.G. (2009). Illumination influences the ability of migrating juvenile salmonids to pass a submerged experimental weir. *Ecology of Freshwater Fish*, 18: 297–304.
- Kirschmer, O. (1926). Untersuchungen über den Gefällsverslut an Rechen (Investigations on the head losses of racks). *Proc. vol. 1. Mitteilungen des hydraulischen Instituts der TH München*. Munich, Germany (in German).
- Klopries, E.; Deng, Z.; Lachmann, T.; Schüttrumpf, H.; Trumbo, B. (2018). Surface bypass as a means of protecting downstream-migrating fish: lack of standardized evaluation criteria complicates evaluation of efficacy. *Marine and Freshwater Research*, 69(12): 1882–1893.

- Kolmogorov, A.N. (1991). The local structure of turbulence in incompressible viscous fluid for very large Reynolds numbers. *Proceedings of the Royal Society*.
- Kriewitz, C.R. (2015). Leitrechen an Fischabstiegsanlagen: Hydraulik und fischbiologische Effizienz (Guidance screens at fish protection facilities: Hydraulics and fish-biological efficiency). *VAW-Mitteilung 230* (R.M. Boes, ed.). VAW, ETH Zurich, Switzerland (in German).
- Kriewitz, C.R.; Albayrak, I.; Boes, R.M. (2012). Massnahmen zur Gewährleistung eines schonenden Fischabstiegs an grösseren, mitteleuropäischen Flusskraftwerken - Zwischenbericht zum Literatur- und Massnahmenstudium (Measures for a safe downstream fish passage at large, Central-European run-of-river hydropower plants - Intermediate report on the literature review). *Technical Report*, VAW, ETH Zurich, Switzerland (in German).
- Kynard, B.; Horgan, M. (2001). Guidance of yearling shortnose and pallid sturgeon using vertical bar rack and louver arrays. *North American Journal of Fisheries Management*, 21(3): 561–570.
- Lacey, R.W.J.; Neary, V.S.; Liao, J.C.; Enders, E.C.; Tritico, H.M. (2012). The IPOS framework: Linking fish swimming performance in altered flows from laboratory experiments to rivers. *River Research and Applications*, 28: 429–443.
- Lane, S. M.; Biron, K. F.; Bradbrook, K. F.; Butler, J. B.; Chandler, J. H.; Crowell, M. D.; McLelland, S. J.; Richards, K. S.; Roy, A. G. (1998). Three-dimensional measurement of river channel flow processes using acoustic Doppler velocimetry. *Earth Surface Processes and Landforms*, 23: 1247–1267.
- Lange, D.; Bezzola, G.R. (2006). Schwemmholz - Probleme und Lösungsansätze (Large wood: problems and countermeasures). *VAW-Mitteilung 188* (H.-E. Minor, ed.). VAW, ETH Zurich, Switzerland (in German).
- Larinier, M. (2008). Fish passage experience at small-scale hydropower plants in France. *Proc. International Conference on Small Hydropower, Kaunas, Lithuania*.
- Larinier, M.; Travade, F. (1999). The development and evaluation of downstream bypasses for juvenile salmonids at small hydroelectric plants in France. *Innovations in fish passage technology*: 25.
- Larinier, M.; Travade, F. (2002). Downstream migration: problems and facilities. *Bulletin Français de la Pêche et de la Pisciculture*, 364: 181–207.
- Lehmann, B.; Adam, B. (2016). Untersuchungen und Empfehlungen zur Dimensionierung und Anordnung von Bypassanlagen bei Wasserkraftanlagen (Investigation and recom-

- mendations for the dimensioning and positioning of bypasses at hydropower plants). *Proc. 18th Wasserbau-Symposium*. Wallgau, Germany (in German).
- Lehmann, B.; Adam, B.; Engler, O.; Hecht, V.; Schneider, K. (2016). Ethohydraulische Untersuchungen zur Verbesserung des Fischschutzes an Wasserkraftanlagen (Ethohydraulic investigation to improve the fish protection at hydropower plants). *Ergebnisse des F+E-Vorhabens (FKZ 3513 85 0300), Naturschutz und Biologische Vielfalt - Heft 151*, Bundesamt für Naturschutz (in German).
- Lemasson, B.; Haefner, J.; Bowen, M. (2008). The effect of avoidance behavior on predicting fish passage rates through water diversion structures. *Ecological Modelling*, 219: 178–188.
- Leuch, C. (2019). Numerical modelling of fish guidance structures. *Master Thesis*, VAW, ETH Zurich, Switzerland.
- Liao, J.C. (2007). A review of fish swimming mechanics and behaviour in altered flows. *Philosophical Transactions of the Royal Society of London B: Biological Sciences*, 362(1487): 1973–1993.
- Liao, J.C.; Beal, D.N.; Lauder, G.V.; Triantafyllou, M.S. (2003). The Karman gait: novel body kinematics of rainbow trout swimming in a vortex street. *Journal of Experimental Biology*, 206(6): 1059–1073.
- Lucas, M.C.; Baras, E.; Thom, T.J.; Duncan, A.; Slavik, O. (2001). Migration of freshwater fishes, vol. 47. *Blackwell Science Ltd*.
- Lupandin, A.I. (2005). Effect of turbulence on swimming speed of fish. *Biology Bulletin*, 32: 461–466.
- Meister, J. (2020). Fish protection at hydropower plants with horizontal bar rack bypass systems. *VAW-Mitteilung 258* (R.M. Boes, ed.). VAW, ETH Zurich, Switzerland.
- Meister, J.; Beck, C.; Roth, A.; Fuchs, H.; Albayrak, I.; Selz, O.; Boes, R.M. (2020a). EthoMoSt, Etho-hydraulische Modellversuche an elektrifizierten Fischleitrechen (Etho-hydraulic model study on electrified fish guidance structures). *Technical Report SI/501758-01*, Swiss Federal Office of Energy, Switzerland (in German).
- Meister, J.; Fuchs, H.; Beck, C.; Albayrak, I.; Boes, R.M. (2020b). Head losses of horizontal bar racks as fish guidance structures. *water*, 12(2).
- Meister, J.; Fuchs, H.; Beck, C.; Albayrak, I.; Boes, R.M. (2020c). Velocity fields at horizontal bar racks as fish guidance structures. *water*, 12(2).
- Meusburger, H. (2002). Energieverluste an Einlaufrechen von Flusskraftwerken (Head losses

- at intake racks of run-of-river hydropower plants). *VAW-Mitteilung 179* (H.-E. Minor, ed.). VAW, ETH Zurich, Switzerland (in German).
- Miehls, S.M.; Johnson, N.S.; Haro, A. (2017). Electrical guidance efficiency of downstream-migrating juvenile sea lampreys decreases with increasing water velocity. *American Fisheries Society*, 146: 299–307.
- Monan, G.E.; Pugh, J.R. (1964). A field test of electrical guiding and louver deflection combined into a single guiding system. *Fish-passage Research Program*. U.S. Bureau of Commercial Fisheries. Seattle, Washington.
- Monten, E. (1985). Fish and turbines. Fish injury during passage through power station turbines. *Vattenfall*, Stockholm, Sweden.
- Moretti, G. (2015). Strömungsstrukturen um fischleitende Strukturen (Flow fields at fish guidance structures). *Master Thesis*, VAW, ETH Zurich, Switzerland (in German).
- Nestler, J.M.; Goodwin, R.A.; Smith, D.L.; Anderson, J.J.; Li, S. (2008). Optimum fish passage and guidance designs are based in the hydrogeomorphology of natural rivers. *River Research and Applications*, 24: 148–168.
- Nezu, I.; Nakagawa, H. (1993). Turbulence in open-channel flows. *IAHR Monograph*.
- Odeh, M.; Orvis, C. (1998). Downstream fish passage design considerations and developments at hydroelectric projects in the Northeast USA. *Proc. Fish Migration and Fish Bypasses*, *Fishing News Books*: 267–280.
- Okland, F.; Teichert, M.A.K.; Thorstad, E.B.; Havn, T.B.; Heermann, L.; Saether, S.A.; Diserud, O.H.; Tambets, M.; Hedger, R.D.; Borchertding, J. (2016). Downstream migration of atlantic salmon smolt at three German hydropower stations. *NINA Report Nr. 1203*, University of Cologne, Norwegian Institute for Nature Research, Cologne, Germany and Trondheim, Norway.
- Ovidio, M.; Dierckx, A.; Bunel, S.; Grandry, L.; Spronck, C.; Benitez, J. (2017). Poor performance of a retrofitted downstream bypass revealed by the analysis of approaching behaviour in combination with a trapping system. *River Research and Applications*, 33: 27–36.
- Pahud, C. (2013). Schonender Fischabstieg an grösseren mitteleuropäischen Flusskraftwerken (Downstream fish migration at large Central European run-of-river hydropower plants). *Master Thesis*, VAW, ETH Zurich, Switzerland (in German).
- Parasiewicz, P.; Wisniewolski, W.; Mokwa, M.; Ziola, S.; Prus, P.; Godlewska, M. (2016). A low-voltage electric fish guidance system - NEPTUN. *Fisheries Research*, 181: 25–33.

- Pavlov, D.S. (1989). Structures assisting the migrations of non-salmonid fish: USSR. ISBN 92-5-102857-5. FAO fisheries technical paper. *Food and Agriculture Organization of the United Nations*.
- Pavlov, D.S. (1994). The downstream migration of young fishes in rivers: mechanisms and distribution. *Folia Zoologica*, 43(3): 193–208.
- Pavlov, D.S.; Lupandin, A.I.; Skorobogatov, M.A. (2000). The effects of flow turbulence on the behavior and distribution of fish. *Journal of Ichthyology*, 40: 232–261.
- Pelicice, F.; Agostinho, C.S. (2012). Deficient downstream passage through fish ladders: the case of Peixe Angical Dam, Tocantins River, Brazil. *Neotropical Ichthyology*, 10(4).
- Peter, A. (2015). Lachsmonitoring Möhlinbach ('Salmon monitoring at Möhlinbach'). *Technical Report*, Bundesamt für Umwelt, Olten, Switzerland (in German).
- Pope, S.B. (2013). Turbulent flows. ISBN 9780511840531. *Cambridge University Press*, Cornell University, New York, United States.
- Pugh, J.R.; Monan, G.E.; Smith, J.R. (1970). Effect of water velocity on the fish-guiding efficiency of an electrical guiding system. *Fishery Bulletin of the U.S. fish and wildlife service*, 68(2): 307–324.
- Quaranta, E.; Katopodis, C.; Revelli, R.; Comoglio, C. (2017). Turbulent flow field comparison and realted suitability for fish passage of a standard and a simplified low-gradient vertical slot fishway. *River Research and Applications*, 33: 1295–1305.
- Quené, H.; van den Bergh, H. (2004). On multi-level modeling of data from repeated measures designs: a tutorial. *Speech Communication*, 43: 103–121.
- Raynal, S.; Chatellier, L.; Courret, D.; Larinier, M.; David, L. (2014). Streamwise bars in fish-friendly angled trashracks. *Journal of Hydraulic Research*, 52(3): 426–431.
- Raynal, S.; Courret, D.; Chatellier, L.; Larinier, M.; David, L. (2013a). An experimental study on fish-friendly trashracks – Part 2: Angled trashracks. *Journal of Hydraulic Research*, 51(1): 67–75.
- Raynal, S.; Courret, D.; Chatellier, L.; Larinier, M.; David, L. (2013b). An experimental study on fish-friendly trashracks - Part 1. Inclined trashracks. *Journal of Hydraulic Research*, 51(1): 56–66.
- Ristroph, L.; Liao, J.C.; Zhang, J. (2015). Lateral line layout correlates with the differential hydrodynamic pressure on swimming fish. *Physical Review Letters*, 114.
- Rodi, W. (1984). Turbulence models and their application in hydraulics. ISBN 90-5410-

- 150-4. second edn. *IAHR Monograph*, Delft, the Netherlands.
- Rost, U.; Weibel, U.; Wüst, S.; Haupt, O. (2014). Versuche zum Scheuchen und Leiten von Fischen mit elektrischem Strom (Experimental investigation on the fish guidance with an electric current). *Biologische Durchgängigkeit von Fließgewässern - Ausgewählte Beiträge aus der Fachzeitschrift WasserWirtschaft*, 7-8: 492–499 (in German).
- Rouvé, G. (1958). Der Krafthaustrennpfeiler - Strömungsverhältnisse an gekrümmten Wänden (The separation pier - Flow conditions at curved walls). *PhD Thesis*, Technische Hochschule Karlsruhe, Germany (in German).
- Ruggles, C.P.; Ryan, P. (1964). An investigation of louvers as a method of guiding juvenile Pacific salmon. *The Canadian Fish Culturist*, 33.
- Russon, I.J.; Kemp, P.S. (2011). Advancing provision of multi-species fish passage: behaviour of adult European eel (*Anguilla anguilla*) and brown trout (*Salmo trutta*) in response to accelerating flow. *Ecological Engineering*, 37(12): 2018–2024.
- Sandlund, O.T.; Diserud, O.H.; Poole, R.; Bergesen, K.; Dillane, M.; Rogan, G.; Durif, C.; Thorstad, E.B.; Vollestad, L.A. (2017). Timing and pattern of annual silver eel migration in two European watersheds are determined by similar cues. *Ecology and Evolution*, 7: 5956–5966.
- Scaramuzza, D.; Martinelli, A.; Siegwart, R. (2006). A toolbox for easy calibrating omnidirectional cameras. *Proc. IEEE International Conference on Intelligent Robots and Systems (IROS)*. Beijing, China.
- Schalke, Isabella (2018). Modeling hazards related to large wood in rivers. *VAW-Mitteilung 249* (R.M. Boes, ed.). VAW, ETH Zurich, Switzerland.
- Schmalz, M.; Kranawettreiser, J.; Thürmer, K. (2012). Optimierung von Bypässen für den Fischabstieg (Optimisation of bypasses for fish downstream migration). *Technical Report*, Bauhaus-Universität Weimar, Schleusingen, Germany (in German).
- Schmalz, W.; Wagner, F.; Sonny, D. (2015). Arbeitshilfe zur standörtlichen Evaluierung des Fischschutzes und Fischabstieges (Practice guideline for the site-specific evaluation of fish protection and fish downstream migration). Ecologic Institute GmbH, Germany (in German).
- Schwevers, U. (1998). Die Biologie der Fischabwanderung (The biology of fish downstream migration). *Verlag Natur & Wissenschaft* (in German).
- Schwevers, U.; Adam, B. (2019). Fish protection technologies and fish ways for downstream migration. ISBN 978-3-030-19241-9. *Springer*.

- Schwinn, M.; Aarestrup, K.; Baktoft, H.; Koed, A. (2017). Survival of migrating sea trout smolts during their passage of an artificial lake in a Danish lowland stream. *River Research and Applications*, 33: 558–566.
- Scruton, D.A.; McKinley, R.S.; Kouwen, N.; Eddy, W.; Booth, R.K. (2003). Improvement and optimization of fish guidance efficiency (FGE) at a behavioural fish protection system for downstream migrating Atlantic salmon (*Salmo salar*) smolts. *River Research and Applications*, 19(5-6): 605–617.
- Shepherd, D. (1998). A preliminary study of the hydraulics of louver arrays. *PhD Thesis*, University of Alberta, Department of Civil and Environmental Engineering, Alberta, Canada.
- Shepherd, D.; Katopodis, C.; Rajaratnam, N. (2007). An experimental study of louvers for fish diversion. *Canadian Journal of Civil Engineering*, 34(6): 770–776.
- Silva, A.T.; Katopodis, C.; Santos, M.J.; Ferreira, M.T.; Pinheiro, A.N. (2012a). Cyprinid swimming behaviour in response to turbulent flow. *Ecological Engineering*, 44: 314–328.
- Silva, A.T.; Katopodis, C.; Tachie, M.F.; Santos, J.M.; Ferreira, M.T. (2016). Downstream swimming behaviour of catadromous and potamodromous fish over spillways. *River Research and Applications*, 32: 935–945.
- Silva, A.T.; Santos, J.M.; Ferreira, M.T.; Pinheiro, A.N.; Katopodis, C. (2012b). Passage efficiency of offset and straight orifices for upstream movements of Iberian barbel in a pool-type fishway. *River Research and Applications*, 28: 529–542.
- Simmons, R.A. (2000). Effectiveness of a fish bypass with an angled bar rack at passing Atlantic salmon and steelhead trout smolts at the Lower Saranac Hydroelectric Project. *Advances in fish passage technology - bioengineering section*: 95–102.
- Spalart, P.; Rumsey, C. (2007). Effective inflow conditions for turbulence models in aerodynamic calculations. *AIAA Journal*, 45(10).
- Spangler, J. (1928). Untersuchungen über den Verlust an Rechen bei schräger Zuströmung (Investigations on the head losse of rack with oblique approach flow). *Proc. Mitteilung H2 des hydraulischen Instituts der TH München*. Munich, Germany (in German).
- Stira, R.J.; Robinson, D.A. (1997). Effectiveness of a louver bypass system for downstream passage of Atlantic salmon smolts and juvenile clupeids in the Holyoke Canal, Connecticut River, Holyoke, Massachusetts. *Proc. Fish Passage Workshop*. Milwaukee (WI), United States: 6–8.
- Surek, D.; Stempin, S. (2007). Angewandte Strömungsmechanik (Applied hydromechanics).

- ISBN 978-3-8351-0118-0. *B.G. Teubner Verlag* (in German).
- Taylor, J.R. (1997). An introduction to error analysis - The study of uncertainties in physical measurements. ISBN 978-0935702750. 2nd edn. *Cambridge University Press*.
- Tomanova, S.; Courret, D.; Alric, A.; de Oliveira, E.; Lagarrigue, T.; Tétard, S. (2018). Protecting efficiently sea-migrating salmon smolts from entering hydropower plant turbines with inclined or oriented low bar spacing racks. *Ecological Engineering*, 122: 143–152.
- Townsend, A.A. (1980). The structure of turbulent shear flow. ISBN 978-0521298193. 2nd edn. *Cambridge University Press*.
- Travade, F.; Larinier, M. (1992). La migration de dévalaison: problèmes et dispositifs (Downstream migration: problems and solutions). *Bulletin Français de la Pêche et de la Pisciculture* (in French).
- Travade, F.; Larinier, M.; Subra, S.; Gomes, P.; De-Oliveira, E. (2010). Behaviour and passage of European silver eels (*Anguilla anguilla*) at a small hydropower plant during their downstream migration. *Knowledge and Management of Aquatic Ecosystems*, 398.
- Tritico, H.M.; Cotel, A.J. (2010). The effects of turbulent eddies on the stability and critical swimming speed of creek chub (*Semotilus atromaculatus*). *Journal of Experimental Biology*, 213(13): 2284–2293.
- Tsikata, J.; Tachie, M.; Katopodis, C. (2009). Particle image velocimetry study of flow near trashrack models. *Journal of Hydraulic Engineering*, 135(8).
- Tsikata, J.M.; Tachie, M.F.; Katopodis, C. (2014). Open-channel turbulent flow through bar racks. *Journal of Hydraulic Research*, 52(5): 630–643.
- Turnpenny, A.W.H.; O’Keeffe, N. (2005). Screening for intake and outfalls: a best practice guide. *Technical Report SC030231*, Environment Agency, Bristol, United Kingdom.
- Turnpenny, A.W.H.; Struthers, G.; Hanson, P. (1998). A UK guide to intake fish-screening regulations, policy and best practice with particular reference to hydroelectric power schemes. *Fawley Aquatic Research Laboratories Ltd.*, United Kingdom.
- Tutzer, R.; Brinkmeier, B.; Böttcher, H.; Aufleger, M. (2019). Der Elektro-Seilrechen als integrales Fischschutzkonzept. (The electric fish fence as an integral fish protection concept). *Wasserwirtschaft*, 109(2-3): 36–40 (in German).
- USBR (2006). Fish protection at water diversions – A guide for planning and designing fish exclusion facilities. *Technical Report*, U.S. Department of the Interior, Bureau of Reclamation, Denver, Colorado.

- USBR (2011). Modifications to bypass system operations to improve hydraulics at the Tracy fish collection facility. *Technical Report*, U.S. Department of the Interior, Bureau of Reclamation.
- VAW (2020). Fischleitrechen Kraftwerk Wildeggen-Brugg - Numerische Modelluntersuchung (Numerical model study of a fish guidance structure at the hydropower plant Wildeggen-Brugg). *Technical Report 4390*, Axpo Power AG (in German, unpublished).
- Venturelli, R.; Akanyeti, O.; Visentin, F.; Jezov, J.; Chambers, L.; Toming, G.; Brown, J.; Kruusmaa, M.; Megill, W.; Fiorini, P. (2012). Hydrodynamic pressure sensing with an artificial lateral line in steady and unsteady flows. *Bioinspiration & Biomimetics*, 7.
- Vowles, A.S.; Anderson, J.J.; Gessel, M.H.; Williams, J.G.; Kemp, P.S. (2014). Effects of avoidance behaviour on downstream fish passage through areas of accelerating flow when light and dark. *Animal Behaviour*, 92: 101–109.
- Vowles, A.S.; Kemp, P.S. (2012). Effect of light on the behaviour of brown trout (*Salmo trutta*) encountering accelerating flow: Application to downstream fish passage. *Ecological Engineering*, 47: 247–253.
- Wagner, F.; Warth, P.; Schmalz, W. (2019). Evaluierung von Fischschutz- und Fischabstiegsmaßnahmen an einem Wasserkraftstandort für die Umsetzung des WHG Art. 35. (Evaluation of fish protection and guidance measures at a hydroelectric facility for the implementation of the WFD Art. 35). *Technical Report*, Umweltbundesamt.
- Wahl, T. (2003). Discussion of "Despiking Acoustic Doppler Velocimeter Data" by Derek G. Goring and Vladimir I. Nikora. *Journal of Hydraulic Engineering*, 129(6): 484–487.
- Wardle, C.; Videler, J.; Altringham, J. (1995). Tuning in to fish swimming waves: body form, swimming mode and muscle function. *Journal of experimental Biology*, 198(8): 1629–1636.
- Webb, P.W.; Cotel, A.J. (2010). Turbulence: Does vorticity affect the structure and shape of body and fin propulsors? *Integrative and Comparative Biology*, 50(6): 1155–1166.
- Wilke, T.; Gnaudschn, E.; Schneider, T.; Teggers-Junge, S.; Ingendahl, D.; Weimer, P. (2019). Abschlussbericht zum Projekt Fischschutz und Fischabstieg der Pilotanlage Unkelmühle ('Final report on the fish protection and fish downstream migration protect at the pilot study site Unkelmühle'). *Technical Report*, Bezirksregierung Köln, innogy SE, Ministerium für Umwelt, Landwirtschaft, Natur- und Verbraucherschutz Nordrhein-Westfalen.
- Yates, F. (1934). Contingency tables involving small numbers and the chi-square test. *Royal Statistical Society*, 1(2): 217–235.

- Zaugg, C.; Mendez, R. (2018). Kleinwasserkraftwerk Stoppel – Wirkungskontrolle Fischabstieg am Horizontalrechen mit Bypass ('Small hydropower plant Stoppel – Fish downstream migration monitoring at the horizontal bar rack bypass system'). *Technical Report*, Axpo Power AG, Baden, Switzerland (in German).
- Zimmermann, J. (1969). Widerstand schräg angeströmter Rechengitter (Resistance of rack with oblique approach flow). *Institut für Wasserbau und Kulturtechnik, Versuchsanstalt für Wasserbau* (in German).